

# Kinetic Monte Carlo Simulation of Electrochemical Systems

Novel Algorithms for an Optimized Runtime Efficiency

**Manuel Otto Walter Gößwein, M.Sc.**

Vollständiger Abdruck der von der TUM School of Computation, Information and Technology der Technischen Universität München zur Erlangung des akademischen Grades eines

**Doktors der Ingenieurwissenschaften (Dr.-Ing.)**

genehmigten Dissertation.

**Vorsitz:**

Prof. Dr. Bernhard Wolfrum

**Prüfende der Dissertation:**

1. Prof. Dr. Alessio Gagliardi
2. Prof. Dr. Aliaksandr Bandarenka
3. Assoc. Prof. Andrea Reale

Die Dissertation wurde am 06.08.2024 bei der Technischen Universität München eingereicht und durch die TUM School of Computation, Information and Technology am 29.01.2025 angenommen.



*Se non è vero è molto ben trovato.*



# Preface

This thesis is a publication-based dissertation. It represents a concise summary of the cumulative scientific outcome from articles which have already been published in international peer-reviewed journals. The introduction outlines the motivation and broader context of the work regarding previous scientific contributions on the simulation of electrochemical systems with an emphasis on the kinetic Monte Carlo method. The methods section provides a summary of the developed concepts, methodologies and models to simulate electrochemical systems via the kinetic Monte Carlo method. The article summaries and the corresponding cross-article discussion demonstrate the contribution of the cumulative scientific results to progress in the associated research field. Concluding, the perspectives section discusses how the presented methods and models could be extended.



# Scientific Contributions

## Publications in International Peer-Reviewed Journals

### Core Publication I

Gößwein M.; Kaiser W.; Gagliardi A. Local Temporal Acceleration Scheme to Couple Transport and Reaction Dynamics in Kinetic Monte Carlo Models of Electrochemical Systems. *J. Chem. Theory Comput.* **2022**, *18*, 2749-2763.

### Core Publication II

Katzenmeier L.<sup>‡</sup>; Gößwein M.<sup>‡</sup>; Gagliardi A.; Bandarenka A.S. Modeling of Space-Charge Layers in Solid-State Electrolytes: A Kinetic Monte Carlo Approach and Its Validation. *J. Phys. Chem. C* **2022**, *126*, 10900-10909.

Katzenmeier L.<sup>‡</sup>; Gößwein M.<sup>‡</sup>; Carstensen L.; Sterzinger J.; Ederer M.; Müller-Buschbaum P.; Gagliardi A.; Bandarenka A.S. Mass Transport and Charge Transfer through an Electrified Interface between Metallic Lithium and Solid-State Electrolytes. *Comm. Chem.* **2023**, *6*, 124.

Kouroudis I.<sup>‡</sup>; Gößwein M.<sup>‡</sup>; Gagliardi A. Utilizing Data-Driven Optimization to Automate the Parametrization of Kinetic Monte Carlo Models. *J. Phys. Chem. A* **2023**, *127* (28), 5967-5978.

### Additional Publications

Kaiser, W.; Gößwein, M.; Gagliardi, A. Acceleration Scheme for Particle Transport in Kinetic Monte Carlo Methods *J. Chem. Phys.* **2020**, *152*, 174106.

## International Conference Contributions

M. Gößwein, A. Gagliardi. Origin of Exciton Dissociation in Hybrid Organic-Aqueous Electrolyte Devices. GEP-SLAP2022 Congress (XVI Meeting of the Specialized Group of Polymers – GEP 2022 and XVII Latin American Symposium of Polymers - SLAP 2022), Donostia-San Sebastián, Spain, May 8-12, 2022, *Poster Presentation*.

L. Katzenmeier, M. Gößwein, A.S. Bandarenka. Charge Distribution in Polarized Li-ion Solid Electrolytes: A Kinetic Monte Carlo Approach. 32nd Topical Meeting of the International Society of Electrochemistry, Stockholm, Sweden, June 19-22, 2022, *Poster Presentation*.

Kouroudis I., Gößwein M., Gagliardi A. Rationalizing Space Charge Layer Formation in Li<sup>+</sup> Solid-State Electrolytes: Data-Driven Surrogate and Bayesian Optimized Inverse Problem. MRS Spring Meeting & Exhibit, San Francisco, USA, April 10-14, 2023, *Oral Presentation*.

---

<sup>‡</sup>Shared first authorship: The authors contributed equally to this work.

## Miscellaneous Academic Contributions

M. Gößwein. Investigation of the Time-Dependent Double-Layer Formation in Saline Solutions. Hauptseminar Nanoelektronik, Technical University of Munich, Munich, Germany, November 25, 2020, *Oral Presentation*.

M. Gößwein, A. Gagliardi. Kinetic Monte Carlo Simulation of the Organic-Aqueous Electrolyte Interface. ECS Workshop on Advances in the Physics and Chemistry of Energy Conversion and Storage, Technical University of Munich, Raitenhaslach, Germany, July 8, 2022, *Oral Presentation*.

M. Gößwein. Local Temporal Acceleration in Kinetic Monte Carlo Models. TheoBiophysics Podcast, September, 2022. URL: <https://open.spotify.com/episode/4ktC7Ej864uZiaT26BwW6G>



# Abstract

Simulations based on the kinetic Monte Carlo (kMC) method are a popular tool to rationalize the dynamic behavior of a broad range of non-deterministic systems and processes. In recent years, kMC simulations have proven to be very suitable for gaining a deeper mechanistic understanding of many important electrochemical systems such as batteries, fuel cells or catalysts. However, one major limitation remains, namely their comparatively high computational costs - even though in the last three decades considerable research attention has been devoted to increasing the runtime efficiency of kMC models. In the context of electrochemical systems, large computational costs mainly arise from a combination of the following three issues: (1) inclusion of particle-particle interactions for high particle densities, (2) large time-scale disparities between two or more implemented physical processes, and (3) systematic input parametrization for systems with many degrees of freedom. While the first issue is nowadays well manageable by corresponding algorithms and access to high-performance computing clusters the latter two still remain problematic and are often the reasons to discard the kMC method for certain systems.

In this thesis, we present two distinct methodologies to improve the runtime efficiency of the original kMC algorithm for electrochemical systems. Firstly, we introduce a novel local temporal acceleration scheme to bridge the time scale disparity between fast charge and mass transport phenomena and slow reaction dynamics. Secondly, we present an innovative and robust data-driven optimization pipeline to automate the parametrization of kMC models. To showcase the working principles and the effectivity of our methodologies we apply each to an electrochemical test system of growing practical relevance: The local temporal acceleration scheme is demonstrated via a simplified kMC model of the photocurrent generation in hybrid organic/aqueous electrolyte devices whereas the data-driven feedback loop for automated parametrization is showcased via a kMC model for the space charge layer formation in solid-state electrolytes.

The core ideas of the local temporal acceleration scheme are (1) to combine the superbasin concept with a local, particle-based criterion for the quasi-equilibrium detection, and (2) a partitioning of transitions and particles in the system into process chains. Scaling of entire quasi-equilibrated process chains considerably reduces the computational effort without disturbing the relative dynamics of transitions within a process chain. As a core feature, our algorithm captures local inhomogeneities such that local physical quantities can be reproduced accurately. Additionally, we show that previous accelerated superbasin algorithms fail in presence of spatially varying time scale disparities. Our algorithm achieves an acceleration of several orders of magnitude ( $\approx 10^6$ ) providing a serious alternative to replace existing multiscale models by stand-alone kMC simulations.

To enable a systematic and data-efficient input parametrization we equip the original kMC algorithm with a feedback loop consisting of Gaussian Processes (GPs) and Bayesian optimization (BO). We utilize the results from fast-converging kMC simulations to construct a database for training a cheap-to-evaluate surrogate model based on Gaussian processes. Combining the surrogate model with a target-specific acquisition function enables us to apply Bayesian optimization for the guided prediction of suitable input parameters. Thus, the amount of trial simulation runs can be considerably reduced facilitating an efficient utilization of arbitrary kMC models. Our data-driven approach requires only 1 to 2 iterations to reconstruct the input parameters from different baseline simulations within the training data set. Moreover, we show that the methodology is even capable of accurately extrapolating into regions outside the training data set which are computationally expensive for direct kMC simulation. Further, we demonstrate the high accuracy of the underlying surrogate model via a full parameter space investigation eventually making the original kMC simulation for certain use cases obsolete.



# Zusammenfassung

Simulationen basierend auf der kinetischen Monte Carlo Methode sind ein beliebtes Werkzeug, um das dynamische Verhalten einer Vielzahl von stochastischen Systemen und Prozessen zu erklären. In den letzten Jahren haben kMC Simulationen entscheidend dazu beigetragen, ein tieferes Verständnis für viele wichtige elektrochemische Systeme zu erlangen wie beispielsweise Batterien, Brennstoffzellen oder Katalysatoren. Eine große Einschränkung von kMC Simulationen sind allerdings ihr verhältnismäßig hoher Rechenaufwand, und das obwohl in den letzten drei Dekaden viel Forschungsarbeit aufgewandt wurde, um ihre Laufzeit effizienter zu gestalten. Im Kontext von elektrochemischen Systemen kann der hohe Rechenaufwand auf eine Kombination der folgenden drei Ursachen zurückgeführt werden: (1) Einbindung von Teilchen-Teilchen Wechselwirkungen für hohe Teilchendichten, (2) große Zeitskalendifferenzen zwischen zwei oder mehr implementierten physikalischen Prozessen, und (3) systematische Parametrisierung von Eingangsgrößen für Systeme mit vielen Freiheitsgraden. Während der erste Punkt heutzutage durch entsprechende Algorithmen und Hochleistungsrechenzentren gut kontrollierbar ist, sind die letzten beiden Punkte nach wie vor problematisch und führen mitunter dazu, dass die kMC Methode für bestimmte Systeme nicht mehr verwendet wird.

In dieser Arbeit werden zwei neuartige Methoden vorgestellt, um die Laufzeit von kMC Simulationen für elektrochemische Systeme effizienter zu gestalten. Zunächst wird ein neuartiger lokaler Beschleunigungsalgorithmus eingeführt mit dem Ziel, die Zeitskalendifferenz zwischen schnellen Ladungs-/Massentransport und langsamer Reaktionsdynamik zu reduzieren. In einem zweiten Schritt wird eine innovative und robuste datengestützte Optimierungsstrategie präsentiert, um die Parametrisierung von kMC Modellen zu automatisieren. Die Funktionsweise und Wirksamkeit der eingeführten Algorithmen wird unter Beweis gestellt, indem sie jeweils auf ein elektrochemisches Testsystem mit wachsender praktischer Relevanz angewendet werden. Der lokale Beschleunigungsalgorithmus wird durch ein vereinfachtes kMC Modell für die Photostrom-Generation in hybriden organischen Bauelementen demonstriert, die eine Grenzfläche zwischen einem organischen Halbleiter und einem flüssigen Elektrolyten aufweisen. Die datengestützte Rückkopplungsschleife zur automatisierten Parametrisierung wird hingegen durch ein kMC Modell für die Raumladungszonen-Formation in Festkörperelektrolyten demonstriert.

Der lokale Beschleunigungsalgorithmus beruht auf den folgenden zwei zentralen Ideen: (1) Verwendung eines lokalen, teilchen-basierten Kriteriums zur Erkennung, ob sich das System in einem energetischen Minimum verbunden mit einem Quasi-Gleichgewichtszustand befindet, und (2) Aufteilung von Transitionen und Teilchen im System in entsprechende Prozessketten. Die Skalierung ganzer Prozessketten, die sich in einem Quasi-Gleichgewichtszustand befinden, führt zu einer enormen Laufzeitverkürzung, ohne dabei die relative Dynamik der Transitionen innerhalb einer Prozesskette zu verfälschen. Ein zentrales Merkmal des entwickelten Algorithmus ist die Erhaltung lokaler Inhomogenitäten, sodass lokale physikalische Eigenschaften auch in der beschleunigten Simulation korrekt abgebildet werden. Darüber hinaus wird gezeigt, dass bisherige Beschleunigungsalgorithmen fehlerhafte Ergebnisse liefern, wenn Zeitskalendifferenzen räumlich verteilt sind. Der neuartige Algorithmus hingegen erreicht bei unveränderter Genauigkeit eine Beschleunigung im Bereich mehrerer Größenordnungen ( $\approx 10^6$ ) und ist somit eine ernsthafte Alternative, um bestehende Multiskalen-Modelle durch einzelne kMC Modelle zu ersetzen.

Zur systematischen und daten-effizienten Parametrisierung von Eingangsgrößen wird der ursprüngliche kMC Algorithmus durch eine Rückkopplungsschleife bestehend aus Gauß-Prozessen und Bayes'scher Optimierung erweitert. Mit den Ergebnissen schnell-konvergierender kMC Simulationen wird eine Datenbank erzeugt, um ein Surrogatmodell basierend auf Gauß-Prozessen zu trainieren, das mit wenig Rechenaufwand ausgewertet werden kann. Die Kombination des Surrogatmodells mit einer an die Ausgangsgrößen angepassten Akquisitionsfunktion ermöglicht dann den Einsatz von Bayes'scher Optimierung zur

zielgerichteten Vorhersage von geeigneten Eingangsparametern. Somit kann die Anzahl an Testsimulationsdurchläufen deutlich reduziert werden, was einem effizienteren Einsatz beliebiger kMC Modelle gleichkommt. Der datengestützte Ansatz benötigt maximal zwei Iterationen, um die Eingangsgrößen von unterschiedlichen Referenzsimulationen innerhalb des Trainingsdatensatzes zu rekonstruieren. Darüber hinaus besitzt der datengestützte Algorithmus die Fähigkeit mit hoher Genauigkeit in Gebiete außerhalb des Trainingsdatensatzes zu extrapolieren, was insbesondere dann nützlich ist, wenn die direkte Simulation mittels kMC in solchen Gebieten äußerst rechenaufwendig ist. Weiterhin wird die hohe Genauigkeit des zugrundeliegenden Surrogatmodells durch eine vollständige Abtastung des Parameterraums demonstriert, was die ursprüngliche kMC Simulation für bestimmte Anwendungsfälle gänzlich obsolet macht.

# Contents

<b>Preface</b>	<b>v</b>
<b>Scientific Contributions</b>	<b>vii</b>
<b>Abstract</b>	<b>ix</b>
<b>Zusammenfassung</b>	<b>xi</b>
<b>1 Introduction</b>	<b>1</b>
1.1 Broader Context . . . . .	1
1.2 Temporal Acceleration of Kinetic Monte Carlo Models . . . . .	2
1.3 Automated Parametrization of Kinetic Monte Carlo Models . . . . .	3
1.4 Electrochemical Test Systems . . . . .	4
1.4.1 Hybrid Organic/Aqueous Electrolyte Interface . . . . .	4
1.4.2 Space-Charge Layer Formation in Solid-State Electrolytes . . . . .	5
<b>2 Methods</b>	<b>7</b>
2.1 The Kinetic Monte Carlo Method . . . . .	7
2.1.1 Generic Algorithm . . . . .	7
2.1.2 Algorithm Procedure . . . . .	7
2.2 Local Temporal Acceleration of Kinetic Monte Carlo Models . . . . .	9
2.2.1 Extended Algorithm Procedure . . . . .	9
2.2.2 Partitioning into Process Chains . . . . .	9
2.2.3 Detection of Local Quasi-Equilibrium . . . . .	9
2.2.4 Dynamic Scaling of Quasi-Equilibrated Process Chains . . . . .	12
2.3 Automated Parametrization of Kinetic Monte Carlo Models . . . . .	13
2.3.1 Extended Algorithm Procedure . . . . .	13
2.3.2 Bayesian Optimization . . . . .	13
2.3.3 Gaussian Processes . . . . .	15
2.4 Kinetic Monte Carlo Model of the Space Charge Layer Formation in Solid-State Electrolytes	17
2.4.1 Experimental and Simulation Set-Up . . . . .	17
2.4.2 Modeling of Li-ion Dynamics . . . . .	17
2.5 Kinetic Monte Carlo Model of the Photocurrent Generation at the Organic/Aqueous Electrolyte Interface . . . . .	20
2.5.1 Experimental and Simulation Set-Up . . . . .	20
2.5.2 Modeling of Particle Dynamics . . . . .	22
2.5.3 Parametrization of Temporal Acceleration Scheme . . . . .	22
<b>3 Publications</b>	<b>25</b>
3.1 Local Temporal Acceleration Scheme to Couple Transport and Reaction Dynamics in Kinetic Monte Carlo Models of Electrochemical Systems . . . . .	25
3.2 Utilizing Data-Driven Optimization to Automate the Parametrization of Kinetic Monte Carlo Models . . . . .	27
3.3 Modeling of Space-Charge Layers in Solid-State Electrolytes. A Kinetic Monte Carlo Approach and its Validation . . . . .	29

3.4 Mass Transport and Charge Transfer Through an Electrified Interface Between Metallic Lithium and Solid-State Electrolytes . . . . .	31
<b>4 Cross-Article Discussion and Conclusions</b>	<b>33</b>
<b>5 Perspectives</b>	<b>35</b>
<b>Bibliography</b>	<b>39</b>
<b>Original Publications and Reuse Permissions</b>	<b>51</b>

# List of Figures

2.1	Flowchart of a generic, particle-based kinetic Monte Carlo algorithm. . . . .	8
2.2	Extended flowchart of a generic kinetic Monte Carlo algorithm including steps for a local temporal acceleration scheme . . . . .	10
2.3	Schematic representation of the concepts utilized in the local temporal acceleration scheme	11
2.4	Extended flowchart of a generic, particle-based kinetic Monte Carlo algorithm including a feedback loop for automated parametrization . . . . .	14
2.5	Experimental setups and kinetic Monte Carlo model for the space charge layer formation in solid-state electrolytes. . . . .	18
2.6	Experimental setup and kinetic Monte Carlo model for the photocurrent generation at the organic-aqueous electrolyte interface. . . . .	21
3.1	Local temporal acceleration scheme for coupled transport-reaction simulations in kinetic Monte Carlo models of electrochemical systems . . . . .	26
3.2	Automated parametrization of kinetic Monte Carlo models via data-driven optimization . .	28
3.3	Kinetic Monte Carlo modeling of space-charge layers in solid-state electrolytes under blocking conditions . . . . .	30
3.4	Kinetic Monte Carlo modeling of the mass/charge transfer at the SSE/lithium metal interface under non-blocking conditions . . . . .	32





# List of Tables

- 2.1 Input parameters of the temporal acceleration scheme for the organic-liquid interface model. 23



# 1 Introduction

## 1.1 Broader Context

The following overview is reprinted in parts with permission from (1) ref. 1, *J. Phys. Chem. A* **2023**, 127 (28), 5967-5978. Copyright 2023 American Chemical Society (ACS), and (2) ref. 2, *J. Chem. Theory Comput.* **2022**, 18, 2749-2763. Copyright 2022 American Chemical Society (ACS).

The term *Monte Carlo method* denotes a variety of different computer-aided algorithms which apply random numbers to obtain a numerical solution for real world problems. A particularly relevant subclass are kinetic Monte Carlo (kMC) simulations. They have been used extensively to model the dynamic behavior of a broad range of non-deterministic physical and electrochemical processes and systems such as crystal growth [3, 4, 5], vacancy diffusion [6, 7, 8], charge transport in disordered materials [9, 10, 11], catalysis [12, 13, 14, 15, 16] and organic solar cells [17, 18, 19, 20]. An increasingly important but yet demanding field for kMC simulations are electrochemical systems. For instance, Alkire and coworkers investigated the early stages of kinetically limited electrodeposition [21]. Another study dealt with the CO adlayer electrooxidation on nanoparticle catalysts [22]. In the context of renewable energy cycles, electrochemical kMC simulations helped to gain a detailed mechanistic understanding of battery [23, 24, 25, 26] and fuel cell operation [27, 28, 29]. The popularity of kMC is due to several favorable intrinsic properties [30]:

- 1 As a mesoscopic approach, kMC often provides a good tradeoff in spatio-temporal resolution.
- 2 Individual particle-based processes can be included to investigate their time-/frequency-dependent behavior.
- 3 Arbitrarily complex morphologies/geometries can be incorporated without facing potential convergence issues.
- 4 kMC simulations are no mean-field approximations but inherently discrete, and therefore enable to take into account local structural effects and the influence of particle-particle interactions.

In the context of electrochemical systems, kMC models map material properties, in particular structural and energetic information, onto a discrete set of states [11, 31]. Discrete transitions propagate the system, e.g. by the motion of particles or electrochemical reactions, resulting in a stochastic time-evolution of the system within its phase space. The kinetic information results from the details of the transition rates which capture the underlying physics and define the probability of performing the respective transition.

However, one major limitation of kMC models are their comparatively high computational costs. Due to the stochastic nature of the kMC algorithm a sufficient number of independent simulation runs is required to make reliable statements about the average time-evolution of output quantities. For stationary quantities this issue is at least partially alleviated as it is sufficient to perform block-averaging over steady-state configurations of a single simulation run [18]. Another potential computational bottleneck arises from the inclusion of particle-particle interactions as their algorithmic complexity inherently scales as  $\mathcal{O}(N^2)$  where  $N$  is the number of particles. In literature, there are numerous different approaches for the efficient treatment of particle-particle interactions ranging from the classical Ewald Summation [32, 33] with  $\mathcal{O}(N^{\frac{3}{2}})$  to more advanced strategies such as the fast multipole method [34, 35] with  $\mathcal{O}(N)$ . Additional improvements in runtime efficiency can be achieved by applying precalculations [18] and local caching schemes [36]. Further, large computational costs occur in kMC models which feature large time-scale disparities between two or more implemented processes [37]. The kMC algorithm naturally favors the

execution of fast processes due to their higher relative probabilities. Consequently, a system with fast processes on time scale  $t_f$  and slow processes on time scale  $t_s \gg t_f$  requires approximately  $t_s/t_f$  kMC steps to sample the slow process only once. The insufficient sampling of slow processes is in particular problematic if they represent the critical transition to obtain certain system properties. A concrete example of time scale disparities in electrochemical systems can be found in the intermediate diffusion within surface catalytic processes [22]. Mass transport of ionic or molecular species between active surface sites can be much faster than the catalytic surface reactions. To keep the computational effort low, many studies either neglect mass transport and with this potential mass transport limitations [28] or limit their studies to systems without distinct time scale disparities [24, 29]. Finally, in electrochemical systems with several unknown input parameters most of the simulation time is often required for systematic input parametrization. Systems with many degrees of freedom would highly profit from a data-efficient parametrization scheme. Otherwise, kMC models remain restricted to a basic mechanistic analysis of the system dynamics. Exact reproduction of experimental results, device optimization and material screening require streamlined guidance in input parameter search to become feasible.

In this thesis, we present two distinct methodologies to improve the runtime efficiency of the original kMC algorithm for electrochemical systems. Firstly, we introduce a novel local temporal acceleration scheme to bridge the time scale disparity between fast charge and mass transport phenomena and slow reaction dynamics. Secondly, we present an innovative and robust data-driven optimization pipeline to automate the parametrization of kMC models. To showcase the working principles and the effectivity of our methodologies we apply each to an electrochemical test system of growing relevance: The local temporal acceleration scheme is demonstrated via a simplified kMC model of the photocurrent generation in hybrid organic/aqueous electrolyte devices whereas the data-driven feedback loop for automated parametrization is showcased via a kMC model for the space charge layer formation in solid-state electrolytes. In the following two sections, we provide a brief literature review on temporal acceleration as well as automated parametrization of kinetic Monte Carlo models. We conclude with a brief introduction to the electrochemical test systems considered in this thesis.

## 1.2 Temporal Acceleration of Kinetic Monte Carlo Models

The following literature review is reprinted with permission from ref. 2, *J. Chem. Theory Comput.* **2022**, *18*, 2749-2763. Copyright 2022 American Chemical Society (ACS).

There are two approaches to bridge time scale disparities in electrochemical systems: multiscale models and temporal acceleration schemes. Multiscale models typically couple continuum models using partial differential equations to derive system properties such as mass or charge distribution which are fed into kMC *e.g.* in form of background potentials [38]. Applications of multiscale methods cover *e.g.* heterogeneous catalytic reactors [39, 40], fuel cells [41, 42, 43], and lithium-ion batteries [44, 45]. Continuum models are mean-field approximations [46] and consequently assume isotropic mass transport. For active interfaces with complex shapes, this assumption fundamentally breaks down as mass transport may become heterogeneous due to the interaction with charged species and the local interface geometry [22, 24].

Different procedures have been developed to overcome large time scale disparities to accelerate kMC simulations [37]. A popular choice in the community is the  $\tau$ -leaping method which accelerates kMC simulations by the execution of multiple fast events in a single kMC step [47] and is frequently applied when time scale disparities arise from strongly differing particle concentrations [48]. However,  $\tau$ -leaping is only viable if the system state does not change too much during the leap [49]. Another acceleration procedure is the probability weighted kMC method [50] which, by normalization of transition probabilities, increases the sampling of rare events. While ensemble averages are typically well reproduced, statistical errors may be amplified leading to physically inconsistent behavior. Snyder *et al.* proposed the net-event kMC technique [51] which lumps fast, reversible processes into a single net-event. An appealing property of this approach is that a substantial speed-up is accompanied with correct ensemble averaged quantities, while fluctuations in corresponding transients are considerably reduced. Nevertheless, problems may arise in

the presence of large time scale disparities, especially if the fluctuations of net-rates become significantly larger than the transition rates of slow processes. In such cases, heuristic criteria must decide whether the instantaneous net-rate is statistically significant.

A major milestone has been achieved by the introduction of the accelerated superbasin-kMC method (AS-kMC) [52]. The rationale of AS-kMC is to detect superbasins in which the system is being trapped, and to subsequently raise the activation barrier of quasi-equilibrated processes to facilitate the escape from superbasins. AS-kMC has been shown to perform well for several simple toy systems [52] and to small silicon nanocrystal networks [53]. The applicability is limited to small systems as the superbasin detection requires large databases and efficient search algorithms. For large superbasins, the dynamical sampling procedure becomes unfeasible and, in the worst case, may not generate any speed-up at all. Recently, we extended the AS-kMC concept for the temporal acceleration of particle transport simulations through disordered semiconductors [54] by the detection of potential superbasins during system initialization resulting in a substantial speed-up.

Inspired by the AS-kMC, Dybeck *et al.* [55] developed a generalized temporal acceleration scheme, further referred to as the Dybeck scheme, for kMC simulations of surface catalytic processes. Their algorithm partitions the reaction network into quasi-equilibrated and non-equilibrated reaction channels, and detects and scales the rate constants of quasi-equilibrated reaction channels on the fly. The Dybeck scheme has been applied successfully to several surface catalytic kMC studies [14, 15, 16, 56, 57, 58], while its potential limitations are not fully explored. Exemplary, its accuracy in the presence of local inhomogeneities and strong fluctuations is not ensured. Existing applications of the Dybeck scheme further assume evenly distributed time scale disparities over the active nanoparticle surface, which may not be guaranteed in presence of mass and charge transport. Finally, it is questionable whether charge/mass transport towards the active interface can be handled accurately by treating it as a quasi-equilibrated reaction channel as suggested by Dybeck *et al.* [55].

### 1.3 Automated Parametrization of Kinetic Monte Carlo Models

The following literature review is reprinted with permission from ref. 1, *J. Phys. Chem. A* **2023**, 127 (28), 5967-5978. Copyright 2023 American Chemical Society (ACS)

So far, different methodologies have been proposed to parametrize kMC models. The most common choice in the research community is still the straightforward parameter sweep [59, 60] supported by a literature review for existing parameters [61]. Other methods automate parametrization via the utilization of a random walk [25, 62] or a genetic algorithm such as particle swarm optimization [63]. More advanced approaches are based on replacing the kMC simulation by a corresponding surrogate model. For instance, Sestito *et al.* applied multi-objective Bayesian optimization (BO) in the context of a dimensionality reduction scheme for kMC diffusion models to calibrate the parameters of a simplified one-dimensional kMC diffusion model. [64] Another surrogate-assisted kinetic Monte Carlo method utilizes Gaussian processes (GPs) to predict the stationary shape in kinetically controlled copper electrodeposition. [65] However, the combination of BO and GPs in terms of a strong, data-driven surrogate model is yet relatively unexplored. It has been proven to be powerful in the field of compositional engineering [66, 67], for high throughput laboratories [68], for the optimization of quantum cascade detectors [69] and in kMC models for structural prediction [70].

## 1.4 Electrochemical Test Systems

### 1.4.1 Hybrid Organic/Aqueous Electrolyte Interface

Minor parts of the following overview are reprinted with permission from ref. 2, *J. Chem. Theory Comput.* **2022**, *18*, 2749-2763. Copyright 2022 American Chemical Society (ACS).

As an application of the local temporal acceleration scheme for electrochemical systems, we consider the interface between a photoactive polymer and an aqueous electrolyte - the inherent feature of so-called hybrid organic/aqueous electrolyte devices. The hybrid device structure paved the path for a manifold of novel applications ranging from organic photoelectrodes for water-splitting [71, 72, 73, 74, 75, 76, 77] to electrolyte-gated field effect transistors (EGTs) [78, 79, 80, 81] as well as organic electrochemical transistors (OECTs) and most importantly bioelectronics [82, 83, 84, 85, 86, 87, 88]. The latter applications rely on organic materials as exogeneous light-sensitive actuators for optical modulation/stimulation of cell electrophysiological activity [89]. However, the actual mechanism(s) causing photostimulation of cell activity *in vitro/vivo* are still under debate, with photocapacitive charging [90, 87, 91, 76], photothermal processes [92] and photoelectrochemical reactions (*i.e.* photofaradaic processes) [90, 88, 76] as the three prevailing alternative mechanisms.

To gain a full theoretical understanding of the photoelectrochemical processes at the organic/aqueous electrolyte interface it is vital that experiments are accompanied by numerical simulations. Quantum mechanical simulations have been utilized to investigate the electronic structure of the P3HT/water interface revealing that the outermost layer of the polymer is affected by water-induced polarization which leads to polaron formation [93] and a marked energetic downshift of HOMO and LUMO levels [94]. Molecular dynamics simulations could confirm a molecular reorientation in the surface structure of regio-regular P3HT thin films exposed to aqueous electrolytes, with respect to their surface structure in air [95]. One-dimensional drift-diffusion models have been formulated to rationalize the photovoltage build-up on different time-scales [96, 97]. Electrochemical impedance spectroscopy has been applied to model photocapacitive and photofaradaic processes at the hybrid interface on a circuit level [90, 76]. Beyond these studies, considerable research attention has been devoted to the reversible and irreversible interactions of P3HT with molecular oxygen, resulting in the unambiguous identification of a reversible charge transfer complex between P3HT and triplet oxygen in air as well as in water [98, 99, 100, 101, 102]. However, a clear mechanistic picture regarding the complex dynamic interplay of processes and particles leading to the generation of a measurable photocurrent remains still elusive, *e.g.* the contribution of different exciton dissociation mechanisms is highly controversial.

A modeling approach that has been largely overlooked so far is the kinetic Monte Carlo method. As outlined above, there are stand-alone kMC models for mass-transport in batteries [24, 103, 104, 1], charge transport in disordered organic devices [105, 106, 107, 10, 11] as well as reaction networks [55, 13, 14, 15]. The latter three systems lay the theoretical groundwork for a kMC model of the organic/aqueous electrolyte interface. The challenge in kMC modeling is to couple the slow reaction dynamics ( $\approx$  s to  $\mu$ s) at the vicinity of the hybrid interface with the fast electronic processes ( $\approx$  ns to ps). As the time scale disparity is involving the crucial reduction reactions at the hybrid interface, the transport of electrons to the interface is expected to play a crucial role in the system dynamics and consequently must be treated accurately. In the scope of this thesis, we simulate a simplified version of the organic/aqueous electrolyte interface to illustrate the capabilities of the algorithm as well as its sensitivity to different sets of input parameters. Additionally, the set-up is suitable for a comparison to the Dybeck scheme [55].

## 1.4.2 Space-Charge Layer Formation in Solid-State Electrolytes

The following overview is in parts reprinted with permission from (1) ref. 1, *J. Phys. Chem. A* **2023**, 127 (28), 5967-5978. Copyright 2023 American Chemical Society (ACS), and (2) ref. 103, *J. Phys. Chem. C* **2022**, 126, 10900-10909. Copyright 2022 American Chemical Society (ACS).

To demonstrate the capabilities of the data-driven optimization pipeline for automated parametrization we consider a physically more intuitive process from the field of electrochemistry: the space-charge layer (SCL) formation in solid-state electrolytes (SSEs) under blocking conditions as it occurs in all-solid-state batteries (ASSB). In recent years, ASSBs have gained increasing attention as a promising substitute for traditional Li-ion batteries due to their potentially longer lifespan, higher energy density, and enhanced safety [108, 109].

The transport of ions in SSEs can be described by a thermally activated hopping mechanism between unoccupied lattice vacancies [110, 111]. Unless a hopping transition is executed, each ion is spatially assigned to a vacancy. Such a configuration can be interpreted as a kind of localized state. Accordingly, the overall transport dynamics can be described by hops from one localized state to another. In this sense, ionic motion in SSEs fulfills the criteria of a so-called infrequent-event system. A very well-established theoretical approach to model such systems is the kinetic Monte Carlo (kMC) method. In the direct context of solid-state electrolytes, kMC also has been applied. For instance, Wolverton and coworkers calculated the room-temperature ion conductivities of cation- and anion-substituted  $\text{LiBH}_4$ -based SSEs [112]. Very recently, Dean et al. showed that grain boundary space-charge regions in SSEs can exhibit over- as well as underscreening [113].

During the thesis, we developed a simple yet predictive kMC model to simulate the mass-transport phenomenon occurring in SSEs under blocking and non-blocking conditions [103, 104]. The model was able to reproduce the quantitative trends in SCL thicknesses (accumulation and depletion layer) as previously determined by electrochemical impedance spectroscopy [114] and spectroscopic ellipsometry [115]. The SCL formation in SSEs showcases a perfect example for a system with several open input parameters, which extremely profits from a guided and data-efficient parametrization scheme. In the original study for blocking conditions, we conducted a total of 153 simulations to investigate the influence of different input quantities. This brute-force parameter space exploration served as a starting point for constructing a database to train the surrogate model of the data-driven optimization pipeline. We later on added almost exclusively the results of fast-converging simulations and additionally implemented a smart sparse sampling strategy for low-impact input parameters.





## 2 Methods

### 2.1 The Kinetic Monte Carlo Method

The following concepts are adapted and in parts reprinted with permission from ref. 1, J. Phys. Chem. A 2023, 127, 28, 5967–5978. Copyright 2023 American Chemical Society (ACS).

#### 2.1.1 Generic Algorithm

The kinetic Monte Carlo method is a numerical algorithm to sequentially propagate a system through different states within its configuration space. Fundamental contributions to the modern kMC algorithm have been made by Bortz *et al.* in 1975 [116] and Gillespie in the late 1970s [117, 31]. In general, the kMC method is based on *coarse-graining* the system dynamics into a set of long-term states  $\{i\}$  which are interconnected by discrete transitions. Given an arbitrary initial state  $i$  the system may transition into a set of potential final states  $\{j\}$ . Each transition  $i \rightarrow j$  is linked to a transition rate,  $k_{ij}$ , which is proportional to the relative execution probability,  $p_{ij}$ , of the underlying physical process:

$$p_{ij} = \frac{k_{ij}}{k_{\text{tot}}} = \frac{k_{ij}}{\sum_j k_{ij}} \quad (2.1)$$

where  $k_{\text{tot}}$  is the cumulative transition rate. The transition rates are a subset of the input parameters required by the kMC model. Usually, they are taken from experimental measurements or underlying physical models. The stochastic time-evolution of the system is computed in the so-called *Monte Carlo step*. In each simulation step, two uniform random numbers  $r_1, r_2 \in (0, 1)$  are drawn to determine which transition,  $\mu$ , is executed and how much simulated time,  $\tau$ , elapsed before the execution of the transition. In the  $n$ -fold or direct method as outlined in ref. 31, we may use  $r_1$  to pick  $\mu$  from the set  $\{p_{ij}\}$  via

$$\sum_{j=1}^{\mu-1} p_{ij} < r_1 \leq \sum_{j=1}^{\mu} p_{ij} \quad (2.2)$$

and  $r_2$  to calculate a corresponding time-step

$$\tau = -\frac{\log(r_2)}{k_{\text{tot}}} \quad (2.3)$$

Based on (2.2) and (2.3) the system state  $i \rightarrow j$  and the simulated time  $t_i \rightarrow t_j = t_i + \tau$  are updated. To perform the next Monte Carlo step the transition rates must be recomputed in the new system state. The stochastic time-evolution of the investigated system results from repeated execution of the outlined procedure often denoted as the so-called *Monte Carlo loop*. The simulation is terminated when a user-defined condition is fulfilled, *e.g.* a stationary state is reached or the simulated time exceeds a certain predefined threshold,  $t \geq t_{\text{stop}}$ .

#### 2.1.2 Algorithm Procedure

From a user's point of view the theoretical framework of the kinetic Monte Carlo algorithm boils down to the repeated execution of the Monte Carlo loop which results in a trajectory in the configuration space of the considered physical system. The complete algorithm procedure of a generic, particle-based kMC

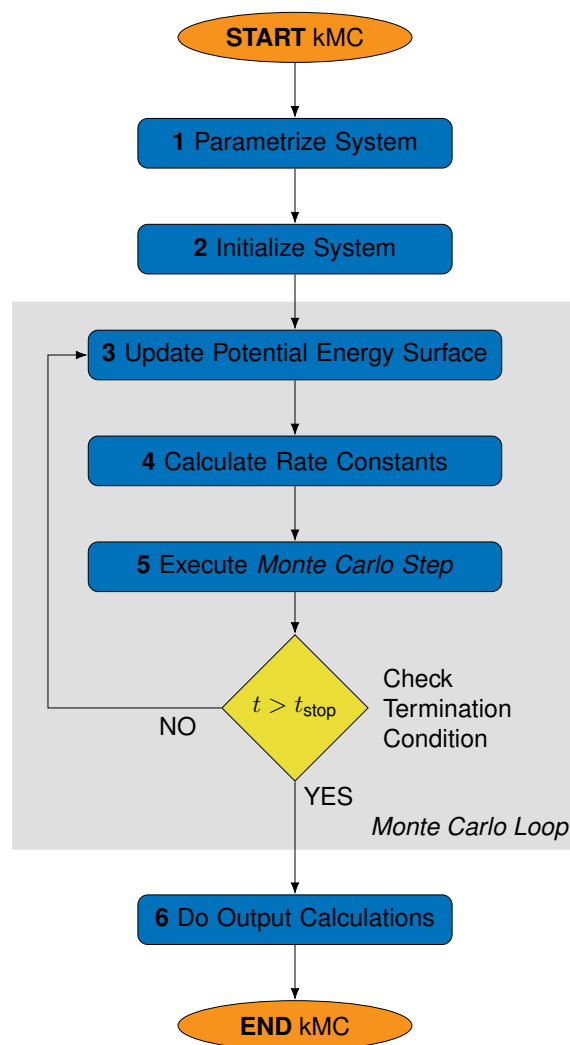


**Figure 2.1 Flowchart of a generic, particle-based kinetic Monte Carlo algorithm.** The repeated execution of the Monte Carlo loop generates a phase-space trajectory for the system under investigation. The kinetic Monte Carlo algorithm is obtained by adding parametrization and initialization as well as post-processing steps. Adapted with permission from ref. [1]. Copyright 2023 American Chemical Society (ACS).

algorithm is obtained by adding parametrization and initialization steps before and post-processing steps after the Monte Carlo loop, see Figure 2.1 for a flowchart. The individual steps can be summarized briefly as follows:

- 1 Parametrize System: Selection of appropriate input parameters to generate given output quantities.
- 2 Initialize System: Generation of a discrete grid with geometrical and physical information (e.g. positions and static energies); population of the grid with particles.
- 3 Update Potential Energy Surface: Recalculation of Coulomb interactions of each charged particle with all other charged particles according to current system configuration.
- 4 Calculate Rate Constants: Computation of the local transition rates based on the updated potential energy surface.
- 5 Execution of Monte Carlo Step: Generation of two uniform random numbers to select a transition via (2.2) and a corresponding time-step via (2.3).
- 6 Do Output Calculations: Calculation of output quantities from the raw tracking data of the kMC simulation.

## 2.2 Local Temporal Acceleration of Kinetic Monte Carlo Models

The following concepts are adapted and in parts reprinted with permission from ref. 2, J. Chem. Theory Comput. 2022, 18, 5, 2749–2763. Copyright 2022 American Chemical Society (ACS).

### 2.2.1 Extended Algorithm Procedure

To couple transport and reaction dynamics in kMC models of electrochemical systems we developed a local temporal acceleration scheme which substantially extends the original Monte Carlo loop, see Figure 2.2. In the following, we focus on the additional computational steps required by the acceleration scheme: (1) partitioning of processes and particles into process chains, (2) detection of local quasi-equilibrium, and (3) dynamic scaling of quasi-equilibrated process chains. For means of visualization, we apply the acceleration scheme to a hybrid organic-aqueous electrolyte device (OLI) made of an energetically disordered organic semiconductor coupled to an aqueous electrolyte solution, see Section 2.5 for a detailed description of the underlying kMC model.

### 2.2.2 Partitioning into Process Chains

The acceleration scheme starts with the partitioning of the processes and the particles into *process chains*. Process chains consist of concrete transitions, which ideally are of similar time scales, and of a set of particles for the quasi-equilibrium detection. In case of the OLI, we can partition the system into three process chains: (1) charge transport, generation and recombination in the semiconductor, (2) mass transport of the cations  $C^+$  and the product  $C$  in the electrolyte and the oxidation at the counter electrode, and (3) the reduction reaction at the interface. The interplay of these process chains determines the local densities of the individual species in the system and especially at the interface. As process chain (1), *i.e.* the fast processes of the charge carriers, is substantially faster than process chain (3), *i.e.* the slow reduction reaction at the interface, *local quasi-equilibria* of the particle densities in the environment of the interface will arise and consequently the local reaction activity will remain essentially constant. Thus, we say that process chain (1) is *quasi-equilibrated* and consequently further sampling of the fast processes in process chain (1) produces no additional information with respect to the system dynamics. Accordingly, it is possible to downscale the rates of quasi-equilibrated process chains by appropriate scaling factors to decrease the time scale disparity and enable a more frequent sampling of slow reduction reactions. Figure 2.3a illustrates the scaling procedure for the investigated system. Each of the three process chains ( $m$ ) is represented by a corresponding rate  $r_m$ . The fast process chains (1) and (2) comprise three different transitions including fast transport rates which are substantially larger than reduction rate  $r_3$ . The algorithm reduces  $r_1$  and  $r_2$  to  $r_s = N_f r_3$  such that on average  $N_f$  transitions of process chains (1) and (2) are executed before a transition of the slow process chain (3) is sampled. In this way, the time scale disparity is decreased while the relative dynamics within fast process chains remains unaffected upon scaling.

### 2.2.3 Detection of Local Quasi-Equilibrium

The local quasi-equilibrium of each process chain  $m$  is assessed for a subset of particles  $\mathcal{P}_m \in \mathcal{P}$ .  $\mathcal{P}_m$  does not necessarily contain the particles which belong to the transition rates in the respective process chain  $m$ . It may even be a good choice to define  $\mathcal{P}_m$  as particles belonging to subsequent process chains with slower transition rates. To assess the quasi-equilibrium of process chain  $m$ , we observe the *local environment* of the particles in  $\mathcal{P}_m$ . For an arbitrary particle  $i \in \mathcal{P}$ , we define a quasi-potential (QP)

$$\tilde{V}_i = \tilde{V}(\mathbf{r}_i) = \sum_{j=1}^N \frac{w_{ij}}{r_{ij}} \Theta(r_{\text{cut}}^{\text{QP}} - r_{ij}) \quad (2.4)$$

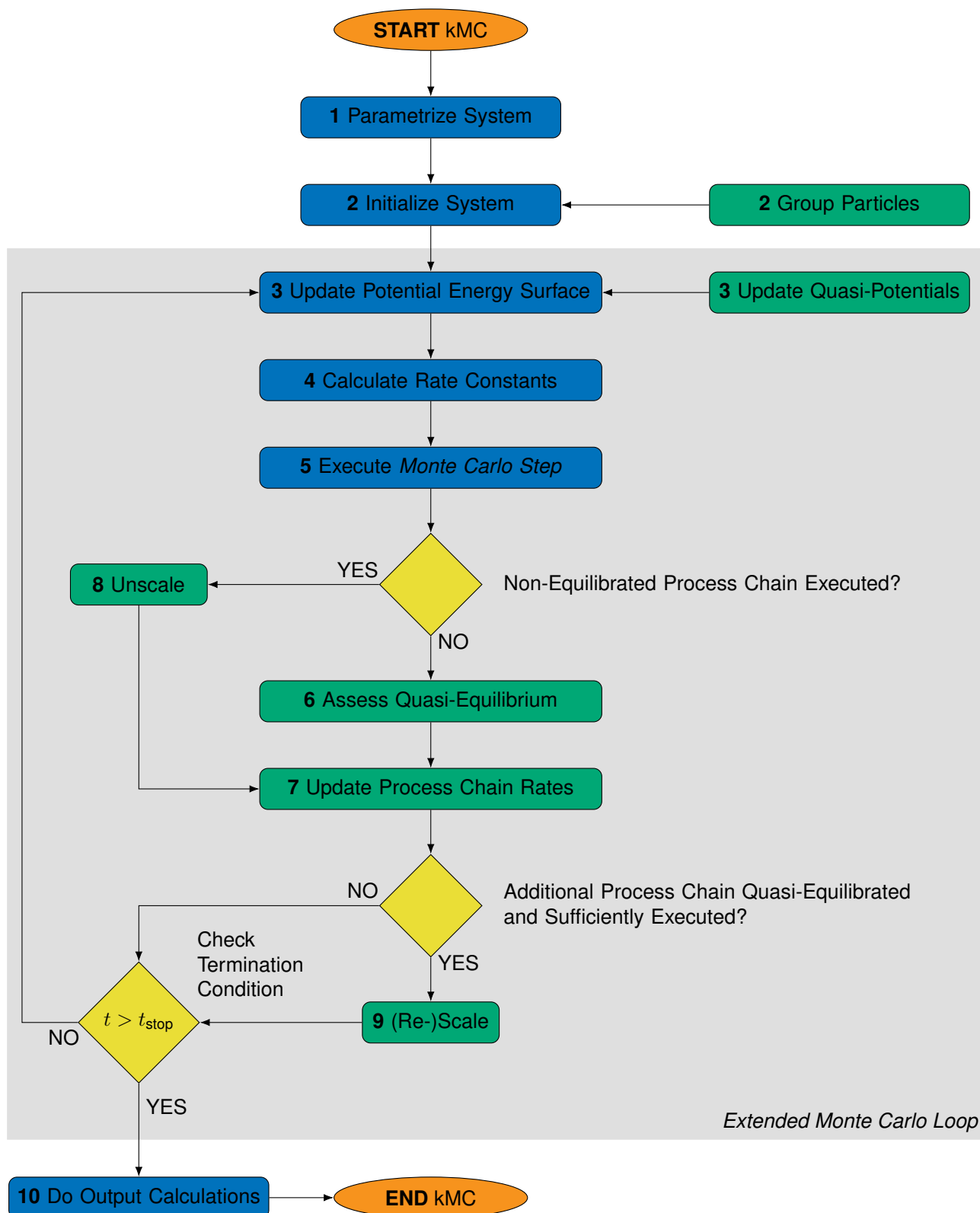


**Figure 2.2 Extended flowchart of a generic kinetic Monte Carlo algorithm including steps for a local temporal acceleration scheme.** In the initialization step, processes and particles are partitioned into process chains (step 2). The original Monte Carlo loop is extended by several computational steps including in particular quasi-equilibrium assessment (step 6) and the dynamic scaling of quasi-equilibrated process chains (steps 7, 8 and 9). The detection of local quasi-equilibrium relies on the definition of quasi-potentials which are updated in each kMC step (step 3). Green blocks mark the additional steps required by the local temporal acceleration scheme. Adapted with permission from ref. [2]. Copyright 2022 American Chemical Society (ACS).

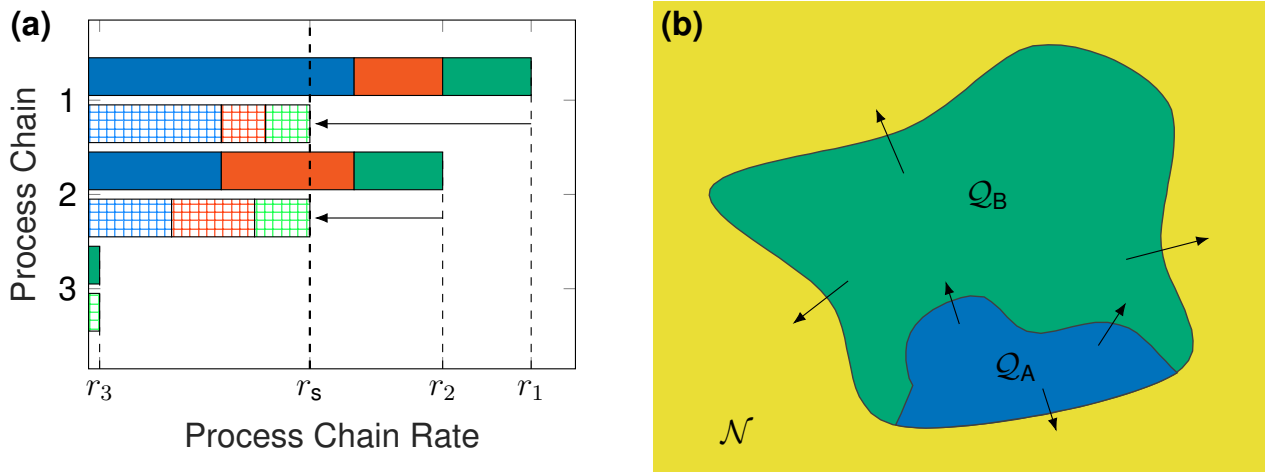


**Figure 2.3 Schematic representation of the concepts utilized in the local temporal acceleration scheme. (a)** Scaling procedure for a system containing three process chains ( $i$ ) with rates  $r_i$ . Process chains (1) and (2) contain each three transitions as indicated by the different colors, while only one process is in process chain (3). The acceleration scheme decreases the transition rates  $r_1$  and  $r_2$  of the fast process chains to  $r_s = N_f r_3$ , while each individual transition rate in process chains (1) and (2) is equally scaled. Hereby, the slow process chain is more frequently executed and the relative dynamics within each process chain is preserved. **(b)** Schematic representation of an arbitrary superbasin  $\mathcal{S} = \mathcal{Q}_A \cup \mathcal{Q}_B$ :  $\mathcal{Q}_A$  represents the quasi-equilibrated and sufficiently executed phase space,  $\mathcal{Q}_B$  the quasi-equilibrated but not sufficiently executed phase space, and  $\mathcal{N}$  the non-equilibrated phase space. Adapted with permission from ref. 2. Copyright 2022 American Chemical Society (ACS).

where  $w_{ij}$  are user-specified weights,  $r_{ij} = |\mathbf{r}_j - \mathbf{r}_i|$  is the distance between particle  $i$  and particle  $j$ ,  $\Theta$  is the Heaviside step function and  $r_{\text{cut}}^{\text{QP}}$  is a cutoff radius. Note that  $r_{\text{cut}}^{\text{QP}}$  taken for the QP calculation differs from  $r_{\text{cut}}^{\text{C}}$  for Coulomb interactions. The double-dagger  $\ddagger$  indicates that the self-interaction term ( $i = j$ ) is omitted. Via  $w_{ij}$ , fluctuations arising from different particles can be weighted differently. In practice,  $w_{ij}$  contains quantities like the charge magnitude  $\mathcal{Z}_j$ , the particle mass, or the effective relative permittivity  $\epsilon_r$ .

Tracking  $\tilde{V}_i(n)$  at each kMC step  $n$  yields a sequence of QP values which, in quasi-equilibrium, oscillate more or less strongly around a given average value. The evolution of this average value is given by

$$\langle \tilde{V}_i \rangle(k) = \frac{1}{k} \sum_{n=1}^k \tilde{V}_i(n). \quad (2.5)$$

The average fluctuations in  $\tilde{V}_i(k)$  in the local environment of the  $i$ th particle is captured by

$$\langle \Delta \tilde{V}_i \rangle(k) = \frac{\langle \tilde{V}_i^{\text{mavg}} \rangle(k) - \langle \tilde{V}_i \rangle(k)}{\langle \tilde{V}_i \rangle(k)} \quad (2.6)$$

where

$$\langle \tilde{V}_i^{\text{mavg}} \rangle(k) = \frac{1}{N_{\text{ob}}} \sum_{n=1}^{N_{\text{ob}}} \tilde{V}_i(k - N_{\text{ob}} + n) \quad (2.7)$$

is the moving average QP and  $N_{\text{ob}}$  denotes a user-defined window size. If the relative fluctuations remains within a user-defined threshold  $\delta$

$$|\langle \Delta \tilde{V}_i \rangle(k)| \leq \delta, \quad (2.8)$$

particle  $i$  is considered to be *locally quasi-equilibrated*. If all particles in  $\mathcal{P}_m$  fulfill the quasi-equilibration condition, Eq. (2.8), we define process chain  $m$  as quasi-equilibrated. At the beginning of a simulation, the local environment of all particles is considered to be non-equilibrated. The same is valid for newly generated/injected particles. After  $N_{\text{ob}}$  kMC steps, local quasi-equilibrium is assessed via (2.8) and subsequently updated in intervals of  $N_s$  kMC steps. In this way, we ensure the sensitivity of quasi-equilibrium detection with respect to changes in the system dynamics.

## 2.2.4 Dynamic Scaling of Quasi-Equilibrated Process Chains

To resolve existing time scale disparities, the transition rates  $k_i$  of each process  $i$  in the quasi-equilibrated process chains  $m$  are artificially decreased using a scaling factor  $0 < \alpha_m < 1$ :

$$k_i^* = \alpha_m k_i \quad (2.9)$$

where  $k_i^*$  denotes the scaled transition rate of process  $i$ . The value of each scaling factor  $\alpha_m$  is calculated and updated dynamically during the simulation such that on average  $N_f$  processes of each quasi-equilibrated process chain are executed before a process from a slow non-equilibrated process chain occurs. The dynamic calculation of scaling factors is based on the superbasin concept of the Dybeck scheme [55]. For this purpose, the  $m$  process chains are subdivided into three sets:

- 1 Quasi-equilibrated and sufficiently executed:  $Q_A$
- 2 Quasi-equilibrated but not sufficiently executed:  $Q_B$
- 3 Non-equilibrated:  $\mathcal{N}$

The union of the explored region,  $Q_A$ , and of the unexplored region,  $Q_B$ , forms the current superbasin  $\mathcal{S}$ , see Figure Figure 2.3b. An arbitrary process chain  $m$  is considered to be sufficiently executed if it was at least  $N_e$  times executed in the current superbasin  $\mathcal{S}$ .  $Q_A$  can either be exited by a process from  $Q_B$  or  $\mathcal{N}$ . Hence, the effective escape rate  $r_{es}$  from  $Q_A$  is determined by the sum of all rates  $r_{m,\mathcal{S}}$  of process chains belonging to the sets  $\mathcal{N}$  and  $Q_B$ :

$$r_{es} = \sum_{m \in \mathcal{N}, Q_B} r_{m,\mathcal{S}}. \quad (2.10)$$

In general, the rate of any process chain  $m$  within the current superbasin  $\mathcal{S}$  can be approximated by temporal averaging:

$$r_{m,\mathcal{S}} = \frac{1}{\Delta t_{\mathcal{S}}} \sum_{n \in \mathcal{S}} k_m(n) \Delta t_n \quad (2.11)$$

where  $\Delta t_{\mathcal{S}} = \sum_n \Delta t_n$  is the total time spent in  $\mathcal{S}$ ,  $k_m(n)$  is the rate constant of process chain  $m$  at kMC step  $n$  given by

$$k_m(n) = \sum_{i \in m} k_i(n). \quad (2.12)$$

and  $\Delta t_n$  denotes the corresponding time step. Consequently, the ratio

$$\langle N_m \rangle = \frac{r_{m,\mathcal{S}}}{r_{es}} \quad (2.13)$$

represents the average number of executions in process chain  $m$  before  $Q_A$  is left. To ensure that an average number of  $N_f$  executions in process chain  $m$  are sampled, we can define the scaling parameter  $\alpha_m$  by

$$\alpha_m = N_f \frac{r_{es}}{r_{m,\mathcal{S}}}. \quad (2.14)$$

If  $\alpha_m > 1$ , we set  $\alpha_m = 1$  to prevent an increase of the transition rate. Eventually, the process chains in  $Q_A$  allow the system to exit the superbasin via a process of a non-equilibrated process chain. Upon entering the new superbasin, all scaling factors are reset to 1 and new scaling factors are computed using equations (2.10) to (2.14). In this context, all previously quasi-equilibrated process chains remain quasi-equilibrated, but they are no longer considered to be sufficiently executed such that  $\alpha_m$  is set to 1 in line with the Dybeck scheme [55]. All process chains need to be sufficiently executed again before the scaling is activated again. This ensures that the processes in the respective process chains are sufficiently executed and with this limits the perturbation of the system dynamics.

## 2.3 Automated Parametrization of Kinetic Monte Carlo Models

The following concepts are adapted and in parts reprinted with permission from ref. 1, J. Phys. Chem. A 2023, 127, 28, 5967–5978. Copyright 2023 American Chemical Society (ACS).

### 2.3.1 Extended Algorithm Procedure

To automate the parametrization of kMC models we developed a computational pipeline which extends the original kinetic Monte Carlo algorithm by a data-driven feedback loop, see Figure 2.4. In the following, we outline successively the additional computational steps required by the data-driven feedback loop: (1) Bayesian optimization, (2) selection of an appropriate acquisition function, and (3) Gaussian processes. Each step of the pipeline is firstly described in an abstract fashion and subsequently concretized by means of an electrochemical showcase - the space-charge layer formation in solid-state electrolytes under blocking conditions, see Section 2.4 for a detailed description of the underlying kMC model.

### 2.3.2 Bayesian Optimization

In a majority of cases, the parametrization of kMC models relies on a combination of literature review, physical intuition and brute force (*e.g.* parameter sweeps). The main goal of this work is to make the process of input parametrization *prediction-guided* via an efficient Bayesian optimization scheme, see step 8 in Figure 2.4. BO is a global optimization pipeline which has proven to be both data efficient and robust in non-convex/concave problems. Considering an arbitrary optimization problem with a costly-to-query target quantity such as time-consuming experimental measurements or computationally expensive *ab initio* simulations, Bayesian optimization is among the most suitable algorithms as it requires only a minimal amount of target querying and may reach a *global* minimum. The two main components of BO are a surrogate model and an acquisition function, see steps 7 and 9 in Figure 2.4, respectively. The surrogate model can be any probabilistic algorithm that provides a prediction and an uncertainty quantification, for instance Gaussian processes (GPs), deep GPs or Bayesian neural networks. The acquisition function defines the function that will be directly optimized. It should be as convex/concave as possible, computationally efficient to evaluate and incorporate both the prediction of the original process and the uncertainty of the model on this point. A very intuitive example of an acquisition function is given by the so-called upper confidence bound (UCB):

$$\mathbf{x}_{\text{opt}} = \arg \max_{\mathbf{x}_{\text{opt}}} \mu(\mathbf{x}_{\text{opt}}) + \epsilon \sigma(\mathbf{x}_{\text{opt}}) \quad (2.15)$$

where  $\mu$  and  $\sigma$  are the predictions for the mean and standard deviation, respectively, of the predictor on the corresponding point  $\mathbf{x}_{\text{opt}}$  and  $\epsilon$  is a trade-off parameter. The parameter  $\epsilon$  is directly linked to the *exploration* and *exploitation* phase of the optimization process. In the beginning of the process the model does not have enough information about the whole parameter space. Thus, it is more important to acquire observations which improve the model than to optimize the original problem. This initial stage is denoted as exploration and becomes manifest in high values of  $\epsilon$ . As the model improves progressively the focus of the optimization process begins to shift on optimal points. This stage is denoted as exploitation and reflected by decreasing values of  $\epsilon$ . In general, there are numerous potential acquisition functions with different convexity properties and prioritizations. In this work, the so-called expected improvement acquisition function was utilized:

$$EI(x) = \mathbb{E} \max(f(\mathbf{x}) - f(\mathbf{x}^+), 0) \quad (2.16)$$

where the superscript  $+$  denotes the best point so far and the function  $f$  is the trained surrogate model based on Gaussian processes. A complete derivation of Equation (2.16) can be found in Ref. [118] along with resources on additional acquisition functions. For completeness we note that other acquisition functions such as probability of improvement and UCB were also implemented but yielded inferior results

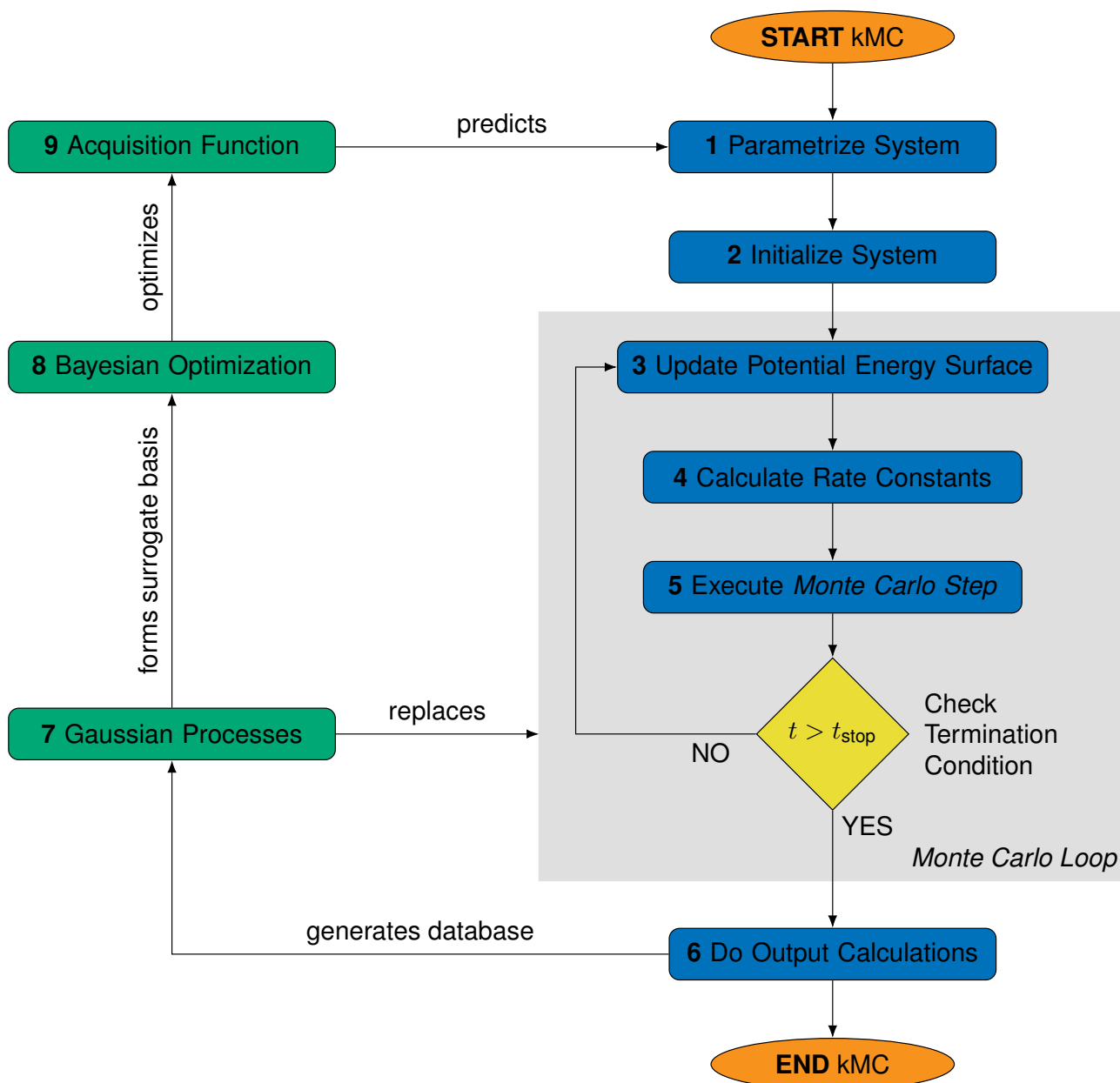


**Figure 2.4 Extended flowchart of a generic, particle-based kinetic Monte Carlo algorithm including a feedback loop for automated parametrization.** The original kinetic Monte Carlo algorithm on the right-hand side is extended by a feedback loop consisting of Gaussian processes and Bayesian optimization on the left-hand side. Fast-converging kMC simulations are used to generate a database to train a cheap-to-evaluate surrogate model based on Gaussian processes. The surrogate model and a system specific acquisition function form the two main components of Bayesian optimization which is utilized to predict the system parametrization for the next simulation run. Depending on its accuracy the surrogate model may fully replace the original kMC simulation. The green blocks mark the additional computational steps required by the data-driven feedback loop. Reprinted with permission from ref. 1. Copyright 2023 American Chemical Society (ACS).

compared to expected improvement.

The generic acquisition function outlined above has to be modified to match with the requirements of the investigated physical process. In ref. [1] our goal is to reconstruct the depletion layer thickness as function of the applied bias potential, that is  $d_{n-scl}(\phi_{bias})$ . For this purpose, we define the objective function

$$\mu_{obj} = -\frac{1}{N_{\phi_{bias}}} \sum_{\phi_{bias}} \frac{|d_{n-scl}^*(\phi_{bias}) - d_{n-scl}(\phi_{bias})|}{d_{n-scl}(\phi_{bias})}, \quad (2.17)$$



where the superscript  $\star$  denotes the mean of the predicted values and  $N_{\phi_{\text{bias}}}$  is the number of investigated potential points. In principle, we are considering a minimization problem, as we wish to minimize the distance between the predicted values and a baseline. However, in the context of Bayesian Optimization it is more intuitive to reformulate the task as a maximization problem indicated by the negative sign in (2.17). The corresponding standard deviation is given by

$$\sigma_{\text{obj}} = \frac{1}{N_{\phi_{\text{bias}}}} \sum_{\phi_{\text{bias}}} \frac{\sigma(\phi_{\text{bias}})}{d_{n\text{-scl}}(\phi_{\text{bias}})} \quad (2.18)$$

where  $\sigma(\phi_{\text{bias}})$  corresponds to the standard deviation of a prediction with respect to a specific value of  $\phi_{\text{bias}}$ . The final form of the acquisition function can be constructed by combining (2.17) and (2.18) with (2.16):

$$EI = \begin{cases} (f_{\text{obj}}(\mathbf{x}) - f(\mathbf{x}^+) - \xi)\Phi(\mathbf{Z}) + \sigma_{\text{obj}}(\mathbf{x})(\mathbf{Z}) & \text{if } \sigma_{\text{obj}}(\mathbf{x}) \geq 0 \\ 0 & \text{if } \sigma_{\text{obj}}(\mathbf{x}) = 0 \end{cases} \quad (2.19)$$

where

$$f(x) = \begin{cases} \frac{f_{\text{obj}}(\mathbf{x}) - f(\mathbf{x}^+) - \xi}{\sigma_{\text{obj}}(\mathbf{x})} & \text{if } \sigma_{\text{obj}}(\mathbf{x}) \geq 0 \\ 0 & \text{if } \sigma_{\text{obj}}(\mathbf{x}) = 0 \end{cases} \quad (2.20)$$

with  $\phi$  and  $\Phi$  denoting the probability and the cumulative distribution functions respectively.

### 2.3.3 Gaussian Processes

As outlined above Bayesian optimization requires a robust and computationally efficient surrogate model. In the scope of this work, we selected Gaussian processes (see step 7 in Figure 2.4) - a data-driven stochastic prediction algorithm that models predictions as Gaussian distributions whose parameters are determined by the distance to already measured samples. Therefore, the algorithm inherently provides an uncertainty quantification for its predictions, which can be crucial in applications with small datasets. Gaussian processes rely on the fundamental assumption that a true process  $\mathbf{y}$  can be modeled by a model  $\mathbf{f}$  on a set of points  $\mathbf{X}$  using a multivariate Gaussian distribution centered around zero, denoted as the so-called prior distribution:

$$\mathbf{f}|\mathbf{X} \sim \mathcal{N}(0, \mathbf{K}_{\mathbf{x},\mathbf{x}}) \quad (2.21)$$

where  $\mathbf{K}_{\mathbf{x},\mathbf{x}}$  is the covariance matrix which encodes the correlation between two points and is defined by a user chosen kernel function. Additionally, the likelihood of the observations given the model can be represented as a noisy normal distribution around the model predictions:

$$\mathbf{y}|\mathbf{f} \sim \mathcal{N}(\mathbf{f}, \sigma^2\mathbf{I}) \quad (2.22)$$

Equation (2.21) and Equation (2.22) can be manipulated to create the so-called posterior distribution which will be used for prediction and is given by

$$P(\theta|\mathbf{D}) = \frac{P(\mathbf{D}|\theta)P(\theta)}{P(\mathbf{D})} \quad (2.23)$$

where  $\mathbf{D}$  corresponds to the acquired observations and  $\theta$  denotes the model parameters. Solving the above process analytically yields

$$\mu_{\mathbf{x}^\star} = \mathbf{K}_{\mathbf{x}^\star,\mathbf{x}}[\mathbf{K}_{\mathbf{x},\mathbf{x}} + \sigma^2\mathbf{I}]^{-1}\mathbf{y} \quad (2.24a)$$

$$\sigma_{\mathbf{x}^\star}^2 = \mathbf{K}_{\mathbf{x}^\star,\mathbf{x}^\star} - \mathbf{K}_{\mathbf{x}^\star,\mathbf{x}}[\mathbf{K}_{\mathbf{x},\mathbf{x}} + \sigma^2\mathbf{I}]^{-1}\mathbf{K}_{\mathbf{x},\mathbf{x}^\star} \quad (2.24b)$$

where the points for prediction and training are denoted with and without the superscript  $\star$ , respectively. One crucial aspect is given by the parameter values,  $\theta$ , of the kernel function  $\mathbf{K}$ . In principle, the prior

distribution must be defined in such a way that it is uncorrelated with the observations. However, in practice better results are achieved if the kernel parameters are chosen to maximize the log marginal likelihood (LML)

$$\log p(\mathbf{y}|\mathbf{X}, \theta) = -\frac{1}{2}\mathbf{y}^T [\mathbf{K}_{\mathbf{x},\mathbf{x}} + \sigma^2\mathbf{I}]^{-1} \mathbf{y} - \frac{1}{2} \log [\mathbf{K}_{\mathbf{x},\mathbf{x}} + \sigma^2\mathbf{I}] - \frac{N}{2} \log(2\pi) \quad (2.25)$$

for a given number of points  $N$ . Here, the first term captures the quality of the model fit, the second term indicates that complex models are less probable and the third term expresses that points become less probable in larger datasets. In essence, the LML maximization attempts to define the simplest model that describes the observations. Note, that a complete mathematical analysis of Gaussian processes and their derivation is beyond the scope of this work. A comprehensive description can be found in ref. 119.

In ref. [1], the kernel was the sum of two multilayer perceptron (MLP) kernels [120] whose parameters were trained by maximizing the LML. Note that the kernel itself is *not* a neural network. However, it has been shown that - under certain conditions - certain covariance functions can cause the GPs to converge to the limit of a neural network with an infinite number of layers. Our particular implementation of the kernel mimicks rectified linear activations (ReLU) but the method family is not limited to it. Unfortunately, the detailed theory of the method is beyond the scope this paper. A complete treatment can be found in pertinent literature [120], further publications covering the topic are given by refs. [121, 122, 123, 124]. There is no immediate reason to assume that this kernel outperforms other kernel functions such as the radial basis kernel (RBF). Nevertheless, trial and error showed that in this problem the results were superior both in accuracy and physicality of results.

## 2.4 Kinetic Monte Carlo Model of the Space Charge Layer Formation in Solid-State Electrolytes

The following concepts are reprinted with permission from ref. 104, *Comm. Chem.* 2023, 6, 124. This article is licensed under a Creative Commons Attribution 4.0 International License.<sup>†</sup>

### 2.4.1 Experimental and Simulation Set-Up

In Figure 2.5, the different measurement setups are shown, which were used to perform the two experimental techniques (electrochemical impedance spectroscopy (EIS) in Figure 2.5a and spectroscopic ellipsometry (SE) in Figure 2.5b, respectively) and a sketch of the kMC model in Figure 2.5c. The experimental design was carefully chosen to prevent a tandem of instabilities from interfering with the measurement: (1) the reduction of the Li(s) when in contact with air, and (2) the reaction of the SSE when in touch with Li(s) [125]. As the SE measurements are relatively fast (multiple hours) but are done under ambient conditions, the Au-layer on top of the Li(s) electrode provides protection from the atmosphere. On the other hand, the EIS measurements are relatively slow but can be performed in an argon atmosphere, and the Au-layer between Li(s) and SSE acts as a passivation layer between two materials [126]. More details on the preparation and conditions of the measurement can be found in the experimental section of ref. 104.

Next, we outline the extended model setup for an SSE sample contacted by two metallic Li-electrodes, see Figure 2.5c. Here, we briefly summarize the most important aspects of the original model for blocking conditions [103]. The device is mapped to a three-dimensional Cartesian lattice of volume  $V = X \times Y \times Z = 31.5 \times 31.5 \times 1260 \text{ nm}^3$  with a lattice constant of  $a_L = 6.3 \text{ nm}$  and periodic boundary conditions in the  $xy$ -plane. The bottom and top layer in  $z$ -direction correspond to the Li(s)-electrodes which either act as a sink or source for Li-ions (in the following denoted as removal and injection electrode, respectively). Note that the model does not distinguish between the Au-layer and the Li(s) electrode but instead treats them as an ideal contact with  $\varepsilon_r \rightarrow \infty$ . The region confined between the contacts models the SSE sample where each node  $i$  represents an unoccupied vacancy site. The sample is populated with mobile Li-ions according to a particular bulk concentration  $c_{\text{Li}^+, \text{bulk}}$ . The value of  $c_{\text{Li}^+, \text{bulk}}$  was recently assessed in the scope of an ionic Mott-Schottky formalism to be in the range of  $2\text{-}4 \times 10^{18} \text{ cm}^{-3}$  [127]. In the scope of this work, we utilize the mean value  $c_{\text{Li}^+, \text{bulk}} = 3 \times 10^{18} \text{ cm}^{-3}$  as a first order approximation. In general, the concentration of mobile cations,  $c_{\text{Li}^+}$ , and its physical boundaries play a key role in the asymmetric SCL formation in SSEs. In ref. [103], we established that:

$$c_{\min} \leq c_{\text{Li}^+} \leq c_{\max} \quad (2.26)$$

where  $c_{\min}$  and  $c_{\max}$  denote the minimum and maximum concentration of  $\text{Li}^+$  in a fully depleted and fully occupied lattice, respectively. In the present model, we naturally set  $c_{\min} = 0$ , whereas as the inverse volume of a unit cell imposes the maximum concentration,  $c_{\max} = a_L^{-3}$ . A homogeneously distributed anionic background is implemented to ensure electroneutrality with respect to the sample's initial condition. The presence of immobile Li-ions [128] is neglected as corresponding counter anions locally neutralize them and thus do not alter the underlying energetic landscape for the transport of  $\text{Li}^+$ . Analogously to liquid electrolytes [129], the strength of electrostatic screening also impacts the thicknesses of the resulting SCLs. Here, we control the magnitude of this effect via the relative permittivity  $\varepsilon_r$  of the bulk SSE.

### 2.4.2 Modeling of Li-ion Dynamics

Our model features three different types of dynamic transitions (*cf.* numbers in Figure 2.5c):

- 1  $\text{Li}^+$ -injection from the source electrode.
- 2  $\text{Li}^+$ -transport guided by a thermally activated hopping mechanism [111, 110].

<sup>†</sup><https://creativecommons.org/licenses/by/4.0/>

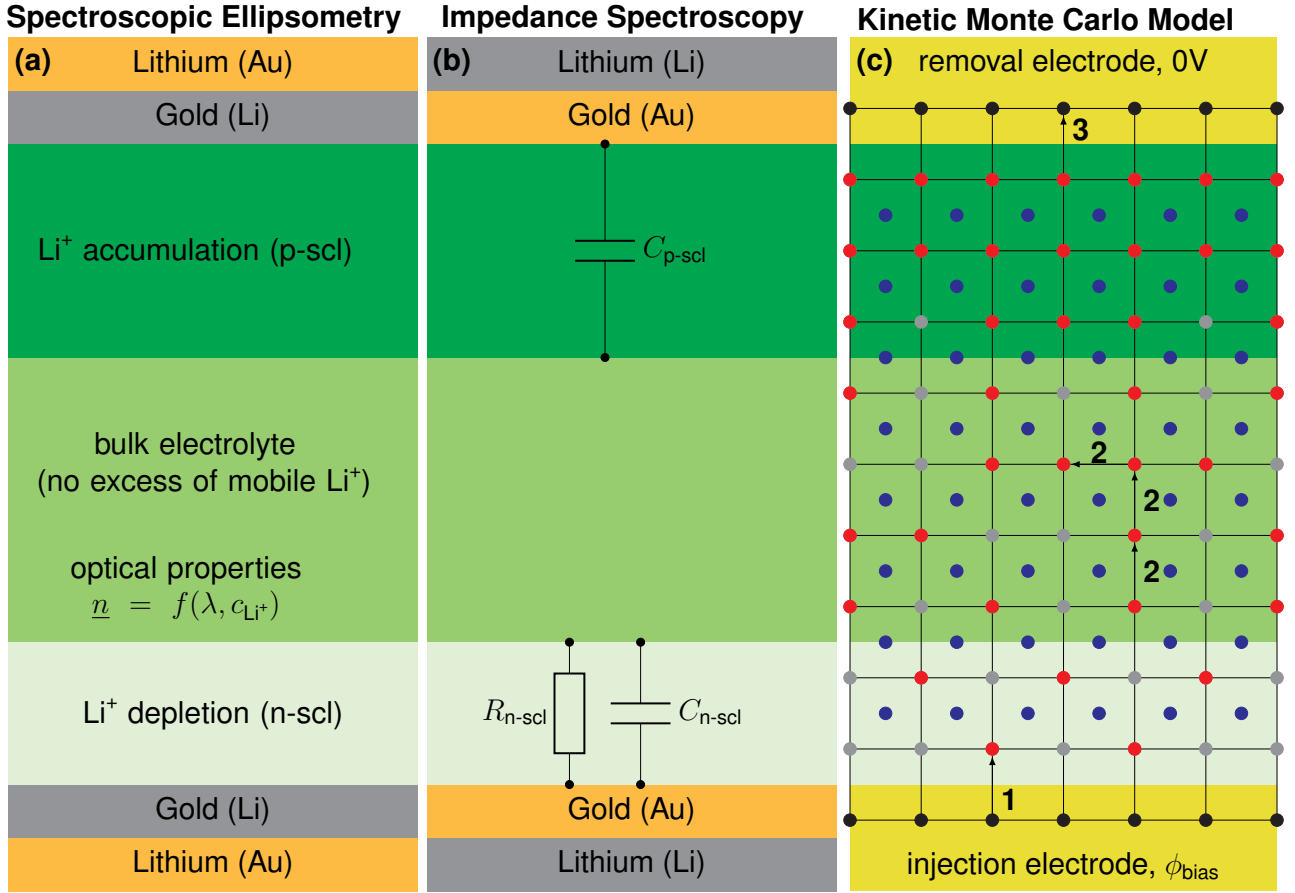


**Figure 2.5 Experimental setups and kinetic Monte Carlo (kMC) model for the space charge layer formation in solid-state electrolytes.** Schematic representation of (a) the spectroscopic ellipsometry (SE) and (b) the electrochemical impedance spectroscopy (EIS) setups used in the experiments. (c) Schematic representation of the kMC model used to simulate the behavior of charge accumulation at the interface between a lithium metal electrode and an oxide solid-state electrolyte. Gray, red, and blue dots represent unoccupied lattice vacancies, mobile Li<sup>+</sup>-ions and their immobile counteranions, respectively. The metallic Li-electrodes are illustrated by black dots and act as source and sink for mass-transport. The numbers correspond to the three implemented dynamic transitions: (1) Li<sup>+</sup>-injection, (2) Li<sup>+</sup>-transport and (3) Li<sup>+</sup>-removal. Reprinted with permission from ref. 104.

### 3 Li<sup>+</sup>-removal from the sink electrode.

Li-ions can move to unoccupied nearest neighbor's vacancies via hopping transport which is affected by the local values of the potential energy surface  $E_i$ . These local energy levels comprise three different energetic contributions: the energy defined by a  $E_i^{ref}$ , the contribution from an external electric field  $E_i^F$  and the influence of Coulomb interactions of mobile cations and their respective immobile counter anions. In summary, the total potential energy at vacancy site  $i$  is given by:

$$E_i = E_i^{ref} + E_i^F + E_i^C. \quad (2.27)$$

In the present model, we only consider energy differences  $\Delta E_{ij}$  between two vacancy sites  $i$  and  $j$  and, thus, we may set  $E_i^{ref} = 0$ .  $E_i^F$  is assumed to drop linearly in  $z$ -direction across the contacted SSE sample, that is:

$$E_i^F = (q\phi_b - \Delta W) \frac{z_i}{Z} \quad (2.28)$$

where  $\phi_b$  denotes the applied bias potential,  $\Delta W$  is the difference in the electrode work functions and  $z_i$  is the  $z$ -coordinate of the site  $i$ . For identical electrodes, we may set  $\Delta W = 0$ . While the first two contributions are held constant during the simulation,  $E_i^C$  must be updated dynamically. The model considers the interaction of mobile cations (cation–cation interactions),  $E_i^{cc}$ , and interaction of mobile cations

with immobile counteranions (cation–anion interaction)  $E_i^{ac}$ . Both contributions are computed accurately via a three-dimensional Ewald summation adjusted for a contacted infinite slab-device as established by Casalegno *et al.* [18, 130]. Due to the fixed positions of anions, the values of  $E_i^{ac}$  can be calculated before the simulation and cached on related vacancy sites. On the other hand,  $E_i^{cc}$  depends on the current spatial distribution of all mobile cations and must be updated accordingly in each kMC step. In the context of Coulomb interactions, special attention must be paid to non-electroneutral device configurations as they can lead to convergence issues [33]. Under non-blocking conditions, such arrangements could arise from strongly asymmetric injection and removal rates. However, please note that the applied electrostatic solver implicitly handles such cases by extending the original simulation box with a corresponding box of image charges representing the polarization of an ideal metal contact. To reduce the computational effort arising from the dynamic calculation of Coulomb interactions, we apply a combination of different strategies [103], particularly the so-called dipole-update method [36].

The thermally activated hopping of cations between vacancies sites  $i \rightarrow j$  is captured via the Miller-Abrahams formula [131]:

$$k_{ij} = k_0 \cdot \begin{cases} \exp\left(\frac{\Delta E_{ij}}{E_{th}}\right), & \Delta E_{ij} < 0 \\ 1, & \Delta E_{ij} \geq 0 \end{cases}, \quad (2.29)$$

where  $k_0$  is attempt-to-hop frequency,  $\Delta E_{ij} = E_j - E_i$  denotes the difference in potential energy between vacancy  $i$  and  $j$  and  $E_{th} = k_B T$  is the thermal energy. The attempt-to-hop frequency is estimated from an Arrhenius equation [132]:

$$k_0 = \frac{k_0^{\max}}{a_L^2} \exp\left(-\frac{E_a}{E_{th}}\right) \quad (2.30)$$

where  $k_0^{\max} = E_{th}/h$  and  $E_a$  denotes an experimentally obtained activation energy for diffusion [133]. We scale  $k_0^{\max}$  by  $a_L^2$  similarly to a three-dimensional random walk based on the Einstein-Smoluchowski treatment for Brownian motion [134]. When Li-ions reside on vacancy sites neighboring to contact nodes, they can be removed from the SSE sample with a constant rate  $k_{rem}$ . Therefore, the cumulative removal rate is given by:

$$K_{rem} = n_{Li^+,contact} k_{rem} \quad (2.31)$$

where  $n_{Li^+,contact}$  is the total number of Li-ions residing next to the contact. Vice versa,  $Li^+$  can be injected into an unoccupied vacancy site from the contact with the rate  $k_{inj}$  and, accordingly, the cumulative injection rate is given by:

$$K_{inj} = (n_{contact} - n_{Li^+,contact}) n_{Li^+,contact} k_{inj} \quad (2.32)$$

where  $n_{contact}$  denotes the total number of contact sites. Details regarding the model parametrization are given in ref. [104]. Note that the presented model is also valid for the SCL formation under blocking conditions [103]. The limiting case of blocking conditions can be simulated by setting  $k_{inj} = k_{rem} = 0$ .

## 2.5 Kinetic Monte Carlo Model of the Photocurrent Generation at the Organic/Aqueous Electrolyte Interface

The following concepts are adapted and in parts reprinted with permission from ref. 2, J. Chem. Theory Comput. 2022, 18, 5, 2749–2763. Copyright 2022 American Chemical Society (ACS).

### 2.5.1 Experimental and Simulation Set-Up

To characterize the hybrid interface electrochemically it is common to utilize a three-electrode set-up for chronoamperometric and voltammetric measurements, see Figure 2.6a. In such a set-up, the organic photoactive layer (most often poly-3-hexylthiophene, P3HT, or a P3HT/fullerene blend) is deposited on a transparent indium tin oxide (ITO) substrate to form a photosensitized working electrode, and immersed in an aqueous electrolyte. Several experimental studies demonstrate that photocurrent generation as well as photovoltage build-up are strongly coupled to the presence of dissolved oxygen in the electrolytic buffer solution indicating the occurrence of faradaic oxygen reactions in the vicinity of the hybrid interface [74, 90, 88, 89, 97, 77]. Cations/Molecules, e.g.  $H^+$  or  $O_2$ , diffuse within the electrolyte and, driven by an applied electric field, accumulate at the organic-liquid interface (OLI). Optical excitation of the organic semiconductor leads to the generation of electrons and holes which subsequently migrate through the semiconductor via a hopping mechanism. After a certain lifetime, charge carriers may recombine non-radiatively. If electrons reach the interface, they may reduce the cations/molecules at the interface forming an uncharged molecule or charged anion.

Next, we outline the simulation set-up of the OLI, made of an organic semiconductor stacked between a metal electrode and a liquid electrolyte, see Figure 2.6b. We model the organic semiconductor and the interface region of the electrolyte by a simplified two-dimensional lattice of size  $X \times Z = 50 \text{ nm} \times 60 \text{ nm}$  with a site spacing of  $r_L = 1 \text{ nm}$ . In  $x$ -direction, periodic boundary conditions are assumed; in  $z$ -direction, the organic layer is stacked between an electrode ( $z = 0 \text{ nm}$ ) and the aqueous electrolyte ( $z_{if} = 50 \text{ nm}$ ). The upper limit of the interface electrolyte at  $Z = 60 \text{ nm}$  implements a reflecting boundary condition [33] with respect to the bulk electrolyte. The energy at site  $i$  is given by

$$E_i = \begin{cases} E_i^{\text{MO}} + E_i^\sigma + E_i^{\text{F}} + E_i^{\text{C}} & \text{in the organic layer} \\ E_i^{\text{ref}} + E_i^{\text{F}} + E_i^{\text{C}} & \text{in the electrolyte} \end{cases} \quad (2.33)$$

where  $E_i^{\text{MO}}$  and  $E_i^{\text{ref}}$  denote the average molecular orbital energy and the energy defined by a reference electrode, respectively,  $E_i^\sigma$  resembles the energetic disorder,  $E_i^{\text{F}}$  is the contribution from an external electric field and  $E_i^{\text{C}}$  is the potential arising from Coulomb interaction with charges/ions in the environment.  $E_i^\sigma$  is modeled by a Gaussian distribution with variance  $\sigma^2$ , resembling the Gaussian density of states in disordered organic semiconductors [9, 135].  $E_i^{\text{F}}$  is modeled as a linear potential drop along the  $z$ -axis:

$$E_i^{\text{F}} = qV_b \frac{z_i}{Z} \quad (2.34)$$

where  $V_b$  denotes the applied bias voltage and  $z_i$  is  $z$ -coordinate of site  $i$ . For charges,  $E_i^{\text{C}}$  is constituted by the electron-electron interaction  $E_i^{\text{ee}}$  and the ion-electron interaction  $E_i^{\text{ie}}$ . For ions,  $E_i^{\text{C}}$  is composed of the ion-ion interaction,  $E_i^{\text{ii}}$ , and the electron-ion interaction  $E_i^{\text{ei}}$ . All components can be approximated by a spherical potential with cutoff radius  $r_{\text{cut}}^{\text{C}}$  by combining the method of image charges in  $z$ -direction [136] with the periodic boundary conditions in  $x$ -direction [137] to account for the interaction with the charged particles in the periodic replicas. A detailed derivation as well as a convergence analysis is presented in the Supporting Information of ref. [2]. All Coulomb interactions must be calculated and updated dynamically during runtime.

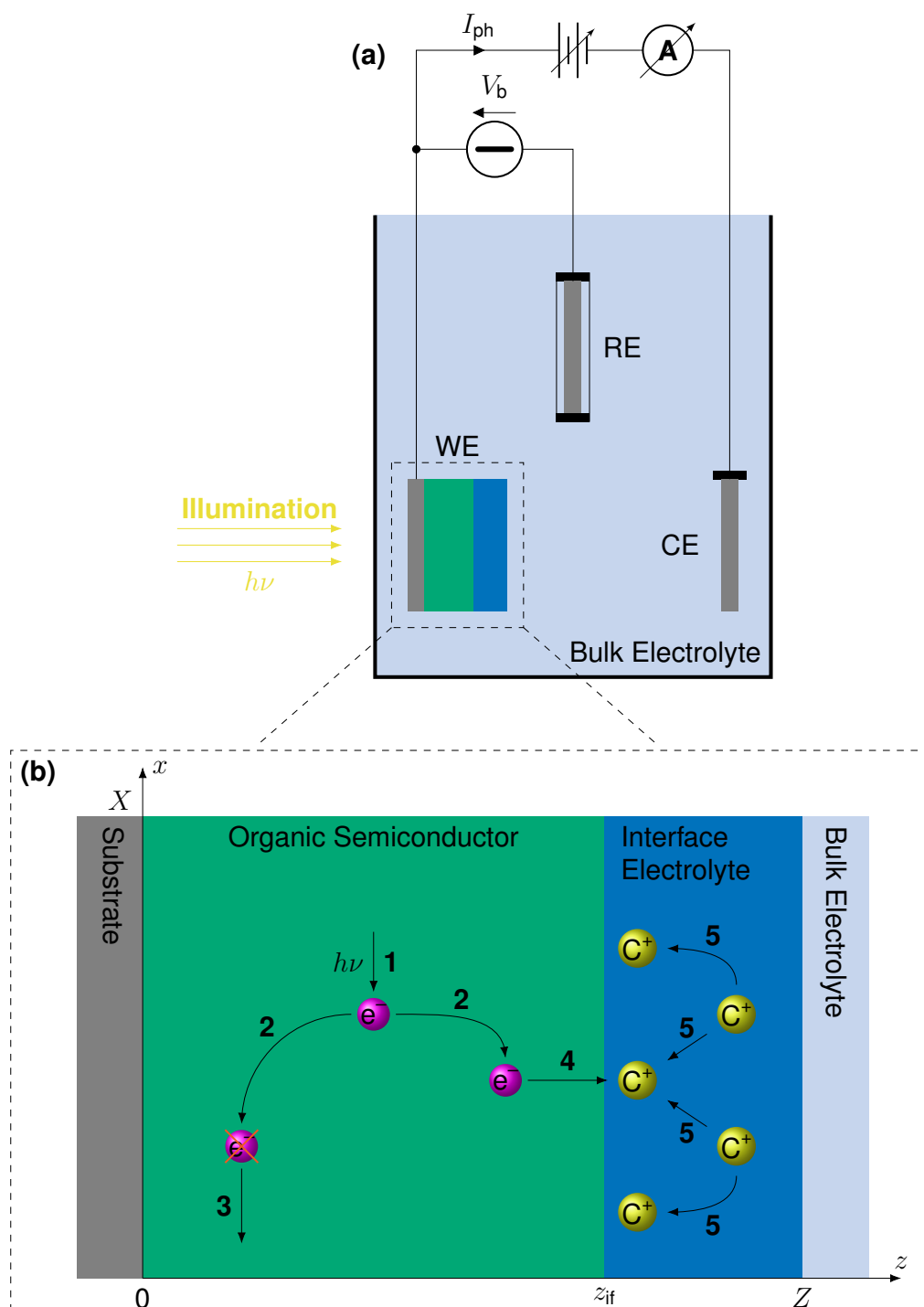


**Figure 2.6 Experimental setup and kinetic Monte Carlo model for the photocurrent generation at the organic-aqueous electrolyte interface.** (a) A typical three-electrode electrochemical cell is utilized for chronoamperometric measurements. By optical excitation of the photosensitized working electrode (WE) a photocurrent,  $I_{ph}$ , can be detected with respect to the counter electrode (CE). The bias potential of the working electrode,  $V_b$ , is defined via a reference electrode (RE). (b) Schematic representation of the simplified kMC model used to simulate the photocurrent generation. Electrons ( $e^-$ ) are optically generated in the organic semiconductor and migrate within their average lifetime to the hybrid interface. Here, electrons may reduce cations ( $C^+$ ) diffusing within the electrolyte. Adapted with permission from ref. 2. Copyright 2022 American Chemical Society (ACS).

## 2.5.2 Modeling of Particle Dynamics

The model contains the following five transitions (*cf.* Figure 2.6b):

- 1 Electron generation (elg)
- 2 Electron hopping (elh)
- 3 Electron decay (eld)
- 4 Ion reduction (red)
- 5 Ion diffusion (iod)

In the beginning of the simulation, we assume that there are no free electrons in the organic layer. Electrons are optically generated (process 1, Figure 2.6b) at random sites with rate

$$K_{\text{exg}} = (n_{\text{org}} - n_{\text{el}}) k_{\text{elg}} \quad (2.35)$$

where  $n_{\text{org}}$  is the number of lattice sites and  $n_{\text{el}}$  is the current number of electrons in the device. The transport of charged species (electrons and cations, processes 2 and 5, respectively, Figure 2.6b) between sites  $i$  and  $j$  is modeled via the Miller-Abrahams formula [131]

$$k_{ij} = k_0 \begin{cases} \exp\left(\frac{\Delta E_{ij}}{E_{\text{th}}}\right) & \text{if } \Delta E_{ij} > 0 \\ 1 & \text{if } \Delta E_{ij} \leq 0 \end{cases} \quad (2.36)$$

where  $k_0$  is the maximum transport rate,  $\Delta E_{ij} = E_j - E_i$  is the difference in potential energy between sites  $i$  and  $j$  and  $E_{\text{th}} = k_{\text{B}}T$  denotes the thermal energy. Particle motion is restricted to nearest-neighbor sites. Here, we set  $k_0 = 5.32 \times 10^9 \text{ s}^{-1}$  for cations corresponding to the two-dimensional random walk of a sodium ion [132]. Electron decay (process 3, Figure 2.6) is modeled as the inverse of the lifetime  $\tau$ , i.e.  $k_{\text{eld}} = \tau^{-1}$ . If an electron reaches the OLI, it may reduce a diffusing ion. The ion reduction (process 4) is formally given by the reaction equation



where C denotes the neutral reduction product and  $k_{\text{red}}$  is a constant reduction rate. In the simulation model, (2.37) is implemented as the consumption of an electron, no reaction product is generated. Accordingly, the cation density remains constant during time-evolution. Here, we assume a cation density of  $n_{\text{C}^+} = 3 \times 10^{12} \text{ cm}^{-2}$  in the electrolyte corresponding to a total number of 15 mobile ions.

## 2.5.3 Parametrization of Temporal Acceleration Scheme

To parameterize the acceleration scheme, we defined  $m = 3$  process chains: the **first** chain merges electron transport, generation and decay; the **second** chain contains ion diffusion; the **third** process chain isolates the rate-limiting reduction reaction. The input parameters for the acceleration scheme are presented in Table 2.1, a detailed summary of their meaning and impact is given in the original publication [2]. Process chain 1 and 2 contain charge and mass transport and, thus, are inherently much faster than the interface reaction. To assess quasi-equilibrium of the two fast process chains, we set  $\mathcal{P}_{(1)} = \mathcal{P}_{(2)} = \{\text{C}^+\}$  to track the quasi-potentials of all cations within  $r_{\text{cut}} = 2 \text{ nm}$ . We set the weights of the electronic and ionic QP contributions to

$$w_{\text{el}} = \frac{-q}{\varepsilon_{\text{r,eff}}} \quad \text{and} \quad w_{\text{ion}} = \frac{+q}{\varepsilon_{\text{r,e}}}, \quad (2.38)$$

respectively, where  $q = 1$  is the unsigned charge magnitude of an electron/cation, and  $\varepsilon_{\text{r,eff}}$  is the effective relative permittivity between the organic material and the electrolyte with  $\varepsilon_{\text{r,e}}$  and  $\varepsilon_{\text{r,o}}$  being the relative



**Table 2.1** Input parameters of the temporal acceleration scheme for the organic-liquid interface model.

$N_{\text{ob}}$	$N_{\text{s}}$	$\delta$	$N_{\text{e}}$	$N_{\text{f}}$
$10^6$	$10^3$	0.2	$10^4$	$10^5$

permittivity of the electrolyte and the organic material, respectively. The latter weight mimics the electrostatic interaction between electrons and ions within different materials. Normally, a reduction event would consume an electron and a cation. Here, we only consider electron consumption. To mimic ion consumption we assume that the formally reduced cation is non-equilibrated after the reduction event, and reset its history of quasi-potential tracking.



## 3 Publications

### 3.1 Local Temporal Acceleration Scheme to Couple Transport and Reaction Dynamics in Kinetic Monte Carlo Models of Electrochemical Systems

**Published By** Gößwein M.; Kaiser W.; Gagliardi A. Local Temporal Acceleration Scheme to Couple Transport and Reaction Dynamics in Kinetic Monte Carlo Models of Electrochemical Systems. *J. Chem. Theory Comput.* **2022**, *18*, 2749-2763.

The following summary is adapted and in parts reprinted with permission from ref. 2, *J. Chem. Theory Comput.* **2022**, *18*, 2749-2763. Copyright 2022 American Chemical Society (ACS).

**Summary** In this work, we present a novel temporal acceleration scheme to couple fast charge and mass transport phenomena with slow reaction dynamics in electrochemical systems. Our algorithm substantially extends the Dybeck scheme [55] by the introduction of a novel partitioning strategy of the system into process chains - a set of processes of similar time scale being connected to a certain particle subset. In contrast to the original algorithm, we formulate a local, particle-based criterion to assess the quasi-equilibrium of entire process chains (see Figure 3.1a) which are defined via subsets of processes and particles. Local quasi-equilibrium is reached if the fluctuation in the local environment of each individual particle, captured by quasi-potentials, remains within a pre-defined threshold. Scaling factors of quasi-equilibrated and sufficiently executed process chains are calculated dynamically based on the Dybeck scheme. Down-scaling of all transition rates within a process chain preserves the relative dynamics. Simultaneously, existing time scale disparities are substantially reduced resulting in a computationally more efficient kMC method.

We demonstrate the performance and the accuracy of our acceleration algorithm using a simplified model of an electrochemical system of growing relevance: a hybrid organic-aqueous electrolyte device which suffers from time scale disparities between fast transport phenomena in an organic semiconductor and slow interface reduction reactions. Reduction currents and local charge densities are investigated and accurately reproduced despite the presence of local inhomogeneities, see Figure 3.1b and Figure 3.1c, respectively. Figure 3.1b showcases that the acceleration scheme only kicks in for  $\hat{k}_{\text{red}} \leq 4 \times 10^{-7}$ . In the accelerated regime, the reference and accelerated values are perfectly matching independent of energetic disorder. For larger  $\hat{k}_{\text{red}}$ , the acceleration scheme does not disturb any of the system dynamics. Moreover, Figure 3.1c underlines that our algorithm also accurately preserves local properties such as the distribution of average charge density per LUMO energy interval. In concrete numbers, we achieve an acceleration up to a factor of  $10^6$  and without any loss in accuracy, see Figure 3.1d. With the efficient detection of local quasi-equilibria, we are able to capture local heterogeneities and to accurately reproduce physical quantities on a local scale. We further demonstrate that the Dybeck scheme is not suitable to capture the interaction between fast charge or mass transport phenomena and interface (surface) reactions accurately.

The central innovation of the presented temporal acceleration scheme is its local quasi-equilibrium approach. Thus, time scale disparities can be handled which are arbitrarily distributed in space, and local physical properties can be preserved upon scaling. The capability of resolving local heterogeneities is one of the main advantages of kMC models with respect to multiscale simulations. Hence, our algorithm provides a viable tool to substitute existing multiparadigm approaches by a stand-alone kMC model.

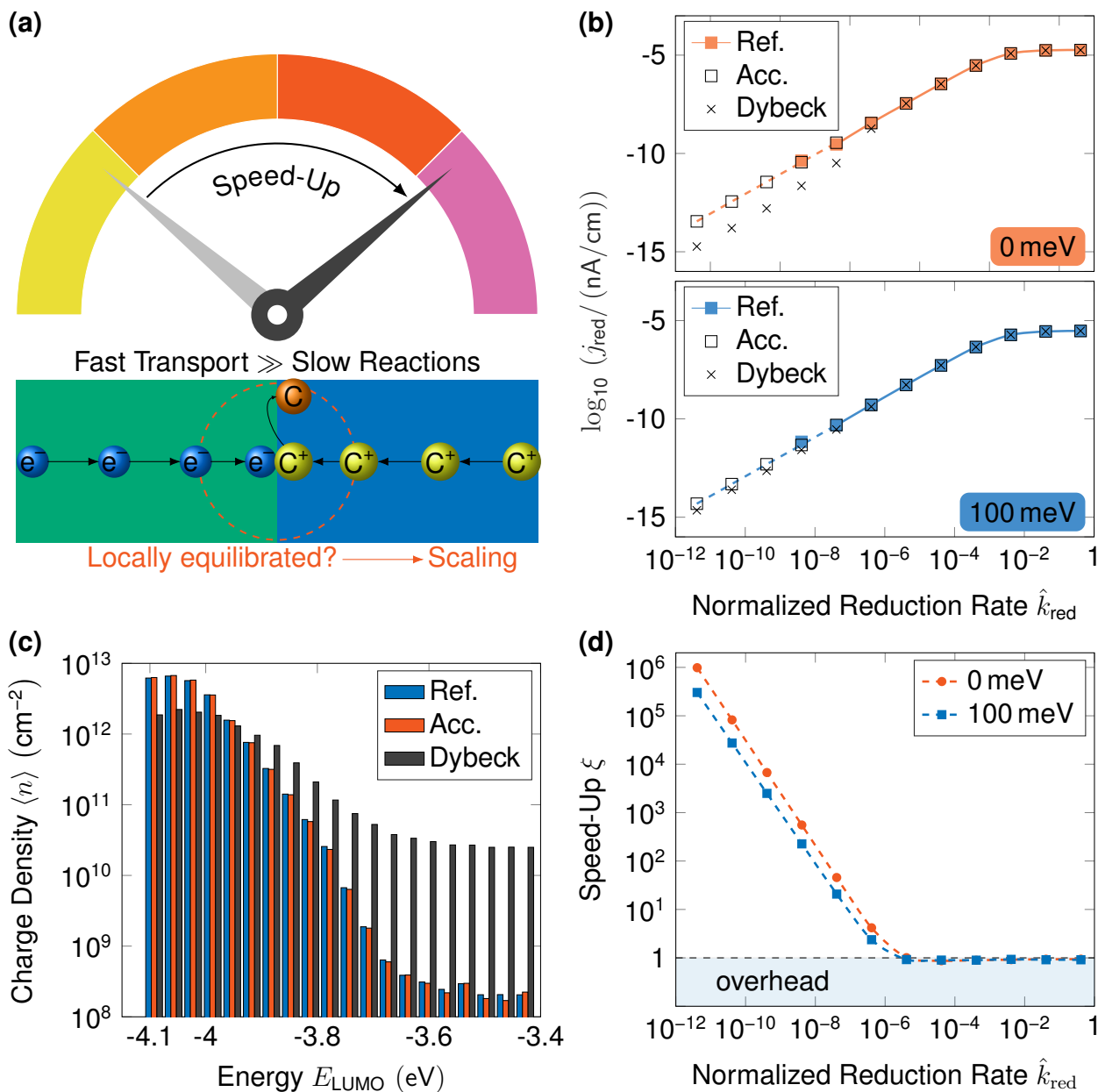


**Figure 3.1 Local temporal acceleration scheme for coupled transport-reaction simulations in kinetic Monte Carlo models of electrochemical systems.** (a) Schematic representation of the fundamental concept of local quasi-equilibrium detection. (b) Reduction current density,  $j_{red}$ , for  $\sigma = 0$  meV (top) and  $\sigma = 100$  meV (bottom) as a function of the normalized reduction rate  $\hat{k}_{red}$ . Filled symbols visualize the current densities obtained from the reference kMC simulations (Ref.); open symbols and crosses visualize the current densities from our local acceleration scheme (Acc.) and from the Dybeck scheme [55] (Dybeck), respectively. Dashed lines extrapolate the trend in  $j_{red}$  for low values of  $\hat{k}_{red}$ . (c) Distribution of average charge density per LUMO energy interval for  $\sigma = 100$  meV and  $\hat{k}_{red} = 4 \times 10^{-12}$ . (d) Speed-up in CPU time,  $\xi$ , for  $\sigma = 0$  meV and  $\sigma = 100$  meV as a function of the normalized reduction rate  $\hat{k}_{red}$ . Adapted with permission from ref. [2]. Copyright 2022 American Chemical Society (ACS).

**Individual Contributions** I substantially contributed to the ideas and concepts of the local temporal acceleration scheme presented in this study. I developed the utilized kinetic Monte Carlo models and implemented the corresponding simulation software within our in-house kinetic Monte Carlo framework [11]. I analyzed, assessed and rationalized all simulation data and transferred the scientific results into coherent figures. I authored the majority of the manuscript considering the broad expertise on kinetic Monte Carlo methods provided by the co-authors.

## 3.2 Utilizing Data-Driven Optimization to Automate the Parametrization of Kinetic Monte Carlo Models

**Published By** Kouroudis I.<sup>‡</sup>; Gößwein M.<sup>‡</sup>; Gagliardi A. Utilizing Data-Driven Optimization to Automate the Parametrization of Kinetic Monte Carlo Models. *J. Phys. Chem. A* **2023**, *127* (28), 5967-5978.

The following summary is adapted and in parts reprinted with permission from ref. 1, *J. Phys. Chem. A* **2023**, *127* (28), 5967-5978. Copyright 2023 American Chemical Society (ACS).

**Summary** In this work, we present an innovative and robust data-driven optimization pipeline to automate the parametrization of kinetic Monte Carlo (kMC) models. Our method couples the original kMC algorithm with a feedback loop consisting of a surrogate model based on Gaussian processes (GPs), a system-specific acquisition function and Bayesian optimization (BO), see Figure 3.2a. The surrogate model and the acquisition function operate as the two main components of Bayesian optimization which enables the guided prediction of suitable input parameters for a given output/target quantity. The surrogate model is cheap-to-evaluate and trained via a database generated from the outputs of *fast-converging* kMC simulations. In contrast to intuition-based parameter searching, we require only 1 to 2 iterations to reconstruct appropriate sets of input parameters, see Figures 3.2b to 3.2d. Remarkably, the latter statement holds inside as well as *outside* the bounds of the training data set demonstrating the extrapolation capabilities of our data-driven approach. Featuring accurate extrapolation is of high relevance when the direct kMC simulation of such regions is connected to large computational costs. Moreover, a sufficiently accurate surrogate model with a well-quantifiable error margin may fully replace potentially expensive kMC simulations which is a viable option in many practical use cases.

The effectiveness of our data-driven optimization pipeline is showcased via a process of growing industrial relevance: the formation of space-charge layers in solid-state electrolytes as it can be observed in all-solid-state batteries. The investigated process showcases a system with several open input parameters which extremely profits from a guided and data-efficient parametrization scheme. We demonstrate that the applied predictor is not only highly accurate but to the same degree data-efficient. Further, we consider different scenarios of inverse problem solution inside and outside the training data set (Figures 3.2b to 3.2c and Figure 3.2d, respectively) and recover suitable sets of input parameters for given values of depletion layer thickness  $d_{n-scl}$ . A full parameter space investigation is performed for all output quantities to highlight the accuracy of the constructed surrogate model.

The surrogate model is well-suited to replace expensive kMC simulations in many practical cases when a local resolution of output quantities is not required. The substitution is threefold:

- 1 The outputs of fast-converging kMC runs, here corresponding to low particle densities, are generated.
- 2 These outputs are utilized to train the GP surrogate model which in turn substitutes the whole parameter space.
- 3 Depending on the required accuracy and application, additional simulation runs can be performed in a selective and automated fashion.

Note that the kMC method itself is a stochastic method and exhibits corresponding statistical fluctuations. Therefore, it is important not to oversample regions in which the dominant uncertainty arises from the physical and not the data-driven model. In this sense, physical intuition still plays an important role even though it can be compensated for by additional data points.

The main innovation of our data-driven optimization pipeline for kMC models is its capability to extrapolate into regions outside of the training data set with a remarkably low error margin. Thus, an efficient parametrization of potentially expensive kMC simulations is enabled. Notably, the underlying surrogate

---

<sup>‡</sup>Shared first authorship: The authors contributed equally to this work.

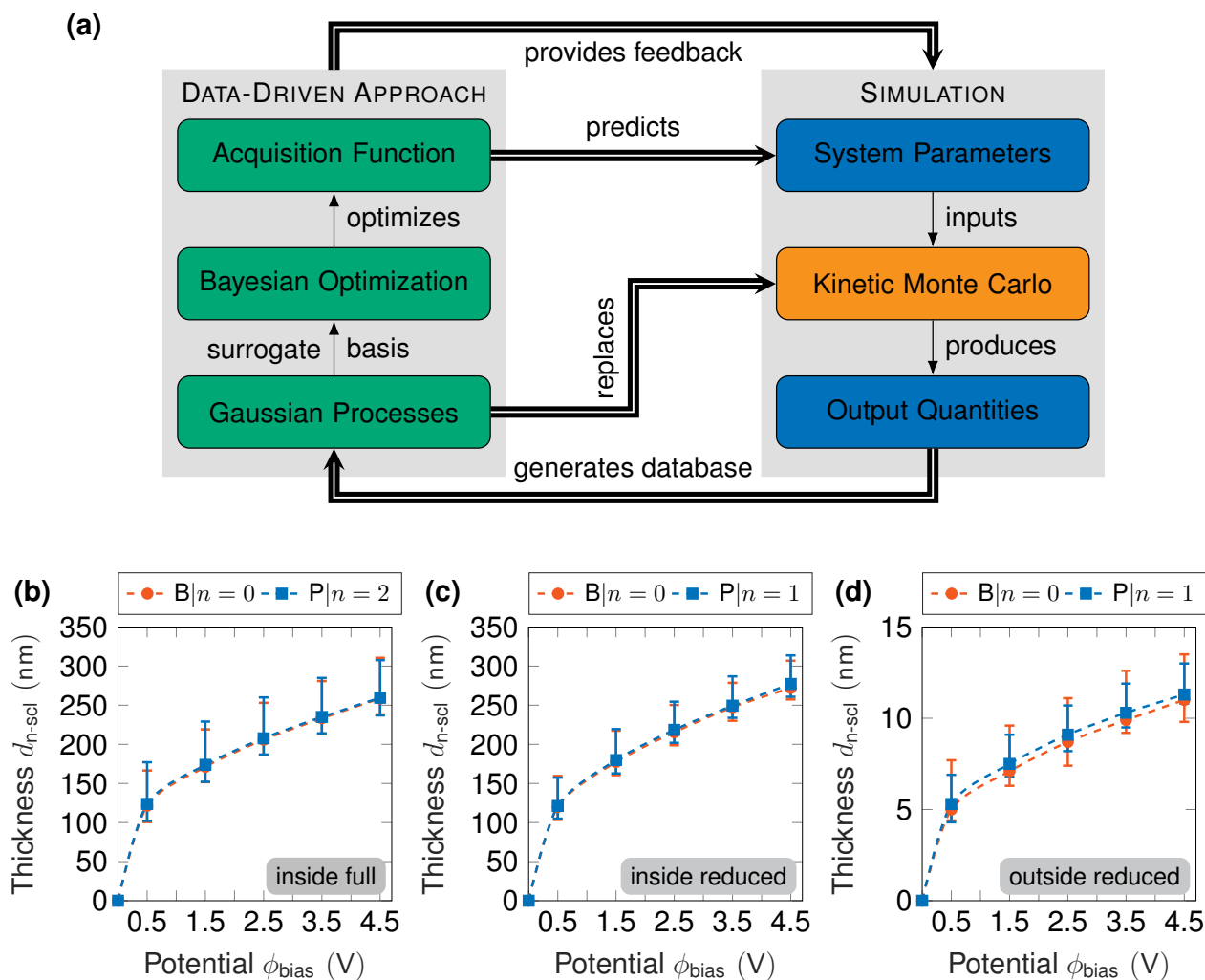


**Figure 3.2 Automated parametrization of kinetic Monte Carlo models via data-driven optimization.** (a) Schematic representation of the proposed computational pipeline including the original kinetic Monte Carlo algorithm on the right-hand side as well as Gaussian processes and Bayesian optimization on the left-hand side. Results of baseline fitting: (b) inside the full, (c) inside the reduced training data set and (d) outside the reduced training data set. In each case, we obtain perfect overlap with respect to the calculated error bars after a maximum of 2 iterations.  $B|n=0$  corresponds to the baseline simulations whereas  $P|n=x$  with  $x=1, 2$  denotes the first/second iteration of the prediction-guided simulation runs. Reprinted with permission from ref. [1]. Copyright 2023 American Chemical Society (ACS).

model based on Gaussian processes relies solely on the outputs of *fast-converging* kMC simulations. Hence, our data-driven methodology opens a pathway for the efficient treatment of complex arbitrary systems via kMC simulations.

**Individual Contributions** I substantially contributed to the ideas and concepts of the data-driven optimization pipeline presented in this study. I implemented the software for the kMC model. I analyzed, assessed and rationalized the simulation data and transferred the scientific results into coherent figures considering the broad expertise on Bayesian optimization and Gaussian processes provided by the co-authors. I authored half of the manuscript, in particular the abstract, introduction and conclusion as well as parts of the methods and results sections.

### 3.3 Modeling of Space-Charge Layers in Solid-State Electrolytes. A Kinetic Monte Carlo Approach and its Validation

**Published By** Katzenmeier L.‡; Gößwein M.‡; Gagliardi A.; Bandarenka A.S. Modeling of Space-Charge Layers in Solid-State Electrolytes: A Kinetic Monte Carlo Approach and Its Validation. *J. Phys. Chem. C* **2022**, *126*, 10900-10909.

The following summary is adapted and in parts reprinted with permission from ref. [103](#), *J. Phys. Chem. C* **2022**, *126*, 10900-10909. Copyright 2022 American Chemical Society (ACS).

**Summary** In this study, we developed a simple yet predictive kinetic Monte Carlo model to simulate the mass-transport phenomenon in solid-state electrolytes (SSEs) under blocking conditions including the electrostatic interactions among ionic species. The validity of our kMC approach is proven by reproducing the quantitative trends in SCL thicknesses and depletion layer capacitance, see Figure [3.3d](#) and Figure [3.3e](#), respectively via a standard input parameter set based on previous investigations. The kMC model requires only a minimal set of physically coherent input parameters mostly available via direct experimental measurement: (1) the bulk concentration of mobile Li-ions,  $c_{\text{Li}^+, \text{bulk}}$ , (2) the maximum concentration of mobile Li-ions in a fully occupied lattice,  $c_{\text{max}}$ , (3) the relative permittivity of the bulk SSE,  $\varepsilon_r$ , and (4) the applied bias potential,  $\phi_{\text{bias}}$ . Further, the kMC simulation enables us to determine inaccessible physical quantities via experiments such as local concentration and potential profiles as well as their time evolution into a steady state, see Figures [3.3a](#) to [3.3c](#). The analysis of local concentration profiles as function of an applied bias potential demonstrates that the depletion and accumulation layers' perpendicular growth regime is directly connected to a fully depleted or fully occupied vacancy lattice, respectively. This observation agrees with previous experimental findings [[114](#), [115](#)] and other modeling approaches, such as thermodynamic simulations [[138](#)].

The central result of the kMC simulations is the time-dependent ion redistribution within the SSE sample. Figure [3.3a](#) illustrates a local steady-state concentration profile,  $c_{\text{Li}^+}(x, y, z)$ , for the standard input parameters. The application of a positive bias potential leads to the formation of depletion and accumulation layers at the respective blocking electrodes whereas the bulk SSE remains in an electroneutral state. The homogeneity of the three-dimensional concentration profiles in the  $xy$ -planes enables us to consider averaged concentration profiles,  $\langle c_{\text{Li}^+}(z) \rangle$ , for the extraction of SCL thicknesses/capacitances. Figure [3.3b](#) shows  $\langle c_{\text{Li}^+}(z) \rangle$  for variable  $\phi_{\text{bias}}$  for the standard input parameters. As expected, the SCL formation only occurs for nonzero bias potentials, and the SCL grows perpendicularly into the SSE when the potential is increased. The  $\text{Li}^+$  accumulation and depletion show an inherent asymmetry - due to the limits of accumulable and depletable charges:  $c_{\text{min}} \leq c_{\text{Li}^+} \leq c_{\text{max}}$ . The SCL formation essentially occurs on a time scale of roughly 500 ms for the given device length of 1500 nm, see Figure [3.3c](#). Assuming a linear relationship between electric field strength and drift velocity, we can scale up the time scale from kMC to an experimentally applied length of 150  $\mu\text{m}$ , which results in an SCL formation time of 50 s.

Figures [3.3a](#) to [3.3c](#) are proof for the physical validity of the kMC model which enables a comparison to experimental results from previous studies [[114](#), [115](#)]. The thickness of the SCLs was, as determined by in situ spectroscopic ellipsometry (SE), is shown in Figure [3.3d](#). Here, the typical asymmetric increase of thickness can be observed. The accumulation layer is roughly 1.5 times larger than the depletion layer. A plateau formation can be observed for potentials larger than 0.5 V, correlating to a fully depleted or filled lattice after which the SCL grows perpendicular to the SSE. Quantitatively, the thicknesses range from 50 nm to 330 nm depending on the applied bias. The kMC simulations agree to all observations if the physical parameters ( $\text{Li}^+$ -ion and vacancy concentration and dielectric constant) are chosen carefully. A second experimental SCL property is the depletion layer capacitance, see Figure [3.3e](#), as obtained by electrochemical impedance spectroscopy (EIS). The experimental capacitance shows a strong decrease with increasing potential ranging between 4  $\mu\text{F cm}^{-2}$  and 12  $\mu\text{F cm}^{-2}$  which is in good quantitative agreement with the simulated capacitances.

‡Shared first authorship: The authors contributed equally to this work.

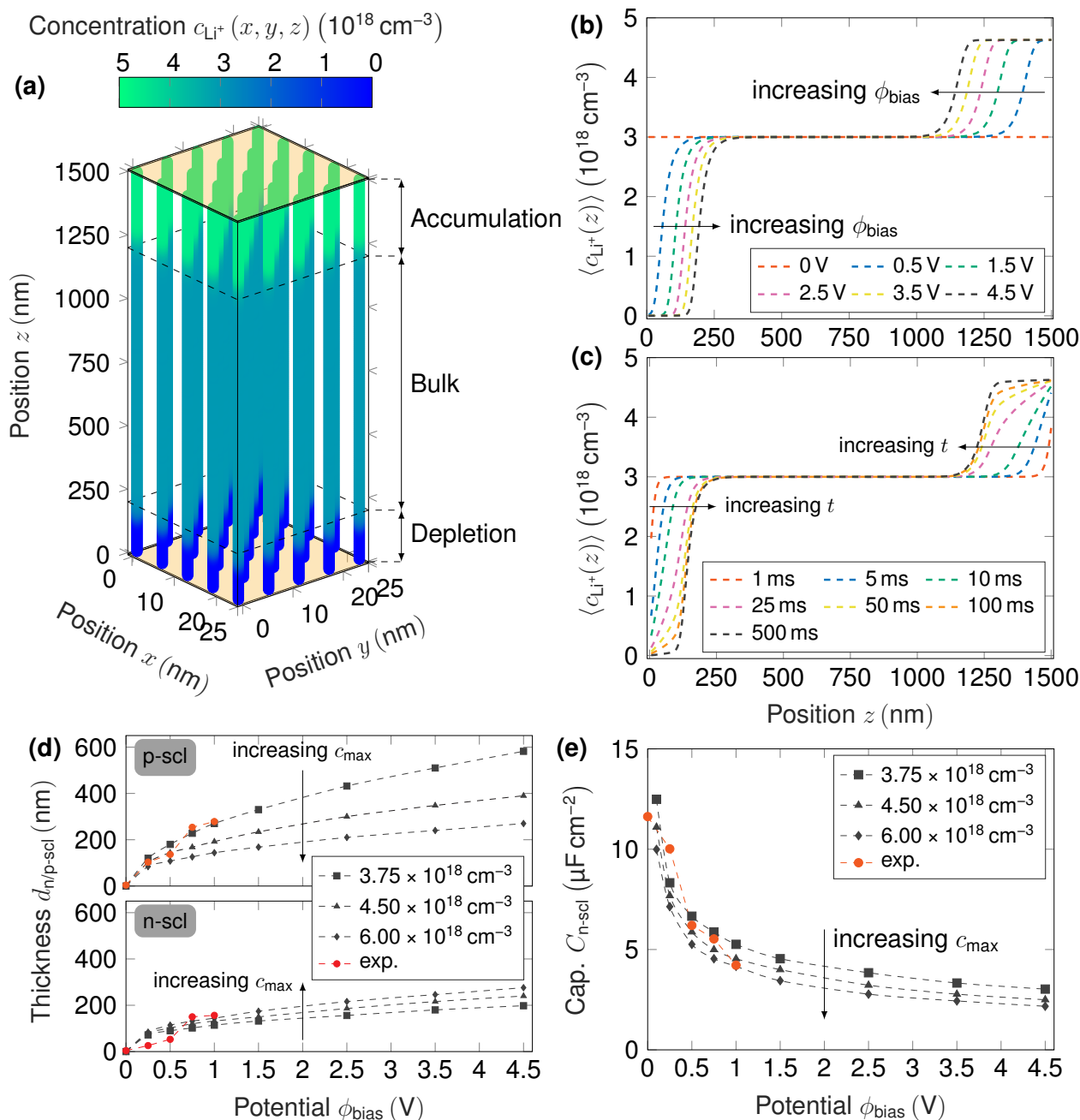


**Figure 3.3 Kinetic Monte Carlo modeling of space-charge layers in solid-state electrolytes under blocking conditions.** Simulation results for a standard parameter set: **(a)** Three-dimensional local concentration profile,  $c_{\text{Li}^+}(x, y, z)$ , **(b)** time evolution of an averaged concentration profile,  $\langle c_{\text{Li}^+}(z) \rangle$ , for  $\phi_{\text{bias}} = 2.5 \text{ V}$  and **(c)** averaged concentration profiles for variable  $\phi_{\text{bias}}$ . Comparison to experimental results: **(d)** SCL thicknesses  $d_{\text{n/p-scl}}$  as function of  $\phi_{\text{bias}}$ . Red dots correspond to the experimental results obtained by SE. **(e)** Depletion layer capacitance,  $C_{\text{n-scl}}$ , as function of  $\phi_{\text{bias}}$ . Red dots correspond to the experimental results obtained by EIS. In the latter two plots, black squares, triangles, and diamonds illustrate the kMC results for different values of  $c_{\text{max}}$ . Reprinted with permission from ref. [103]. Copyright 2022 American Chemical Society (ACS).

**Individual Contributions** I have developed the kinetic Monte Carlo model taking into account the broad expertise on solid-state electrolytes provided by the co-authors. I implemented the software for the kMC model and as well as for data analysis. I analyzed, assessed and rationalized all experimental and simulation data and transferred the scientific results into coherent figures. I have authored half of the manuscript, in particular all computational aspects as well as parts of the introduction and results and discussion sections.



### 3.4 Mass Transport and Charge Transfer Through an Electrified Interface Between Metallic Lithium and Solid-State Electrolytes

**Published By** Katzenmeier L.<sup>‡</sup>; Gößwein M.<sup>‡</sup>; Carstensen L.; Sterzinger J.; Ederer M.; Müller-Buschbaum P.; Gagliardi A.; Bandarenka A.S. Mass Transport and Charge Transfer through an Electrified Interface between Metallic Lithium and Solid-State Electrolytes. *Comm. Chem.* **2023**, 6, 124.

The following summary is adapted and in parts reprinted with permission from ref. 104, *Comm. Chem.* **2023**, 6, 124. This article is licensed under a Creative Commons Attribution 4.0 International License.<sup>¶</sup>

**Summary** In the present work, the application of three methods is aimed at investigating the non-blocking conditions at the SSE/lithium metal interface in solid-state battery-relevant systems, see Figure 3.4a. Spectroscopic ellipsometry is used to measure the optical properties of the SSE to detect the formation of the space charge layers. Impedance spectroscopy helps to measure the ionic resistance of the SSE and formed depletion layers. Kinetic Monte Carlo simulations are used to model the mass transport processes at the interface and the transport within the SSE sample, providing kinetic information about the diffusion and migration of ions in the SSE. These methods are used together to comprehensively understand the mass transport kinetics at the SSE/ lithium metal interface under non-blocking and blocking conditions. Spectroscopic ellipsometry allows for direct measurement of the SCL thicknesses for different applied bias potentials. With the occurrence of a highly resistive layer in the SSE upon application of a potential in our sample, a deeper look into its properties is used to shed light on the size and Li-ion concentration change. With its occurrence proven by SE, the electrochemical properties are tested through electrochemical impedance spectroscopy. Finally, the parameterized kMC model is shown to have large predictive power and can be used in the future to assess the impact of ionic charge accumulation at the interface of a newly developed anode and solid-state electrolytes. Despite the controversies in existing literature, the occurrence of SCLs is reliably and reproducibly shown by three different methods, wherein each method has its own unique capability to characterize the SCL. Importantly, the consistency of the approaches is shown with single parameters that can be very easily compared. The nature of these highly charged layers can explain the widely known degradation at the interface between Li(s) anodes and the SSEs and therefore lay the foundation for a better understanding of how to prevent this instability. Once the interface can be engineered by tuning the materials or creating an interfacial layer to prevent such SCL formation, this can greatly benefit the enabling of all-solid-state batteries with Li(s) anodes.

The consistency of the different approaches, which, except for the feedback loops from the experimentally determined current densities to the injection and removal rates of the kMC electrodes, are completely independent of one another, can be seen in Figure 3.4b. To understand the correlations between the three methods, the electrochemical property of a charged layer near the interface can be explained as follows: a region of lower Li-ion concentration such as the SCL is equivalent to an SSE with lower conductivity, which leads to an increase of resistance in the impedance. The charge accumulation is proportional to the SCL thickness, as the model suggests a perpendicular growth into the SSE. The thickness of the SCLs, all in the range of 100 nm to 600 nm and asymmetrically rising with increasing potentials, are consistent within the three techniques. The overestimation of the SCL thicknesses at positive potentials, can be explained by the way it is calculated from the impedance data. The geometric capacitance (see Fig. S1a Supporting Information) is used to calculate the dielectric constant of the (bulk) SSE, which is then used to calculate the thickness from the SCL capacitance. Herein, we assume that the concentration of Li-ions does not change the dielectric constant of the SSE, which is clearly not true for larger concentration changes. Finally, SE also enables us to extract the fraction change of Li-content,  $\psi_{\text{Li}^+}$ , with respect to the bulk concentration in vol%, see Figure 3.4c. Negative and positive concentration changes are another indicator of the existence of a depletion and accumulation layer. A direct comparison of with the results from the kMC model is not possible as the kMC model only considers mobile  $\text{Li}^+$ , and the volume fraction

<sup>‡</sup>Shared first authorship: The authors contributed equally to this work.

<sup>¶</sup><https://creativecommons.org/licenses/by/4.0/>

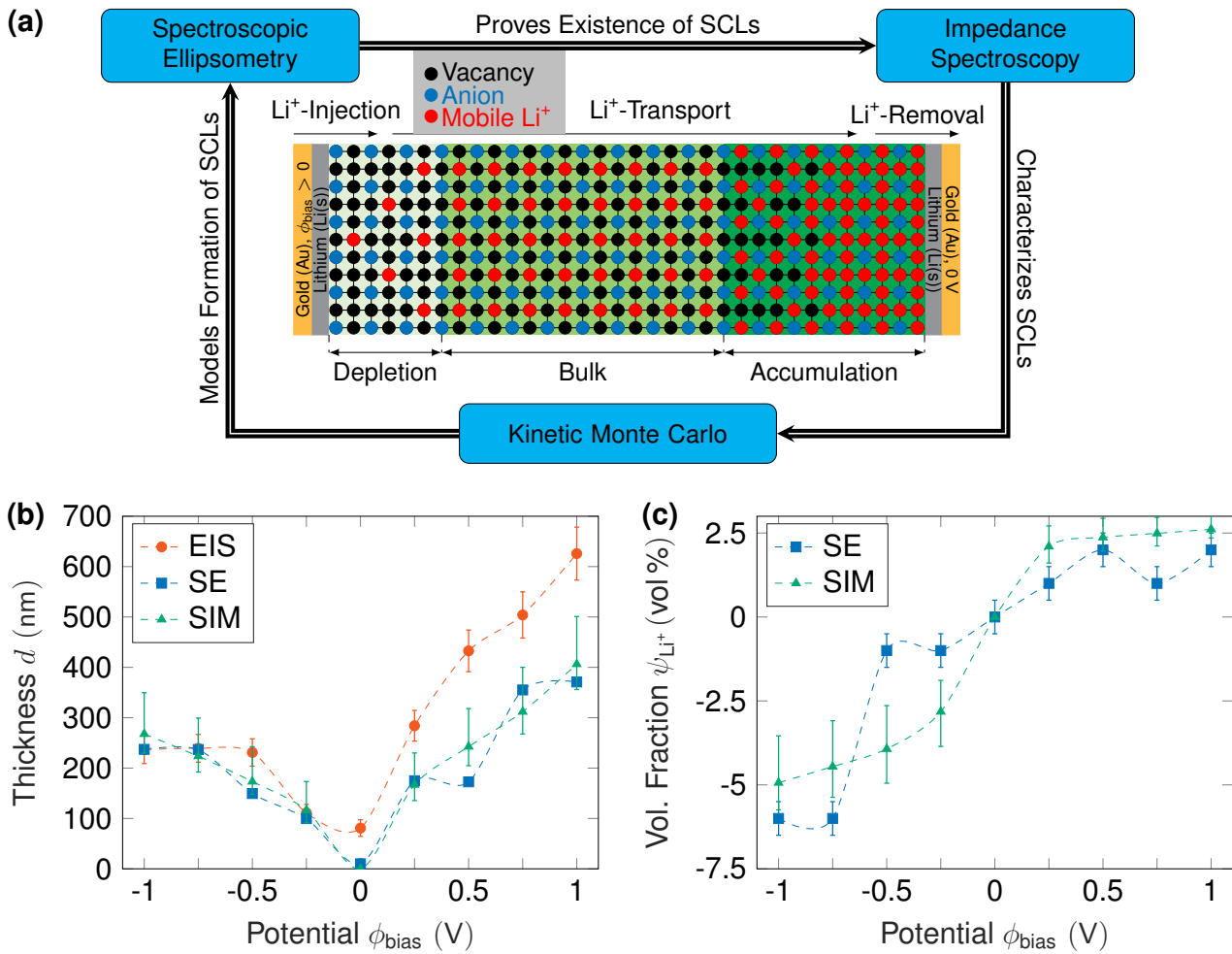


**Figure 3.4 Kinetic Monte Carlo modeling of the mass/charge transfer at the SSE/lithium metal interface under non-blocking conditions.** (a) Schematic representation of the applied workflow is illustrated. (b) Comparison of SCL thicknesses calculated from different methods. The thicknesses calculated from EIS, SE, and kMC simulations for different applied potentials. It demonstrates that the thicknesses calculated from all three methods are in good agreement with the different applied potentials. This confirms the consistency and reliability of the results obtained from the different techniques used in this study. (c) Volume fraction change in vol % based on the fit of the SE data and the kMC simulations, based on a Li-ion density of  $\text{cm}^{-3}$ , including mobile and immobile ions. Reprinted with permission from ref. 104.

change is calculated with respect to the total bulk concentration, that is, mobile and immobile Li-ions. However, we may perform an indirect comparison by adopting a fixed total bulk concentration for the kMC model. In Figure 3.4c, we obtain a decent match with the experimental profile by assuming a total Li-ion density of to compute a corresponding profile from the simulation data. The given total bulk concentration is by a factor of 1500 larger than the bulk concentration of mobile  $\text{Li}^+$  used in the kMC model, which is in good agreement with values from pertinent literature [127].

**Individual Contributions** I have developed the kinetic Monte Carlo model taking into account the broad expertise on solid-state electrolytes provided by the co-authors. I implemented the software for the kMC model and as well as for data analysis. I analyzed, assessed and rationalized all experimental and simulation data and transferred the scientific results into coherent figures. I have authored half of the manuscript, in particular all computational aspects as well as parts of the introduction and results and discussion sections.

## 4 Cross-Article Discussion and Conclusions

Both methodologies presented in this work aim at increasing in the runtime efficiency of kinetic Monte Carlo models for electrochemical systems. However, the way in which both algorithms achieve that target differs heavily. The local temporal acceleration scheme modifies the original kinetic Monte Carlo loop by lowering the sampling rate of quasi-equilibrated process chains and, thus, decreases the simulation time required for converging into a steady-state of a *single* simulation run. In contrast the data-driven feedback loop for automated parametrization does not modify the original kMC algorithm but rather extends it by making the input parametrization dependent on the simulation output. Accordingly, automated parametrization decreases the *total* amount of trial simulation runs required for exploring the input parameter space. As both methods affect different parts of the original kMC algorithm shown in Figure 2.1, from a mere technical point of view it is rather straightforward to merge both algorithms simultaneously into the original one.

Another question arises regarding the generality of both methodologies, *i.e.* to which (electrochemical) systems and in which context can they actually be applied. To benefit from the local temporal acceleration scheme it has to be integrated into a kMC model which suffers from large time-scale disparities. Otherwise, the additional computational steps required by the local temporal acceleration scheme will cause a slight overhead with respect to the original kMC algorithm. An instructive example for a system to which the local temporal acceleration is not applicable is the space-charge layer formation under (non-)blocking conditions in SSEs. Here, extensive simulation times are not caused by large time-scale disparities but rather by high particle densities and the corresponding regular update of the potential energy surface. A direct route for avoiding simulations with high particle densities is an accurate surrogate model, which has been trained via a data set generated from the output of fast-converging kMC runs - one of the fundamental concepts that our data-driven feedback loop relies on. In contrast, our algorithm for automated parametrization is in principle applicable to any kMC model which is restrained by the existence of several open input parameters. However, we have to distinguish between inverse problem solution inside and *outside* the data base. While the former one will always result in suitable input parameters if the training data set is sufficiently large enough, the success of the latter one very much depends on the qualitative physical behavior of the system outside of the training data set. The present form of the data-driven algorithm is in particular for extrapolation limited by a lack of knowledge regarding the underlying physical models. In this context, making our parametrization scheme *physics-informed* opens a potential pathway for improvement, see Chapter 5.

One last interesting aspect to discuss is the local quasi-equilibrium approach of the presented temporal acceleration scheme. In this work, we defined a particle-based criterion to detect whether the local environment enters a state of quasi-equilibrium. Apparently, this criterion is not transferable to arbitrary electrochemical kMC models whereas the remaining computational steps of the acceleration scheme are rather generic. Consider for instance a catalytic system such as the reduction of oxygen on platinum nanoparticles [139, 140, 141]. Here, the occurrence of a certain reaction step does not only depend on the involved particles but in particular also on the involved reaction site. The geometry-dependent reactivity of certain reaction sites is in fact the more important aspect. Thus, it is sensible to switch from a local particle-based to a local *site*-based quasi-equilibrium criterion, see ref. [2] Supporting Information for a concrete example. In general, the argument can be made that a local quasi-equilibrium approach for conserving local physical properties upon scaling is a much broader concept, and could also be utilized in kMC models of non-electrochemical systems. How the criterion is eventually realized for a concrete system is an implementation detail which has to be reconsidered on a case-by-case basis.

In conclusion, we have presented two novel algorithms to optimize the runtime efficiency of kMC models for electrochemical systems. We have demonstrated that both methods may substantially increase the runtime efficiency of the original algorithm making the kinetic Monte Carlo method a serious alternative again when simulating electrochemical systems.



## 5 Perspectives

The following ideas are in parts reprinted with permission from ref. 1, J. Phys. Chem. A 2023, 127, 28, 5967–5978. Copyright 2023 American Chemical Society (ACS).

Firstly, we want to provide some routes for additionally improving the proposed data-driven pipeline for automated parameterization. In general, we advise to fully exploit the physical intuition present for the investigated system. For instance, in the present case study it is apparent that  $d_{n-scl}(\phi_{bias})$  grows non-linearly for  $\phi_{bias} \leq 0.5\text{ V}$  and linearly otherwise, see ref. [1]. Hence, a further increase in data efficiency can be achieved if the potential range is restricted to  $\phi_{bias} > 0.5\text{ V}$ . Further, a lot of qualitative physical insight exists for the given application. In particular, the monotonicity of the space-charge layer formation with respect to the input parameters is well-established, see ref. [103]. This knowledge can be directly included in the form of gradient classification as outlined in ref. [142, 143]. Additionally, we may incorporate a quantification for the kMC-inherent statistical fluctuations via a noise kernel. In this way, not only a realistic estimation of the prediction with respect to the kMC model can be added but also with respect to innately error-prone real-world measurements. By combining the uncertainty of the data-driven and the physics-based model a multi-fidelity model can be implemented in which a data-driven model trained on kMC simulations will provide predictions. The uncertainty of this model will then determine whether an additional simulation or a real world experiment is necessary.

The presented methodologies open a pathway to simulate electrochemical systems for which the kMC method had been discarded so far due to excessive simulation times. An instructive example is a kMC model for the origin of photocurrent generation at the organic/aqueous electrolyte interface - a system which features both large time-scale disparities and several open input parameters. To showcase the working principle and the effectivity of the local temporal acceleration scheme we considered only a simplified version of the hybrid interface to put the emphasis on the accurate treatment of large time-scale disparities. However, the simplified test-system already demonstrates that photocurrent generation is coupled to reduction reactions at the hybrid interface confirming a central experimental finding [88, 89, 90]. With the methodological part established, the next step is to build a physically accurate model for the photocurrent generation at the organic/aqueous electrolyte interface. In this context, the following aspects should be covered with support of experiments and *ab initio* calculations:

- 1 Enhanced process activation in the organic material including a detailed resolution of exciton and charge related process chains. An investigation of the contribution of different exciton dissociation mechanisms to photocurrent generation is crucial for understanding the exact working mechanism of hybrid organic devices.
- 2 Design of a sophisticated reaction network at organic/aqueous electrolyte interface including penetration of the electrolyte into the polymer matrix. The current canonical experimental finding is that oxygen is reduced to hydrogen peroxide [77, 144].
- 3 Investigation of different models for the transition of particles from the interface to the bulk electrolyte which defines a boundary condition with respect to particle concentrations. The simplest solution is to treat the bulk as a reservoir for ionic/molecular species with a given constant bulk concentration.

From a methodological point of view, it is sensible to integrate the local temporal acceleration scheme first. Subsequently, a database can be generated to enable automated parametrization. Applying both algorithms to a complex real-world system successfully will further establish their usefulness in the research community making them part of the standard approach to simulate electrochemical systems via the kMC method.



# Acknowledgement

I am very grateful to my PhD supervisor Alessio Gagliardi for giving me many exciting opportunities in diverse research programmes and working with collaborators on interdisciplinary projects. This has provided me with the creative space to develop innovative ideas and effective novel approaches. Further, I am very thankful for his insights into how the "game of academia" is played nowadays.

I am very grateful to the European Union's Horizon 2020 FETOPEN 2018-2020 program "LION-HEARTED" for funding my research activities at the TUM. Further, I want to express cordial thanks to all members/contributors of the program for sharing their broad expertise during scientific discussions at several workshops.

I whole-heartedly appreciate the collaborative work with Aliaksandr Bandarenka and Leon Katzenmeier on solid-state electrolytes used in all-solid-state batteries. I am grateful for our joint achievements and it was a pleasure working with you.

I am very grateful to all my great colleagues and friends from the SNE research group, that are Ioannis, Marlon, Michael, Felix, Kashif, Gohar, Milan, Poonam, Ajay, Siby and Waldemar. Working with you was amazing and I will keep our mostly non-scientific lunch discussions in good memory.

I would like to show my greatest thanks and respect to my PhD mentor Michael Haider for just letting me go down my own scientific road and, thus, learn from my mistakes. I still remember very vividly joining Michael's lecture "Computational Nanoelectronics" during my first semester at TUM in 2017 - the best lecture I participated in during 10 years of university. Michael has a unique style of leadership and I was able to learn a thing or two from observing him.

I want to express a special acknowledgement to my colleague and friend Ioannis Kouroudis. We became close friends over the last four years sharing the same humor and interests outside of academia. I still believe it is a fair conclusion from the Trojan horse incident that all Greeks have a bit of a conman in their hearts.

Last but not least, I want express my deepest gratitude and appreciation to family and in particular to my parents. I have nothing but respect for the achievements in life, and they did a great job in raising four children with very diverging characters. A special shoutout goes to my younger brother Daniel who is also taking the road of becoming a software engineer. Being the youngest child is both a blessing and a curse and I very much prefer being just another "kid in the middle".





# Bibliography

- [1] I. Kouroudis, M. Gößwein, and A. Gagliardi, "Utilizing Data-Driven Optimization to Automate the Parametrization of Kinetic Monte Carlo Models," *J. Phys. Chem. A*, vol. 127, no. 28, pp. 5967–5978, 2023, pMID: 37421601. [Online]. Available: <https://doi.org/10.1021/acs.jpca.3c02482>
- [2] M. Gößwein, W. Kaiser, and A. Gagliardi, "Local Temporal Acceleration Scheme to Couple Transport and Reaction Dynamics in Kinetic Monte Carlo Models of Electrochemical Systems," *J. Chem. Theory Comput.*, vol. 18, no. 5, pp. 2749–2763, 2022. [Online]. Available: <https://doi.org/10.1021/acs.jctc.1c01010>
- [3] P. Zhu and R. W. Smith, "Dynamic Simulation of Crystal Growth by Monte Carlo Method—I. Model Description and Kinetics," *Acta Metall. Mater.*, vol. 40, no. 4, pp. 683–692, 1992. [Online]. Available: <https://www.sciencedirect.com/science/article/pii/0956715192900094>
- [4] M. Rak, M. Izdebski, and A. Brozi, "Kinetic Monte Carlo Study of Crystal Growth from Solution," *Comput. Phys. Commun.*, vol. 138, no. 3, pp. 250–263, 2001. [Online]. Available: <https://www.sciencedirect.com/science/article/pii/S0010465501002387>
- [5] S. Piana and J. D. Gale, "Three-Dimensional Kinetic Monte Carlo Simulation of Crystal Growth from Solution," *J. Cryst. Growth*, vol. 294, no. 1, pp. 46–52, 2006, new Advances in Crystal Growth and Nucleation. [Online]. Available: <https://www.sciencedirect.com/science/article/pii/S0022024806005197>
- [6] A. L. Magna, S. Coffa, and L. Colombo, "A Lattice Kinetic Monte Carlo Code for the Description of Vacancy Diffusion and Self-Organization in Si," *Nucl. Instrum. Methods Phys. Res. Sect. B Beam Interact. Mater. At.*, vol. 148, no. 1, pp. 262–267, 1999. [Online]. Available: <https://www.sciencedirect.com/science/article/pii/S0168583X98007988>
- [7] P. P. Dholabhai, S. Anwar, J. B. Adams, P. Crozier, and R. Sharma, "Kinetic Lattice Monte Carlo Model for Oxygen Vacancy Diffusion in Praseodymium Doped Ceria: Applications to Materials Design," *J. Solid State Chem.*, vol. 184, no. 4, pp. 811–817, 2011. [Online]. Available: <https://www.sciencedirect.com/science/article/pii/S0022459611000582>
- [8] M. Grabowski, J. Rogal, and R. Drautz, "Kinetic Monte Carlo Simulations of Vacancy Diffusion in Nondilute Ni- $x$  ( $x = \text{Re}, \text{W}, \text{Ta}$ ) Alloys," *Phys. Rev. Mater.*, vol. 2, p. 123403, Dec 2018. [Online]. Available: <https://link.aps.org/doi/10.1103/PhysRevMaterials.2.123403>
- [9] H. Bässler, "Charge Transport in Disordered Organic Photoconductors a Monte Carlo Simulation Study," *Phys. Status Solidi B*, vol. 175, no. 1, pp. 15–56, 1993. [Online]. Available: <https://onlinelibrary.wiley.com/doi/abs/10.1002/pssb.2221750102>
- [10] W. Kaiser, T. Albes, and A. Gagliardi, "Charge Carrier Mobility of Disordered Organic Semiconductors with Correlated Energetic and Spatial Disorder," *Phys. Chem. Chem. Phys.*, vol. 20, pp. 8897–8908, 2018. [Online]. Available: <http://dx.doi.org/10.1039/C8CP00544C>
- [11] W. Kaiser, J. Popp, M. Rinderle, T. Albes, and A. Gagliardi, "Generalized Kinetic Monte Carlo Framework for Organic Electronics," *Algorithms*, vol. 11, no. 4, p. 37, 2018. [Online]. Available: <https://www.mdpi.com/1999-4893/11/4/37>

- [12] K. Reuter and M. Scheffler, "First-Principles Kinetic Monte Carlo Simulations for Heterogeneous Catalysis: Application to the Co Oxidation at RuO<sub>2</sub>(110)," *Phys. Rev. B*, vol. 73, p. 045433, Jan 2006. [Online]. Available: <https://link.aps.org/doi/10.1103/PhysRevB.73.045433>
- [13] M. Jørgensen and H. Grönbeck, "Scaling Relations and Kinetic Monte Carlo Simulations to Bridge the Materials Gap in Heterogeneous Catalysis," *ACS Catal.*, vol. 7, no. 8, pp. 5054–5061, 2017. [Online]. Available: <https://doi.org/10.1021/acscatal.7b01194>
- [14] —, "Montecoffee: A Programmable Kinetic Monte Carlo Framework," *J. Chem. Phys.*, vol. 149, no. 11, p. 114101, 2018. [Online]. Available: <https://doi.org/10.1063/1.5046635>
- [15] —, "Selective Acetylene Hydrogenation Over Single-Atom Alloy Nanoparticles by Kinetic Monte Carlo," *J. Am. Chem. Soc.*, vol. 141, no. 21, pp. 8541–8549, 2019. [Online]. Available: <https://doi.org/10.1021/jacs.9b02132>
- [16] —, "Perspectives on Computational Catalysis for Metal Nanoparticles," *ACS Catal.*, vol. 9, no. 10, pp. 8872–8881, 2019. [Online]. Available: <https://doi.org/10.1021/acscatal.9b02228>
- [17] P. K. Watkins, A. B. Walker, and G. L. B. Verschoor, "Dynamical Monte Carlo Modelling of Organic Solar Cells: The Dependence of Internal Quantum Efficiency on Morphology," *Nano Lett.*, vol. 5, no. 9, pp. 1814–1818, 2005. [Online]. Available: <https://doi.org/10.1021/nl051098o>
- [18] M. Casalegno, G. Raos, and R. Po, "Methodological Assessment of Kinetic Monte Carlo Simulations of Organic Photovoltaic Devices: The Treatment of Electrostatic Interactions," *J. Chem. Phys.*, vol. 132, no. 9, p. 094705, 2010. [Online]. Available: <https://doi.org/10.1063/1.3337909>
- [19] D. Kipp and V. Ganesan, "A Kinetic Monte Carlo Model with Improved Charge Injection Model for the Photocurrent Characteristics of Organic Solar Cells," *J. Appl. Phys.*, vol. 113, no. 23, p. 234502, 2013. [Online]. Available: <https://doi.org/10.1063/1.4811337>
- [20] W. Kaiser and A. Gagliardi, "Kinetic Monte Carlo Study of the Role of the Energetic Disorder on the Open-Circuit Voltage in Polymer/fullerene Solar Cells," *J. Phys. Chem. Lett.*, vol. 10, no. 20, pp. 6097–6104, 2019. [Online]. Available: <https://doi.org/10.1021/acs.jpcllett.9b02144>
- [21] T. O. Drews, A. Radisic, J. Erlebacher, R. D. Braatz, P. C. Searson, and R. C. Alkire, "Stochastic Simulation of the Early Stages of Kinetically Limited Electrodeposition," *J. Electrochem. Soc.*, vol. 153, no. 6, p. C434, apr 2006. [Online]. Available: <https://dx.doi.org/10.1149/1.2191167>
- [22] B. Andreaus and M. Eikerling, "Active Site Model for Co Adlayer Electrooxidation on Nanoparticle Catalysts," *J. Electroanal. Chem.*, vol. 607, no. 1, pp. 121–132, 2007, theoretical and Computational Electrochemistry. [Online]. Available: <https://www.sciencedirect.com/science/article/pii/S0022072807000691>
- [23] R. N. Methekar, P. W. C. Northrop, K. Chen, R. D. Braatz, and V. R. Subramanian, "Kinetic Monte Carlo Simulation of Surface Heterogeneity in Graphite Anodes for Lithium-Ion Batteries: Passive Layer Formation," *J. Electrochem. Soc.*, vol. 158, no. 4, p. A363, feb 2011. [Online]. Available: <https://dx.doi.org/10.1149/1.3548526>
- [24] G. Blanquer, Y. Yin, M. A. Quiroga, and A. A. Franco, "Modeling Investigation of the Local Electrochemistry in Lithium-O<sub>2</sub>Batteries: A Kinetic Monte Carlo Approach," *J. Electrochem. Soc.*, vol. 163, no. 3, pp. A329–A337, dec 2015. [Online]. Available: <https://doi.org/10.1149/2.0841602jes>
- [25] E. M. Gavilán-Arriazu, O. A. Pinto, B. A. López de Mishima, D. E. Barraco, O. A. Oviedo, and E. P. M. Leiva, "Kinetic Monte Carlo Applied to the Electrochemical Study of the Li-ion Graphite System," *Electrochim. Acta*, vol. 331, p. 135439, 2020. [Online]. Available: <https://www.sciencedirect.com/science/article/pii/S0013468619323114>

- [26] E. M. Gavilán-Arriazu, M. P. Mercer, D. E. Barraco, H. E. Hoster, and E. P. M. Leiva, "Kinetic Monte Carlo Simulations Applied to Li-Ion and Post Li-Ion Batteries: A Key Link in the Multi-Scale Chain," *Prog. Energy*, vol. 3, no. 4, p. 042001, aug 2021. [Online]. Available: <https://dx.doi.org/10.1088/2516-1083/ac1a65>
- [27] R. Pornprasertsuk, J. Cheng, H. Huang, and F. B. Prinz, "Electrochemical Impedance Analysis of Solid Oxide Fuel Cell Electrolyte Using Kinetic Monte Carlo Technique," *Solid State Ion.*, vol. 178, no. 3, pp. 195–205, 2007. [Online]. Available: <https://www.sciencedirect.com/science/article/pii/S0167273807000045>
- [28] S. Liu, M. G. White, and P. Liu, "Mechanism of Oxygen Reduction Reaction on Pt(111) in Alkaline Solution: Importance of Chemisorbed Water on Surface," *J. Phys. Chem. C*, vol. 120, no. 28, pp. 15 288–15 298, 2016. [Online]. Available: <https://doi.org/10.1021/acs.jpcc.6b05126>
- [29] B. Bai and Y.-T. Chen, "Simulation of the Oxygen Reduction Reaction (ORR) inside the Cathode Catalyst Layer (CCL) of Proton Exchange Membrane Fuel Cells Using the Kinetic Monte Carlo Method," *Energies*, vol. 11, no. 10, 2018. [Online]. Available: <https://www.mdpi.com/1996-1073/11/10/2529>
- [30] T. Albes, "Kinetic Monte Carlo Simulations of Organic Solar Cells," Ph.D. dissertation, Technische Universität München, 2019.
- [31] D. T. Gillespie, "Exact Stochastic Simulation of Coupled Chemical Reactions," *J. Phys. Chem.*, vol. 81, no. 25, pp. 2340–2361, 1977. [Online]. Available: <https://doi.org/10.1021/j100540a008>
- [32] P. P. Ewald, "Die Berechnung Optischer Und Elektrostatischer Gitterpotentiale," *Ann. Phys.*, vol. 369, no. 3, pp. 253–287, 1921. [Online]. Available: <https://onlinelibrary.wiley.com/doi/abs/10.1002/andp.19213690304>
- [33] M. P. Allen and D. J. Tildesley, *Computer Simulation of Liquids*. Oxford, UK: Oxford University Press, 2017.
- [34] L. Greengard and V. Rokhlin, "A Fast Algorithm for Particle Simulations," *J. Comput. Phys.*, vol. 73, no. 2, pp. 325–348, 1987. [Online]. Available: <https://www.sciencedirect.com/science/article/pii/0021999187901409>
- [35] W. R. Saunders, J. Grant, E. H. Müller, and I. Thompson, "Fast Electrostatic Solvers for Kinetic Monte Carlo Simulations," *J. Comput. Phys.*, vol. 410, p. 109379, 2020. [Online]. Available: <https://www.sciencedirect.com/science/article/pii/S0021999120301534>
- [36] N. J. van der Kaap and L. J. A. Koster, "Massively Parallel Kinetic Monte Carlo Simulations of Charge Carrier Transport in Organic Semiconductors," *J. Comput. Phys.*, vol. 307, pp. 321–332, 2016. [Online]. Available: <https://www.sciencedirect.com/science/article/pii/S0021999115008153>
- [37] A. Chatterjee and D. G. Vlachos, "An Overview of Spatial Microscopic and Accelerated Kinetic Monte Carlo Methods," *J. Comput. Aided Mol. Des.*, vol. 14, no. 2, pp. 253–308, 2007. [Online]. Available: <https://doi.org/10.1007/s10820-006-9042-9>
- [38] F. Röder, R. D. Braatz, and U. Krewer, "Direct Coupling of Continuum and Kinetic Monte Carlo Models for Multiscale Simulation of Electrochemical Systems," *Comput. Chem. Eng.*, vol. 121, pp. 722–735, 2019. [Online]. Available: <https://www.sciencedirect.com/science/article/pii/S0098135418309013>
- [39] C. Schaefer and A. P. J. Jansen, "Coupling of Kinetic Monte Carlo Simulations of Surface Reactions to Transport in a Fluid for Heterogeneous Catalytic Reactor Modeling," *J. Chem. Phys.*, vol. 138, no. 5, p. 054102, 2013. [Online]. Available: <https://doi.org/10.1063/1.4789419>

- [40] S. Matera, M. Maestri, A. Cuoci, and K. Reuter, "Predictive-Quality Surface Reaction Chemistry in Real Reactor Models: Integrating First-Principles Kinetic Monte Carlo Simulations into Computational Fluid Dynamics," *ACS Catal.*, vol. 4, no. 11, pp. 4081–4092, 2014. [Online]. Available: <https://doi.org/10.1021/cs501154e>
- [41] R. F. de Morais, P. Sautet, D. Loffreda, and A. A. Franco, "A Multiscale Theoretical Methodology for the Calculation of Electrochemical Observables from Ab Initio Data: Application to the Oxygen Reduction Reaction in a Pt(111)-Based Polymer Electrolyte Membrane Fuel Cell," *Electrochim. Acta*, vol. 56, no. 28, pp. 10 842–10 856, 2011, selected Papers from the 61st ISE Meeting, Nice, France, 2010. [Online]. Available: <https://www.sciencedirect.com/science/article/pii/S001346861100853X>
- [42] M. A. Quiroga and A. A. Franco, "A Multi-Paradigm Computational Model of Materials Electrochemical Reactivity for Energy Conversion and Storage," *J. Electrochem. Soc.*, vol. 162, no. 7, pp. E73–E83, 2015. [Online]. Available: <https://doi.org/10.1149/2.1011506jes>
- [43] M. A. Quiroga, K. Malek, and A. A. Franco, "A Multiparadigm Modeling Investigation of Membrane Chemical Degradation in PEM Fuel Cells," *J. Electrochem. Soc.*, vol. 163, no. 2, pp. F59–F70, nov 2015. [Online]. Available: <https://doi.org/10.1149/2.0931514jes>
- [44] F. Röder, R. D. Braatz, and U. Krewer, "Multi-Scale Modeling of Solid Electrolyte Interface Formation in Lithium-Ion Batteries," in *26th European Symposium on Computer Aided Process Engineering*, ser. Computer Aided Chemical Engineering, Z. Kravanja and M. Bogataj, Eds. Elsevier, 2016, vol. 38, pp. 157–162. [Online]. Available: <https://www.sciencedirect.com/science/article/pii/B978044463428350031X>
- [45] C. Shinagawa, H. Ushiyama, and K. Yamashita, "Multiscale Simulations for Lithium-Ion Batteries: SEI Film Growth and Capacity Fading," *J. Electrochem. Soc.*, vol. 164, no. 13, pp. A3018–A3024, 2017. [Online]. Available: <https://doi.org/10.1149/2.0381713jes>
- [46] A. A. Franco, "Multiscale Modelling and Numerical Simulation of Rechargeable Lithium Ion Batteries: Concepts, Methods and Challenges," *RSC Adv.*, vol. 3, pp. 13 027–13 058, 2013. [Online]. Available: <http://dx.doi.org/10.1039/C3RA23502E>
- [47] D. T. Gillespie, "Approximate Accelerated Stochastic Simulation of Chemically Reacting Systems," *J. Chem. Phys.*, vol. 115, no. 4, pp. 1716–1733, 2001. [Online]. Available: <https://doi.org/10.1063/1.1378322>
- [48] Z. Zheng, R. M. Stephens, R. D. Braatz, R. C. Alkire, and L. R. Petzold, "A Hybrid Multiscale Kinetic Monte Carlo Method for Simulation of Copper Electrodeposition," *J. Comput. Phys.*, vol. 227, no. 10, pp. 5184–5199, 2008. [Online]. Available: <https://www.sciencedirect.com/science/article/pii/S0021999108000727>
- [49] D. J. Higham, "Modeling and Simulating Chemical Reactions," *SIAM Rev.*, vol. 50, no. 2, pp. 347–368, 2008. [Online]. Available: <https://doi.org/10.1137/060666457>
- [50] H. Resat, H. S. Wiley, and D. A. Dixon, "Probability-Weighted Dynamic Monte Carlo Method for Reaction Kinetics Simulations," *J. Phys. Chem. B*, vol. 105, no. 44, pp. 11 026–11 034, 2001. [Online]. Available: <https://doi.org/10.1021/jp011404w>
- [51] M. A. Snyder, A. Chatterjee, and D. G. Vlachos, "Net-Event Kinetic Monte Carlo for Overcoming Stiffness in Spatially Homogeneous and Distributed Systems," *Comput. Chem. Eng.*, vol. 29, no. 4, pp. 701–712, 2005, control of Multiscale and Distributed Process Systems. [Online]. Available: <https://www.sciencedirect.com/science/article/pii/S0098135404002789>
- [52] A. Chatterjee and A. F. Voter, "Accurate Acceleration of Kinetic Monte Carlo Simulations through the Modification of Rate Constants," *J. Chem. Phys.*, vol. 132, no. 19, p. 194101, 2010. [Online]. Available: <https://doi.org/10.1063/1.3409606>

- [53] H. Lepage, A. Kaminski-Cachopo, A. Poncet, and G. le Carval, "Simulation of Electronic Transport in Silicon Nanocrystal Solids," *J. Phys. Chem. C*, vol. 116, no. 20, pp. 10873–10880, 2012. [Online]. Available: <https://doi.org/10.1021/jp301713v>
- [54] W. Kaiser, M. Gößwein, and A. Gagliardi, "Acceleration Scheme for Particle Transport in Kinetic Monte Carlo Methods," *J. Chem. Phys.*, vol. 152, no. 17, p. 174106, 2020. [Online]. Available: <https://doi.org/10.1063/5.0002289>
- [55] E. C. Dybeck, C. P. Plaisance, and M. Neurock, "Generalized Temporal Acceleration Scheme for Kinetic Monte Carlo Simulations of Surface Catalytic Processes by Scaling the Rates of Fast Reactions," *J. Chem. Theory Comput.*, vol. 13, no. 4, pp. 1525–1538, 2017. [Online]. Available: <https://doi.org/10.1021/acs.jctc.6b00859>
- [56] M. Andersen, C. P. Plaisance, and K. Reuter, "Assessment of Mean-Field Microkinetic Models for Co Methanation on Stepped Metal Surfaces Using Accelerated Kinetic Monte Carlo," *J. Chem. Phys.*, vol. 147, no. 15, p. 152705, 2017. [Online]. Available: <https://doi.org/10.1063/1.4989511>
- [57] S. Matera, W. F. Schneider, A. Heyden, and A. Savara, "Progress in Accurate Chemical Kinetic Modeling, Simulations, and Parameter Estimation for Heterogeneous Catalysis," *ACS Catalysis*, vol. 9, no. 8, pp. 6624–6647, 2019. [Online]. Available: <https://doi.org/10.1021/acscatal.9b01234>
- [58] J. Li, I. Maresi, Y. Lum, and J. W. Ager, "Effects of Surface Diffusion in Electrocatalytic Co2 Reduction on Cu Revealed by Kinetic Monte Carlo Simulations," *J. Chem. Phys.*, vol. 155, no. 16, p. 164701, 2021. [Online]. Available: <https://doi.org/10.1063/5.0068517>
- [59] A. Nichol and G. J. Ackland, "Property Trends in Simple Metals: An Empirical Potential Approach," *Phys. Rev. B*, vol. 93, p. 184101, May 2016. [Online]. Available: <https://link.aps.org/doi/10.1103/PhysRevB.93.184101>
- [60] R. H. Gilmore, E. M. Y. Lee, M. C. Weidman, A. P. Willard, and W. A. Tisdale, "Charge Carrier Hopping Dynamics in Homogeneously Broadened Pbs Quantum Dot Solids," *Nano Lett.*, vol. 17, no. 2, pp. 893–901, 2017. [Online]. Available: <https://doi.org/10.1021/acs.nanolett.6b04201>
- [61] B. Ghalami Choobar, H. Modarress, R. Halladj, and S. Amjad-Iranagh, "Electrodeposition of Lithium Metal on Lithium Anode Surface, a Simulation Study by: Kinetic Monte Carlo-embedded Atom Method," *Comput. Mater. Sci.*, vol. 192, p. 110343, 2021. [Online]. Available: <https://www.sciencedirect.com/science/article/pii/S0927025621000689>
- [62] B. Hosemann, M. Drache, and S. Beuermann, "Advanced Kinetic Parameter Fit Applied to Radical Copolymerizations," *Macromol. Symp.*, vol. 370, no. 1, pp. 17–25, 2016. [Online]. Available: <https://onlinelibrary.wiley.com/doi/abs/10.1002/masy.201600095>
- [63] A. S. C. Rego and A. L. T. Brandão, "Parameter Estimation and Kinetic Monte Carlo Simulation of Styrene and N-butyl Acrylate Copolymerization through Atrp," *Ind. Eng. Chem. Res.*, vol. 60, no. 23, pp. 8396–8408, 2021. [Online]. Available: <https://doi.org/10.1021/acs.iecr.1c00943>
- [64] J. M. Sestito, T. A. L. Harris, and Y. Wang, "Reduced-Order Kinetic Monte Carlo Model to Simulate Water Diffusion in Biodegradable Polymers," *Comput. Mater. Sci.*, vol. 203, p. 111141, 2022. [Online]. Available: <https://www.sciencedirect.com/science/article/pii/S092702562100803X>
- [65] D. Crevillén-García, P. Leung, and A. A. Shah, "An Emulator for Kinetic Monte Carlo Simulations of Kinetically Controlled Metal Electrodeposition," *J. Phys. Conf. Ser.*, vol. 1053, no. 1, p. 012081, jul 2018. [Online]. Available: <https://dx.doi.org/10.1088/1742-6596/1053/1/012081>
- [66] H. C. Herbol, W. Hu, P. Frazier, P. Clancy, and M. Poloczek, "Efficient Search of Compositional Space for Hybrid Organic-Inorganic Perovskites Via Bayesian Optimization," *Npj Comput. Mater.*, vol. 4, no. 1, p. 51, 2018. [Online]. Available: <https://doi.org/10.1038/s41524-018-0106-7>

- [67] C. Lampe, I. Kouroudis, M. Harth, S. Martin, A. Gagliardi, and A. S. Urban, "Rapid Data-Efficient Optimization of Perovskite Nanocrystal Syntheses through Machine Learning Algorithm Fusion," *Adv. Mater.*, vol. 35, no. 16, p. 2208772, 2023. [Online]. Available: <https://onlinelibrary.wiley.com/doi/abs/10.1002/adma.202208772>
- [68] J. Chang, P. Nikolaev, J. Carpena-Núñez, R. Rao, K. Decker, A. E. Islam, J. Kim, M. A. Pitt, J. I. Myung, and B. Maruyama, "Efficient Closed-Loop Maximization of Carbon Nanotube Growth Rate Using Bayesian Optimization," *Sci. Rep.*, vol. 10, no. 1, pp. 1–9, 2020. [Online]. Available: <https://doi.org/10.1038/s41598-020-64397-3>
- [69] J. Popp, M. Haider, M. Franckić, J. Faist, and C. Jirauschek, "Bayesian Optimization of Quantum Cascade Detectors," *Opt. Quantum. Electron.*, vol. 53, no. 6, p. 287, 2021. [Online]. Available: <https://doi.org/10.1007/s11082-021-02885-0>
- [70] A. Tran, J. A. Mitchell, L. P. Swiler, and T. Wildey, "An Active Learning High-Throughput Microstructure Calibration Framework for Solving Inverse Structure–Process Problems in Materials Informatics," *Acta Mater.*, vol. 194, pp. 80–92, 2020. [Online]. Available: <https://www.sciencedirect.com/science/article/pii/S1359645420303220>
- [71] E. Lanzarini, M. R. Antognazza, M. Biso, A. Ansaldo, L. Laudato, P. Bruno, P. Metrangolo, G. Resnati, D. Ricci, and G. Lanzani, "Polymer-Based Photocatalytic Hydrogen Generation," *J. Phys. Chem. C*, vol. 116, no. 20, pp. 10944–10949, 2012. [Online]. Available: <https://doi.org/10.1021/jp212107f>
- [72] G. Suppes, E. Ballard, and S. Holdcroft, "Aqueous Photocathode Activity of Regioregular Poly(3-Hexylthiophene)," *Polym. Chem.*, vol. 4, pp. 5345–5350, 2013. [Online]. Available: <http://dx.doi.org/10.1039/C3PY00143A>
- [73] S. Bellani, M. Porro, C. Caddeo, M. I. Saba, P. B. Miranda, A. Mattoni, G. Lanzani, and M. R. Antognazza, "The Study of Polythiophene/water Interfaces by Sum-Frequency Generation Spectroscopy and Molecular Dynamics Simulations," *J. Mater. Chem. B*, vol. 3, pp. 6429–6438, 2015. [Online]. Available: <http://dx.doi.org/10.1039/C5TB00388A>
- [74] F. Fumagalli, S. Bellani, M. Schreier, S. Leonardi, H. C. Rojas, A. Ghadirzadeh, G. Tullii, A. Savoini, G. Marra, L. Meda, M. Grätzel, G. Lanzani, M. T. Mayer, M. R. Antognazza, and F. Di Fonzo, "Hybrid Organic–Inorganic H<sub>2</sub>-Evolving Photocathodes: Understanding the Route Towards High Performance Organic Photoelectrochemical Water Splitting," *J. Mater. Chem. A*, vol. 4, pp. 2178–2187, 2016. [Online]. Available: <http://dx.doi.org/10.1039/C5TA09330A>
- [75] K. Oka, B. Winther-Jensen, and H. Nishide, "Organic  $\pi$ -conjugated Polymers As Photocathode Materials for Visible-light-enhanced Hydrogen and Hydrogen Peroxide Production from Water," *Adv. Energy. Mater.*, vol. 11, no. 43, p. 2003724, 2021. [Online]. Available: <https://onlinelibrary.wiley.com/doi/abs/10.1002/aenm.202003724>
- [76] T. Paltrinieri, L. Bondi, V. Đerek, B. Fraboni, E. D. Głowacki, and T. Cramer, "Understanding Photocapacitive and Photofaradaic Processes in Organic Semiconductor Photoelectrodes for Optobioelectronics," *Adv. Funct. Mater.*, vol. 31, no. 16, p. 2010116, 2021. [Online]. Available: <https://onlinelibrary.wiley.com/doi/abs/10.1002/adfm.202010116>
- [77] L. Bondi, C. Marzuoli, E. Gutiérrez-Fernández, G. Tullii, J. Martín, B. Fraboni, D. Mecerreyes, M. R. Antognazza, and T. Cramer, "P-Type Semiconducting Polymers As Photocathodes: A Comparative Study for Optobioelectronics," *Adv. Electron. Mater.*, vol. n/a, no. n/a, p. 2300146, 2023. [Online]. Available: <https://onlinelibrary.wiley.com/doi/abs/10.1002/aelm.202300146>

- [78] L. Kergoat, L. Herlogsson, D. Braga, B. Piro, M.-C. Pham, X. Crispin, M. Berggren, and G. Horowitz, "A Water-Gate Organic Field-Effect Transistor," *Adv. Mater.*, vol. 22, no. 23, pp. 2565–2569, 2010. [Online]. Available: <https://onlinelibrary.wiley.com/doi/abs/10.1002/adma.200904163>
- [79] Y. Xia, W. Xie, P. P. Ruden, and C. D. Frisbie, "Carrier Localization on Surfaces of Organic Semiconductors Gated with Electrolytes," *Phys. Rev. Lett.*, vol. 105, p. 036802, Jul 2010. [Online]. Available: <https://link.aps.org/doi/10.1103/PhysRevLett.105.036802>
- [80] F. Buth, D. Kumar, M. Stutzmann, and J. A. Garrido, "Electrolyte-Gated Organic Field-Effect Transistors for Sensing Applications," *Appl. Phys. Lett.*, vol. 98, no. 15, p. 153302, 04 2011. [Online]. Available: <https://doi.org/10.1063/1.3581882>
- [81] F. Torricelli, D. Z. Adrahtas, Z. Bao, M. Berggren, F. Biscarini, A. Bonfiglio, C. A. Bortolotti, C. D. Frisbie, E. Macchia, G. G. Malliaras, I. McCulloch, M. Moser, T.-Q. Nguyen, R. M. Owens, A. Salleo, A. Spanu, and L. Torsi, "Electrolyte-Gated Transistors for Enhanced Performance Bioelectronics," *Nat. Rev. Methods Primers*, vol. 1, no. 1, p. 66, 2021. [Online]. Available: <https://doi.org/10.1038/s43586-021-00065-8>
- [82] D. Ghezzi, M. R. Antognazza, M. Dal Maschio, E. Lanzarini, F. Benfenati, and G. Lanzani, "A Hybrid Bioorganic Interface for Neuronal Photoactivation," *Nat. Commun.*, vol. 2, no. 1, p. 166, 2011. [Online]. Available: <https://doi.org/10.1038/ncomms1164>
- [83] D. Ghezzi, M. R. Antognazza, R. Maccarone, S. Bellani, E. Lanzarini, N. Martino, M. Mete, G. Pertile, S. Bisti, G. Lanzani, and F. Benfenati, "A Polymer Optoelectronic Interface Restores Light Sensitivity in Blind Rat Retinas," *Nat. Photonics*, vol. 7, no. 5, pp. 400–406, 2013. [Online]. Available: <https://doi.org/10.1038/nphoton.2013.34>
- [84] M. R. Antognazza, M. Di Paolo, D. Ghezzi, M. Mete, S. Di Marco, J. F. Maya-Vetencourt, R. Maccarone, A. Desii, F. Di Fonzo, M. Bramini, A. Russo, L. Laudato, I. Donelli, M. Cilli, G. Freddi, G. Pertile, G. Lanzani, S. Bisti, and F. Benfenati, "Characterization of a Polymer-Based, Fully Organic Prosthesis for Implantation into the Subretinal Space of the Rat," *Adv. Healthcare Mater.*, vol. 5, no. 17, pp. 2271–2282, 2016. [Online]. Available: <https://onlinelibrary.wiley.com/doi/abs/10.1002/adhm.201600318>
- [85] C. Tortiglione, M. R. Antognazza, A. Tino, C. Bossio, V. Marchesano, A. Bauduin, M. Zangoli, S. V. Morata, and G. Lanzani, "Semiconducting Polymers Are Light Nanotransducers in Eyeless Animals," *Sci. Adv.*, vol. 3, no. 1, p. e1601699, 2017. [Online]. Available: <https://www.science.org/doi/abs/10.1126/sciadv.1601699>
- [86] E. Zucchetti, M. Zangoli, I. Bargigia, C. Bossio, F. Di Maria, G. Barbarella, C. D'Andrea, G. Lanzani, and M. R. Antognazza, "Poly(3-Hexylthiophene) Nanoparticles for Biophotonics: Study of the Mutual Interaction with Living Cells," *J. Mater. Chem. B*, vol. 5, pp. 565–574, 2017. [Online]. Available: <http://dx.doi.org/10.1039/C6TB02047J>
- [87] D. Rand, M. Jakešová, G. Lubin, I. Vèbraitè, M. David-Pur, V. Đerek, T. Cramer, N. S. Sariciftci, Y. Hanein, and E. D. Glowacki, "Direct Electrical Neurostimulation with Organic Pigment Photocapacitors," *Adv. Mater.*, vol. 30, no. 25, p. 1707292, 2018. [Online]. Available: <https://onlinelibrary.wiley.com/doi/abs/10.1002/adma.201707292>
- [88] C. Bossio, I. Abdel Aziz, G. Tullii, E. Zucchetti, D. Debellis, M. Zangoli, F. Di Maria, G. Lanzani, and M. R. Antognazza, "Photocatalytic Activity of Polymer Nanoparticles Modulates Intracellular Calcium Dynamics and Reactive Oxygen Species in HEK-293 Cells," *Front. Bioeng. Biotechnol.*, vol. 6, 2018. [Online]. Available: <https://www.frontiersin.org/articles/10.3389/fbioe.2018.00114>

- [89] F. Lodola, V. Rosti, G. Tullii, A. Desii, L. Tapella, P. Catarsi, D. Lim, F. Moccia, and M. R. Antognazza, "Conjugated Polymers Optically Regulate the Fate of Endothelial Colony-Forming Cells," *Sci. Adv.*, vol. 5, no. 9, p. eaav4620, 2019. [Online]. Available: <https://www.science.org/doi/abs/10.1126/sciadv.aav4620>
- [90] G. Tullii, A. Desii, C. Bossio, S. Bellani, M. Colombo, N. Martino, M. R. Antognazza, and G. Lanzani, "Bimodal Functioning of a Mesoporous, Light Sensitive Polymer/electrolyte Interface," *Org. Electron.*, vol. 46, pp. 88–98, 2017. [Online]. Available: <https://www.sciencedirect.com/science/article/pii/S1566119917301568>
- [91] M. Jakešová, M. Silverå Ejneby, V. Đerek, T. Schmidt, M. Gryszel, J. Brask, R. Schindl, D. T. Simon, M. Berggren, F. Elinder, and E. D. Głowacki, "Optoelectronic Control of Single Cells Using Organic Photocapacitors," *Sci. Adv.*, vol. 5, no. 4, p. eaav5265, April 2019. [Online]. Available: <https://europepmc.org/articles/PMC6450690>
- [92] N. Martino, P. Feyen, M. Porro, C. Bossio, E. Zucchetti, D. Ghezzi, F. Benfenati, G. Lanzani, and M. R. Antognazza, "Photothermal Cellular Stimulation in Functional Bio-Polymer Interfaces," *Sci. Rep.*, vol. 5, no. 1, p. 8911, 2015. [Online]. Available: <https://doi.org/10.1038/srep08911>
- [93] T. Cramer, T. Steinbrecher, T. Koslowski, D. A. Case, F. Biscarini, and F. Zerbetto, "Water-Induced Polaron Formation at the Pentacene Surface: Quantum Mechanical Molecular Mechanics Simulations," *Phys. Rev. B*, vol. 79, p. 155316, Apr 2009. [Online]. Available: <https://link.aps.org/doi/10.1103/PhysRevB.79.155316>
- [94] E. Mosconi, P. Salvatori, M. I. Saba, A. Mattoni, S. Bellani, F. Bruni, B. Santiago Gonzalez, M. R. Antognazza, S. Brovelli, G. Lanzani, H. Li, J.-L. Brédas, and F. De Angelis, "Surface Polarization Drives Photoinduced Charge Separation at the P3ht/water Interface," *ACS Energy Lett.*, vol. 1, no. 2, pp. 454–463, 2016. [Online]. Available: <https://doi.org/10.1021/acsenergylett.6b00197>
- [95] S. Bellani, A. Ghadirzadeh, L. Meda, A. Savoini, A. Tacca, G. Marra, R. Meira, J. Morgado, F. Di Fonzo, and M. R. Antognazza, "Hybrid Organic/Inorganic Nanostructures for Highly Sensitive Photoelectrochemical Detection of Dissolved Oxygen in Aqueous Media," *Adv. Funct. Mater.*, vol. 25, no. 28, pp. 4531–4538, 2015. [Online]. Available: <https://onlinelibrary.wiley.com/doi/abs/10.1002/adfm.201500701>
- [96] M. Porro, "Bio-Polymer Interfaces for Optical Cellular Stimulation: A Computational Modeling Approach," PhD Thesis, Politecnico di Milano, 2014. [Online]. Available: <http://hdl.handle.net/10589/98548>
- [97] G. Chiaravalli, G. Manfredi, R. Sacco, and G. Lanzani, "Photoelectrochemistry and Drift–diffusion Simulations in a Polythiophene Film Interfaced with an Electrolyte," *ACS Appl. Mater. Interfaces*, vol. 13, no. 30, pp. 36 595–36 604, 2021. [Online]. Available: <https://doi.org/10.1021/acsami.1c10158>
- [98] M. S. A. Abdou, F. P. Orfino, Y. Son, and S. Holdcroft, "Interaction of Oxygen with Conjugated Polymers: Charge Transfer Complex Formation with Poly(3-Alkylthiophenes)," *J. Am. Chem. Soc.*, vol. 119, no. 19, pp. 4518–4524, 1997. [Online]. Available: <https://doi.org/10.1021/ja964229j>
- [99] H. Hintz, H. Peisert, H.-J. Egelhaaf, and T. Chassé, "Reversible and Irreversible Light-induced P-doping of P3HT by Oxygen Studied by Photoelectron Spectroscopy (xps/ups)," *J. Phys. Chem. C*, vol. 115, no. 27, pp. 13 373–13 376, 2011. [Online]. Available: <https://doi.org/10.1021/jp2032737>
- [100] A. Sperlich, H. Kraus, C. Deibel, H. Blok, J. Schmidt, and V. Dyakonov, "Reversible and Irreversible Interactions of Poly(3-Hexylthiophene) with Oxygen Studied by Spin-Sensitive Methods," *J. Phys. Chem. B*, vol. 115, no. 46, pp. 13 513–13 518, 2011, pMID: 21972826. [Online]. Available: <https://doi.org/10.1021/jp2077215>



- [101] H. T. Nicolai, M. Kuik, G. A. H. Wetzelaer, B. de Boer, C. Campbell, C. Risko, J. L. Brédas, and P. W. M. Blom, "Unification of Trap-Limited Electron Transport in Semiconducting Polymers," *Nat. Mater.*, vol. 11, no. 10, pp. 882–887, 2012. [Online]. Available: <https://doi.org/10.1038/nmat3384>
- [102] S. Bellani, D. Fazzi, P. Bruno, E. Giussani, E. V. Canesi, G. Lanzani, and M. R. Antognazza, "Reversible P3HT/Oxygen Charge Transfer Complex Identification in Thin Films Exposed to Direct Contact with Water," *J. Phys. Chem. C*, vol. 118, no. 12, pp. 6291–6299, 2014. [Online]. Available: <https://doi.org/10.1021/jp4119309>
- [103] L. Katzenmeier, M. Gößwein, A. Gagliardi, and A. S. Bandarenka, "Modeling of Space-charge Layers in Solid-state Electrolytes: A Kinetic Monte Carlo Approach and Its Validation," *J. Phys. Chem. C*, vol. 126, no. 26, pp. 10900–10909, 2022. [Online]. Available: <https://doi.org/10.1021/acs.jpcc.2c02481>
- [104] L. Katzenmeier, M. Gößwein, L. Carstensen, J. Sterzinger, M. Ederer, P. Müller-Buschbaum, A. Gagliardi, and A. S. Bandarenka, "Mass Transport and Charge Transfer through an Electrified Interface between Metallic Lithium and Solid-State Electrolytes," *Commun. Chem.*, vol. 6, no. 1, p. 124, 2023. [Online]. Available: <https://doi.org/10.1038/s42004-023-00923-4>
- [105] T. Albes and A. Gagliardi, "Influence of Permittivity and Energetic Disorder on the Spatial Charge Carrier Distribution and Recombination in Organic Bulk-Heterojunctions," *Phys. Chem. Chem. Phys.*, vol. 19, pp. 20974–20983, 2017. [Online]. Available: <http://dx.doi.org/10.1039/C7CP03513F>
- [106] T. Albes, L. Xu, J. Wang, J. W. P. Hsu, and A. Gagliardi, "Origin of Photocurrent in Fullerene-Based Solar Cells," *J. Phys. Chem. C*, vol. 122, no. 27, pp. 15140–15148, 2018. [Online]. Available: <https://doi.org/10.1021/acs.jpcc.8b03941>
- [107] T. Albes and A. Gagliardi, "Charge Pair Separation Dynamics in Organic Bulk-Heterojunction Solar Cells," *Adv. Theory Simul.*, vol. 1, no. 7, p. 1800032, 2018. [Online]. Available: <https://onlinelibrary.wiley.com/doi/abs/10.1002/adts.201800032>
- [108] Y. Horowitz, C. Schmidt, D.-h. Yoon, L. M. Riegger, L. Katzenmeier, G. M. Bosch, M. Noked, Y. Ein-Eli, J. Janek, W. G. Zeier, C. E. Diesendruck, and D. Golodnitsky, "Between Liquid and All Solid: A Prospect on Electrolyte Future in Lithium-Ion Batteries for Electric Vehicles," *Energy Technol.*, vol. 8, no. 11, p. 2000580, 2020. [Online]. Available: <https://onlinelibrary.wiley.com/doi/abs/10.1002/ente.202000580>
- [109] O. B. Chae and B. L. Lucht, "Interfacial Issues and Modification of Solid Electrolyte Interphase for Li Metal Anode in Liquid and Solid Electrolytes," *Adv. Energy Mater.*, vol. 13, no. 14, p. 2203791, 2023. [Online]. Available: <https://onlinelibrary.wiley.com/doi/abs/10.1002/aenm.202203791>
- [110] M. Park, X. Zhang, M. Chung, G. B. Less, and A. M. Sastry, "A Review of Conduction Phenomena in Li-Ion Batteries," *J. Power Sources*, vol. 195, no. 24, pp. 7904–7929, 2010. [Online]. Available: <https://www.sciencedirect.com/science/article/pii/S0378775310010463>
- [111] K. Funke, "Debye-Hückel-Type Relaxation Processes in Solid Ionic Conductors: The Model," *Solid State Ion.*, vol. 18-19, pp. 183–190, 1986. [Online]. Available: <https://www.sciencedirect.com/science/article/pii/0167273886901098>
- [112] Z. Yao, S. Kim, K. Michel, Y. Zhang, M. Aykol, and C. Wolverton, "Stability and conductivity of cation- and anion-substituted LiBH<sub>4</sub>-based solid-state electrolytes," *Phys. Rev. Mater.*, vol. 2, p. 065402, Jun 2018. [Online]. Available: <https://link.aps.org/doi/10.1103/PhysRevMaterials.2.065402>
- [113] J. M. Dean, S. W. Coles, W. R. Saunders, A. R. McCluskey, M. J. Wolf, A. B. Walker, and B. J. Morgan, "Overscreening and Underscreening in Solid-Electrolyte Grain Boundary Space-Charge Layers," *Phys. Rev. Lett.*, vol. 127, p. 135502, Sep 2021. [Online]. Available: <https://link.aps.org/doi/10.1103/PhysRevLett.127.135502>


- [114] L. Katzenmeier, S. Helmer, S. Braxmeier, E. Knobbe, and A. S. Bandarenka, "Properties of the Space Charge Layers Formed in Li-Ion Conducting Glass Ceramics," *ACS Appl. Mater. Interfaces*, vol. 13, no. 4, pp. 5853–5860, 2021. [Online]. Available: <https://doi.org/10.1021/acsami.0c21304>
- [115] L. Katzenmeier, L. Carstensen, S. J. Schaper, P. Müller-Buschbaum, and A. S. Bandarenka, "Characterization and Quantification of Depletion and Accumulation Layers in Solid-State Li+-Conducting Electrolytes Using in Situ Spectroscopic Ellipsometry," *Adv. Mater.*, vol. 33, no. 24, p. 2100585, 2021. [Online]. Available: <https://onlinelibrary.wiley.com/doi/abs/10.1002/adma.202100585>
- [116] A. B. Bortz, M. H. Kalos, and J. L. Lebowitz, "A New Algorithm for Monte Carlo Simulation of Ising Spin Systems," *J. Comput. Phys.*, vol. 17, no. 1, pp. 10–18, 1975. [Online]. Available: <https://www.sciencedirect.com/science/article/pii/0021999175900601>
- [117] D. T. Gillespie, "A General Method for Numerically Simulating the Stochastic Time Evolution of Coupled Chemical Reactions," *J. Comput. Phys.*, vol. 22, no. 4, pp. 403–434, 1976. [Online]. Available: <https://www.sciencedirect.com/science/article/pii/0021999176900413>
- [118] E. Brochu, V. M. Cora, and N. De Freitas, "A Tutorial on Bayesian Optimization of Expensive Cost Functions, with Application to Active User Modeling and Hierarchical Reinforcement Learning," *arXiv preprint*, vol. abs/1012.2599, 2010.
- [119] C. E. Rasmussen and C. K. I. Williams, *Gaussian Processes for Machine Learning*. Cambridge, Massachusetts, USA: The MIT Press, 11 2005. [Online]. Available: <https://doi.org/10.7551/mitpress/3206.001.0001>
- [120] C. Williams, "Computing with Infinite Networks," in *Advances in Neural Information Processing Systems*, ser. NIPS'96, M. Mozer, M. Jordan, and T. Petsche, Eds., vol. 9. Cambridge, Massachusetts, USA: MIT Press, 1996, p. 295–301. [Online]. Available: <https://proceedings.neurips.cc/paper/1996/file/ae5e3ce40e0404a45ecacaaf05e5f735-Paper.pdf>
- [121] R. M. Neal, *Priors for Infinite Networks*. New York, NY: Springer New York, 1996, pp. 29–53. [Online]. Available: [https://doi.org/10.1007/978-1-4612-0745-0\\_2](https://doi.org/10.1007/978-1-4612-0745-0_2)
- [122] Y. Cho and L. K. Saul, "Kernel Methods for Deep Learning," in *Proceedings of the 22nd International Conference on Neural Information Processing Systems*, ser. NIPS'09. Red Hook, NY, USA: Curran Associates Inc., 2009, p. 342–350.
- [123] T. Hazan and T. Jaakkola, "Steps toward Deep Kernel Methods from Infinite Neural Networks," *arXiv preprint*, vol. arXiv:1508.05133, 2015.
- [124] J. Lee, Y. Bahri, R. Novak, S. S. Schoenholz, J. Pennington, and J. Sohl-Dickstein, "Deep Neural Networks As Gaussian Processes," *arXiv preprint*, vol. arXiv:1711.00165, 2017.
- [125] K. Nakajima, T. Katoh, Y. Inada, and B. Hoffman, "Lithium Ion Conductive Glass Ceramics: Properties and Application in Lithium Metal Batteries," in *Symposium on Energy Storage Beyond Lithium Ion: Materials Perspective*. Oak Ridge National Laboratory, 2010.
- [126] P. Hartmann, T. Leichtweiss, M. R. Busche, M. Schneider, M. Reich, J. Sann, P. Adelhelm, and J. Janek, "Degradation of Nasion-Type Materials in Contact with Lithium Metal: Formation of Mixed Conducting Interphases (mci) on Solid Electrolytes," *J. Phys. Chem. C*, vol. 117, no. 41, pp. 21 064–21 074, 2013. [Online]. Available: <https://doi.org/10.1021/jp4051275>
- [127] L. Katzenmeier, M. M. Kaye, and A. S. Bandarenka, "Ionic Mott-Schottky Formalism Allows the Assessment of Mobile Ion Concentrations in Li+-Conducting Solid Electrolytes," *J. Electroanal. Chem.*, vol. 922, p. 116750, 2022. [Online]. Available: <https://www.sciencedirect.com/science/article/pii/S1572665722007421>

- [128] S. W. Martin, W. Yao, and K. Berg, "Space Charge Polarization Measurements As a Method to Determine the Temperature Dependence of the Number Density of Mobile Cations in Ion Conducting Glasses," *Z. Phys. Chem.*, vol. 223, no. 10-11, pp. 1379–1393, 2009. [Online]. Available: <https://doi.org/10.1524/zpch.2009.6085>
- [129] E. Hückel and P. Debye, "Zur Theorie der Elektrolyte. I. Gefrierpunktserniedrigung und Verwandte Erscheinungen," *Phys. Z.*, vol. 24, no. 9, pp. 185–206, 1923.
- [130] M. Casalegno, A. Bernardi, and G. Raos, "Numerical Simulation of Photocurrent Generation in Bilayer Organic Solar Cells: Comparison of Master Equation and Kinetic Monte Carlo Approaches," *J. Chem. Phys.*, vol. 139, no. 2, p. 024706, 07 2013. [Online]. Available: <https://doi.org/10.1063/1.4812826>
- [131] A. Miller and E. Abrahams, "Impurity Conduction at Low Concentrations," *Phys. Rev.*, vol. 120, pp. 745–755, Nov 1960. [Online]. Available: <https://link.aps.org/doi/10.1103/PhysRev.120.745>
- [132] P. W. Atkins, J. De Paula, and J. Keeler, *Atkins' Physical Chemistry*. Oxford, UK: Oxford University Press, 2023.
- [133] L. M. Katzenmeier, "Nature of Space Charge Layers in Li+ Conducting Glass Ceramics," Ph.D. dissertation, Technische Universität München, 2022.
- [134] S. Chandrasekhar, "Stochastic Problems in Physics and Astronomy," *Rev. Mod. Phys.*, vol. 15, pp. 1–89, Jan 1943. [Online]. Available: <https://link.aps.org/doi/10.1103/RevModPhys.15.1>
- [135] S. D. Baranovskii, "Theoretical Description of Charge Transport in Disordered Organic Semiconductors," *Phys. Status Solidi B*, vol. 251, no. 3, pp. 487–525, 2014. [Online]. Available: <https://onlinelibrary.wiley.com/doi/abs/10.1002/pssb.201350339>
- [136] M. Ianovici and J.-j. Morf, "Calculation of the Potential Distribution Around a Charge or a Current in the Presence of Three Dielectric Media Using the Image Method," *IEEE Trans. Elect. Insulation*, vol. EI-12, no. 2, pp. 165–170, 1977.
- [137] M. Born and T. Karman, "Über Schwingungen in Raumgittern," *Physik. Z.*, vol. 13, no. 8, pp. 297–309, 1912.
- [138] S. Braun, C. Yada, and A. Latz, "Thermodynamically Consistent Model for Space-Charge-Layer Formation in a Solid Electrolyte," *J. Phys. Chem. C*, vol. 119, no. 39, pp. 22 281–22 288, 2015. [Online]. Available: <https://doi.org/10.1021/acs.jpcc.5b02679>
- [139] M. Rück, A. Bandarenka, F. Calle-Vallejo, and A. Gagliardi, "Oxygen Reduction Reaction: Rapid Prediction of Mass Activity of Nanostructured Platinum Electrocatalysts," *J. Phys. Chem. Lett.*, vol. 9, no. 15, pp. 4463–4468, 2018, pMID: 30028631. [Online]. Available: <https://doi.org/10.1021/acs.jpcllett.8b01864>
- [140] Rück, Marlon and Bandarenka, Aliaksandr and Calle-Vallejo, Federico and Gagliardi, Alessio, "Fast Identification of Optimal Pure Platinum Nanoparticle Shapes and Sizes for Efficient Oxygen Electroreduction," *Nanoscale Adv.*, vol. 1, pp. 2901–2909, 2019. [Online]. Available: <http://dx.doi.org/10.1039/C9NA00252A>
- [141] Garlyyev, Batyr and Kratzl, Kathrin and Rück, Marlon and Michalička, Jan and Fichtner, Johannes and Macak, Jan M. and Kratky, Tim and Günther, Sebastian and Cokoja, Mirza and Bandarenka, Aliaksandr S. and Gagliardi, Alessio and Fischer, Roland A., "Optimizing the Size of Platinum Nanoparticles for Enhanced Mass Activity in the Electrochemical Oxygen Reduction Reaction," *Angew. Chem. Int. Ed.*, vol. 58, no. 28, pp. 9596–9600, 2019. [Online]. Available: <https://onlinelibrary.wiley.com/doi/abs/10.1002/anie.201904492>


- [142] J. Riihimäki and A. Vehtari, "Gaussian Processes with Monotonicity Information," in *Proceedings of the Thirteenth International Conference on Artificial Intelligence and Statistics*, ser. Proceedings of Machine Learning Research, Y. W. Teh and M. Titterton, Eds., vol. 9. Chia Laguna Resort, Sardinia, Italy: PMLR, 13–15 May 2010, pp. 645–652. [Online]. Available: <https://proceedings.mlr.press/v9/riihimaki10a.html>
- [143] A. Tran, K. Maupin, and T. Rodgers, "Monotonic Gaussian Process for Physics-Constrained Machine Learning With Materials Science Applications," *J. Comput. Inf. Sci. Eng.*, vol. 23, no. 1, p. 011011, 10 2022. [Online]. Available: <https://doi.org/10.1115/1.4055852>
- [144] I. Abdel Aziz, M. Malferrari, F. Roggiani, G. Tullii, S. Rapino, and M. R. Antognazza, "Light-Triggered Electron Transfer between a Conjugated Polymer and Cytochrome C for Optical Modulation of Redox Signaling," *iScience*, vol. 23, no. 5, p. 101091, 2020. [Online]. Available: <https://www.sciencedirect.com/science/article/pii/S2589004220302765>

# Original Publications and Reuse Permissions

## Local Temporal Acceleration Scheme to Couple Transport and Reaction Dynamics in Kinetic Monte Carlo Models of Electrochemical Systems

Sign in/Register ? 🔍

---



**Local Temporal Acceleration Scheme to Couple Transport and Reaction Dynamics in Kinetic Monte Carlo Models of Electrochemical Systems**

Author: Manuel Gößwein, Waldemar Kaiser, Alessio Gagliardi

Publication: Journal of Chemical Theory and Computation

Publisher: American Chemical Society

Date: May 1, 2022

*Copyright © 2022, American Chemical Society*

**PERMISSION/LICENSE IS GRANTED FOR YOUR ORDER AT NO CHARGE**

This type of permission/license, instead of the standard Terms and Conditions, is sent to you because no fee is being charged for your order. Please note the following:

- Permission is granted for your request in both print and electronic formats, and translations.
- If figures and/or tables were requested, they may be adapted or used in part.
- Please print this page for your records and send a copy of it to your publisher/graduate school.
- Appropriate credit for the requested material should be given as follows: "Reprinted (adapted) with permission from {COMPLETE REFERENCE CITATION}. Copyright {YEAR} American Chemical Society." Insert appropriate information in place of the capitalized words.
- One-time permission is granted only for the use specified in your RightsLink request. No additional uses are granted (such as derivative works or other editions). For any uses, please submit a new request.

If credit is given to another source for the material you requested from RightsLink, permission must be obtained from that source.

**BACK**

**CLOSE WINDOW**

The following publication is reprinted with permission from ref. 2, *J. Chem. Theory Comput.* **2022**, *18*, 2749-2763. Copyright 2022 American Chemical Society (ACS).

# Local Temporal Acceleration Scheme to Couple Transport and Reaction Dynamics in Kinetic Monte Carlo Models of Electrochemical Systems

Manuel Gößwein, Waldemar Kaiser,\* and Alessio Gagliardi



Cite This: *J. Chem. Theory Comput.* 2022, 18, 2749–2763



Read Online

ACCESS |



Metrics & More

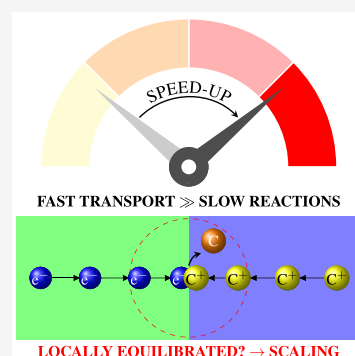


Article Recommendations



Supporting Information

**ABSTRACT:** Kinetic Monte Carlo (kMC) simulations are a well-established tool for investigating the operation of electrochemical systems. Standard kMC algorithms become unfeasible in the presence of processes on vastly different time scales. In electrochemical systems, such time scale disparities often arise between fast transport processes and slow electrochemical reactions. A promising approach to overcome time scale disparities in kMC models is given by temporal acceleration schemes. In this work, we present a local temporal acceleration scheme to bridge the time scale disparity between fast transport and slow reaction dynamics. We combine the superbasin concept with a local, particle-based criterion for the quasi-equilibrium detection and a partitioning of transitions and particles in the system into process chains. Scaling of entire quasi-equilibrated process chains considerably reduces the computational effort without disturbing the relative dynamics of transitions within a process chain. The methodology is outlined for a hybrid organic–aqueous electrolyte device which links fast electronic processes in an organic semiconductor with slow reduction reactions at its interface to the electrolyte. Our approach captures local inhomogeneities such that local physical quantities can be reproduced accurately. Additionally, we show that previous accelerated superbasin algorithms are limited by the presence of spatially varying time scale disparities. Our algorithm achieves an acceleration of several orders of magnitude providing a serious alternative to replace existing multiscale models by stand-alone kMC simulations.



## INTRODUCTION

Kinetic Monte Carlo (kMC) simulations are a subclass of Monte Carlo procedures which describe the time-evolution of a wide range of stochastic physical and electrochemical processes such as crystal growth,<sup>1,2</sup> vacancy diffusion,<sup>3</sup> chemical reaction networks,<sup>4–6</sup> and charge transport in disordered semiconductors.<sup>7–9</sup> A particularly important but yet demanding field for kMC simulations are electrochemical systems. For instance, Alkire and co-workers investigated the early stages of kinetically limited electrodeposition.<sup>10</sup> Another study dealt with the CO adlayer electrooxidation on nanoparticle catalysts.<sup>11</sup> In the context of renewable energy cycles, electrochemical kMC simulations helped to gain a detailed mechanistic understanding of battery<sup>12–14</sup> and fuel cell operation.<sup>15–17</sup>

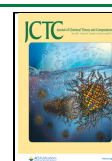
kMC models map material properties, in particular structural and energetic information, onto a discrete set of states.<sup>8,18</sup> Discrete transitions propagate the system, e.g., by the motion of particles or electrochemical reactions, resulting in a stochastic time evolution of the system within its phase space. The kinetic information results from the details of the transition rates which capture the underlying physics and define the probability of performing the respective transition. Consequently, the system is propagated along transitions of large transition rates which results in a substantial computa-

tional bottleneck: a system that is controlled by fast processes of time scale  $t_f$  and slow processes of time scale  $t_s \gg t_f$  requires statistically  $t_s/t_f$  kMC steps to execute the slow process once. Accordingly, such time scale disparities prevent the sufficient sampling of slow processes which, however, often represent the crucial step of the desired system properties. A concrete example of time scale disparities in electrochemical systems can be found in the intermediate diffusion within surface catalytic processes.<sup>11</sup> Mass transport of ionic or molecular species between active surface sites can be much faster than the catalytic surface reactions. To keep the computational effort low, many studies either neglect mass transport and with this potential mass transport limitations<sup>16</sup> or limit their studies to systems without distinct time scale disparities.<sup>13,17</sup>

There are two approaches to bridge time scale disparities in electrochemical systems: multiscale models and temporal acceleration schemes. Multiscale models typically couple continuum models using partial differential equations to derive

Received: October 6, 2021

Published: April 15, 2022



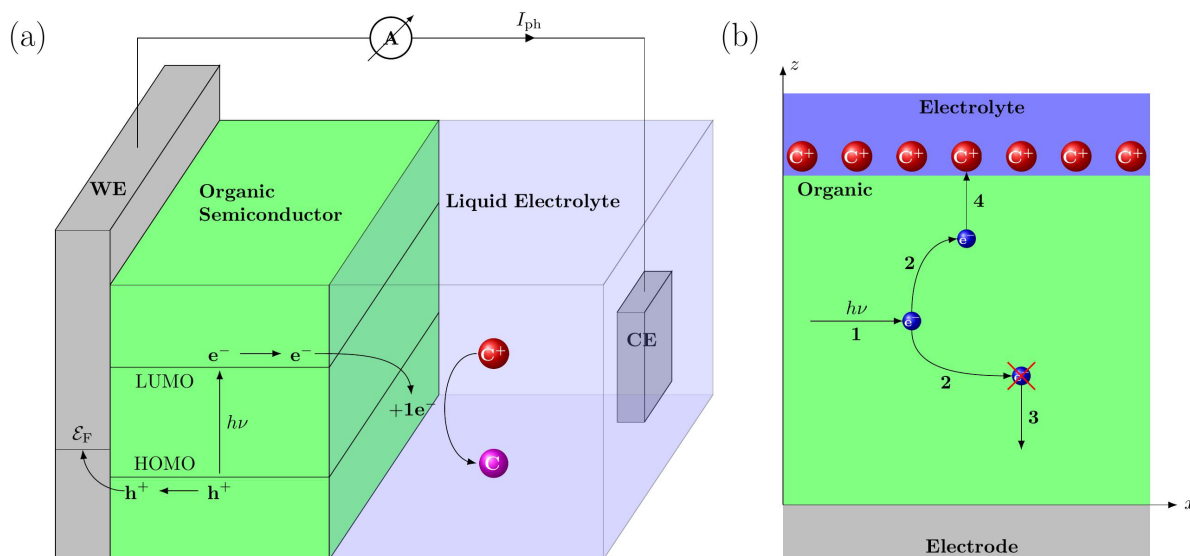


**Figure 1.** (a) Setup of a hybrid organic–aqueous electrolyte device consisting of an organic semiconductor on top of a working electrode (WE) put into a liquid electrolyte with the counter electrode (CE) completing the electronic circuit. Adapted with permission from Mosconi et al. *ACS Energy Lett.* 2016, 1 (2), 454–463. Copyright 2016 American Chemical Society.<sup>47</sup> (b) Schematic representation of the simplified organic–liquid interface and its transition rates studied by kMC simulations.

system properties such as mass or charge distribution which are fed into kMC, e.g., in the form of background potentials.<sup>19</sup> Applications of multiscale methods cover, e.g., heterogeneous catalytic reactors,<sup>20,21</sup> fuel cells,<sup>22–24</sup> and lithium-ion batteries.<sup>25,26</sup> Continuum models are mean-field approximations<sup>27</sup> and consequently assume isotropic mass transport. For active interfaces with complex shapes, this assumption fundamentally breaks down as mass transport may become heterogeneous due to the interaction with charged species and the local interface geometry.<sup>11,13</sup>

Different procedures have been developed to overcome large time scale disparities to accelerate kMC simulations.<sup>28</sup> A popular choice in the community is the  $\tau$ -leaping method which accelerates kMC simulations by the execution of multiple fast events in a single kMC step<sup>29</sup> and is frequently applied when time scale disparities arise from strongly differing particle concentrations.<sup>30</sup> However,  $\tau$ -leaping is only viable if the system state does not change too much during the leap.<sup>31</sup> Another acceleration procedure is the probability weighted kMC method<sup>32</sup> which, by normalization of transition probabilities, increases the sampling of rare events. While ensemble averages are typically well reproduced, statistical errors may be amplified leading to physically inconsistent behavior. Snyder et al. proposed the net-event kMC technique<sup>33</sup> which lumps fast, reversible processes into a single net-event. An appealing property of this approach is that a substantial speed-up is accompanied by correct ensemble averaged quantities, while fluctuations in corresponding transients are considerably reduced. Nevertheless, problems may arise in the presence of large time scale disparities, especially if the fluctuations of net-rates become significantly larger than the transition rates of slow processes. In such cases, heuristic criteria must decide whether the instantaneous net-rate is statistically significant.

A major milestone has been achieved by the introduction of the accelerated superbasin-kMC method (AS-kMC).<sup>34</sup> The rationale of AS-kMC is to detect superbasins in which the system is being trapped and to subsequently raise the

activation barrier of quasi-equilibrated processes to facilitate the escape from superbasins. AS-kMC has been shown to perform well for several simple toy systems<sup>34</sup> and to small silicon nanocrystal networks.<sup>35</sup> The applicability is limited to small systems as the superbasin detection requires large databases and efficient search algorithms. For large superbasins, the dynamical sampling procedure becomes unfeasible and, in the worst case, may not generate any speed-up at all. Recently, we extended the AS-kMC concept for the temporal acceleration of particle transport simulations through disordered semiconductors<sup>36</sup> by the detection of potential superbasins during system initialization resulting in a substantial speed-up.

Inspired by the AS-kMC, Dybeck et al.<sup>37</sup> developed a generalized temporal acceleration scheme, further referred to as the Dybeck scheme, for kMC simulations of surface catalytic processes. Their algorithm partitions the reaction network into quasi-equilibrated and nonequilibrated reaction channels and detects and scales the rate constants of quasi-equilibrated reaction channels on the fly. The Dybeck scheme has been applied successfully to several surface catalytic kMC studies,<sup>5,6,38–41</sup> while its potential limitations are not fully explored. Exemplary, its accuracy in the presence of local inhomogeneities and strong fluctuations is not ensured. Existing applications of the Dybeck scheme further assume evenly distributed time scale disparities over the active nanoparticle surface, which may not be guaranteed in the presence of mass and charge transport. Finally, it is questionable whether charge/mass transport toward the active interface can be handled accurately by treating it as a quasi-equilibrated reaction channel as suggested by Dybeck et al.<sup>37</sup>

In this work, we present a novel temporal acceleration scheme to couple fast charge and mass transport phenomena with slow reaction dynamics in electrochemical systems. Our algorithm substantially extends the Dybeck scheme by the introduction of a novel partitioning strategy of the system into process chains—a set of processes of similar time scale being connected to a certain particle subset—and the development

of a local, particle-based criterion to assess a local quasi-equilibrium. We trace the local environment of individual particles by use of quasi-potentials to efficiently detect locally quasi-equilibrated process chains, which represent the counterpart to reaction channels in the Dybeck scheme. By scaling quasi-equilibrated process chains, we accurately capture the system dynamics and substantially reduce the computational demand. We demonstrate the capability of the local acceleration scheme using an electrochemical system of growing relevance: a hybrid organic–aqueous electrolyte device which couples fast electronic processes in an organic semiconductor with slow interface reduction reactions. With the efficient detection of local quasi-equilibria, we are able to capture local heterogeneities and to accurately reproduce physical quantities on a local scale. We further demonstrate that the Dybeck scheme is not suitable to capture the interaction between fast charge or mass transport phenomena and interface (surface) reactions accurately. We strongly believe that our local acceleration scheme can overcome limitations of existing acceleration schemes to make kMC a suitable tool for coupled transport–reaction simulations in electrochemical systems independent of the time scale disparities of competing processes.

## METHOD

As an application of the acceleration scheme for electrochemical systems, we consider a hybrid organic–aqueous electrolyte device made of an energetically disordered organic semiconductor coupled to an aqueous electrolyte solution; see Figure 1a for a standard device architecture. In recent years, such hybrid devices have gained a lot of interest in the context of photoelectrochemical water splitting<sup>42,43</sup> and bioelectronic applications,<sup>44,45</sup> such as neuronal stimulation under pulsed light illumination restoring the light sensitivity in blind retinas.<sup>46</sup>

First, we outline the working mechanism of hybrid organic–aqueous interfaces and the implementation in kMC. Then, the acceleration scheme is outlined stepwise using the hybrid device for visualization. A flowchart representing the integration of the temporal acceleration scheme within generic kMC algorithms is visualized in Figure S1, Supporting Information.

**Hybrid Organic–Aqueous Interface.** The working mechanism of hybrid organic–aqueous devices relies on electrochemical reactions at the organic–liquid interface (OLI), in terms of oxygen and hydrogen reduction reactions. Cations, e.g.,  $H^+$ , diffuse within the electrolyte and, driven by an applied electric field, accumulate at the OLI. Optical excitation of the organic semiconductor (elg) leads to the generation of electrons and holes which subsequently migrate through the semiconductor via a hopping mechanism (elh). After a certain lifetime, charge carriers may recombine nonradiatively (eld). If electrons reach the OLI, they may reduce the cations at the OLI, forming an uncharged molecule/atom (red). The challenge in modeling such hybrid devices is to couple the slow reaction dynamics ( $\approx$  seconds to microseconds) at the OLI with the fast electronic processes ( $\approx$  nanoseconds to picoseconds). As the time scale disparity involves the crucial reduction reactions at the OLI, the transport of electrons to the interface is expected to play a crucial role in the system dynamics and consequently must be accurately treated. Here, we simulate a simplified version of the OLI (see Figure 1b) with kMC to illustrate the capabilities of

the algorithm as well as its sensitivity to different sets of input parameters. Additionally, the setup is suitable for a comparison to the Dybeck scheme.<sup>37</sup> We first outline the model setup of the OLI, made of an organic semiconductor stacked between a metal electrode and a liquid electrolyte; see Figure 1b. We model the organic semiconductor by a simplified two-dimensional lattice of size  $X \times Z = 50 \text{ nm} \times 50 \text{ nm}$  with a site spacing of  $r_L = 1 \text{ nm}$ . In the  $x$ -direction, periodic boundary conditions are assumed; in the  $z$ -direction, the organic layer is stacked between an electrode ( $z = 0$ ) and an aqueous electrolyte ( $z = Z$ ). For simplicity, we neglect the motion of cations in the electrolyte and assume a fixed density of cations at the OLI, which now act as ionic reaction centers. Each site  $i$  represents a localized state for the electronic charge carriers with potential energy

$$\mathcal{E}_i = \mathcal{E}_i^{\text{MO}} + \mathcal{E}_i^\sigma + \mathcal{E}_i^F + \mathcal{E}_i^C \quad (1)$$

where  $\mathcal{E}_i^{\text{MO}}$  denotes the average molecular orbital energy,  $\mathcal{E}_i^\sigma$  resembles the energetic disorder,  $\mathcal{E}_i^F$  is the contribution from an external electric field, and  $\mathcal{E}_i^C$  is the potential arising from the Coulomb interaction with charges in the environment.  $\mathcal{E}_i^\sigma$  is modeled by a Gaussian distribution with variance  $\sigma^2$ , resembling the Gaussian density of states in disordered organic semiconductors.<sup>7,48</sup>  $\mathcal{E}_i^F$  is modeled as a linear potential drop along the  $z$ -axis:

$$\mathcal{E}_i^F = qV_b \frac{z_i}{Z} \quad (2)$$

where  $V_b$  denotes the applied bias voltage and  $z_i$  is the  $z$ -coordinate of site  $i$ .  $\mathcal{E}_i^C$  is constituted by the electron–electron interaction  $\mathcal{E}_i^{\text{ee}}$  and the ion–electron interaction  $\mathcal{E}_i^{\text{ie}}$ . Both components can be approximated by a spherical potential with cutoff radius  $r_{\text{cut}}^C$  by combining the method of image charges in the  $z$ -direction<sup>49</sup> with the periodic boundary conditions in the  $x$ -direction<sup>50</sup> to account for the interaction with the charged particles in the periodic replicas (see Section S4, Supporting Information, for a detailed derivation and convergence analysis). Since the cations are assumed to be fixed,  $\mathcal{E}_i^{\text{ie}}$  can be calculated at the beginning of the simulation. In contrast,  $\mathcal{E}_i^{\text{ee}}$  depends on the current position of the electrons and consequently must be updated in each simulation step.

In the beginning of the simulation, we assume that there are no free electrons in the organic layer. Electrons are optically generated (process 1, Figure 1b) at random sites with rate

$$K_{\text{exg}} = (n_{\text{org}} - n_{\text{el}})k_{\text{elg}} \quad (3)$$

where  $n_{\text{org}}$  is the number of lattice sites and  $n_{\text{el}}$  is the current number of electrons in the device. Electron hopping (process 2, Figure 1b) between sites  $i$  and  $j$  is modeled via the Miller–Abrahams formula<sup>51</sup>

$$k_{ij} = k_{0,\text{elh}} \begin{cases} \exp\left(-\frac{\Delta\mathcal{E}_{ij}}{k_B T}\right) & \text{if } \Delta\mathcal{E}_{ij} > 0 \\ 1 & \text{else} \end{cases} \quad (4)$$

where  $k_{0,\text{elh}}$  is the attempt-to-hop frequency,  $\Delta\mathcal{E}_{ij} = \mathcal{E}_j - \mathcal{E}_i$  denotes the potential energy difference between sites  $i$  and  $j$ ,  $k_B$  is the Boltzmann constant, and  $T$  is the temperature. We restrict electron hopping to the nearest-neighbor sites. Electron



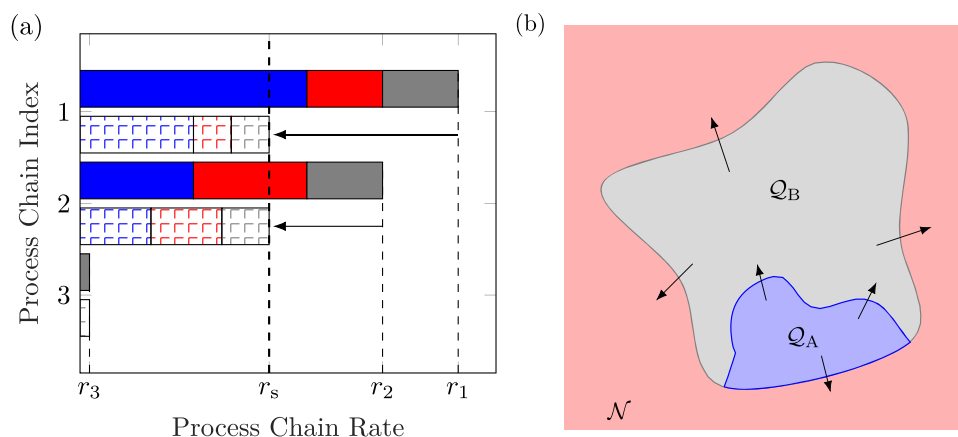


**Figure 2.** (a) Schematic representation of the scaling procedure for a system containing three process chains ( $i$ ) with rates  $r_i$ . Process chains (1) and (2) contain each three transitions as indicated by the different colors, while only one process is in process chain (3). The acceleration scheme decreases the transition rates  $r_1$  and  $r_2$  of the fast process chains to  $r_s = N_f r_3$ , while each individual transition rate in process chains (1) and (2) is equally scaled. Hereby, the slow process chain is more frequently executed, and the relative dynamics within each process chain is preserved. (b) Schematic representation of an arbitrary superbasin  $S = Q_A \cup Q_B$ :  $Q_A$  represents the quasi-equilibrated and sufficiently executed phase space,  $Q_B$  the quasi-equilibrated but not sufficiently executed phase space, and  $N$  the nonequilibrated phase space. Adapted with permission from Dybeck et al. *J. Chem. Theory Comput.* **2017**, *13* (4), 1525–1538. Copyright 2017 American Chemical Society.<sup>37</sup>

decay (process 3, Figure 1b) is modeled as the inverse of the lifetime  $\tau$ , i.e.,  $k_{\text{eld}} = \tau^{-1}$ . If an electron reaches the OLI, it may reduce an ionic reaction center  $C^+$ , i.e.,  $C^+ + e^- \rightarrow C$ , with constant reduction rate  $k_{\text{red}}$  (process 4, Figure 1b). For simplicity, we assume that after a reduction event the product  $C$  is instantly removed from the interface and replaced by a new reaction center  $C^+$  to keep the density of cations at the OLI constant.

**Partitioning into Process Chains.** Our acceleration scheme starts with the partitioning of the processes and the particles into *process chains*. Process chains consist of concrete transitions, which ideally are of similar time scales, and of a set of particles for the quasi-equilibrium detection. In the case of the OLI, we can partition the system into three process chains: (1) charge transport, generation, and recombination in the semiconductor, (2) mass transport of the cations  $C^+$  and the product  $C$  in the electrolyte and the oxidation at the counter electrode, and (3) the reduction reaction at the interface.

The interplay of these process chains determines the local densities of the individual species in the system and especially at the interface. As process chain (1), i.e., the fast processes of the charge carriers, is substantially faster than process chain (3), i.e., the slow reduction reaction at the interface, *local quasi-equilibria* of the particle densities in the environment of the interface will arise and consequently the local reaction activity will remain essentially constant. Thus, we say that process chain (1) is *quasi-equilibrated*, and consequently further sampling of the fast processes in process chain (1) produces no additional information with respect to the system dynamics. Accordingly, it is possible to downscale the rates of quasi-equilibrated process chains by appropriate scaling factors to decrease the time scale disparity and enable a more frequent sampling of slow reduction reactions. Figure 2a illustrates the scaling procedure for the investigated system. Each of the three process chains ( $m$ ) is represented by a corresponding rate  $r_m$ . The fast process chains (1) and (2) comprise three different transitions, including fast transport rates which are substantially larger than reduction rate  $r_3$ . The algorithm reduces  $r_1$  and  $r_2$  to  $r_s = N_f r_3$  such that on average  $N_f$  transitions of process

chains (1) and (2) are executed before a transition of the slow process chain (3) is sampled. In this way, the time scale disparity is decreased while the relative dynamics within the fast process chain remains unaffected upon scaling.

In the simplified kMC model (see Figure 1b), we neglect the mass transport in the electrolyte and the oxidation reaction at the counter electrode. Thus, we consider two process chains, i.e., process chain (1) and process chain (3), to systematically analyze the working principle of the local temporal acceleration scheme. This means that the net generation and the transport of electrons are lumped into a fast organic process chain, and the reduction reaction defines a slow process chain, which yields  $m = 2$  process chains. The working principle of the acceleration scheme for the complete system including mass transport, i.e., with all three process chains, is demonstrated in Section S6, Supporting Information, and briefly discussed in the Results and Discussion.

**Detection of Local Quasi-equilibrium.** The local quasi-equilibrium of each process chain  $m$  is assessed for a subset of particles  $\mathcal{P}_m \in \mathcal{P}$ .  $\mathcal{P}_m$  does not necessarily contain the particles which belong to the transition rates in the respective process chain  $m$ . It may even be a good choice to define  $\mathcal{P}_m$  as particles belonging to subsequent process chains with slower transition rates. To assess the quasi-equilibrium of process chain  $m$ , we observe the *local environment* of the particles in  $\mathcal{P}_m$ . For an arbitrary particle  $i \in \mathcal{P}$ , we define a quasi-potential (QP)

$$\tilde{V}_i = \tilde{V}(\mathbf{r}_i) = \sum_{j=1}^{N \ddagger} \frac{w_{ij}}{r_{ij}} \Theta(r_{\text{cut}}^{\text{QP}} - r_{ij}) \quad (5)$$

where  $w_{ij}$  are user-specified weights,  $r_{ij} = |\mathbf{r}_j - \mathbf{r}_i|$  is the distance between particle  $i$  and particle  $j$ ,  $\Theta$  is the Heaviside step function, and  $r_{\text{cut}}^{\text{QP}}$  is a cutoff radius. Note that  $r_{\text{cut}}^{\text{QP}}$  taken for the QP calculation differs from  $r_{\text{cut}}^{\text{C}}$  for Coulomb interactions. The double-dagger  $\ddagger$  indicates that the self-interaction term ( $i = j$ ) is omitted. Via  $w_{ij}$ , fluctuations arising from different particles can be weighted differently. In practice,  $w_{ij}$  contains quantities

like the charge magnitude  $Z_j$ , the particle mass, or the effective relative permittivity  $\epsilon_r$ .

Tracking  $\tilde{V}_i(n)$  at each kMC step  $n$  yields a sequence of QP values which, in quasi-equilibrium, oscillate more or less strongly around a given average value. The evolution of this average value is given by

$$\langle \tilde{V}_i \rangle(k) = \frac{1}{k} \sum_{n=1}^k \tilde{V}_i(n) \quad (6)$$

The average fluctuations in  $\tilde{V}_i(k)$  in the local environment of the  $i$ th particle are captured by

$$\langle \Delta \tilde{V}_i \rangle(k) = \frac{\langle \tilde{V}_i^{\text{mavg}} \rangle(k) - \langle \tilde{V}_i \rangle(k)}{\langle \tilde{V}_i \rangle(k)} \quad (7)$$

where

$$\langle \tilde{V}_i^{\text{mavg}} \rangle(k) = \frac{1}{N_{\text{ob}}} \sum_{n=1}^{N_{\text{ob}}} \tilde{V}_i(k - N_{\text{ob}} + n) \quad (8)$$

is the moving average QP and  $N_{\text{ob}}$  denotes a user-defined window size. If the relative fluctuations remain within a user-defined threshold  $\delta$

$$|\langle \Delta \tilde{V}_i \rangle(k)| \leq \delta \quad (9)$$

particle  $i$  is considered to be *locally quasi-equilibrated*. If all particles in  $\mathcal{P}_m$  fulfill the quasi-equilibration condition, eq 9, we define process chain  $m$  as quasi-equilibrated.

At the beginning of a simulation, the local environment of all particles is considered to be nonequilibrated. The same is valid for newly generated/injected particles. After  $N_{\text{ob}}$  kMC steps, local quasi-equilibrium is assessed via eq 9 and subsequently updated in intervals of  $N_s$  kMC steps. In this way, we ensure the sensitivity of quasi-equilibrium detection with respect to changes in the system dynamics.

For the acceleration of the kMC simulation of the OLI, we define the set of particles associated with the fast process chain (1) as all cations, i.e.,  $\mathcal{P}_{(1)} = \{C^+\}$ . We track the QP for all cations  $C^+$  using  $r_{\text{cut}}^{\text{QP}} = 2$  nm. Note that all attempts using electrons as the particle set  $\mathcal{P}_{(1)}$  did not provide an acceleration, as electrons tended to decay before a local quasi-equilibrium around electrons was reached. Since the ionic reaction centers are assumed to be fixed, we can set the weights of the ionic QP contribution to  $w^{\text{ion}} = 0$ . In contrast, the weights of the electronic contributions are set to

$$w^{\text{el}} = \frac{q}{\epsilon_{r,\text{eff}}} \quad \text{with} \quad \epsilon_{r,\text{eff}} = \frac{(\epsilon_{r,e} + \epsilon_{r,o})}{2} \quad (10)$$

where  $q = -1$  is the charge magnitude of an electron and  $\epsilon_{r,\text{eff}}$  is the effective relative permittivity between the organic material and the electrolyte with  $\epsilon_{r,e}$  and  $\epsilon_{r,o}$  being the relative permittivities of the electrolyte and the organic material, respectively. The latter weight mimics the electrostatic interaction between electrons and ions within different materials. Details regarding the efficient evaluation of QPs and of centered moving averages are given in the Sections S3 and S4 of the Supporting Information, respectively.

**Dynamic Scaling of Quasi-equilibrated Process Chains.** To resolve existing time scale disparities, the transition rates  $k_i$  of each process  $i$  in the quasi-equilibrated

process chains  $m$  are artificially decreased using a scaling factor  $0 < \alpha_m < 1$ :

$$k_i^* = \alpha_m k_i \quad (11)$$

where  $k_i^*$  denotes the scaled transition rate of process  $i$ . The value of each scaling factor  $\alpha_m$  is calculated and updated dynamically during the simulation such that on average  $N_f$  processes of each quasi-equilibrated process chain are executed before a process from a slow nonequilibrated process chain occurs.

The dynamic calculation of scaling factors is based on the superbasis concept of the Dybeck scheme.<sup>37</sup> For this purpose, the  $m$  process chains are subdivided into three sets:

1. Quasi-equilibrated and sufficiently executed:  $Q_A$
2. Quasi-equilibrated but not sufficiently executed:  $Q_B$
3. Nonequilibrated:  $N$

The union of the explored region,  $Q_A$ , and of the unexplored region,  $Q_B$ , forms the current superbasis  $S$ ; see Figure 2b. An arbitrary process chain  $m$  is considered to be sufficiently executed if it was at least  $N_e$  times executed in the current superbasis  $S$ .  $Q_A$  can be exited by a process from either  $Q_B$  or  $N$ . Hence, the effective escape rate  $r_{\text{es}}$  from  $Q_A$  is determined by the sum of all rates  $r_{m,S}$  of process chains belonging to the sets  $N$  and  $Q_B$ :

$$r_{\text{es}} = \sum_{m \in N, Q_B} r_{m,S} \quad (12)$$

In general, the rate of any process chain  $m$  within the current superbasis  $S$  can be approximated by temporal averaging:

$$r_{m,S} = \frac{1}{\Delta t_S} \sum_{n \in S} k_m(n) \Delta t_n \quad (13)$$

where  $\Delta t_S = \sum_n \Delta t_n$  is the total time spent in  $S$ ,  $k_m(n)$  is the rate constant of process chain  $m$  at kMC step  $n$  given by

$$k_m(n) = \sum_{i \in m} k_i(n) \quad (14)$$

and  $\Delta t_n$  denotes the corresponding time step. Consequently, the ratio

$$\langle N_m \rangle = \frac{r_{m,S}}{r_{\text{es}}} \quad (15)$$

represents the average number of executions in process chain  $m$  before  $Q_A$  is left. To ensure that an average number of  $N_f$  executions in process chain  $m$  are sampled, we can define the scaling parameter  $\alpha_m$  by

$$\alpha_m = N_f \frac{r_{\text{es}}}{r_{m,S}} \quad (16)$$

If  $\alpha_m > 1$ , we set  $\alpha_m = 1$  to prevent an increase of the transition rate.

Eventually, the process chains in  $Q_A$  allow the system to exit the superbasis via a process of a nonequilibrated process chain. Upon entering the new superbasis, all scaling factors are reset to 1 and new scaling factors are computed using eqs 12 to 16. In this context, all previously quasi-equilibrated process chains remain quasi-equilibrated, but they are no longer considered to be sufficiently executed such that  $\alpha_m$  is set to 1 in line with the Dybeck scheme.<sup>37</sup> All process chains need to be sufficiently

executed again before the scaling is activated again. This ensures that the processes in the respective process chains are sufficiently executed and with this limits the perturbation of the system dynamics.

For our OLI simulation model, we have selected the set of input parameters as summarized in Table 1. The chosen values

**Table 1. Input Parameters of the Scaling Algorithm for SIM1 for Different Values of Energetic Disorder  $\sigma$**

$\sigma$ (meV)	$N_{\text{ob}}$	$N_s$	$\delta$	$N_e$	$N_f$
0	$1 \times 10^6$	$1 \times 10^3$	0.2	$1 \times 10^4$	$1 \times 10^4$
100	$2 \times 10^6$	$1 \times 10^3$	0.3	$1 \times 10^4$	$1 \times 10^4$

provide high accuracy with respect to all investigated quantities and a tremendous speed-up. In the sensitivity analysis, we will demonstrate that these values approximate the optimal set of scaling parameters for the system at hand.

## RESULTS AND DISCUSSION

We analyze the performance of the acceleration scheme for the hybrid OLI for a wide range of  $k_{\text{red}}$  between  $1 \times 10^{-1} \text{ s}^{-1}$  and  $1 \times 10^{10} \text{ s}^{-1}$  for a set of different energetic disorders  $\sigma \in \{0 \text{ meV}, 100 \text{ meV}\}$  in the organic semiconductor. We evaluate the average time between successive reduction events,  $\langle t_{\text{red}} \rangle$ , averaged across 1000 reduction events, and the reduction current density

$$j_{\text{red}} = \frac{qN_{\text{red}}}{X\Delta t} \quad (17)$$

where  $\Delta t$  is the total simulated time,  $X$  is the dimension of the simulation grid in  $x$ -direction,  $q$  is the elementary charge, and  $N_{\text{red}}$  is the number of reduction events in  $\Delta t$ . As a final output quantity, the local electron density profile is calculated from the occupation times of all sites in the organic layer.<sup>52</sup> All nonaccelerated reference simulations were run for at least  $\Delta t = 50 \text{ ms}$ , while accelerated simulations were extended to longer time scales. A detailed summary of the input parameters for the system setup and rate equations can be found in Table S1 in the Supporting Information.

From a conceptual point of view, the Dybeck scheme can also be applied to the investigated setup. For this purpose, we partition the processes into reaction channels: (1) electron generation and decay, which define a reaction channel; (2) reduction reaction, which gives an irreversible channel; and (3) electron hopping, which is considered as a quasi-equilibrated reaction channel as suggested for surface diffusion in the original publication.<sup>37</sup> For the scaling parameters, we select an equilibration factor  $N_f = 1 \times 10^5$  and a scaling period  $N_s = 2 \times 10^6$ . The quasi-equilibrium of the reaction channels was assessed based on the execution number  $n_e = 2 \times 10^3$  and the threshold value  $\delta = 0.2$ .

Note that the scaling parameters in the Dybeck scheme partially have a different meaning than in our approach. First,  $n_e$  was used in the Dybeck scheme to detect quasi-equilibrated reaction channels and to determine whether a quasi-equilibrated reaction channel is sufficiently executed. We have replaced  $n_e$  by two separate parameters, i.e.,  $N_{\text{ob}}$  to detect quasi-equilibrium and  $N_e$  to sufficiently execute quasi-equilibrated process chains. Second, the Dybeck scheme uses the hyperparameter  $N_s$ , which defined the number of kMC steps after which scaling factors of quasi-equilibrated and sufficiently sampled reaction channels are updated. As

explicitly emphasized by Andersen et al.,<sup>38</sup> the choice of  $N_s$  is of negligible importance for the algorithm accuracy and efficiency. Based on the recent studies and our experience in the system setup, we choose the strategy to update scaling factors of quasi-equilibrated and sufficiently sampled process chains only if an additional process chain in the system becomes quasi-equilibrated and sufficiently executed. By avoiding a regular update after  $N_s$  steps, we can further reduce the computational overhead without loss of accuracy. Instead, we apply the parameter  $N_s$  as the update frequency for the quasi-potential detection. The meanings of  $\delta$  and  $N_f$  are equivalent to the original Dybeck scheme.

**Accuracy of Physical Quantities.** To rationalize the accuracy of our acceleration scheme, we start with the analysis of  $j_{\text{red}}$  at the OLI from the accelerated and reference kMC simulations for different time scale disparities introduced by

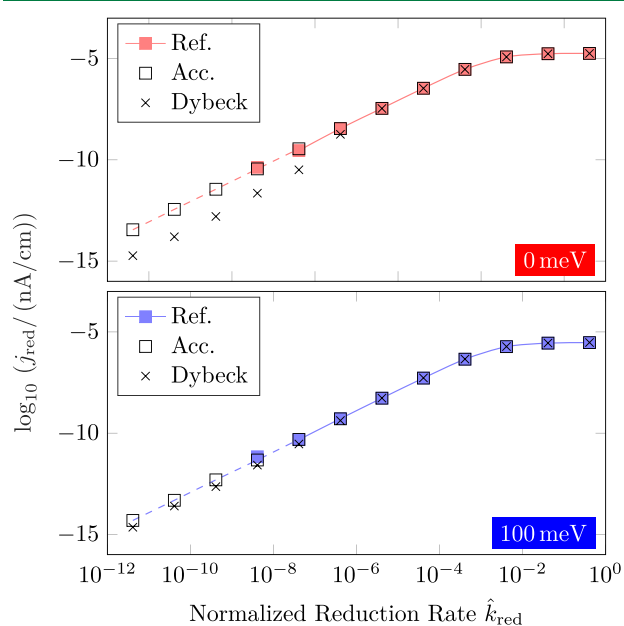


**Figure 3.** Reduction current density,  $j_{\text{red}}$ , for  $\sigma = 0 \text{ meV}$  (top) and  $\sigma = 100 \text{ meV}$  (bottom) as a function of the normalized reduction rate  $\hat{k}_{\text{red}}$ . Filled symbols visualize the current densities obtained from the reference kMC simulations; open symbols and crosses visualize the current densities from our local acceleration scheme (Acc.) and from the Dybeck scheme,<sup>37</sup> respectively. Dashed lines extrapolate the trend in  $j_{\text{red}}$  for low values of  $\hat{k}_{\text{red}}$ .

$k_{\text{red}}$ ; see Figure 3. Here, we introduce the normalized reduction rate

$$\hat{k}_{\text{red}} = \frac{k_{\text{red}}}{k_{0,\text{elh}}} \quad (18)$$

to distinguish if the interface reaction is limited by the electron transport or by the reduction reaction rate. The qualitative trend in the current density is similar for both values of  $\sigma$ , while the absolute value of  $j_{\text{red}}$  gets reduced for  $\sigma = 100 \text{ meV}$ . For  $\hat{k}_{\text{red}} \geq 0.04$ ,  $j_{\text{red}}$  saturates as the average time between two consecutive reduction events,  $\langle t_{\text{red}} \rangle$  (see Figure S6, Supporting Information), is limited by the finite transport of electrons to the OLI. Once electrons reach the OLI, they immediately react with the cations. Consequently,  $j_{\text{red}}$  becomes independent of the reduction rate. For  $\hat{k}_{\text{red}} \leq 4 \times 10^{-5}$ ,  $j_{\text{red}}$  decreases with

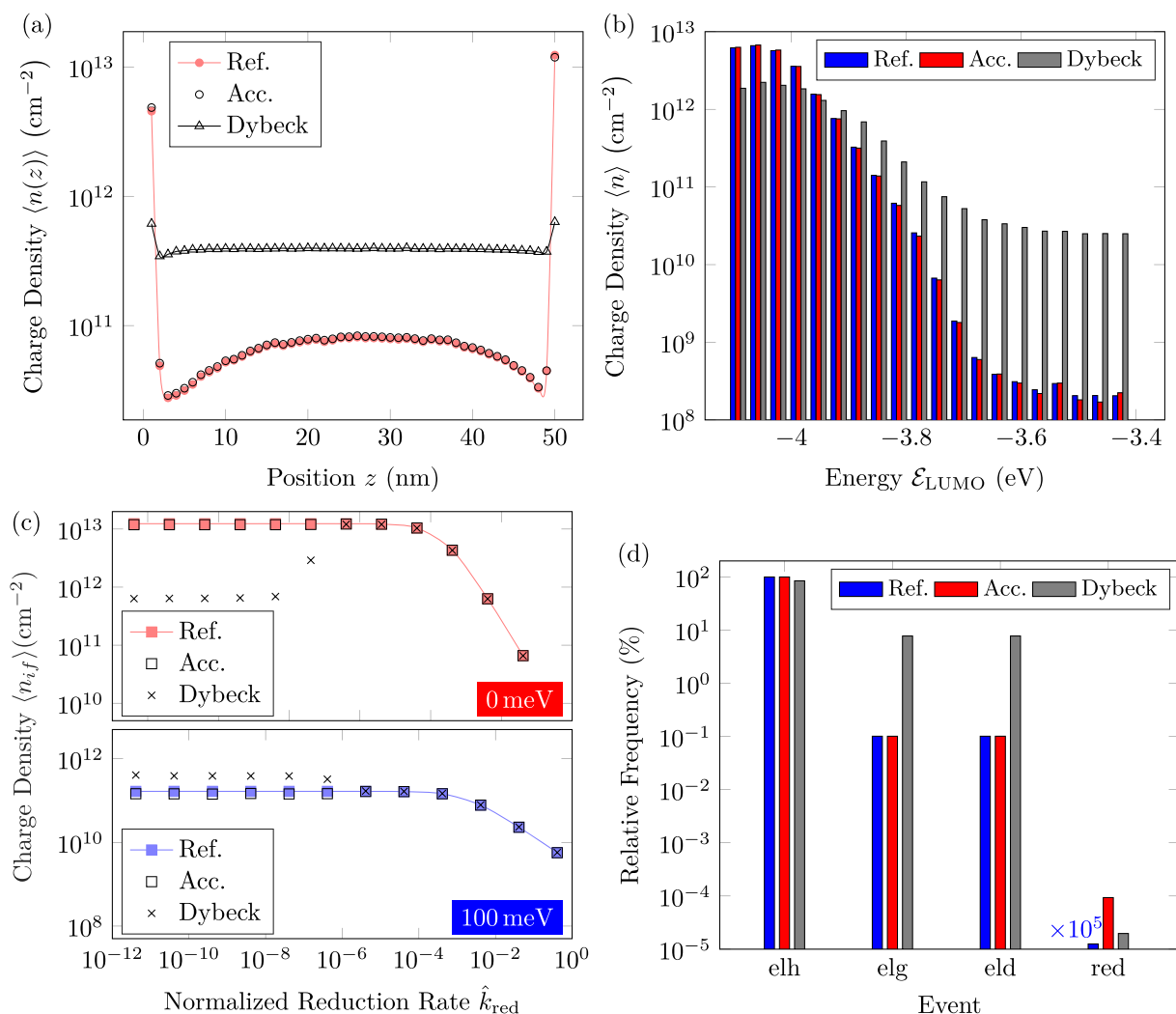


**Figure 4.** (a) Spatially averaged charge density profile,  $\langle n(z) \rangle$ , for  $\sigma = 0$  meV and  $\hat{k}_{\text{red}} = 4 \times 10^{-12}$ . (b) Distribution of average charge density per LUMO energy interval for  $\sigma = 100$  meV and  $\hat{k}_{\text{red}} = 4 \times 10^{-12}$ . (c) Average interface charge density,  $\langle n_{if} \rangle$ , for  $\sigma = 0$  meV and  $\sigma = 100$  meV as a function of the normalized reduction rate  $\hat{k}_{\text{red}}$ . (d) Relative event frequencies for  $\sigma = 0$  meV and  $\hat{k}_{\text{red}} = 4 \times 10^{-12}$ . Note that the frequency of the reduction process for the reference simulation is scaled by a factor of  $1 \times 10^5$  for improved visibility.

decreasing  $\hat{k}_{\text{red}}$  following a power law. In this regime, electron transport to the interface is much faster than the reduction reaction leading to charge accumulation at the OLL. Now, the current density is independent of the charge transport rate and is solely controlled by the reaction rate. Note that, without the use of an acceleration scheme, we were only able to simulate down to reduction rates of  $\hat{k}_{\text{red}} \approx 1 \times 10^{-10}$  due to the large computational demand. As  $j_{\text{red}}$  is solely controlled by the reduction reaction in this regime, we may extrapolate the reference current densities for the lower values of  $\hat{k}_{\text{red}}$ .

A comparison of  $j_{\text{red}}$  from reference and accelerated simulations in Figure 3 yields an excellent agreement. As we will see later, the acceleration scheme only kicks in for  $\hat{k}_{\text{red}} \leq 4 \times 10^{-7}$ . In the accelerated regime, the reference and accelerated values are perfectly matching, and importantly the temporal acceleration scheme is capable of predicting the correct trend in the average reduction current density independent of energetic disorder. For larger  $\hat{k}_{\text{red}}$ , it is important to note that the acceleration scheme does not disturb any of the system dynamics.

In contrast, the application of the Dybeck scheme leads to a severe underestimation of  $j_{\text{red}}$  by more than 1 order of magnitude at  $\sigma = 0$  meV for  $\hat{k}_{\text{red}} \leq 4 \times 10^{-7}$ . At  $\sigma = 100$  meV, fewer deviations are observed with a maximum error of a factor of 2. Again, at larger  $\hat{k}_{\text{red}}$  the reduction reaction is sufficiently fast such that the Dybeck scheme does not reach quasi-equilibrated and sufficiently executed reaction channels.

To further rationalize the accuracy of our acceleration scheme on local properties and further to understand the error observed from the Dybeck scheme, we analyze the charge carrier density as a function of the  $z$ -position for  $\sigma = 0$  meV and  $\hat{k}_{\text{red}} = 4 \times 10^{-12}$  averaged across the  $x$ -axis, see Figure 4a. The prediction of accurate density profiles is of particular importance, as several other relevant quantities (e.g., potential profiles, differential capacitance) can be derived from the local charge density. Due to the low permittivity ( $\epsilon_r = 4$ ) of the organic semiconductor, electrons are strongly attracted by the image charges at the electrode and at the electrolyte. In the absence of charge extraction, electrons accumulate at the electrode, which gives rise to a large charge density at  $z = 1$  nm. At small reduction rates, electrons also accumulate at the

OLI leading to an interface charge density  $n_{if}$  (see Figure 4c) that is orders of magnitude higher than the charge density in the bulk region of the organic semiconductor. Notably, for the given set of scaling parameters, the accelerated simulations perfectly reproduce the charge density profiles from the reference simulations. Also, it can be observed that the Dybeck scheme strongly underestimates the charge density at both interfaces and instead overestimates the electron density in the bulk of the organic semiconductor.

In the presence of a finite energetic disorder, we can further consider the charge density distribution over the disordered molecular orbital energy  $\mathcal{E}_i^{\text{LUMO}} = \mathcal{E}_i^{\text{MO}} + \mathcal{E}_i^\sigma$ . Figure 4b illustrates the charge density as a function of  $\mathcal{E}_{\text{LUMO}}$  for  $\sigma = 100$  meV and  $\hat{k}_{\text{red}} = 4 \times 10^{-12}$ . For a given value of  $\sigma$ ,  $\mathcal{E}_{\text{LUMO}}$  are distributed Gaussian-shaped around  $-3.8$  eV. For electrons, it is energetically favorable to occupy low energy states. To populate states of high  $\mathcal{E}_{\text{LUMO}}$ , electrons need to jump upward in energy which is strongly reduced (see eq 4), resulting in low charge densities. The distribution of the reference densities (see Figure 4b) is physically consistent with our expectation and further is also preserved for the accelerated simulation. Moreover, the average charge densities at each energy interval are equivalent. As briefly mentioned above, the average interface density  $\langle n_{if} \rangle$  is the crucial parameter for the correct prediction of reduction time and current density. Errors in the latter two quantities stem from errors in  $\langle n_{if} \rangle$ . For  $\hat{k}_{\text{red}} \geq 4 \times 10^{-3}$ , the interface density strongly decreases which corresponds to the transport limit outlined above. In contrast,  $\langle n_{if} \rangle$  becomes constant for  $\hat{k}_{\text{red}} \leq 4 \times 10^{-6}$  because the consumption of electrons at the OLI via reduction reactions is much slower than the net generation and the transport of carriers to the interface. The presence of energetic disorder considerably reduces  $\langle n_{if} \rangle$  which leads to the decrease in  $\langle j_{\text{red}} \rangle$ ; see Figure 3. Our local acceleration scheme accurately conserves the electron interface density and, thus, generates correct predictions for the reduction time and current density. The locality of our quasi-equilibrium detection algorithm successfully captures the local density profiles and with this allows an accurate reproduction of global properties such as the reduction current density.

It is noteworthy that the Dybeck scheme results in a substantially different density distribution. Here, high energetic states are strongly oversampled up to a factor of approximately 100; see Figure 4b. As a direct consequence, the occupation of low energetic states (Figure 4c) decreases up to factor of 3.3. The discrepancies in the charge density profiles can be rationalized by the relative frequencies of all simulated processes. Figure 4d shows a comparison of the relative frequency for the different events to occur at  $\sigma = 0$  meV and  $\hat{k}_{\text{red}} = 4 \times 10^{-12}$ . While our local scaling algorithm preserves the relative frequency of all events related to the fast organic process chain, the relative frequency for a reduction event is substantially increased. In contrast, the Dybeck scheme changes the ratio among electron transport, charge generation, and decay as well as the reduction. As the reaction channels are scaled down to comparable rates, electrons react at the surface or decay before the charge density at the OLI reaches steady state. This results in a strong decrease in  $\langle n_{if} \rangle$  (cf. Figure 4c) and, thus, to considerably lower  $j_{\text{red}}$ . For high disorder, a quasi-equilibrium assumption can be justified<sup>53</sup> as observed from the more accurate charge density profile and a reduced error in the reduction current in the Dybeck scheme (see Figure S8,

Supporting Information). This underlines that the assumption of quasi-equilibrium for mass or charge transport needs to be justified when using the Dybeck scheme.

Considering the typical applications of the Dybeck scheme, i.e., surface catalytic reaction networks, it is often reasonable to assume that surface diffusion of species is a quasi-equilibrated reaction channel. The assumption is in particular valid when the time scale disparities are evenly distributed over the surface. In other words, the adlayer of adsorbed species must be well mixed to guarantee the successive execution of nonequilibrated reaction channels. As soon as a time scale disparity is spatially confined, the transport of species becomes a limiting factor, and its dynamics must be reproduced correctly. A simple example is the time scale disparity induced by an interface reaction such as we have studied in the OLI. For such applications, our temporal acceleration scheme can be of high relevance. In this context, we point out that the local quasi-equilibrium detection, a key feature of the local temporal acceleration scheme, allows us to handle time scale disparities which are arbitrarily distributed in space. To demonstrate this aspect, we provide a systematic kMC study of coupled diffusion-reaction of ions at spherical nanoparticles immersed within a liquid electrolyte in Section S7, Supporting Information.

**CPU Speed-Up.** We proceed our analysis by evaluating the acceleration in CPU time,  $\xi$ , by comparison of the CPU time required per reduction event with and without our local acceleration scheme:

$$\xi = \frac{\langle t_{\text{CPU,red}}^{\text{ref}} \rangle}{\langle t_{\text{CPU,red}}^{\text{acc}} \rangle} \quad (19)$$

where  $\langle t_{\text{CPU,red}}^{\text{ref}} \rangle$  and  $\langle t_{\text{sim,red}}^{\text{acc}} \rangle$  denote the CPU time per reduction event of the reference simulations and of the accelerated simulations, respectively. For  $\hat{k}_{\text{red}} = 4 \times 10^{-8}$ , roughly 205 s of CPU time between two consecutive reduction events is required without any acceleration scheme. For lower  $\hat{k}_{\text{red}}$ , the required computational time to get a reliable statistical evaluation of the physical properties exceeds reasonable time scales. Thus, we have extrapolated the values of  $t_{\text{CPU,red}}^{\text{ref}}$  (see Section S5.3 and Table S2 in the Supporting Information for details) to estimate the CPU time per reduction event for the reference simulations for  $\hat{k}_{\text{red}} \leq 4 \times 10^{-9}$ . Figure 5 illustrates the speed-up for 0 meV and for 100 meV. For  $\hat{k}_{\text{red}} \geq 4 \times 10^{-6}$ ,

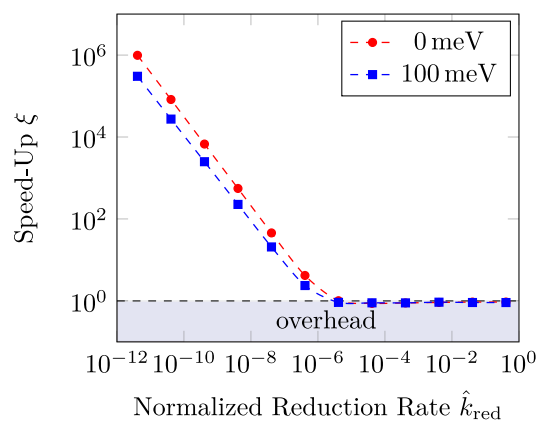


**Figure 5.** Speed-up in CPU time,  $\xi$ , for  $\sigma = 0$  meV and  $\sigma = 100$  meV as a function of the normalized reduction rate  $\hat{k}_{\text{red}}$ .

$\xi \approx 0.9 < 1$  due to the slight overhead introduced by the quasi-equilibrium detection. For  $\hat{k}_{\text{red}} \leq 4 \times 10^{-8}$ , the required CPU time between two successive reduction events is substantially reduced, which gives a maximum speed-up of  $\xi = 4 \times 10^4$  for the lowest  $\hat{k}_{\text{red}}$ . This underlines that accelerating such electrochemical kMC simulation is essential for sampling a statistically significant amount of reduction reactions ( $1 \times 10^3$  up to  $1 \times 10^4$  events) which are necessary for reliable output quantities.

**Transient Behavior.** The use of temporal acceleration schemes inevitably leads to a loss of information about the dynamics of the fast, quasi-equilibrated processes. To illustrate this information loss, we consider

$$\mathcal{R} = \frac{N_{\text{red}}}{N_{\text{elg}} - N_{\text{eld}}} \quad (20)$$

where  $N_{\text{red}}$  is the number of reduction events,  $N_{\text{elg}}$  is the number of generation events, and  $N_{\text{eld}}$  is the number of electron decay events. The denominator represents the net number of electrons available for a reduction reaction being determined by the fast processes, while  $N_{\text{red}}$  represents the slow reduction process. Thus,  $\mathcal{R}$  will eventually converge to 1.

Figure 6 illustrates  $\mathcal{R}$  up to a simulated time of 10 ms for  $\sigma = 0$  meV and  $\hat{k}_{\text{red}} = 4 \times 10^{-8}$ . The reference profile is very noisy.

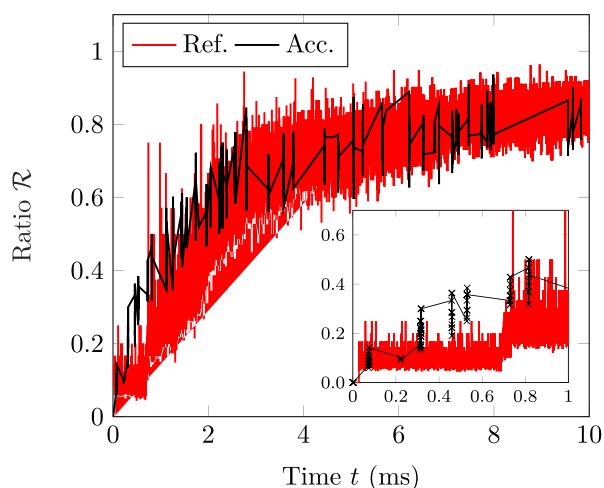


**Figure 6.** Time evolution of the ratio  $\mathcal{R}$  for  $\sigma = 0$  meV and  $\hat{k}_{\text{red}} = 4 \times 10^{-8}$ . The inset demonstrates the alternate occurrence of sampling regions (high density of  $\times$  symbols) and regions with scaled transition rates (low density of  $\times$  symbols) in the accelerated curve. Each  $\times$  symbol labels one kMC step.

This noise arises from the strong oscillations in the denominator around a certain average value. In contrast, the statistical fluctuations are strongly reduced within the accelerated transient resulting from the down-scaling of the fast process chain of the electronic processes in the organic semiconductor. Apparently, the algorithm acts as a filter for higher statistical moments. The inset of Figure 6 demonstrates the concrete impact of the acceleration scheme on the time evolution of  $\mathcal{R}$ . During the quasi-equilibrium assessment and sampling of quasi-equilibrated process chains, a high amount of kMC steps are executed; see high density of  $\times$  symbols in inset of Figure 6. In this regime, naturally the physical quantity  $\mathcal{R}$  fluctuates as much as the nonaccelerated reference curve. Once the fast process chains are scaled, fluctuations in  $\mathcal{R}$  are

substantially reduced; this means that the acceleration scheme acts as a filter for higher moments. In the majority of studies we are not interested in the higher order moments but rather in time-averaged values which, as presented above, are accurately reproduced with our local acceleration scheme. Note that the observed reduction of higher moments has been also reported in other acceleration schemes such as the net-event kMC technique.<sup>33</sup> Additionally, we would like to emphasize that our algorithm does not generate additional stochastic noise unlike the probability-weighted kMC method.<sup>32</sup>

**Sensitivity Analysis.** Now, we analyze the sensitivity of the accuracy and the performance of our local acceleration scheme on the scaling parameters  $N_{\text{ob}}$ ,  $N_e$ , and  $N_f$ . Note that we use the accelerated results from the above analysis as a reference for the sensitivity analysis.

In the beginning of the simulation, the local environment of all reaction centers, and with this also the fast organic process chain, is considered to be nonequilibrated. Subsequently, the QP of each reaction center will be calculated in every kMC step. Figure 7 illustrates the transient of  $\Delta\tilde{V}$  related to an

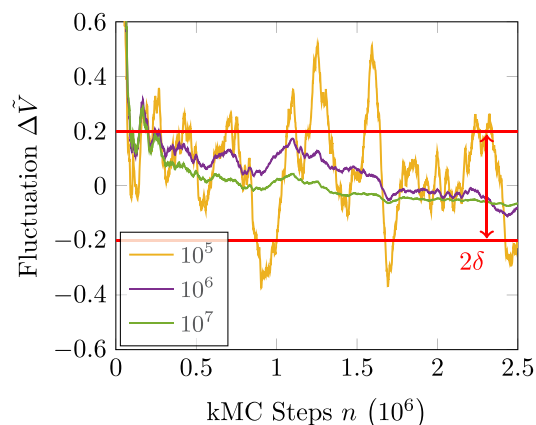


**Figure 7.** Assessment of local quasi-equilibrium: fluctuations  $\Delta\tilde{V}$  in the local environment of an arbitrary ionic reaction center for  $\sigma = 0$  meV and different sizes of observation windows  $N_{\text{ob}}$ . If  $N_{\text{ob}}$  is chosen large enough,  $\Delta\tilde{V}$  remains within the marked threshold region of  $2\delta$ , and the local environment of the considered reaction center is said to be quasi-equilibrated.

arbitrary ionic reaction center for  $\sigma = 0$  meV at different sizes of the observation window  $N_{\text{ob}}$ . After a brief settling period of approximately  $8 \times 10^4$  kMC steps,  $\Delta\tilde{V}$  oscillates around an average of 0. If  $N_{\text{ob}}$  is chosen large enough, the fluctuations remain within the user-defined tolerance range of  $\pm\delta$  and the respective reaction center is considered to be quasi-equilibrated. Note that the value of  $N_{\text{ob}}$  strongly depends on the disorder of the system. For  $\sigma = 0$  meV, a stable quasi-equilibrium is already obtained for  $N_{\text{ob}} = 1 \times 10^6$  and  $\delta = 0.2$  (cf. Figure 7). For  $\sigma = 100$  meV, the same combination of parameters would be highly unstable (cf. Figure S9, Supporting Information). To maintain the same threshold region for high disorder, the observation window must be increased to  $1 \times 10^7$  which, however, limits the speed-up and does not enhance the accuracy. Instead, a good trade-off can be made by increasing  $N_{\text{ob}}$  and  $\delta$ . For the given setup, we found  $N_{\text{ob}} = 2 \times 10^6$  and  $\delta = 0.3$  to be a suitable combination.

The fast organic process chain is assumed to be quasi-equilibrated once the environments of all reaction centers are

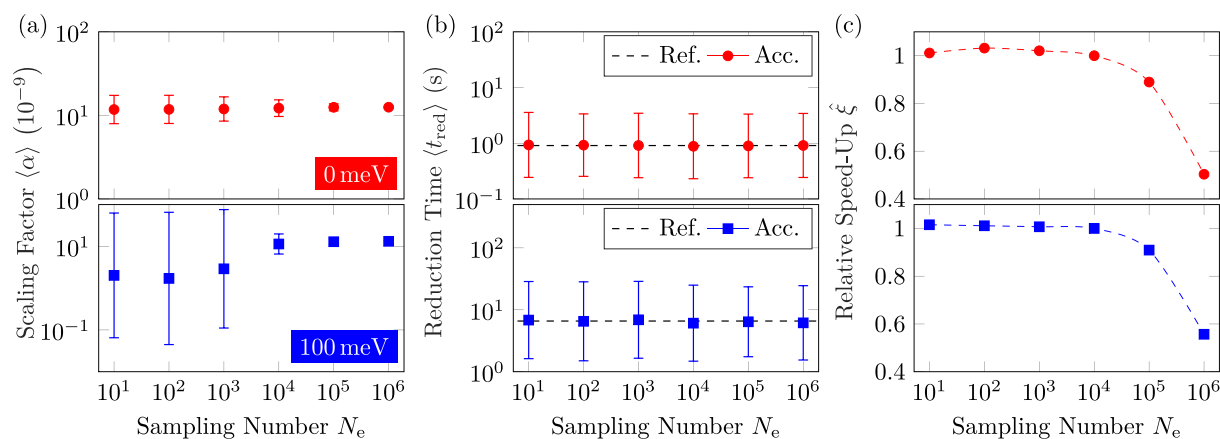


**Figure 8.** Sensitivity on the execution number,  $N_e$ , for a fixed equilibration factor  $N_f = 1 \times 10^4$ : (a) average scaling factor,  $\langle \alpha \rangle$ , for (top)  $\sigma = 0$  meV and (bottom)  $\sigma = 100$  meV; (b) reduction time,  $\langle t_{\text{red}} \rangle$ , for (top)  $\sigma = 0$  meV and (bottom)  $\sigma = 100$  meV at  $\hat{k}_{\text{red}} = 4 \times 10^{-12}$ ; and (c) relative speed-up  $\hat{\xi}$  with respect to the results from Figure 5.

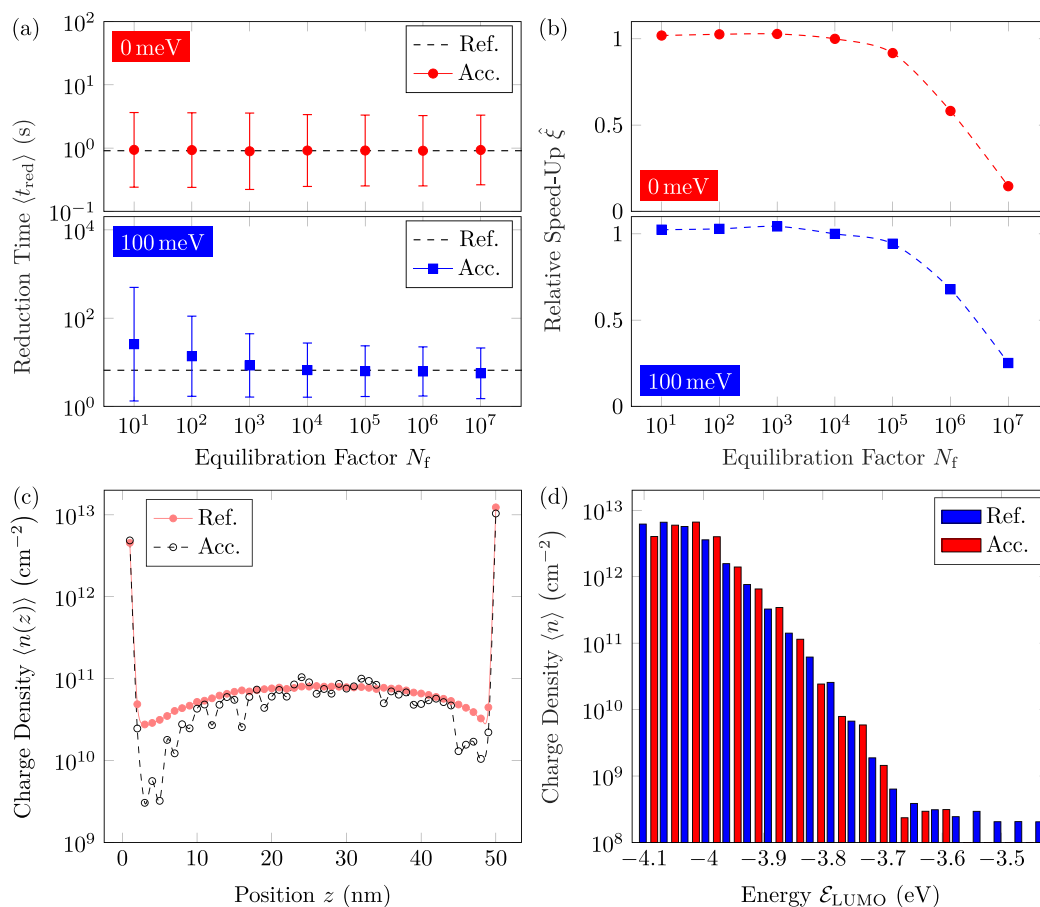


**Figure 9.** Sensitivity on equilibration factor,  $N_f$ , for a fixed execution number of  $N_e = 1 \times 10^4$ : (a) average reduction time,  $\langle t_{\text{red}} \rangle$ , for  $\sigma = 0$  meV and  $\sigma = 100$  meV and  $\hat{k}_{\text{red}} = 4 \times 10^{-12}$  as a function of  $N_f$  and (b) corresponding relative speed-up,  $\hat{\xi}$ , with respect to the results from Figure 5. (c) Spatially averaged charge density profile for  $\sigma = 0$  meV,  $\hat{k}_{\text{red}} = 4 \times 10^{-12}$ , and  $N_f = 1 \times 10^1$ . The error bars from spatial averaging are omitted for reasons of clarity. (d) Distribution of average charge density per LUMO energy interval for  $\sigma = 100$  meV,  $\hat{k}_{\text{red}} = 4 \times 10^{-12}$  and  $N_f = 1 \times 10^1$ .

quasi-equilibrated. Now, the scaling factor for the fast process chain is calculated according to eq 16. For this purpose, we compute the average rate of the fast process chain and the slow process chain over the next  $N_e$  executions of the fast process chain. For a given  $N_f$ ,  $N_e$  must be chosen sufficiently large enough to get reliable scaling factors. Figure 8a shows the

average scaling factor  $\langle \alpha \rangle$  for different values of  $N_e$  and  $\sigma = 0$  meV and  $\sigma = 100$  meV. Taking into account the fluctuations, we see that  $\alpha$  only weakly depends on  $N_e$  and on  $\sigma$ . For decreasing  $N_e$ , however, the fluctuations in  $\langle \alpha \rangle$  increase especially at  $\sigma = 100$  meV. In the worst case, a scaling factor of 0 is calculated which needs to be detected to avoid simulation

abortion, e.g., by a lower threshold for  $\alpha$ . The accuracy of the accelerated kMC simulations is quite insensitive to changes in  $N_e$ . As a concrete example, Figure 8b illustrates the average reduction time for  $\hat{k}_{\text{red}} = 4 \times 10^{-12}$ . Good agreement is obtained with respect to the reference values. However, choosing lower values of  $N_e$  is not favorable with respect to speed-up in simulation time, as shown in Figure 8c. The relative speed-up,  $\xi$ , saturates toward low  $N_e$  independent of the value of  $\sigma$ ; here, the simulation time is determined by the size of  $N_{\text{ob}}$  and  $N_f$ .

The magnitude of  $\alpha$  can be gradually controlled via the equilibration factor  $N_f$  which gives the average number of executions of the fast process chain before a slow process is sampled. Figure 9a illustrates the average reduction time for  $\hat{k}_{\text{red}} = 4 \times 10^{-12}$  and  $\sigma \in \{0 \text{ meV}, 100 \text{ meV}\}$  as a function of  $N_f$ . Without disorder, the results are insensitive to the chosen value of  $N_f$ . For high disorder and small values of  $N_f$ , deviations from the reference value arise. This is linked to an underestimation of the average electron density at the OLI. Increasing  $N_f \geq 1 \times 10^3$  removes the scaling error and restores the physical quantities. Decreasing  $N_f$  below  $1 \times 10^4$  has no benefits in terms of speed-up as indicated in Figure 9b. The reasoning is analogous to above: for low  $N_f$ , the speed-up is essentially determined by the given values of  $N_e$  and  $N_{\text{ob}}$ .

As a last part of this analysis, we investigate the impact of small  $N_f$  on the local electron density, visualized in Figure 9c,d for  $\sigma = 0 \text{ meV}$  and  $\sigma = 100 \text{ meV}$ , respectively, and  $\hat{k}_{\text{red}} = 4 \times 10^{-12}$  and  $N_f = 1 \times 10^1$ . Without disorder, the charge density values at both interfaces are accurately reproduced while substantial deviations are observed within the bulk of the organic layer. This explains the insensitivity of  $\langle t_{\text{red}} \rangle$  on  $N_f$  for  $\sigma = 0 \text{ meV}$ . Considering the energy dependence of the charge density distribution (see Figure 9d), low energy intervals ( $\mathcal{E}_{\text{LUMO}} \leq -3.9 \text{ eV}$ ) are partially oversampled whereas the high energy tail ( $\mathcal{E}_{\text{LUMO}} \geq -3.7 \text{ eV}$ ) is strongly undersampled. These deviations lead to a different local density profile in which on average less electrons are located at the OLI. Accordingly, the average reduction time increases for low values of  $N_f$  as shown in Figure 9d.

**Inclusion of Mass Transport.** We now demonstrate the applicability of the local temporal acceleration scheme for the OLI including ionic mass transport in an extended electrolyte region. We focus on the performance in terms of accuracy of the global and local quantities as well as on the speed-up. The full model details of the extended system as well as an extensive analysis is provided in Section S6, Supporting Information. The system is partitioned into three process chains: process chain (1) merges electron transport, generation, and decay; process chain (2) contains cation diffusion; and process chain (3) isolates the rate-limiting reduction reaction. Thus, we extend the simplified OLI system studied above by a third process chain which includes mass transport in terms of cation diffusion within the electrolyte. The sets of particles for the quasi-equilibrium assessment are  $\mathcal{P}_{(1)} = \mathcal{P}_{(2)} = \{C^+\}$ . The hyperparameters for the acceleration scheme are chosen similarly to the simplified OLI model without mass transport (see Table S3, Supporting Information), with a slightly increased  $N_f = 1 \times 10^5$  to ensure accurate results on a local scale.

The trend in the reduction current density, Figure 10a, does not change upon inclusion of mass transport (cf. Figure S11a, Supporting Information). We see that the accelerated kMC

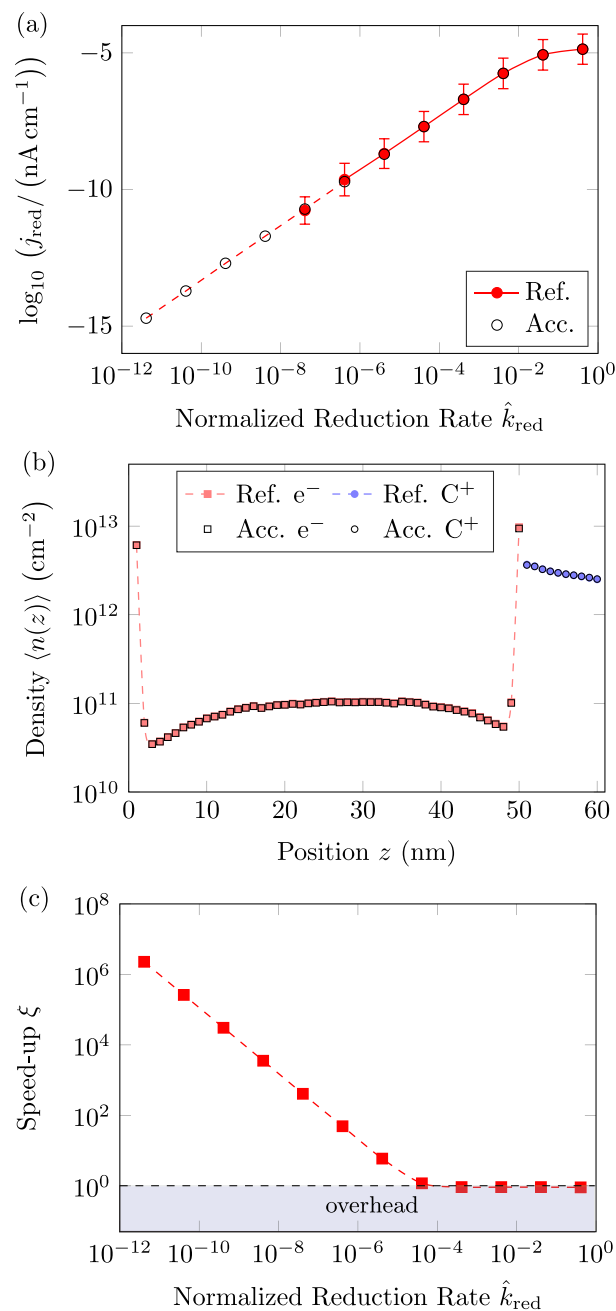


**Figure 10.** (a) Reduction current density,  $j_{\text{red}}$ , as a function of the normalized reduction rate,  $\hat{k}_{\text{red}}$ . Filled symbols visualize the current densities obtained from the reference kMC simulations with mass transport; open symbols visualize the current densities using the local temporal acceleration scheme with mass transport. Dashed lines extrapolate  $j_{\text{red}}$  of the reference simulation to low values of  $\hat{k}_{\text{red}}$ . (b) Average electron ( $e^-$ ) and cation ( $C^+$ ) density profiles over the  $z$ -axis for  $\hat{k}_{\text{red}} = 4 \times 10^{-12}$ . (c) Speed-up in CPU-time,  $\xi$ , as a function of the normalized reduction rate  $\hat{k}_{\text{red}}$ .

simulations accurately reproduce the values of  $j_{\text{red}}$ . Again, the temporal acceleration scheme allows us study configurations of large time scale disparity, which are not in reach within reasonable CPU times in standard kMC simulations. The local charge density profile across the  $z$ -axis of the simulation box, Figure 10b, shows the same shape as previously discussed. Additionally, we see that the cations form a diffuse layer within in the extended electrolyte region ( $50 \text{ nm} < z \leq 60 \text{ nm}$ ). Both



the charge and the ionic density profiles are accurately captured within the accelerated simulations which underlines that the quasi-equilibrium detection does not substantially alter the local distribution of cation and electron diffusion at the OLI. Finally, for  $\hat{k}_{\text{red}} \leq 4 \times 10^{-6}$ , we obtain an increasing CPU speed-up  $\xi$  (see Figure 10c) with a value of  $\xi \approx 2 \times 10^6$  for the lowest value of  $\hat{k}_{\text{red}}$ . For high normalized reduction rates of  $\hat{k}_{\text{red}} \geq 4 \times 10^{-4}$ , the acceleration scheme introduces a slight overhead into the kMC algorithm. Most importantly, the incorporation of mass transport considerably increases the computational demand in standard kMC models without temporal acceleration. Thus, the use of accurate temporal acceleration schemes becomes of even higher importance.

To summarize, we obtain accurate results on local and global physical quantities such as the charge and cation density profiles and the reduction current density, respectively, as well as a tremendous speed-up. The demonstration of the extended OLI suggests that the acceleration scheme can successfully be applied to more complex electrochemical systems including diffusion and reactions of several chemical species by the use of multiple process chains.

**Hyperparameter Guidelines.** Finally, we provide several heuristic guidelines for the parametrization of the acceleration scheme. The detection of local quasi-equilibria requires a suitable combination of observation window size  $N_{\text{ob}}$ , update frequency  $N_{\text{g}}$ , and threshold value  $\delta$ .

To identify a proper value of  $N_{\text{ob}}$ , the user may start with a short kMC simulation to observe when quasi-equilibrium is reached or left again in order to estimate the amplitudes in the QP fluctuations while switching off the scaling, e.g., by setting  $N_{\text{f}} \rightarrow \infty$ .  $N_{\text{ob}}$  should be chosen such that  $\Delta V$  remains within the threshold region of  $2\delta$ , cf. Figure 7. In this context, we suggest starting with  $\delta = 0.2$  for systems with weak local heterogeneities. For strong local heterogeneities, we advise to initially find a suitable value for  $N_{\text{ob}}$  in combination with  $\delta = 0.2$ . If  $N_{\text{ob}}$  is too large for a decent speed-up,  $\delta$  can be raised in steps of 0.05 together with a decrease in  $N_{\text{ob}}$ .

Hyperparameter  $N_{\text{s}}$  determines the number of kMC steps after which the QPs are updated. In this way, the user gains control over the memory requirements related to QP tracking. This can be useful for large particle numbers and/or large observation window sizes  $N_{\text{ob}}$ . Here, an adequate first choice is  $N_{\text{s}} \approx N_{\text{ob}}/(1 \times 10^3)$ , i.e.,  $1 \times 10^3$  QP values within  $N_{\text{ob}}$  need to be calculated. Additionally, appropriate weight factors  $w_{ij}$  and a cutoff radius  $r_{\text{cut}}^{\text{QP}}$  must be chosen for the QP calculation. The latter two parameters can be selected pragmatically, as in the majority of kMC simulations, only nearest-neighbor transitions are considered. Thus,  $r_{\text{cut}}^{\text{QP}}$  should contain at least the corresponding sites. For uncharged particles, the inverse particle mass can be used as weight factors as lightweight particles move faster and consequently control the local fluctuations. For charged particles, we recommend a combination of charge magnitude and (effective) relative permittivity to reproduce the strength of local Coulomb interactions accurately.

When proper quasi-equilibrium assessment is assured, values for the sampling parameter  $N_{\text{e}}$  and the equilibration factor  $N_{\text{f}}$  can be selected. In the sensitivity analysis above, we have demonstrated that  $N_{\text{e}}$  essentially only determines the statistical spread in the calculated scaling factors but not the accuracy of physical quantities. Thus, we recommend a value that is considerably lower than the chosen observation window size

(e.g.,  $N_{\text{e}} \approx N_{\text{ob}}/(1 \times 10^3)$ ) such that the speed-up becomes independent of  $N_{\text{e}}$ . The aggressiveness of the scaling algorithm is controlled by  $N_{\text{f}}$ . A conservative first value for  $N_{\text{f}}$  can be estimated using the ratio of highest and lowest possible transition rates. For instance, in the OLI setup we have  $k_{\text{red}} = 1 \times 10^{-1} \text{ s}^{-1}$  and  $k_{0,\text{elh}} = 3.66 \times 10^{10} \text{ s}^{-1}$  which yields a ratio of  $3.66 \times 10^{11}$ . To reduce the disparity by a factor of approximately  $1 \times 10^7$  we have to set  $N_{\text{f}} = 1 \times 10^4$ . Note that the final choice of  $N_{\text{f}}$  also depends on which physical quantities are of interest. Obtaining a high accuracy on a local scale (e.g., spatially resolved charge densities) generally requires higher equilibration factors than needed for quantities on a global scale (e.g., average current density on a device level).

To complete this discussion, we want to emphasize that a first set of heuristically chosen input parameters does not replace a diligent sensitivity analysis. Each system has specific properties, and accordingly, a sensitivity analysis is recommended to obtain maximum speed-up and accuracy for system-specific output quantities.

## CONCLUSION

In conclusion, we have presented a novel local temporal acceleration scheme to couple fast transport and slow interface reactions in electrochemical systems within kMC simulations. Our algorithm transfers the modified superbasin concept introduced by Dybeck et al.<sup>37</sup> to local time scale disparities which require an accurate treatment of the underlying transport dynamics. In contrast to the original algorithm, we formulate a local, particle-based criterion to assess the quasi-equilibrium of entire process chains which are defined via subsets of processes and particles. Local quasi-equilibrium is reached if the fluctuation in the local environment of each individual particles, captured by quasi-potentials, remains within a predefined threshold. Scaling factors of quasi-equilibrated and sufficiently executed process chains are calculated dynamically based on the Dybeck scheme. Down-scaling of all transition rates within a process chain preserves the relative dynamics. Simultaneously, existing time scale disparities are substantially reduced resulting in a computationally more efficient kMC method.

We have demonstrated the performance and the accuracy of our acceleration algorithm using a simplified model of a hybrid organic–liquid interface which suffer from time scale disparities between fast transport phenomena and slow interface reactions, being exemplary for electrochemical systems. Reduction currents and local charge densities are investigated and accurately reproduced despite the presence of local inhomogeneities. Moreover, we achieve an acceleration up to a factor of  $1 \times 10^6$  and without any loss in accuracy. Additionally, we have shown that the Dybeck scheme introduces a significant error when time scale disparities are nonuniformly distributed in space as for the given system.

The central innovation of the presented temporal acceleration scheme is its local quasi-equilibrium approach. Thus, local physical properties can be preserved upon scaling. The capability of resolving local heterogeneities is one of the main advantages of kMC models with respect to multiscale simulations. Hence, our algorithm provides a viable tool to substitute existing multiparadigm approaches by a stand-alone kMC model.

## ■ COMPUTATIONAL DETAILS

All simulation code of the hybrid organic–liquid interface including the presented acceleration scheme and the generalized temporal acceleration scheme by Dybeck et al.<sup>37</sup> has been implemented within C++ in our VORONOI framework.<sup>8</sup> The simulations were run on independent cores of an AMD Ryzen Threadripper 3990X @2.9 GHz with 64 hardware cores.

## ■ ASSOCIATED CONTENT

### SI Supporting Information

The Supporting Information is available free of charge at <https://pubs.acs.org/doi/10.1021/acs.jctc.1c01010>.

Integration of temporal acceleration scheme into generic kMC algorithm; efficient evaluation of quasi-potentials; efficient evaluation of centered moving average; calculation of Coulomb energies in a three dielectric media system; simulation input parameters; comparison of average reduction times,  $\langle t_{\text{red}} \rangle$ , as a function of normalized reduction rate  $\hat{k}_{\text{red}}$  for  $\sigma = 0$  meV and  $\sigma = 100$  meV; calculation of speed-up; relative event frequencies for  $\sigma = 100$  meV; exemplary quasi-equilibrium assessment for  $\sigma = 100$  meV; simulation of organic–liquid interface including mass transport; and exemplary simulation of a system with arbitrarily distributed time-scale disparities (PDF)

## ■ AUTHOR INFORMATION

### Corresponding Author

**Waldemar Kaiser** – Department of Electrical and Computer Engineering, Technical University of Munich, 80333 Munich, Germany; Computational Laboratory for Hybrid/Organic Photovoltaics (CLHYO), Istituto CNR di Scienze e Tecnologie Chimiche “Giulio Natta” (CNR-SCITEC), 06123 Perugia, Italy; [orcid.org/0000-0001-9069-690X](https://orcid.org/0000-0001-9069-690X); Email: [waldemar.kaiser@scitec.cnr.it](mailto:waldemar.kaiser@scitec.cnr.it)

### Authors

**Manuel Gößwein** – Department of Electrical and Computer Engineering, Technical University of Munich, 80333 Munich, Germany

**Alessio Gagliardi** – Department of Electrical and Computer Engineering, Technical University of Munich, 80333 Munich, Germany; [orcid.org/0000-0002-3322-2190](https://orcid.org/0000-0002-3322-2190)

Complete contact information is available at: <https://pubs.acs.org/doi/10.1021/acs.jctc.1c01010>

### Notes

The authors declare no competing financial interest.

## ■ ACKNOWLEDGMENTS

W.K. and A.G. acknowledge the TUM International Graduate School of Science and Engineering (IGSSE) for funding. M.G. and A.G. acknowledge the European Union’s Horizon 2020 FETOPEN 2018–2020 program “LION-HEARTED” under Grant Agreement No. 828984 for funding. A.G. further acknowledges funding under the Excellence Strategy of the Federal Government and the Länder, TUM innovation network “ARTEMIS” and the excellence cluster *e*-conversion by the German Research Foundation (Deutsche Forschungsgemeinschaft, DFG).

## ■ LIST OF SYMBOLS

$\alpha_m$	Scaling factor of <i>m</i> th process chain, see eq 16
$\Delta\mathcal{E}_{ij}$	Potential energy difference between sites <i>i</i> and <i>j</i> , see eq 4
$\langle \Delta\tilde{V}_i \rangle$	Average fluctuation in the local environment of particle <i>i</i> , see eq 7
$\Delta t$	Simulation time, see eq 17
$\delta$	Threshold for local quasi-equilibrium assessment, see eq 9
$\mathcal{E}_i$	Potential energy at site <i>i</i> , see eq 1
$\mathcal{E}_i^C$	Coulomb potential at site <i>i</i> , see eq 1
$\mathcal{E}_i^F$	Field contribution to potential energy at site <i>i</i> , see eq 1
$\mathcal{E}^{\text{LUMO}}$	LUMO level
$\mathcal{E}_i^{\text{MO}}$	Average molecular orbital energy at site <i>i</i> , see eq 1
$\mathcal{E}_i^{\text{ee}}$	Electron–electron interaction at site <i>i</i>
$\mathcal{E}_i^{\text{ie}}$	Ion–electron interaction at site <i>i</i>
$\mathcal{E}_i^\sigma$	Energetic disorder at site <i>i</i> , see eq 1
$\epsilon_{\text{eff}}$	Effective permittivity between the organic material and the electrolyte, see eq 10
$\epsilon_{\text{r,e}}$	Permittivity of electrolyte material, see eq 10
$\epsilon_{\text{r,o}}$	Permittivity of organic material, see eq 10
$j_{\text{red}}$	Reduction current density, see eq 17
$k_{0,\text{elh}}$	Attempt-to-hop frequency for electron hopping, see eq 4
$k_{\text{eld}}$	Electron decay rate
$k_{\text{elg}}$	Electron generation rate, see eq 3
$k_{\text{red}}$	Cation reduction rate
$\hat{k}_{\text{red}}$	Normalized reduction rate
$\mathcal{N}$	Set of nonequilibrated process chains
$N_e$	Sampling number
$N_f$	Equilibration factor, see eq 16
$N_{\text{ob}}$	Observation window for local quasi-equilibrium assessment, see eq 8
$N_{\text{red}}$	Number of reduction events, see eq 17
$N_s$	Interval for updating quasi-potentials
$\mathcal{Q}_A$	Set of quasi-equilibrated and sufficiently executed process chains; explored region of current superbasin <i>S</i>
$\mathcal{Q}_B$	Set of quasi-equilibrated but not sufficiently executed process chains; unexplored region of current superbasin <i>S</i>
$r_L$	Site spacing of simulation grid
$r_{\text{cut}}^C$	Cutoff radius for Coulomb interactions
$r_{\text{cut}}^{\text{QP}}$	Cutoff radius for quasi-potentials, see eq 5
$r_{\text{es}}$	Effective escape rate from explored superbasin region, see eq 12
$r_{m,S}$	Rate of <i>m</i> th process chain in current superbasin <i>S</i> , see eq 12
<i>S</i>	Current superbasin
$\sigma$	Energetic disorder
$\langle t_{\text{red}} \rangle$	Average time between successive reduction events
$V_b$	Bias potential, see eq 2
$\tilde{V}_i$	Quasi-potential related to particle <i>i</i> , see eq 5
$\langle \tilde{V}_i \rangle$	Average quasi-potential related to particle <i>i</i> , see eq 6
$\langle \tilde{V}_i^{\text{mavg}} \rangle$	Moving average quasi-potential related to particle <i>i</i> , see eq 8
<i>X</i>	Dimension of simulation grid in <i>x</i> -direction
<i>Z</i>	Dimension of simulation grid in <i>z</i> -direction

## REFERENCES

- (1) Piana, S.; Gale, J. Three-dimensional Kinetic Monte Carlo Simulation of Crystal Growth from Solution. *J. Cryst. Growth* **2006**, *294*, 46–52.
- (2) Rak, M.; Izdebski, M.; Brozi, A. Kinetic Monte Carlo Study of Crystal Growth from Solution. *Comput. Phys. Commun.* **2001**, *138*, 250–263.
- (3) Magna, A.; Coffa, S.; Colombo, L. A Lattice Kinetic Monte Carlo Code for the Description of Vacancy Diffusion and Self-organization in Si. *Nucl. Instrum. Methods Phys. Res. Sect. B Beam Interact. Mater. At.* **1999**, *148*, 262–267.
- (4) Jørgensen, M.; Grönbeck, H. Scaling Relations and Kinetic Monte Carlo Simulations To Bridge the Materials Gap in Heterogeneous Catalysis. *ACS Catal.* **2017**, *7*, 5054–5061.
- (5) Jørgensen, M.; Grönbeck, H. Montecoffee: A Programmable Kinetic Monte Carlo Framework. *J. Chem. Phys.* **2018**, *149*, 114101.
- (6) Jørgensen, M.; Grönbeck, H. Selective Acetylene Hydrogenation over Single-Atom Alloy Nanoparticles by Kinetic Monte Carlo. *J. Am. Chem. Soc.* **2019**, *141*, 8541–8549.
- (7) Bäessler, H. Charge Transport in Disordered Organic Photoconductors a Monte Carlo Simulation Study. *Phys. Status Solidi B* **1993**, *175*, 15–56.
- (8) Kaiser, W.; Popp, J.; Rinderle, M.; Albes, T.; Gagliardi, A. Generalized Kinetic Monte Carlo Framework for Organic Electronics. *Algorithms* **2018**, *11*, 37.
- (9) Kaiser, W.; Albes, T.; Gagliardi, A. Charge Carrier Mobility of Disordered Organic Semiconductors with Correlated Energetic and Spatial Disorder. *Phys. Chem. Chem. Phys.* **2018**, *20*, 8897–8908.
- (10) Drews, T. O.; Radisic, A.; Erlebacher, J.; Braatz, R. D.; Searson, P. C.; Alkire, R. C. Stochastic Simulation of the Early Stages of Kinetically Limited Electrodeposition. *J. Electrochem. Soc.* **2006**, *153*, C434.
- (11) Andreaus, B.; Eikerling, M. Active Site Model for Co Adlayer Electrooxidation on Nanoparticle Catalysts. *J. Electroanal. Chem.* **2007**, *607*, 121–132.
- (12) Methekar, R. N.; Northrop, P. W. C.; Chen, K.; Braatz, R. D.; Subramanian, V. R. Kinetic Monte Carlo Simulation of Surface Heterogeneity in Graphite Anodes for Lithium-Ion Batteries: Passive Layer Formation. *J. Electrochem. Soc.* **2011**, *158*, A363.
- (13) Blanquer, G.; Yin, Y.; Quiroga, M. A.; Franco, A. A. Modeling Investigation of the Local Electrochemistry in Lithium-O<sub>2</sub>Batteries: A Kinetic Monte Carlo Approach. *J. Electrochem. Soc.* **2016**, *163*, A329–A337.
- (14) Gavilán-Arriazu, E. M.; Mercer, M. P.; Barraco, D. E.; Hoster, H. E.; Leiva, E. P. M. Kinetic Monte Carlo Simulations Applied to Lithium and Post Li-ion Batteries: A Key Link in the Multi-scale Chain. *Prog. Energy* **2021**, *3*, 042001.
- (15) Pornprasertsuk, R.; Cheng, J.; Huang, H.; Prinz, F. B. Electrochemical Impedance Analysis of Solid Oxide Fuel Cell Electrolyte Using Kinetic Monte Carlo Technique. *Solid State Ion* **2007**, *178*, 195–205.
- (16) Liu, S.; White, M. G.; Liu, P. Mechanism of Oxygen Reduction Reaction on Pt(111) in Alkaline Solution: Importance of Chemisorbed Water on Surface. *J. Phys. Chem. C* **2016**, *120*, 15288–15298.
- (17) Bai, B.; Chen, Y.-T. Simulation of the Oxygen Reduction Reaction (ORR) Inside the Cathode Catalyst Layer (CCL) of Proton Exchange Membrane Fuel Cells Using the Kinetic Monte Carlo Method. *Energies* **2018**, *11*, 2529.
- (18) Gillespie, D. T. Exact Stochastic Simulation of Coupled Chemical Reactions. *J. Phys. Chem.* **1977**, *81*, 2340–2361.
- (19) Röder, F.; Braatz, R. D.; Krewer, U. Direct Coupling of Continuum and Kinetic Monte Carlo Models for Multiscale Simulation of Electrochemical Systems. *Comput. Chem. Eng.* **2019**, *121*, 722–735.
- (20) Schaefer, C.; Jansen, A. P. J. Coupling of Kinetic Monte Carlo Simulations of Surface Reactions to Transport in a Fluid for Heterogeneous Catalytic Reactor Modeling. *J. Chem. Phys.* **2013**, *138*, 054102.
- (21) Matera, S.; Maestri, M.; Cuoci, A.; Reuter, K. Predictive-Quality Surface Reaction Chemistry in Real Reactor Models: Integrating First-Principles Kinetic Monte Carlo Simulations into Computational Fluid Dynamics. *ACS Catal.* **2014**, *4*, 4081–4092.
- (22) de Morais, R. F.; Sautet, P.; Loffreda, D.; Franco, A. A. A Multiscale Theoretical Methodology for the Calculation of Electrochemical Observables from Ab Initio Data: Application to the Oxygen Reduction Reaction in a Pt(111)-based Polymer Electrolyte Membrane Fuel Cell. *Electrochim. Acta* **2011**, *56*, 10842–10856.
- (23) Quiroga, M. A.; Malek, K.; Franco, A. A. A Multiparadigm Modeling Investigation of Membrane Chemical Degradation in PEM Fuel Cells. *J. Electrochem. Soc.* **2016**, *163*, F59–F70.
- (24) Quiroga, M. A.; Franco, A. A. A Multi-Paradigm Computational Model of Materials Electrochemical Reactivity for Energy Conversion and Storage. *J. Electrochem. Soc.* **2015**, *162*, E73–E83.
- (25) Röder, F.; Braatz, R. D.; Krewer, U. Multi-Scale Modeling of Solid Electrolyte Interface Formation in Lithium-Ion Batteries. In *26th European Symposium on Computer Aided Process Engineering*; Kravanja, Z., Bogataj, M., Eds.; Elsevier: 2016; Vol. 38, pp 157–162.
- (26) Shinagawa, C.; Ushiyama, H.; Yamashita, K. Multiscale Simulations for Lithium-Ion Batteries: SEI Film Growth and Capacity Fading. *J. Electrochem. Soc.* **2017**, *164*, A3018–A3024.
- (27) Franco, A. A. Multiscale Modelling and Numerical Simulation of Rechargeable Lithium Ion Batteries: Concepts, Methods and Challenges. *RSC Adv.* **2013**, *3*, 13027–13058.
- (28) Chatterjee, A.; Vlachos, D. G. An Overview of Spatial Microscopic and Accelerated Kinetic Monte Carlo Methods. *J. Comput.-Aided Mater. Des.* **2007**, *14*, 253–308.
- (29) Gillespie, D. T. Approximate Accelerated Stochastic Simulation of Chemically Reacting Systems. *J. Chem. Phys.* **2001**, *115*, 1716–1733.
- (30) Zheng, Z.; Stephens, R. M.; Braatz, R. D.; Alkire, R. C.; Petzold, L. R. A Hybrid Multiscale Kinetic Monte Carlo Method for Simulation of Copper Electrodeposition. *J. Comput. Phys.* **2008**, *227*, 5184–5199.
- (31) Higham, D. J. Modeling and Simulating Chemical Reactions. *SIAM Rev.* **2008**, *50*, 347–368.
- (32) Resat, H.; Wiley, H. S.; Dixon, D. A. Probability-Weighted Dynamic Monte Carlo Method for Reaction Kinetics Simulations. *J. Phys. Chem. B* **2001**, *105*, 11026–11034.
- (33) Snyder, M.; Chatterjee, A.; Vlachos, D. Net-event Kinetic Monte Carlo for Overcoming Stiffness in Spatially Homogeneous and Distributed Systems. *Comput. Chem. Eng.* **2005**, *29*, 701–712.
- (34) Chatterjee, A.; Voter, A. F. Accurate Acceleration of Kinetic Monte Carlo Simulations through the Modification of Rate Constants. *J. Chem. Phys.* **2010**, *132*, 194101.
- (35) Lepage, H.; Kaminski-Cachopo, A.; Poncet, A.; le Carval, G. Simulation of Electronic Transport in Silicon Nanocrystal Solids. *J. Phys. Chem. C* **2012**, *116*, 10873–10880.
- (36) Kaiser, W.; Gösswein, M.; Gagliardi, A. Acceleration Scheme for Particle Transport in Kinetic Monte Carlo Methods. *J. Chem. Phys.* **2020**, *152*, 174106.
- (37) Dybeck, E. C.; Plaisance, C. P.; Neurock, M. Generalized Temporal Acceleration Scheme For Kinetic Monte Carlo Simulations Of Surface Catalytic Processes By Scaling The Rates Of Fast Reactions. *J. Chem. Theory Comput.* **2017**, *13*, 1525–1538.
- (38) Andersen, M.; Plaisance, C. P.; Reuter, K. Assessment of Mean-field Microkinetic Models for Co Methanation on Stepped Metal Surfaces Using Accelerated Kinetic Monte Carlo. *J. Chem. Phys.* **2017**, *147*, 152705.
- (39) Matera, S.; Schneider, W. F.; Heyden, A.; Savara, A. Progress in Accurate Chemical Kinetic Modeling, Simulations, and Parameter Estimation for Heterogeneous Catalysis. *ACS Catal.* **2019**, *9*, 6624–6647.
- (40) Li, J.; Maresi, I.; Lum, Y.; Ager, J. W. Effects of Surface Diffusion in Electrocatalytic CO<sub>2</sub> Reduction on Cu Revealed by Kinetic Monte Carlo Simulations. *J. Chem. Phys.* **2021**, *155*, 164701.
- (41) Jørgensen, M.; Grönbeck, H. Perspectives on Computational Catalysis for Metal Nanoparticles. *ACS Catal.* **2019**, *9*, 8872–8881.

(42) Lanzarini, E.; Antognazza, M. R.; Biso, M.; Ansaldo, A.; Laudato, L.; Bruno, P.; Metrangolo, P.; Resnati, G.; Ricci, D.; Lanzani, G. Polymer-Based Photocatalytic Hydrogen Generation. *J. Phys. Chem. C* **2012**, *116*, 10944–10949.

(43) Fumagalli, F.; Bellani, S.; Schreier, M.; Leonardi, S.; Rojas, H. C.; Ghadirzadeh, A.; Tullii, G.; Savoini, A.; Marra, G.; Meda, L.; Grätzel, M.; Lanzani, G.; Mayer, M. T.; Antognazza, M. R.; Di Fonzo, F. Hybrid Organic–inorganic H<sub>2</sub>-evolving Photocathodes: Understanding the Route Towards High Performance Organic Photoelectrochemical Water Splitting. *J. Mater. Chem. A* **2016**, *4*, 2178–2187.

(44) Antognazza, M. R.; Di Paolo, M.; Ghezzi, D.; Mete, M.; Di Marco, S.; Maya-Vetencourt, J. F.; Maccarone, R.; Desii, A.; Di Fonzo, F.; Bramini, M.; Russo, A.; Laudato, L.; Donelli, I.; Cilli, M.; Freddi, G.; Pertile, G.; Lanzani, G.; Bisti, S.; Benfenati, F. Characterization of a Polymer-Based, Fully Organic Prosthesis for Implantation into the Subretinal Space of the Rat. *Adv. Healthcare Mater.* **2016**, *5*, 2271–2282.

(45) Martino, N.; Feyen, P.; Porro, M.; Bossio, C.; Zucchetti, E.; Ghezzi, D.; Benfenati, F.; Lanzani, G.; Antognazza, M. R. Photo-thermal Cellular Stimulation in Functional Bio-polymer Interfaces. *Sci. Rep.* **2015**, *5*, 8911.

(46) Ghezzi, D.; Antognazza, M. R.; Dal Maschio, M.; Lanzarini, E.; Benfenati, F.; Lanzani, G. A Hybrid Bioorganic Interface for Neuronal Photoactivation. *Nat. Commun.* **2011**, *2*, 166.

(47) Mosconi, E.; Salvatori, P.; Saba, M. I.; Mattoni, A.; Bellani, S.; Bruni, F.; Santiago Gonzalez, B.; Antognazza, M. R.; Brovelli, S.; Lanzani, G.; Li, H.; Brédas, J.-L.; De Angelis, F. Surface Polarization Drives Photoinduced Charge Separation at the P3HT/Water Interface. *ACS Energy Lett.* **2016**, *1*, 454–463.

(48) Baranovskii, S. D. Theoretical Description of Charge Transport in Disordered Organic Semiconductors. *Phys. Status Solidi B* **2014**, *251*, 487–525.

(49) Ianovici, M.; Morf, J.-j. Calculation of the Potential Distribution Around a Charge or a Current in the Presence of Three Dielectric Media Using the Image Method. *IEEE T. Electr. Insul.* **1977**, *EI-12*, 165–170.

(50) Born, M.; von Karman, T. Über Schwingungen in Raumgittern. *Phys. Z.* **1912**, *13*, 297–309.

(51) Miller, A.; Abrahams, E. Impurity Conduction at Low Concentrations. *Phys. Rev.* **1960**, *120*, 745–755.

(52) Casalegno, M.; Raos, G.; Po, R. Methodological Assessment of Kinetic Monte Carlo Simulations of Organic Photovoltaic Devices: The Treatment of Electrostatic Interactions. *J. Chem. Phys.* **2010**, *132*, 094705.

(53) Kaiser, W.; Janković, V.; Vukmirović, N.; Gagliardi, A. Nonequilibrium Thermodynamics of Charge Separation in Organic Solar Cells. *J. Phys. Chem. Lett.* **2021**, *12*, 6389–6397.

## Recommended by ACS

### ScMiles2: A Script to Conduct and Analyze Milestoning Trajectories for Long Time Dynamics

Alfredo E. Cardenas, Ron Elber, *et al.*

OCTOBER 03, 2022  
JOURNAL OF CHEMICAL THEORY AND COMPUTATION

READ 

### Rare Event Kinetics from Adaptive Bias Enhanced Sampling

Dhiman Ray, Michele Parrinello, *et al.*

OCTOBER 04, 2022  
JOURNAL OF CHEMICAL THEORY AND COMPUTATION

READ 

### Force-Based Method to Determine the Potential Dependence in Electrochemical Barriers

Sudarshan Vijay, Karen Chan, *et al.*

JUNE 17, 2022  
THE JOURNAL OF PHYSICAL CHEMISTRY LETTERS

READ 

### Elastic Image Pair Method for Finding Transition States on Potential Energy Surfaces Using Only First Derivatives




Yangqiu Liu, Ming Lei, *et al.*


JUNE 30, 2022  
JOURNAL OF CHEMICAL THEORY AND COMPUTATION

READ 

Get More Suggestions >

# Utilizing Data-Driven Optimization to Automate the Parametrization of Kinetic Monte Carlo Models

Sign in/Register    
**RightsLink**



**Utilizing Data-Driven Optimization to Automate the Parametrization of Kinetic Monte Carlo Models**  
Author: Ioannis Kouroudis, Manuel Gößwein, Alessio Gagliardi  
Publication: The Journal of Physical Chemistry A  
Publisher: American Chemical Society  
Date: Jul 1, 2023  
*Copyright © 2023, American Chemical Society*

**PERMISSION/LICENSE IS GRANTED FOR YOUR ORDER AT NO CHARGE**

This type of permission/license, instead of the standard Terms and Conditions, is sent to you because no fee is being charged for your order. Please note the following:

- Permission is granted for your request in both print and electronic formats, and translations.
- If figures and/or tables were requested, they may be adapted or used in part.
- Please print this page for your records and send a copy of it to your publisher/graduate school.
- Appropriate credit for the requested material should be given as follows: "Reprinted (adapted) with permission from {COMPLETE REFERENCE CITATION}. Copyright {YEAR} American Chemical Society." Insert appropriate information in place of the capitalized words.
- One-time permission is granted only for the use specified in your RightsLink request. No additional uses are granted (such as derivative works or other editions). For any uses, please submit a new request.

If credit is given to another source for the material you requested from RightsLink, permission must be obtained from that source.

**BACK** **CLOSE WINDOW**

The following publication is reprinted with permission from ref. 1, *J. Phys. Chem. A* **2023**, 127 (28), 5967-5978. Copyright 2023 American Chemical Society (ACS).

# Utilizing Data-Driven Optimization to Automate the Parametrization of Kinetic Monte Carlo Models

Published as part of *The Journal of Physical Chemistry A virtual special issue "Machine Learning in Physical Chemistry Volume 2"*.

Ioannis Kouroudis,<sup>‡</sup> Manuel Gößwein,<sup>\*,‡</sup> and Alessio Gagliardi



Cite This: *J. Phys. Chem. A* 2023, 127, 5967–5978



Read Online

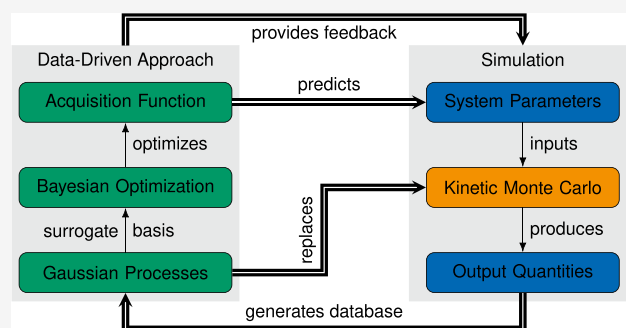
ACCESS |

Metrics & More

Article Recommendations

Supporting Information

**ABSTRACT:** Kinetic Monte Carlo (kMC) simulations are a popular tool to investigate the dynamic behavior of stochastic systems. However, one major limitation is their relatively high computational costs. In the last three decades, significant effort has been put into developing methodologies to make kMC more efficient, resulting in an enhanced runtime efficiency. Nevertheless, kMC models remain computationally expensive. This is in particular an issue in complex systems with several unknown input parameters where often most of the simulation time is required for finding a suitable parametrization. A potential route for automating the parametrization of kinetic Monte Carlo models arises from coupling kMC with a data-driven approach. In this work, we equip kinetic Monte Carlo simulations with a feedback loop consisting of Gaussian Processes (GPs) and Bayesian optimization (BO) to enable a systematic and data-efficient input parametrization. We utilize the results from fast-converging kMC simulations to construct a database for training a cheap-to-evaluate surrogate model based on Gaussian processes. Combining the surrogate model with a system-specific acquisition function enables us to apply Bayesian optimization for the guided prediction of suitable input parameters. Thus, the amount of trial simulation runs can be considerably reduced facilitating an efficient utilization of arbitrary kMC models. We showcase the effectiveness of our methodology for a physical process of growing industrial relevance: the space-charge layer formation in solid-state electrolytes as it occurs in all-solid-state batteries. Our data-driven approach requires only 1–2 iterations to reconstruct the input parameters from different baseline simulations within the training data set. Moreover, we show that the methodology is even capable of accurately extrapolating into regions outside the training data set which are computationally expensive for direct kMC simulation. Concluding, we demonstrate the high accuracy of the underlying surrogate model via a full parameter space investigation eventually making the original kMC simulation obsolete.



## INTRODUCTION

The term *Monte Carlo method* denotes a variety of different computer-aided algorithms which apply random numbers to obtain a numerical solution for real-world problems. A particular relevant subclass is kinetic Monte Carlo (kMC) simulations. They have been used extensively to model the dynamic behavior of a broad range of nondeterministic processes and systems such as crystal growth,<sup>1,2</sup> vacancy diffusion,<sup>3–5</sup> charge transport in disordered materials,<sup>6–9</sup> catalysis,<sup>10–12</sup> organic solar cells,<sup>13–16</sup> and electrochemical devices.<sup>17–20</sup> The popularity of kMC is due to several favorable intrinsic properties: (1) As a mesoscopic approach, kMC often provides a good trade-off in spatio-temporal resolution. (2) Individual particle-based processes can be included to investigate their time/frequency-dependent behavior. (3) Arbitrarily complex morphologies/geometries can be incorporated without facing potential convergence issues. (4) kMC

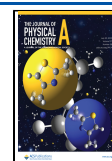
simulations are no mean-field approximations but inherently discrete and therefore enable to take into account local structural effects and the influence of particle–particle interactions.

However, one major limitation of kMC models is their comparatively high computational costs. Due to the stochastic nature of the kMC algorithm, a sufficient number of independent simulation runs is required to make reliable statements about the average time evolution of output quantities. For stationary quantities, this issue is at least

Received: April 14, 2023

Revised: June 16, 2023

Published: July 8, 2023



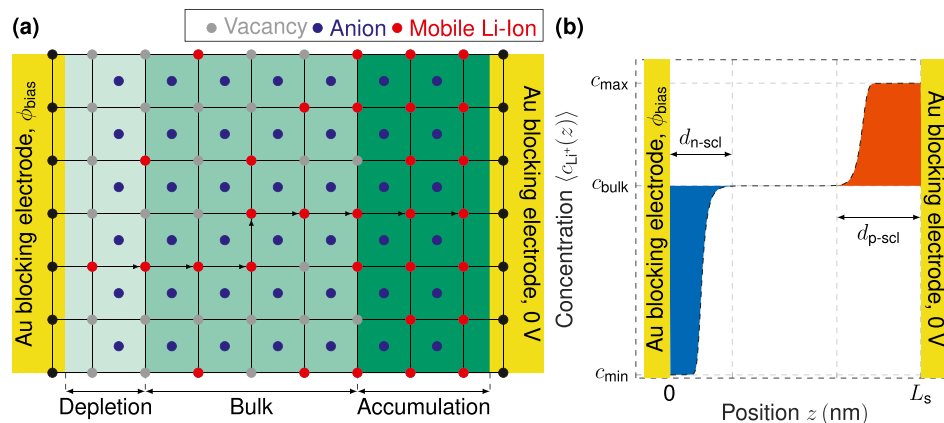


**Figure 1.** (a) Schematic representation of the kMC model for SCL formation in SSEs: Mobile Li ions are migrating toward the blocking electrode with a lower bias potential as indicated by the arrows. The mass transport is described by a thermally activated hopping mechanism between unoccupied vacancies. An immobile anionic background ensures the charge neutrality of the setup. The application of a bias potential,  $\phi_{bias}$ , eventually leads to the formation of a depletion and accumulation layer at the respective electrodes and a charge-neutral bulk region. (b) Schematic representation of a spatially averaged concentration profile to clarify the physical meaning of all input parameters and output quantities. The thicknesses of the depletion and accumulation are denoted as  $d_{n-scl}$  and  $d_{p-scl}$  respectively.

partially alleviated as it is sufficient to perform block-averaging over steady-state configurations of a single simulation run.<sup>14</sup> Another potential computational bottleneck arises from the inclusion of particle–particle interactions as their algorithmic complexity inherently scales as  $O(N^2)$ , where  $N$  is the number of particles. In the literature, there are numerous different approaches for the efficient treatment of particle–particle interactions ranging from the classical Ewald summation<sup>21,22</sup> with  $O(N^{3/2})$  to more advanced strategies such as the fast multipole method<sup>23,24</sup> with  $O(N)$ . Additional improvements in runtime efficiency can be achieved by applying precalculations<sup>14</sup> and local caching schemes.<sup>25</sup> Finally, large computational costs occur in kMC models which feature large time-scale disparities between two or more implemented processes.<sup>26</sup> The kMC algorithm naturally favors the execution of fast processes due to their higher relative probabilities. Consequently, a system with fast processes on time scale  $t_f$  and slow processes on time scale  $t_s \gg t_f$  requires approximately  $t_s/t_f$  kMC steps to sample the slow process only once. The insufficient sampling of slow processes is in particular problematic if they represent the critical transition to obtain certain system properties. The most common approach to bridge time-scale disparities is so-called temporal acceleration schemes.<sup>27–30</sup> In essence, such algorithms define (heuristic) criteria to artificially scale down the transition rates of fast processes to enable a more frequent sampling of the crucial slow processes.

Despite the aforementioned improvements and optimizations, kMC simulations remain computationally expensive. This is especially an issue when kMC models require systematic input parametrization. In particular, complex systems with several unknown input parameters would highly profit from a data-efficient parametrization scheme. Otherwise, kMC models remain restricted to a basic mechanistic analysis of the system dynamics. Exact reproduction of experimental results, device optimization, and material screening require streamlined guidance in input parameter search to become feasible.

So far, different methodologies have been proposed to parametrize kMC models. The most common choice in the

research community is still the straightforward parameter sweep<sup>31,32</sup> supported by a literature review for existing parameters.<sup>33</sup> Other methods automate parametrization via the utilization of a random walk<sup>34,35</sup> or a genetic algorithm such as particle swarm optimization.<sup>36</sup> More advanced approaches are based on replacing the kMC simulation by a corresponding surrogate model. For instance, Sestito et al. applied multiobjective Bayesian optimization (BO) in the context of a dimensionality reduction scheme for kMC diffusion models to calibrate the parameters of a simplified one-dimensional kMC diffusion model.<sup>37</sup> Another surrogate-assisted kinetic Monte Carlo method utilizes Gaussian processes (GPs) to predict the stationary shape in kinetically controlled copper electrodeposition.<sup>38</sup> However, the combination of BO and GPs in terms of a strong, data-driven surrogate model is yet relatively unexplored. It has been proven to be powerful in the field of compositional engineering,<sup>39,40</sup> for high throughput laboratories,<sup>41</sup> for the optimization of quantum cascade detectors,<sup>42</sup> and in kMC models for structural prediction.<sup>43</sup>

In this work, we present an innovative data-driven optimization pipeline to enable an automated parametrization of kinetic Monte Carlo models. Our methodology couples kinetic Monte Carlo simulations with a feedback loop consisting of Gaussian processes and Bayesian optimization, which enables a prediction-guided and data-efficient selection of input parameters. We generate a database from the output of fast-converging kMC simulations to train a cheap-to-evaluate surrogate model based on Gaussian processes. By combining the surrogate model with a system-specific acquisition function, we may apply Bayesian optimization for the systematic prediction of appropriate input parameters. Establishing a data-driven feedback loop considerably reduces the amount of trial simulations required for system parametrization and therefore facilitates an efficient utilization of kMC in particular for complex systems. The effectiveness of our data-driven kMC method is showcased via a process of growing industrial relevance: the formation of space-charge layers in solid-state electrolytes as it can be observed in all-solid-state batteries. Relying on an efficient parametrization framework, we require only 1–2 iterations to accurately

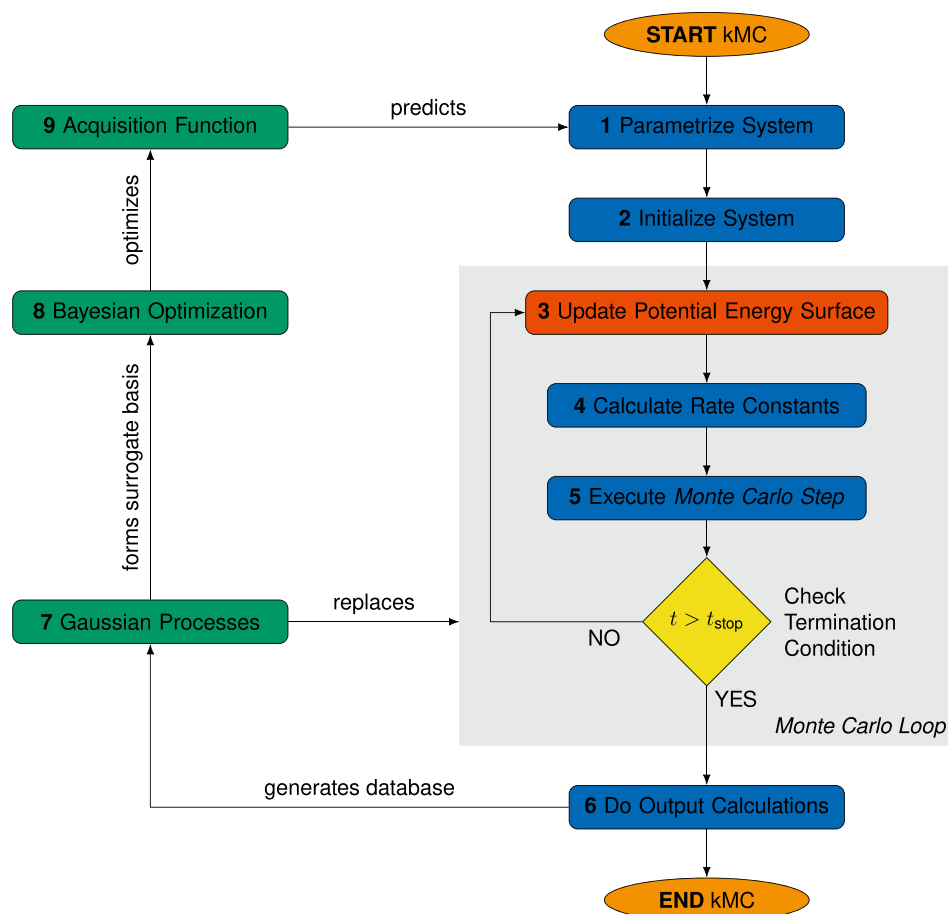


**Figure 2.** Schematic representation of the proposed computational pipeline including the original kinetic Monte Carlo algorithm on the right hand side as well as Gaussian processes and Bayesian optimization on the left hand side. Fast-converging kMC simulations are used to generate a database to train a cheap-to-evaluate surrogate model based on Gaussian processes. The surrogate model and a system-specific acquisition function form the two main components of Bayesian optimization, which is utilized to predict the system parametrization for the next simulation run. Depending on its accuracy the surrogate model may fully replace the original kMC simulation.

reconstruct the input parameters from different baseline simulations within the training data set. Further, we demonstrate that our methodology has remarkable extrapolation capabilities for regions outside the training data set. This feature is particularly relevant when the direct kMC simulation of such regions is computationally expensive. Finally, we perform a full parameter space investigation to emphasize the high accuracy of the underlying surrogate model which eventually may fully replace the original kMC simulation in many practical use cases. We are highly convinced that equipping kMC with a data-driven feedback loop provides a direct pathway for an efficient utilization of kinetic Monte Carlo models independent of the considered system.

## METHODS

To demonstrate the capabilities of our methodology, we consider a physically intuitive process from the field of electrochemistry: the space-charge layer (SCL) formation in solid-state electrolytes (SSEs) under blocking conditions as it occurs in all-solid-state batteries (ASSB). In recent years, ASSBs have gained increasing attention as a promising substitute for traditional Li-ion batteries due to their potentially longer lifespan, higher energy density, and enhanced safety.<sup>44,45</sup> We have recently developed a simple yet predictive kMC model to simulate the mass-transport

phenomenon occurring in SSEs under blocking conditions;<sup>46</sup> see Figure 1a for a schematic representation of the simulation setup. The model was able to reproduce the quantitative trends in SCL thicknesses (accumulation and depletion layer) as previously determined by electrochemical impedance spectroscopy<sup>47</sup> and spectroscopic ellipsometry.<sup>48</sup>

First, a compact summary of our kMC model for SCL formation in SSEs is provided to clarify the physical meaning of all input parameters and output quantities. Then, we outline successively the complete computational pipeline of our data-driven kMC approach: (1) the standalone kMC algorithm, (2) Bayesian optimization, and (3) Gaussian processes. Each step of the pipeline is first described in an abstract fashion and subsequently concretized by means of our electrochemical showcase. A flowchart of the complete computational pipeline is illustrated in Figure 2.

**Space-Charge Layer Formation in Solid-State Electrolytes.** In general, the mass transport of Li ions in SSEs can be captured by a thermally activated hopping mechanism between unoccupied vacancies in a crystal lattice.<sup>49,50</sup> The crystal structure itself consists of *immobile* anions, cations, and vacancies as well as *mobile* cations. The kMC simulation only considers the transport of mobile Li<sup>+</sup> within a three-dimensional regular grid of vacancies with lattice constant  $a_L$ ; see Figure 1a for a schematic representation. Note that the



implemented grid does not resemble the actual morphology of the SSE sample but rather must be regarded as a simple lattice gas model. In this framework, SCL formation is caused by the mere redistribution of mobile Li ions driven by an applied bias potential,  $\phi_{\text{bias}}$ . Immobile Li ions and their respective counteranions are neglected due to local electrostatic neutrality. Mobile Li ions are electrostatically compensated by a corresponding homogeneous anionic background. The local concentration of mobile cations,  $c_{\text{Li}}^+(x, y, z)$ , including its physical boundary values, strongly impacts the thicknesses of the resulting accumulation and depletion layer. In this context, the model distinguishes three different cases (cf. Figure 1b):

1. The *bulk concentration*,  $c_{\text{bulk}}$ , corresponding to the equilibrium state encountered in an electroneutral lattice where all mobile cations are compensated by their respective immobile anions.
2. The *maximum concentration*,  $c_{\text{max}}$ , which defines the upper limit of mobile cations in a fully occupied lattice as encountered in the accumulation layer.
3. The *minimum concentration*,  $c_{\text{min}}$ , which defines the lower limit of mobile cations in a fully depleted lattice as encountered in the depletion layer.

Therefore,  $c_{\text{Li}}^+(x, y, z)$  may vary between  $c_{\text{min}}$  and  $c_{\text{max}}$  reaching the equilibrium value  $c_{\text{bulk}}$  within the bulk of the SSE. The upper and lower concentration limits determine the degree of asymmetry with respect to accumulation and depletion layer thickness. In the scope of this model, the maximum concentration is imposed by the reciprocal volume of a unit cell,  $c_{\text{max}} = a_{\text{L}}^{-3}$ , whereas the minimum concentration is naturally set to  $c_{\text{min}} = 0$ . Analogously to the liquid electrolyte (cf. Debye length), the strength of electrostatic screening also impacts the thicknesses of the resulting SCLs. Here, we control the magnitude of this effect by the relative permittivity of the bulk SSE,  $\epsilon_r$ . Note that our model does not include spatial variations in permittivity induced by either depletion or accumulation of Li ions. For a detailed discussion of the model, see ref 46.

Overall, our kMC model requires 4 physically consistent input parameters:  $c_{\text{bulk}}$ ,  $c_{\text{max}}$ ,  $\epsilon_r$ , and  $\phi_{\text{bias}}$ . For a given input parametrization, the kMC simulation generates a stationary three-dimensional concentration profile,  $c_{\text{Li}}^+(x, y, z)$ , from which the depletion and accumulation layer thicknesses ( $d_{\text{n-scl}}$  and  $d_{\text{p-scl}}$ , respectively) as well as their ratio,  $\mathcal{D} = d_{\text{n-scl}}/d_{\text{p-scl}}$ , may be extracted. Additionally, Poisson's equation is utilized to transform  $c_{\text{Li}}^+(x, y, z)$  into a corresponding potential profile to determine the potential within the bulk of the SSE, denoted as  $\phi_{\text{bulk}}$ . To ensure comparability between different parametrizations, we rather consider the potential ratio  $\mathcal{V} = \phi_{\text{bulk}}/\phi_{\text{bias}}$  than absolute values. A summary of all input parameters and output quantities is presented in Table 1.

**Kinetic Monte Carlo Method.** The kinetic Monte Carlo method is a numerical algorithm to sequentially propagate a

system through different states within its configuration space. Fundamental contributions to the modern kMC algorithm have been made by Bortz et al.<sup>51</sup> and Gillespie.<sup>52,53</sup> In general, the kMC method is based on *coarse-graining* the system dynamics into a set of long-term states  $\{i\}$ , which are interconnected by discrete transitions. Given an arbitrary initial state  $i$ , the system may transition into a set of potential final states  $\{j\}$ . Each transition  $i \rightarrow j$  is linked to a transition rate,  $k_{ij}$ , which is proportional to the relative execution probability,  $p_{ij}$ , of the underlying physical process

$$p_{ij} = \frac{k_{ij}}{k_{\text{tot}}} = \frac{k_{ij}}{\sum_j k_{ij}} \quad (1)$$

where  $k_{\text{tot}}$  is the cumulative transition rate. The transition rates are a subset of the input parameters required by the kMC model. Usually, they are taken from experimental measurements or underlying physical models. The stochastic time evolution of the system is computed in the so-called *Monte Carlo step*. In each simulation step, two uniform random numbers  $r_1, r_2 \in (0,1)$  are drawn to determine which transition,  $\mu$ , is executed and how much simulated time,  $\tau$ , is elapsed before the execution of the transition. In the  $n$ -fold or direct method as outlined in ref 53, we may use  $r_1$  to pick  $\mu$  from the set  $\{p_{ij}\}$  via

$$\sum_{j=1}^{\mu-1} p_{ij} < r_1 \leq \sum_{j=1}^{\mu} p_{ij} \quad (2)$$

and  $r_2$  to calculate a corresponding time step

$$\tau = -\frac{\log(r_2)}{k_{\text{tot}}} \quad (3)$$

Based on (2) and (3), the system state  $i \rightarrow j$  and the simulated time  $t_i \rightarrow t_j = t_i + \tau$  are updated. To perform the next Monte Carlo step, the transition rates must be recomputed in the new system state. The stochastic time evolution of the investigated system results from repeated execution of the outlined procedure often denoted as the so-called *Monte Carlo loop*. The simulation is terminated when a user-defined condition is fulfilled, e.g., a stationary state is reached or the simulated time exceeds a certain predefined threshold,  $t \geq t_{\text{stop}}$ .

To simulate the SCL formation in SSEs, the general kMC algorithm has to be adjusted accordingly; see the right hand side of Figure 2 for a detailed flowchart, which results in 6 fundamental steps:

1. *System Parametrization*: Selection of appropriate input parameters to generate given output quantities.
2. *System Initialization*: Generation of a discrete grid with geometrical and physical information (e.g., positions and static energies); population of the grid with mobile  $\text{Li}^+$  according to  $c_{\text{bulk}}$ .
3. *Update of the Potential Energy Surface*: Recalculation of Coulomb interactions of each Li ion with all other mobile cations according to current system configuration.
4. *Calculation of Transition Rates*: Computation of the local hopping rates of each Li ion to all unoccupied nearest-neighbor vacancies based on the updated potential energy surface.
5. *Execution of the Monte Carlo Step*: Generation of two uniform random numbers to select an  $\text{Li}^+$ -hopping

**Table 1. Summary of Input Parameters and Output Quantities**

input parameters		output quantities	
$c_{\text{bulk}}$	bulk concentration	$d_{\text{n-scl}}$	depletion layer thickness
$c_{\text{max}}$	maximum concentration	$d_{\text{p-scl}}$	accumulation layer thickness
$\epsilon_r$	bulk permittivity	$\mathcal{V}$	potential ratio
$\phi_{\text{bias}}$	bias potential	$\mathcal{D}$	thickness ratio

transition via (2) and a corresponding time step via (3). Return to 3 if simulated time  $t$  is less than steady-state time  $t_{\text{stop}}$ .

6. **Output Calculation:** Calculation of output quantities (cf. Table 1) from the raw tracking data of the kMC simulation.

For the given system, the regular update of the potential energy surface (step 3) may impose a computational bottleneck. The crucial factor is the number of mobile Li ions,  $N$ , imposed by the chosen value for  $c_{\text{bulk}}$ . While the computational effort connected to the recalculation of Coulomb energies can be optimized to  $O(N)$  (cf. ref 46), the simulation times for  $c_{\text{bulk}} > 10^{19} \text{ cm}^{-3}$  become practically unfeasible. For  $c_{\text{bulk}} \in [10^{17} \text{ cm}^{-3}, \dots, 10^{20} \text{ cm}^{-3}]$ , the corresponding linearly increasing simulation times  $t_{\text{sim}} \in [1 \text{ h}, \dots, 1000 \text{ h}]$  can be obtained. Thus, it would be highly desirable to replace simulations with high particle densities by an accurate surrogate model, which has been trained via a data set generated from the output of fast-converging kMC runs.

In the scope of this work, we constructed a data set from the output of 279 kMC simulations from which 153 were conducted in our reference study.<sup>46</sup> Table 2 presents a

**Table 2. Summary of the Input Parameters Used to Generate the Original Data Set<sup>a</sup>**

input parameter	values
$c_{\text{bulk}}$ ( $\text{cm}^{-3}$ )	$5 \times 10^{17}$ , $3 \times 10^{18}$ , $10^{19}$
$c_{\text{max}}$ ( $c_{\text{bulk}}$ )	1.25, 1.5, 2
$\epsilon_r$	100, 677, 1400
$\phi_{\text{bias}}$ (V)	0.05, 0.1, 0.2, 0.25, 0.5, 0.75, 1, 1.5, 2.5, 3.5, 4.5

<sup>a</sup>Note that only a subset of the possible parameter permutations was simulated.

summary of the input parameters to generate this original data set. From the additional data points, 106 were gained from fast-converging simulations with  $c_{\text{bulk}} \leq 4 \times 10^{18} \text{ cm}^{-3}$  and another 5 for  $c_{\text{bulk}} = 1 \times 10^{19} \text{ cm}^{-3}$ . The remaining 15 data points were generated for  $c_{\text{bulk}} = 1 \times 10^{20} \text{ cm}^{-3}$  to assess the extrapolative qualities of the surrogate model.

**Bayesian Optimization.** In a majority of cases, the parametrization of kMC models relies on a combination of literature review, physical intuition, and brute force (e.g., parameter sweeps). The main goal of this work is to make the process of input parametrization *prediction-guided* via an efficient Bayesian optimization scheme; see step 8 in Figure 2. BO is a global optimization pipeline, which has proven to be both data-efficient and robust in non-convex/concave problems. Considering an arbitrary optimization problem with a costly-to-query target quantity such as time-consuming experimental measurements or computationally expensive *ab initio* simulations, Bayesian optimization is among the most suitable algorithms as it requires only a minimal amount of target querying and may reach a *global* minimum. The two main components of BO are a surrogate model and an acquisition function; see steps 7 and 9 in Figure 2. The surrogate model can be any probabilistic algorithm that provides a prediction and an uncertainty quantification, for instance, Gaussian processes (GPs), deep GPs, or Bayesian neural networks. The acquisition function defines the function that will be directly optimized. It should be as convex/concave as possible, computationally efficient to evaluate and incorporate both the prediction of the original process and the uncertainty of the

model on this point. A very intuitive example of an acquisition function is given by the so-called upper confidence bound (UCB)

$$\mathbf{x}_{\text{opt}} = \arg \max_{\mathbf{x}_{\text{opt}}} \mu(\mathbf{x}_{\text{opt}}) + \epsilon \sigma(\mathbf{x}_{\text{opt}}) \quad (4)$$

where  $\mu$  and  $\sigma$  are the predictions for the mean and standard deviation, respectively, of the predictor on the corresponding point  $\mathbf{x}_{\text{opt}}$  and  $\epsilon$  is a trade-off parameter. The parameter  $\epsilon$  is directly linked to the *exploration* and *exploitation* phase of the optimization process. In the beginning of the process, the model does not have enough information about the whole parameter space. Thus, it is more important to acquire observations which improve the model than to optimize the original problem. This initial stage is denoted as *exploration* and becomes manifest in high values of  $\epsilon$ . As the model improves progressively, the focus of the optimization process begins to shift on optimal points. This stage is denoted as *exploitation* and reflected by decreasing values of  $\epsilon$ . In general, there are numerous potential acquisition functions with different convexity properties and prioritizations. In this work, the so-called expected improvement acquisition function was utilized

$$EI(x) = \mathbb{E} \max(f(\mathbf{x}) - f(\mathbf{x}^+), 0) \quad (5)$$

where the superscript + denotes the best point so far and the function  $f$  is the trained surrogate model based on Gaussian processes. A complete derivation of eq (5) can be found in ref 54 along with resources on additional acquisition functions. For completeness, we note that other acquisition functions such as probability of improvement and UCB were also implemented but yielded inferior results compared to expected improvement.

The generic acquisition function outlined above has to be modified to match with the requirements of the investigated electrochemical process. Our goal is to reconstruct the depletion layer thickness as a function of the applied bias potential, that is,  $d_{\text{n-scl}}(\phi_{\text{bias}})$ . For this purpose, we define the objective function

$$\mu_{\text{obj}} = -\frac{1}{N_{\phi_{\text{bias}}}} \sum_{\phi_{\text{bias}}} \frac{|d_{\text{n-scl}}^*(\phi_{\text{bias}}) - d_{\text{n-scl}}(\phi_{\text{bias}})|}{d_{\text{n-scl}}(\phi_{\text{bias}})} \quad (6)$$

where the superscript \* denotes the mean of the predicted values and  $N_{\phi_{\text{bias}}}$  is the number of investigated potential points. In principle, we are considering a minimization problem, as we wish to minimize the distance between the predicted values and a baseline. However, in the context of Bayesian optimization, it is more intuitive to reformulate the task as a maximization problem indicated by the negative sign in (6). The corresponding standard deviation is given by

$$\sigma_{\text{obj}} = \frac{1}{N_{\phi_{\text{bias}}}} \sum_{\phi_{\text{bias}}} \frac{\sigma(\phi_{\text{bias}})}{d_{\text{n-scl}}(\phi_{\text{bias}})} \quad (7)$$

where  $\sigma(\phi_{\text{bias}})$  corresponds to the standard deviation of a prediction with respect to a specific value of  $\phi_{\text{bias}}$ . The final form of the acquisition function can be constructed by combining (6) and (7) with (5)

$$EI = \begin{cases} (f_{\text{obj}}(\mathbf{x}) - f(\mathbf{x}^+) - \xi)\Phi(\mathbf{Z}) & \text{if } \sigma_{\text{obj}}(\mathbf{x}) \geq 0 \\ + \sigma_{\text{obj}}(\mathbf{x})(\mathbf{Z}) & \\ 0 & \text{if } \sigma_{\text{obj}}(\mathbf{x}) = 0 \end{cases} \quad (8)$$

where

$$f(x) = \begin{cases} \frac{f_{\text{obj}}(\mathbf{x}) - f(\mathbf{x}^+) - \xi}{\sigma_{\text{obj}}(\mathbf{x})} & \text{if } \sigma_{\text{obj}}(\mathbf{x}) \geq 0 \\ 0 & \text{if } \sigma_{\text{obj}}(\mathbf{x}) = 0 \end{cases} \quad (9)$$

with  $\phi$  and  $\Phi$  denoting the probability and the cumulative distribution functions, respectively. The optimization of the acquisition function is accomplished by generating 100 000 random points and selecting those which maximizes the acquisition function. To further ensure accuracy and efficiency, the values of these random points were constrained through physical intuition. The trade-off factor was initially set to 1 and gradually decreased. Note that this procedure is orders of magnitude faster than a kMC simulation and, thus, even high numbers of points can be processed in a few seconds on a single core.

**Gaussian Processes.** As outlined above, Bayesian optimization requires a robust and computationally efficient surrogate model. In the scope of this work, we selected Gaussian processes—a data-driven stochastic prediction algorithm that models predictions as Gaussian distributions whose parameters are determined by the distance to already measured samples. Therefore, the algorithm inherently provides an uncertainty quantification for its predictions, which can be crucial in applications with small data sets. Gaussian processes rely on the fundamental assumption that a true process  $y$  can be modeled by a model  $f$  on a set of points  $\mathbf{X}$  using a multivariate Gaussian distribution centered around zero, denoted as the so-called prior distribution

$$f|\mathbf{X} \sim \mathcal{N}(0, \mathbf{K}_{\mathbf{x},\mathbf{x}}) \quad (10)$$

where  $\mathbf{K}_{\mathbf{x},\mathbf{x}}$  is the covariance matrix which encodes the correlation between two points and is defined by a user-chosen kernel function. Additionally, the likelihood of the observations given by the model can be represented as a noisy normal distribution around the model predictions

$$y|f \sim \mathcal{N}(f, \sigma^2 I) \quad (11)$$

Equations (10) and (11) can be manipulated to create the so-called posterior distribution, which will be used for prediction and is given by

$$P(\theta|\mathbf{D}) = \frac{P(\mathbf{D}|\theta)P(\theta)}{P(\mathbf{D})} \quad (12)$$

where  $\mathbf{D}$  corresponds to the acquired observations and  $\theta$  denotes the model parameters. Solving the above process analytically yields

$$\mu_{\mathbf{x}^*} = \mathbf{K}_{\mathbf{x}^*,\mathbf{x}}^{-1}[\mathbf{K}_{\mathbf{x},\mathbf{x}} + \sigma^2 I]^{-1} \mathbf{y} \quad (13a)$$

$$\sigma_{\mathbf{x}^*}^2 = \mathbf{K}_{\mathbf{x}^*,\mathbf{x}^*} - \mathbf{K}_{\mathbf{x}^*,\mathbf{x}}[\mathbf{K}_{\mathbf{x},\mathbf{x}} + \sigma^2 I]^{-1} \mathbf{K}_{\mathbf{x},\mathbf{x}^*} \quad (13b)$$

where the points for prediction and training are denoted with and without the superscript \*, respectively. One crucial aspect is given by the parameter values,  $\theta$ , of the kernel function  $\mathbf{K}$ . In

principle, the prior distribution must be defined in such a way that it is uncorrelated with the observations. However, in practice, better results are achieved if the kernel parameters are chosen to maximize the log marginal likelihood (LML)

$$\log p(\mathbf{y}|\mathbf{X}, \theta) = -\frac{1}{2} \mathbf{y}^T [\mathbf{K}_{\mathbf{x},\mathbf{x}} + \sigma^2 \mathbf{I}]^{-1} \mathbf{y} - \frac{1}{2} \log[\mathbf{K}_{\mathbf{x},\mathbf{x}} + \sigma^2 \mathbf{I}] - \frac{N}{2} \log(2\pi) \quad (14)$$

for a given number of points  $N$ . Here, the first term captures the quality of the model fit, the second term indicates that complex models are less probable, and the third term expresses that points become less probable in larger data sets. In essence, the LML maximization attempts to define the simplest model that describes the observations. Note that a complete mathematical analysis of Gaussian processes and their derivation is beyond the scope of this work. A comprehensive description can be found in ref 55.

In this work, the kernel was the sum of two multilayer perceptron (MLP) kernels<sup>56</sup> whose parameters were trained by maximizing the LML. Note that the kernel itself is *not* a neural network. However, it has been shown that—under certain conditions—certain covariance functions can cause the GPs to converge to the limit of a neural network with an infinite number of layers. Our particular implementation of the kernel mimicks rectified linear activations (ReLU), but the method family is not limited to it. Unfortunately, the detailed theory of the method is beyond the scope this paper. A complete treatment can be found in a pertinent literature;<sup>56</sup> further publications covering the topic are given by refs 57–60. There is no immediate reason to assume that this kernel outperforms other kernel functions such as the radial basis kernel (RBF). Nevertheless, trial and error showed that in this problem the results were superior both in accuracy and physicality of results.

## RESULTS AND DISCUSSION

If not stated otherwise, we evaluate the effectiveness of our data-driven kMC method exemplarily by optimizing for the thickness of the depletion layer,  $d_{\text{n-scl}}$ , as it is a crucial quantity for ASSB performance. First, we demonstrate the importance of data preprocessing for the predictor quality. Then, we analyze the data efficiency of our approach by discussing the evolution of the mean and median relative error as a function of the training sample number. Subsequently, we consider different scenarios of *inverse problem solution*, and specifically, we utilize our method to reconstruct the input parameters from different baseline simulations inside *and* outside of the training data set. By accurately solving the inverse problem outside of the training data set, we showcase the remarkable and computationally inexpensive extrapolation capabilities of our data-driven optimization approach. With the accuracy and efficiency of the method proven, we proceed by performing a full parameter space investigation of different output quantities for a wide range of  $c_{\text{bulk}}$  and  $c_{\text{max}}$ . The results of the parameter space investigation clearly indicate that expensive kMC simulations can be replaced readily by a cheap-to-evaluate surrogate model based on Gaussian processes. Concluding, we outline potential routes for future improvements.

**Data Preprocessing.** To emphasize the importance of data preprocessing, we first analyze the effect of target normalization on the predictor quality; see Figure 3. It is

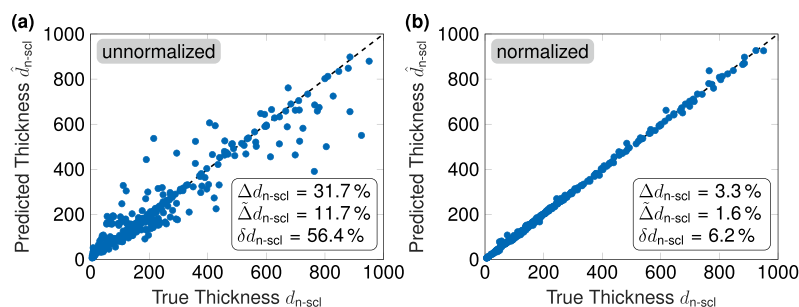


**Figure 3.** Effect of target normalization on the predictor quality: (a) un-normalized and (b) normalized target quantities. All predictions were generated by a 270-fold validation to guarantee a high predictor quality. Strong deviations from  $x = y$  indicate a diminishing predictor quality. The insets quantify the mean relative error  $\Delta d_{n-scl}$ , the median relative error  $\bar{\Delta} d_{n-scl}$ , and the relative standard deviation  $\delta d_{n-scl}$  with respect to the full data set.

important to note that *input* normalization is necessarily required as an un-normalized input result in nonpositive definite covariance matrices. Apparently, un-normalized target data induce a strongly underperforming predictor; see Figure 3a. The large range of output values causes the gradients to take vastly different values, which in turn skews the actual error. As a direct consequence, the algorithm implicitly prioritizes certain ranges over others. This effect can be mitigated by normalizing the target data. A straightforward solution is a simple min–max normalization to constrain all target values between 0 and 1. The normalization of target quantities results in excellent predictor accuracy which becomes manifest in almost vanishing error characteristics; see Figure 3b.

**Data Efficiency.** A high predictor quality is ultimately only a necessary criterion for the effectiveness of any data-driven approach. Simultaneously, we require that high predictor accuracy comes along with sufficiently high data efficiency. Therefore, it is crucial to increase the impact of every newly added point to the data set. For instance, in the current system, the effect of the applied bias potential,  $\phi_{bias}$ , is almost trivially learned by the algorithm. Consequently, we can considerably reduce the data load by undersampling  $\phi_{bias}$ . As a matter of fact, this strategy leads to a significant increase of the predictor accuracy over the naive sampling; see Table 3. Apparently, changes in the other input parameters ( $c_{bulk}$ ,  $c_{max}$  and  $\epsilon_r$ ) have a

more complex effect on the depletion layer thickness (e.g., linear vs nonlinear behavior). Thus, a more efficient algorithm training can be achieved by putting the focus of data acquisition on the latter input parameters. As an additional metric for the model quality, we calculated the so-called model calibration; see Table 3. The calibration of a model shows how many predicted points fall within  $2\sigma$  of the true value. Fewer than 95% of the test points falling within this credible interval is a sign of overfitting or overconfident predictions. Vice versa, more than 95% of the test points falling within the  $2\sigma$  interval is a sign of underconfident predictions. The model calibration strongly supports our previous statement that undersampling  $\phi_{bias}$  leads to an increase in predictor quality and a simultaneous decrease in data load.

To further rationalize the data efficiency of our methodology, we analyze the mean and median relative errors  $\Delta d_{n-scl}$  and  $\bar{\Delta} d_{n-scl}$  respectively, as a function of the training sample number  $N_s$ ; see Figure 4. The full error progression in Figure 4a illustrates that  $\Delta d_{n-scl}$  exhibits strong fluctuations for  $N_s \leq 50$  (up to over 300%), whereas  $\bar{\Delta} d_{n-scl}$  steadily decreases in the same region. From a practical point of view, it is of high relevance to know for which amount of training samples the relative error falls below a certain predefined threshold, e.g., 10%, as illustrated in Figure 4b. In the present study, the median and mean relative errors remain consistently below 10% for only 50 and 100 training samples, respectively. Remarkably, the original data set as generated in ref 46 would have been sufficient to achieve the given level of accuracy. Further, please note that the presented errors relate to the *entire* parameter space, that is, constraining the investigation to a smaller parameter subset would have decreased the number of required training samples even more.

**Inverse Problem Solution.** With the predictor quality and data efficiency proven, we may proceed our analysis by considering different scenarios of so-called inverse problem solution. In general, an inverse problem describes the process of reconstructing system input from observed output. We may transfer this universal concept to the present case study by recovering a set of input parameters ( $c_{bulk}$ ,  $c_{max}$ ,  $\epsilon_r$ ) from a given output quantity (e.g.,  $d_{n-scl}$ ). In the following, we will demonstrate the capabilities of our pipeline by reconstructing suitable input parameters for three different baseline simulations of  $d_{n-scl}$ . For the first two test cases, the input parameters of the baseline were chosen to reside inside the training set. On the other hand, the baseline for the third test case was generated with input parameters *outside* the training set. We show that for all three test cases, the algorithm

**Table 3.** Comparison of Full and Refined Potential Exploration in Terms of the Relative Mean and Median Errors as well as Model Calibration  $\Delta d_{n-scl}$ ,  $\bar{\Delta} d_{n-scl}$ , and  $\Delta_{95} d_{n-scl}$ , Respectively, for Different Training Sample Numbers  $N_s$ <sup>a</sup>

$N_s$	full exploration (naive sampling)			refined exploration (undersampling)		
	$\Delta d_{n-scl}$ (%)	$\bar{\Delta} d_{n-scl}$ (%)	$\Delta_{95} d_{n-scl}$ (%)	$\Delta d_{n-scl}$ (%)	$\bar{\Delta} d_{n-scl}$ (%)	$\Delta_{95} d_{n-scl}$ (%)
10	198.35	53.24	40.86	164.61	49.23	80.93
20	121.10	41.85	55.55	80.58	40.23	87.41
50	76.74	22.74	84.22	27.07	11.84	89.2
70	42.21	16.53	86.73	12.26	5.8	91.37
100	33.5	11.25	91.75	9.35	4.35	94.24
150	19.12	7.21	90.68	5.71	2.81	96.01
200	17.55	4.99	92.11	4.95	2.36	96.04
250	12.83	4.15	93.18	3.84	1.77	96.4

<sup>a</sup>Both evaluations were performed multiple times with different random splits to generate a realistic view of accuracy.

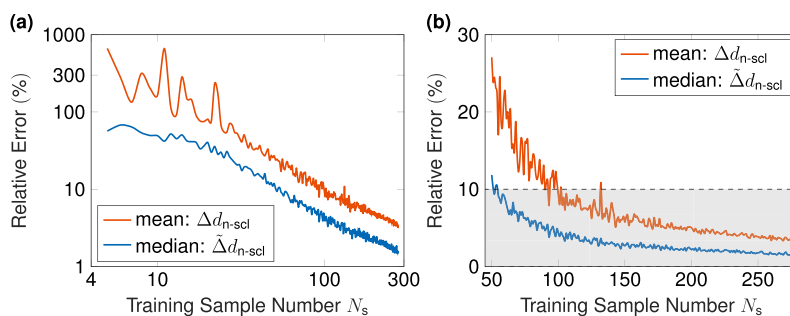


**Figure 4.** Mean and median relative errors  $\Delta d_{n\text{-scl}}$  and  $\tilde{\Delta} d_{n\text{-scl}}$ , respectively, as a function of the training sample number  $N_s$ : (a) full error progression on a log–log scale and (b) the threshold region for which both errors fall below 10%. The median and mean relative errors require only 50 and 100 training samples, respectively, to remain consistently below the threshold of 10%.

accurately and efficiently reproduces the baseline for the complete range of potential values. For all three test cases, the baseline values were removed from the data set to avoid biasing the pipeline.

**Fitting Inside the Training Set.** First, we showcase the validity of our method by reconstructing the reference parametrization determined in ref 46 via a heuristic parameter sweep; see the first row in Table 4 for a parameter comparison

**Table 4.** Comparison of Parametrizations for the Baseline and the Prediction-Guided Simulation Runs Denoted as  $B|n = 0$  and  $P|n = x$  with  $x = 1, 2$ , Respectively<sup>a</sup>

input parameter	baseline ( $B n = 0$ )	prediction ( $P n = 2$ )	rel. deviation $\langle \Delta d_{n\text{-scl}} \rangle$ (%)
$c_{\text{bulk}}$ ( $\text{cm}^{-3}$ )	$4.5 \times 10^{18}$	$2.9 \times 10^{18}$	
$c_{\text{max}}$ ( $c_{\text{bulk}}$ )	1.54	1.62	1.05
$\epsilon_r$	677	695	
input parameter	baseline ( $B n = 0$ )	prediction ( $P n = 1$ )	rel. deviation $\Delta d_{n\text{-scl}}$ (%)
$c_{\text{bulk}}$ ( $\text{cm}^{-3}$ )	$2 \times 10^{18}$	$3 \times 10^{18}$	
$c_{\text{max}}$ ( $c_{\text{bulk}}$ )	2	2.13	0.83
$\epsilon_r$	400	593	
input parameter	baseline ( $B n = 0$ )	prediction ( $P n = 1$ )	rel. deviation $\Delta d_{n\text{-scl}}$ (%)
$c_{\text{bulk}}$ ( $\text{cm}^{-3}$ )	$1 \times 10^{20}$	$1.15 \times 10^{20}$	
$c_{\text{max}}$ ( $c_{\text{bulk}}$ )	1.25	1.6	4.59
$\epsilon_r$	50	49	

<sup>a</sup>The first two rows correspond to baseline fitting inside the full and reduced training data set (cf. Figure 5a,b, respectively), whereas the third row corresponds to baseline fitting outside the reduced training data set (cf. Figure 5c).  $\langle \Delta d_{n\text{-scl}} \rangle$  denotes the average relative deviation of the potential-dependent mean values of  $\Delta d_{n\text{-scl}}$ .

and Figure 5a for the corresponding  $d_{n\text{-scl}}(\phi_{\text{bias}})$  profiles. In this scenario, the model was trained on the full data set of 279 points. Without any human intuition, we require only 2 prediction-guided iterations to obtain perfectly overlapping  $d_{n\text{-scl}}(\phi_{\text{bias}})$  profiles, which are quantified by an average relative deviation of approximately of 1%.

Next, we demonstrate the strength of our data-driven pipeline by training the model on a subset of the complete data set, specifically only 165 of 279 data points and  $c_{\text{bulk}} \leq 3 \times 10^{18} \text{ cm}^{-3}$ . Here, low values of  $c_{\text{bulk}}$  guarantee that the data set was generated solely from *fast-converging* kMC runs. Further, we apply the sparse potential sampling method as outlined in the previous section about data efficiency. To test the reduced data set, we generated an artificial baseline with a parametrization summarized in the second row of Table 4. After only one round of optimization, baseline and prediction-guided  $d_{n\text{-scl}}(\phi_{\text{bias}})$  profiles perfectly match; see Figure 5b. These findings underline that meaningful results can be obtained from quick and strategic sampling. The simulation results for baseline fitting inside the full and reduced training data set are summarized in Tables S1 and S2 in the Supporting Information, respectively.

**Fitting Outside the Training Set.** The results from baseline fitting within the training data set prove the effectiveness and validity of our methodology. However, the crucial feature of our data-driven methodology is its capability to accurately extrapolate into regions outside of the training data set. In the present case study, we selected a corresponding baseline with a very large particle density,  $c_{\text{bulk}} = 10^{20} \text{ cm}^{-3}$ ; see third row in Table 4 for the full parametrization. This results in a simulation setup containing several thousand mobile Li ions ( $\approx 8000$ ).

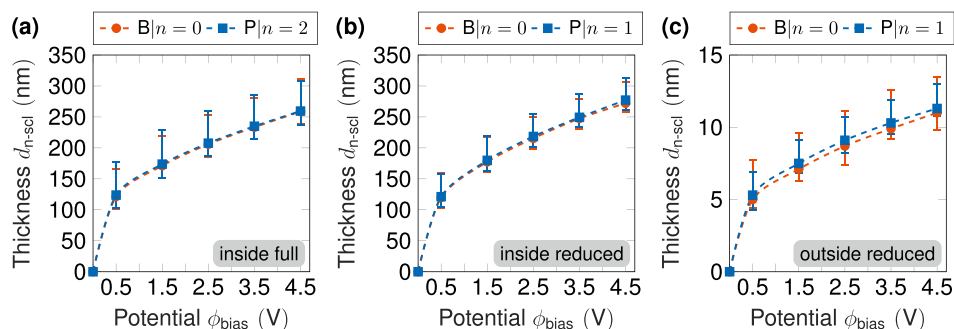


**Figure 5.** Results of baseline fitting (a) inside the full training data set, (b) inside the reduced training data set, and (c) outside the reduced training data set. In each case, we obtain perfect overlap with respect to the calculated error bars after a maximum of 2 iterations.  $B|n = 0$  corresponds to the baseline simulations, whereas  $P|n = x$  with  $x = 1, 2$  denotes the first/second iteration of the prediction-guided simulation runs, respectively.

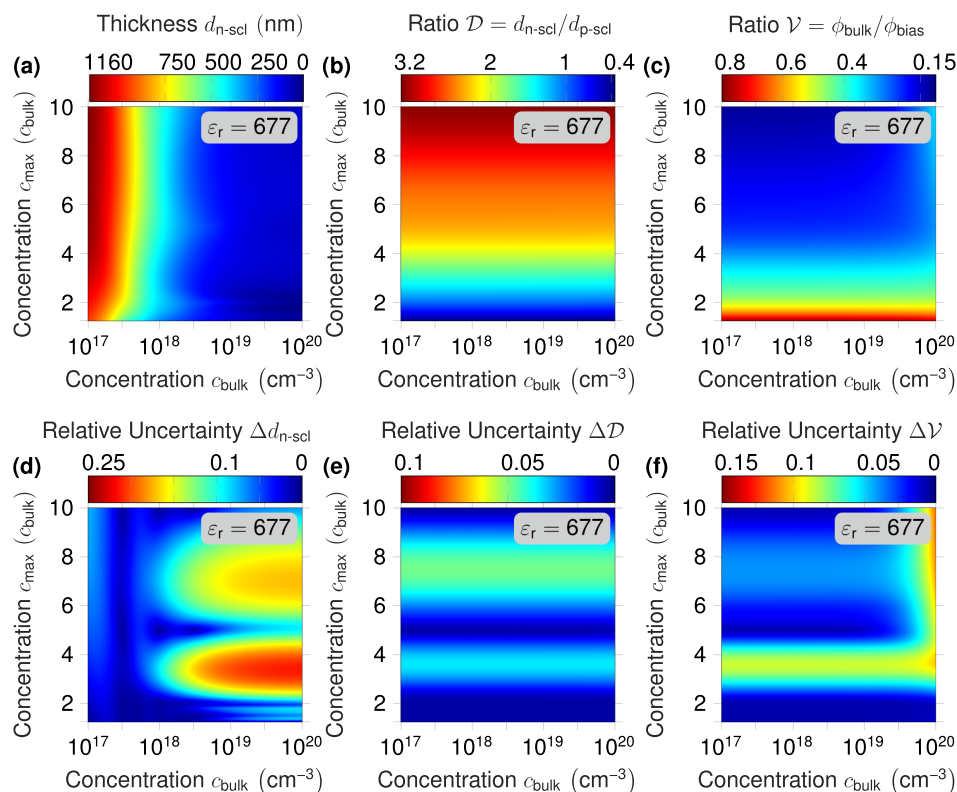


**Figure 6.** Full parameter space investigation for a fixed permittivity of  $\epsilon_r = 677$  and a fixed potential of  $\phi_{\text{bias}} = 2.5$  V: (a) depletion layer thickness,  $d_{\text{n-scl}}$  (b) thickness ratio  $\mathcal{D}$ , and (c) potential ratio  $\mathcal{V}$ . The corresponding relative uncertainty  $\Delta d_{\text{n-scl}}$ ,  $\Delta \mathcal{D}$ , and  $\Delta \mathcal{V}$  are shown in (d), (e), and (f), respectively. Regions with  $c_{\text{bulk}} > 10^{19}$   $\text{cm}^{-3}$  were fully extrapolated by the surrogate model.

Simulations with such high particle numbers usually take 5–6 weeks to fully converge even with an optimized code framework. Thus, it is crucial to minimize the amount of trial simulations required for finding a suitable set of input parameters.

The results of the corresponding baseline and prediction-guided simulations are shown in Figure 5c. Note that we applied the same reduced data set as in the previous scenario to train the model. Remarkably, we obtain good agreement with respect to the calculated error bars after only one prediction-guided simulation run. The average relative deviation between the two  $d_{\text{n-scl}}(\phi_{\text{bias}})$  profiles is given by 4.6%. In this context, it is particularly noteworthy that the data points in the training set closest to the baseline are at least two orders of magnitude smaller than the baseline. Accordingly, the computational effort required to sample them was orders of magnitude lower than for the predicted baseline. This finding alone can prove to be crucial in future studies as a high level of understanding for the physical phenomenon can be generated with minimal effort and strategic sampling. The simulation results for baseline fitting outside the reduced training data set are summarized in Table S3 in the Supporting Information.

**Full Parameter Space Investigation.** The hitherto analysis demonstrates the high accuracy of the constructed surrogate model inside and outside of the training data set. Therefore, we may utilize the surrogate model for a full parameter space investigation to visualize the influence of several input parameters on the output quantities presented in Table 1. Here, we consider the depletion layer thickness  $d_{\text{n-scl}}$ , the thickness ratio  $\mathcal{D}$ , and the potential ratio  $\mathcal{V}$  for a wide range of  $c_{\text{bulk}}$  and  $c_{\text{max}}$  as well as fixed  $\epsilon_r$  and  $\phi_{\text{bias}}$ ; see Figure 6.

In general, the presented results are physically consistent, which indicates that the algorithm has gained enough information about the process to interpolate inside and to extrapolate outside the training data set.  $d_{\text{n-scl}}$  is increasing with increasing  $c_{\text{max}}$  and decreasing with increasing  $c_{\text{bulk}}$ ; see Figure 6a. The former dependency can be rationalized by a growing number of available vacancy sites, whereas the latter dependency arises from a more effective electric-field screening for higher Li-ion densities (*cf.* Debye length for liquid electrolytes). In contrast, the thickness and potential ratios (*cf.* Figure 6b,c, respectively) are essentially independent of  $c_{\text{bulk}}$  as the depletion as well as the accumulation layer respond similarly to changes in  $c_{\text{bulk}}$ . Further,  $\mathcal{D}$  increases with increasing  $c_{\text{max}}$ , while  $\mathcal{V}$  exhibits a reverse dependency on  $c_{\text{max}}$ . This behavior can be rationalized by considering  $d_{\text{p-scl}}$  (see Figure S1, Supporting Information), which naturally decreases with increasing  $c_{\text{max}}$ . The simultaneous increase and decrease of  $d_{\text{n-scl}}$  and  $d_{\text{p-scl}}$  respectively, with increasing  $c_{\text{max}}$  leads to a corresponding increase in the thickness ratio  $\mathcal{D}$ . Finally, the decrease of  $\mathcal{V}$  as a function of  $c_{\text{max}}$  can be explained by the decreasing potential drop over the accumulation layer for increasing  $c_{\text{max}}$  as the accumulation layer capacitance becomes the bigger component in a series connection with the depletion layer capacitance. Additionally, we have performed similar parameter space investigations for variable permittivity (see Figures S2 and S3, Supporting Information), specifically  $\epsilon_r = 100$  and  $\epsilon_r = 1400$  for  $\phi_{\text{bias}} = 2.5$  V. It can be observed that  $d_{\text{n-scl}}$  and  $d_{\text{p-scl}}$  increase with increasing permittivity due to an enhanced screening of electrostatic interactions.

It is noteworthy that the surrogate model based on GPs has a built-in uncertainty quantification; see the relative

uncertainties in Figure 6d–f for  $d_{\text{n-scl}}$ ,  $\mathcal{D}$ , and  $\mathcal{V}$ , respectively. In general, higher relative uncertainties correspond to rather undersampled regions. However, considering the overall level of uncertainty (maximum of 25%), the constructed surrogate model can be considered to be sufficiently accurate even in unsampled areas—another indicator for the remarkable extrapolation capabilities of our methodology. On the other hand, if a higher resolution is required, the uncertainty quantification enables an informed decision on subsequent sampling.

In summary, the surrogate model is well-suited to replace expensive kMC simulations in many practical cases when a local resolution of output quantities is not required. The substitution is threefold: (1) The outputs of fast-converging kMC runs, here, corresponding to low particle densities, are generated. (2) These outputs are utilized to train the GP surrogate model, which in turn substitutes the whole parameter space. (3) Depending on the required accuracy and application, additional simulation runs can be performed in a selective and automated fashion. However, please note that the kMC method itself is a stochastic method and exhibits corresponding statistical fluctuations. Therefore, it is important not to oversample regions in which the dominant uncertainty arises from the physical and not the data-driven model. In this sense, physical intuition still plays an important role even though it can be compensated for by additional data points.

**Future Improvements.** Concluding, we want to provide some routes for additionally improving the proposed data-driven pipeline. In general, we advise to fully exploit the physical intuition present for the investigated system. For instance, in the present case study, it is apparent that  $d_{\text{n-scl}}(\phi_{\text{bias}})$  grows nonlinearly for  $\phi_{\text{bias}} \leq 0.5$  V and linearly otherwise; see Figure 5. Hence, a further increase in data efficiency can be achieved if the potential range is restricted to  $\phi_{\text{bias}} > 0.5$  V. Further, a lot of qualitative physical insight exists for the given application. In particular, the monotonicity of the space-charge layer formation with respect to the input parameters is well-established; see ref 46. This knowledge can be directly included in the form of gradient classification as outlined in ref 61. Additionally, we may incorporate a quantification for the kMC-inherent statistical fluctuations via a noise kernel. In this way, not only a realistic estimation of the prediction with respect to the kMC model can be added but also with respect to innately error-prone real-world measurements. By combining the uncertainty of the data-driven and the physics-based model, a multifidelity model can be implemented in which a data-driven model trained on kMC simulations will provide predictions. The uncertainty of this model will then determine whether an additional simulation or a real-world experiment is necessary.

**Conclusions.** In conclusion, we have presented an innovative and robust data-driven approach to automate the parametrization of kinetic Monte Carlo models. Our method couples the original kMC algorithm with a feedback loop consisting of a surrogate model based on Gaussian processes, a system-specific acquisition function, and Bayesian optimization. The surrogate model and the acquisition function operate as the two main components of Bayesian optimization, which enables the guided prediction of suitable input parameters for a given output/target quantity. The surrogate model is cheap to evaluate and trained via a database generated from the outputs of *fast-converging* kMC simulations. In contrast to intuition-based parameter searching, we require only 1 to 2 iterations to

reconstruct appropriate sets of input parameters. Remarkably, the latter statement holds inside and *outside* the bounds of the training data set demonstrating the extrapolation capabilities of our data-driven approach. Featuring accurate extrapolation is of high relevance when the direct kMC simulation of such regions is connected to large computational costs. Moreover, a sufficiently accurate surrogate model with a well-quantifiable error margin may fully replace potentially expensive kMC simulations, which is a viable option in many practical use cases.

The effectiveness of our data-driven optimization pipeline has been demonstrated by means of a highly significant electrochemical process for all-solid-state battery operation—the space-charge layer formation in solid-state electrolytes. The investigated process showcases a system with several open input parameters, which extremely profits from a guided and data-efficient parametrization scheme. We demonstrate that the applied predictor is not only highly accurate but to the same degree also data-efficient. Further, we consider different scenarios of inverse problem solution inside and outside the training data set and recover suitable sets of input parameters for given values of depletion layer thickness  $d_{\text{n-scl}}$ . Finally, a full parameter space investigation is performed for all output quantities ( $d_{\text{n-scl}}$ ,  $d_{\text{p-scl}}$ ,  $\mathcal{D}$ , and  $\mathcal{V}$ ) to highlight the accuracy of the constructed surrogate model.

The main innovation of our data-driven optimization pipeline for kMC models is its capability to extrapolate into regions outside of the training data set with a remarkably low error margin. Thus, an efficient parametrization of potentially expensive kMC simulations is enabled. Notably, the underlying surrogate model based on Gaussian processes relies solely on the output of *fast-converging* kMC simulations. Hence, our data-driven methodology opens a pathway for the efficient treatment of complex arbitrary systems via kMC simulations.

## ■ COMPUTATIONAL DETAILS

The simulation code of the space-charge layer formation in solid-state electrolytes has been implemented in C++ in our in-house kinetic Monte Carlo framework.<sup>6</sup> Each kMC simulation was run on eight cores of an AMD Ryzen Threadripper 3990X @2.9 GHz with 64 hardware cores. The source code is not yet open accessible as it is part of a larger software project which is going to be published separately at a later time. Bayesian optimization for parameter searching and the surrogate model based on Gaussian processes have been implemented in-house in Python. For the surrogate model, the GPY library<sup>62</sup> has been utilized. The corresponding source code and the complete data set are accessible via GitHub <https://github.com/benkour/Utilizing-Data-Driven-Optimization-to-Automate-the-Parametrization-of-Kinetic-Monte-Carlo-Models>.

## ■ ASSOCIATED CONTENT

### SI Supporting Information

The Supporting Information is available free of charge at <https://pubs.acs.org/doi/10.1021/acs.jpca.3c02482>.

Tabulated values of baseline fitting within the training data set; tabulated values of baseline fitting outside the training data set; full parameter space investigation of  $d_{\text{p-scl}}$  for  $\epsilon_r \in [100, 677, 1400]$  and  $\phi_{\text{bias}} = 2.5$  V; full parameter space investigation of  $d_{\text{n-scl}}$ ,  $\mathcal{D}$ , and  $\mathcal{V}$  for  $\epsilon_r = 100$  and  $\phi_{\text{bias}} = 2.5$  V; and full parameter space

investigation of  $d_{n\text{-scb}}$ ,  $\mathcal{D}$ , and  $\mathcal{V}$  for  $\epsilon_r = 1400$  and  $\phi_{\text{bias}} = 2.5$  V (PDF)

## AUTHOR INFORMATION

### Corresponding Author

**Manuel Gößwein** – Department of Electrical and Computer Engineering, Technical University of Munich, 85748 Garching bei München, Germany; Email: [manuel.goesswein@tum.de](mailto:manuel.goesswein@tum.de)

### Authors

**Ioannis Kouroudis** – Department of Electrical and Computer Engineering, Technical University of Munich, 85748 Garching bei München, Germany

**Alessio Gagliardi** – Department of Electrical and Computer Engineering, Technical University of Munich, 85748 Garching bei München, Germany; [orcid.org/0000-0002-3322-2190](https://orcid.org/0000-0002-3322-2190)

Complete contact information is available at: <https://pubs.acs.org/10.1021/acs.jpca.3c02482>

### Author Contributions

<sup>‡</sup>I.K. and M.G. contributed equally to this work.

### Notes

The authors declare no competing financial interest.

## ACKNOWLEDGMENTS

J.K. acknowledges funding from the Project ProperPhotoMile, supported under the umbrella of SOLAR-ERA.NET Cofund 2 by the Spanish Ministry of Science and Education and the AEI under the project PCI2020-112185 and CDTI project number IDI-20210171; the Federal Ministry for Economic Affairs and Energy on the basis of a decision by the German Bundestag project number FKZ 03EE1070B and FKZ 03EE1070A, and the Israel Ministry of Energy with project number 220-11-031. SOLAR-ERA.NET is supported by the European Commission within the EU Framework Programme for Research and Innovation HORIZON 2020 (Cofund ERA-NET Action, No. 786483). Further, M.G. acknowledges funding from the European Union's Horizon 2020 FETOPEN 2018–2020 program "LION-HEARTED" under grant agreement no. 828984. Finally, A.G. acknowledges financial support from TUM Innovation Network for Artificial Intelligence powered Multifunctional Material Design (ARTEMIS) and funding in the framework of Deutsche Forschungsgemeinschaft (DFG, German Research Foundation) under Germany's Excellence Strategy—EXC 2089/1—390776260 (e-conversion).




## REFERENCES

- (1) Zhu, P.; Smith, R. W. Dynamic Simulation of Crystal Growth by Monte Carlo Method—I. Model Description and Kinetics. *Acta Metall. Mater.* **1992**, *40*, 683–692.
- (2) Piana, S.; Gale, J. D. Three-Dimensional Kinetic Monte Carlo Simulation of Crystal Growth from Solution. *J. Cryst. Growth* **2006**, *294*, 46–52.
- (3) Magna, A. L.; Coffa, S.; Colombo, L. A Lattice Kinetic Monte Carlo Code for the Description of Vacancy Diffusion and Self-Organization in Si. *Nucl. Instrum. Methods Phys. Res. Sect. B Beam Interact. Mater. At.* **1999**, *148*, 262–267.
- (4) Dholabhai, P. P.; Anwar, S.; Adams, J. B.; Crozier, P.; Sharma, R. Kinetic Lattice Monte Carlo Model for Oxygen Vacancy Diffusion in Praseodymium Doped Ceria: Applications to Materials Design. *J. Solid State Chem.* **2011**, *184*, 811–817.
- (5) Grabowski, M.; Rogal, J.; Drautz, R. Kinetic Monte Carlo Simulations of Vacancy Diffusion in Nondilute Ni- $x$  ( $x = \text{Re, W, Ta}$ ) Alloys. *Phys. Rev. Mater.* **2018**, *2*, No. 123403.
- (6) Kaiser, W.; Popp, J.; Rinderle, M.; Albes, T.; Gagliardi, A. Generalized Kinetic Monte Carlo Framework for Organic Electronics. *Algorithms* **2018**, *11*, 37.
- (7) Kaiser, W.; Albes, T.; Gagliardi, A. Charge Carrier Mobility of Disordered Organic Semiconductors with Correlated Energetic and Spatial Disorder. *Phys. Chem. Chem. Phys.* **2018**, *20*, 8897–8908.
- (8) Groves, C.; Greenham, N. C. In *Multiscale Modelling of Organic and Hybrid Photovoltaics*; Beljonne, D.; Cornil, J., Eds.; Springer Berlin Heidelberg: Berlin, Heidelberg, 2014; pp 257–278.
- (9) Bässler, H. Charge Transport in Disordered Organic Photoconductors a Monte Carlo Simulation Study. *Phys. Status Solidi B* **1993**, *175*, 15–56.
- (10) Reuter, K.; Scheffler, M. First-Principles Kinetic Monte Carlo Simulations for Heterogeneous Catalysis: Application to the Co Oxidation at RuO<sub>2</sub>(110). *Phys. Rev. B* **2006**, *73*, No. 045433.
- (11) Jørgensen, M.; Grönbeck, H. Scaling Relations and Kinetic Monte Carlo Simulations to Bridge the Materials Gap in Heterogeneous Catalysis. *ACS Catal.* **2017**, *7*, 5054–5061.
- (12) Jørgensen, M.; Grönbeck, H. Selective Acetylene Hydrogenation Over Single-Atom Alloy Nanoparticles by Kinetic Monte Carlo. *J. Am. Chem. Soc.* **2019**, *141*, 8541–8549.
- (13) Watkins, P. K.; Walker, A. B.; Verschoor, G. L. B. Dynamical Monte Carlo Modelling of Organic Solar Cells: The Dependence of Internal Quantum Efficiency on Morphology. *Nano Lett.* **2005**, *5*, 1814–1818.
- (14) Casalegno, M.; Raos, G.; Po, R. Methodological Assessment of Kinetic Monte Carlo Simulations of Organic Photovoltaic Devices: The Treatment of Electrostatic Interactions. *J. Chem. Phys.* **2010**, *132*, No. 094705.
- (15) Kipp, D.; Ganesan, V. A Kinetic Monte Carlo Model with Improved Charge Injection Model for the Photocurrent Characteristics of Organic Solar Cells. *J. Appl. Phys.* **2013**, *113*, No. 234502.
- (16) Kaiser, W.; Gagliardi, A. Kinetic Monte Carlo Study of the Role of the Energetic Disorder on the Open-Circuit Voltage in Polymer/fullerene Solar Cells. *J. Phys. Chem. Lett.* **2019**, *10*, 6097–6104.
- (17) Drews, T. O.; Radisic, A.; Erlebacher, J.; Braatz, R. D.; Seanson, P. C.; Alkire, R. C. Stochastic Simulation of the Early Stages of Kinetically Limited Electrodeposition. *J. Electrochem. Soc.* **2006**, *153*, C434.
- (18) Methekar, R. N.; Northrop, P. W. C.; Chen, K.; Braatz, R. D.; Subramanian, V. R. Kinetic Monte Carlo Simulation of Surface Heterogeneity in Graphite Anodes for Lithium-Ion Batteries: Passive Layer Formation. *J. Electrochem. Soc.* **2011**, *158*, A363.
- (19) Liu, S.; White, M. G.; Liu, P. Mechanism of Oxygen Reduction Reaction on Pt(111) in Alkaline Solution: Importance of Chemisorbed Water on Surface. *J. Phys. Chem. C* **2016**, *120*, 15288–15298.
- (20) Gavilán-Arriazu, E. M.; Mercer, M. P.; Barraco, D. E.; Hoster, H. E.; Leiva, E. P. M. Kinetic Monte Carlo Simulations Applied to Li-Ion and Post Li-Ion Batteries: A Key Link in the Multi-Scale Chain. *Prog. Energy* **2021**, *3*, No. 042001.
- (21) Ewald, P. P. Die Berechnung Optischer Und Elektrostatistischer Gitterpotentiale. *Ann. Phys.* **1921**, *369*, 253–287.
- (22) Allen, M. P.; Tildesley, D. J. *Computer Simulation of Liquids*; Oxford University Press: Oxford, UK, 2017.
- (23) Greengard, L.; Rokhlin, V. A Fast Algorithm for Particle Simulations. *J. Comput. Phys.* **1987**, *73*, 325–348.
- (24) Saunders, W. R.; Grant, J.; Müller, E. H.; Thompson, I. Fast Electrostatic Solvers for Kinetic Monte Carlo Simulations. *J. Comput. Phys.* **2020**, *410*, No. 109379.
- (25) van der Kaap, N. J.; Koster, L. J. A. Massively Parallel Kinetic Monte Carlo Simulations of Charge Carrier Transport in Organic Semiconductors. *J. Comput. Phys.* **2016**, *307*, 321–332.
- (26) Chatterjee, A.; Vlachos, D. G. An Overview of Spatial Microscopic and Accelerated Kinetic Monte Carlo Methods. *J. Comput. Aided Mol. Des.* **2007**, *14*, 253–308.




- (27) Chatterjee, A.; Voter, A. F. Accurate Acceleration of Kinetic Monte Carlo Simulations through the Modification of Rate Constants. *J. Chem. Phys.* **2010**, *132*, No. 194101.
- (28) Dybeck, E. C.; Plaisance, C. P.; Neurock, M. Generalized Temporal Acceleration Scheme for Kinetic Monte Carlo Simulations of Surface Catalytic Processes by Scaling the Rates of Fast Reactions. *J. Chem. Theory Comput.* **2017**, *13*, 1525–1538.
- (29) Kaiser, W.; Gößwein, M.; Gagliardi, A. Acceleration Scheme for Particle Transport in Kinetic Monte Carlo Methods. *J. Chem. Phys.* **2020**, *152*, No. 174106.
- (30) Gößwein, M.; Kaiser, W.; Gagliardi, A. Local Temporal Acceleration Scheme to Couple Transport and Reaction Dynamics in Kinetic Monte Carlo Models of Electrochemical Systems. *J. Chem. Theory Comput.* **2022**, *18*, 2749–2763.
- (31) Nichol, A.; Ackland, G. J. Property Trends in Simple Metals: An Empirical Potential Approach. *Phys. Rev. B* **2016**, *93*, No. 184101.
- (32) Gilmore, R. H.; Lee, E. M. Y.; Weidman, M. C.; Willard, A. P.; Tisdale, W. A. Charge Carrier Hopping Dynamics in Homogeneously Broadened Pbs Quantum Dot Solids. *Nano Lett.* **2017**, *17*, 893–901.
- (33) Ghalami Choobar, B.; Modarress, H.; Halladj, R.; Amjad-Iranagh, S. Electrodeposition of Lithium Metal on Lithium Anode Surface, a Simulation Study by: Kinetic Monte Carlo-embedded Atom Method. *Comput. Mater. Sci.* **2021**, *192*, No. 110343.
- (34) Hosemann, B.; Drache, M.; Beuermann, S. Advanced Kinetic Parameter Fit Applied to Radical Copolymerizations. *Macromol. Symp.* **2016**, *370*, 17–25.
- (35) Gavilán-Arriazu, E.; Pinto, O. A.; López de Mishima, B. A.; Barraco, D. E.; Oviedo, O. A.; Leiva, E. P. M. Kinetic Monte Carlo Applied to the Electrochemical Study of the Li-ion Graphite System. *Electrochim. Acta* **2020**, *331*, No. 135439.
- (36) Rego, A. S. C.; Brandão, A. L. T. Parameter Estimation and Kinetic Monte Carlo Simulation of Styrene and N-butyl Acrylate Copolymerization through Atrp. *Ind. Eng. Chem. Res.* **2021**, *60*, 8396–8408.
- (37) Sestito, J. M.; Harris, T. A. L.; Wang, Y. Reduced-Order Kinetic Monte Carlo Model to Simulate Water Diffusion in Biodegradable Polymers. *Comput. Mater. Sci.* **2022**, *203*, No. 111141.
- (38) Crevillén-García, D.; Leung, P.; Shah, A. A. An Emulator for Kinetic Monte Carlo Simulations of Kinetically Controlled Metal Electrodeposition. *J. Phys. Conf. Ser.* **2018**, *1053*, No. 012081.
- (39) Herbol, H. C.; Hu, W.; Frazier, P.; Clancy, P.; Poloczek, M. Efficient Search of Compositional Space for Hybrid Organic-Inorganic Perovskites Via Bayesian Optimization. *Npj Comput. Mater.* **2018**, *4*, 51.
- (40) Lampe, C.; Kouroudis, I.; Harth, M.; Martin, S.; Gagliardi, A.; Urban, A. S. Rapid Data-Efficient Optimization of Perovskite Nanocrystal Syntheses through Machine Learning Algorithm Fusion. *Adv. Mater.* **2023**, *35*, No. 2208772.
- (41) Chang, J.; Nikolaev, P.; Carpena-Núñez, J.; Rao, R.; Decker, K.; Islam, A. E.; Kim, J.; Pitt, M. A.; Myung, J. I.; Maruyama, B. Efficient Closed-Loop Maximization of Carbon Nanotube Growth Rate Using Bayesian Optimization. *Sci. Rep.* **2020**, *10*, No. 9040.
- (42) Popp, J.; Haider, M.; Franckić, M.; Faist, J.; Jirauschek, C. Bayesian Optimization of Quantum Cascade Detectors. *Opt. Quantum. Electron.* **2021**, *53*, 287.
- (43) Tran, A.; Mitchell, J. A.; Swiler, L. P.; Wildey, T. An Active Learning High-Throughput Microstructure Calibration Framework for Solving Inverse Structure-Process Problems in Materials Informatics. *Acta Mater.* **2020**, *194*, 80–92.
- (44) Horowitz, Y.; Schmidt, C.; Yoon, D.-h.; Riegger, L. M.; Katzenmeier, L.; Bosch, G. M.; Noked, M.; Ein-Eli, Y.; Janek, J.; Zeier, W. G.; et al. Between Liquid and All Solid: A Prospect on Electrolyte Future in Lithium-Ion Batteries for Electric Vehicles. *Energy Technol.* **2020**, *8*, No. 2000580.
- (45) Chae, O. B.; Lucht, B. L. Interfacial Issues and Modification of Solid Electrolyte Interphase for Li Metal Anode in Liquid and Solid Electrolytes. *Adv. Energy Mater.* **2023**, *13*, No. 2203791.
- (46) Katzenmeier, L.; Gößwein, M.; Gagliardi, A.; Bandarenka, A. S. Modeling of Space-charge Layers in Solid-state Electrolytes: A Kinetic Monte Carlo Approach and Its Validation. *J. Phys. Chem. C* **2022**, *126*, 10900–10909.
- (47) Katzenmeier, L.; Helmer, S.; Braxmeier, S.; Knobbe, E.; Bandarenka, A. S. Properties of the Space Charge Layers Formed in Li-Ion Conducting Glass Ceramics. *ACS Appl. Mater. Interfaces* **2021**, *13*, 5853–5860.
- (48) Katzenmeier, L.; Carstensen, L.; Schaper, S. J.; Müller-Buschbaum, P.; Bandarenka, A. S. Characterization and Quantification of Depletion and Accumulation Layers in Solid-State Li<sup>+</sup>-Conducting Electrolytes Using in Situ Spectroscopic Ellipsometry. *Adv. Mater.* **2021**, *33*, No. 2100585.
- (49) Funke, K. Debye-Hückel-Type Relaxation Processes in Solid Ionic Conductors: The Model. *Solid State Ion.* **1986**, *18–19*, 183–190.
- (50) Park, M.; Zhang, X.; Chung, M.; Less, G. B.; Sastry, A. M. A Review of Conduction Phenomena in Li-Ion Batteries. *J. Power Sources* **2010**, *195*, 7904–7929.
- (51) Bortz, A. B.; Kalos, M. H.; Lebowitz, J. L. A New Algorithm for Monte Carlo Simulation of Ising Spin Systems. *J. Comput. Phys.* **1975**, *17*, 10–18.
- (52) Gillespie, D. T. A General Method for Numerically Simulating the Stochastic Time Evolution of Coupled Chemical Reactions. *J. Comput. Phys.* **1976**, *22*, 403–434.
- (53) Gillespie, D. T. Exact Stochastic Simulation of Coupled Chemical Reactions. *J. Phys. Chem. A* **1977**, *81*, 2340–2361.
- (54) Brochu, E.; Cora, V. M.; De Freitas, N. A Tutorial on Bayesian Optimization of Expensive Cost Functions, with Application to Active User Modeling and Hierarchical Reinforcement Learning *arXiv preprint* **2010**, *abs/1012.2599*.
- (55) Rasmussen, C. E.; Williams, C. K. I. *Gaussian Processes for Machine Learning*; The MIT Press: Cambridge, Massachusetts, USA, 2005.
- (56) Williams, C. Computing with Infinite Networks. In *Advances in Neural Information Processing Systems*; Cambridge: Massachusetts, USA, 1996; pp 295–301.
- (57) Neal, R. M. *Bayesian Learning for Neural Networks*; Springer New York: New York, NY, 1996; pp 29–53.
- (58) Cho, Y.; Saul, L. K. In *Kernel Methods for Deep Learning*, Proceedings of the 22nd International Conference on Neural Information Processing Systems Red Hook, NY, USA, 2009; pp 342–350.
- (59) Hazan, T.; Jaakkola, T. Steps toward Deep Kernel Methods from Infinite Neural Networks. 2015, arXiv:1508.05133. arXiv.org e-Print archive. <https://arxiv.org/abs/1508.05133>.
- (60) Lee, J.; Bahri, Y.; Novak, R.; Schoenholz, S. S.; Pennington, J.; Sohl-Dickstein, J. Neural Networks As Gaussian Processes. 2017, arXiv:1711.00165. arXiv.org e-Print archive. <https://arxiv.org/abs/1711.00165>.
- (61) Riihimäki, J.; Vehtari, A. In *Gaussian Processes with Monotonicity Information*, Proceedings of the Thirteenth International Conference on Artificial Intelligence and Statistics, 2010; pp 645–652.
- (62) GPy A Gaussian Process Framework in Python. 2012, <http://github.com/SheffieldML/GPy> (accessed June 11, 2023).

# Modeling of Space-Charge Layers in Solid-State Electrolytes. A Kinetic Monte Carlo Approach and its Validation

Sign in/Register  

---



**Modeling of Space-Charge Layers in Solid-State Electrolytes: A Kinetic Monte Carlo Approach and Its Validation**

Author: Leon Katzenmeier, Manuel Gößwein, Alessio Gagliardi, et al

Publication: The Journal of Physical Chemistry C

Publisher: American Chemical Society

Date: Jul 1, 2022

*Copyright © 2022, American Chemical Society*

**PERMISSION/LICENSE IS GRANTED FOR YOUR ORDER AT NO CHARGE**

This type of permission/license, instead of the standard Terms and Conditions, is sent to you because no fee is being charged for your order. Please note the following:

- Permission is granted for your request in both print and electronic formats, and translations.
- If figures and/or tables were requested, they may be adapted or used in part.
- Please print this page for your records and send a copy of it to your publisher/graduate school.
- Appropriate credit for the requested material should be given as follows: "Reprinted (adapted) with permission from {COMPLETE REFERENCE CITATION}. Copyright {YEAR} American Chemical Society." Insert appropriate information in place of the capitalized words.
- One-time permission is granted only for the use specified in your RightsLink request. No additional uses are granted (such as derivative works or other editions). For any uses, please submit a new request.

If credit is given to another source for the material you requested from RightsLink, permission must be obtained from that source.

**BACK**

**CLOSE WINDOW**

The following publication is reprinted with permission from ref. 103, *J. Phys. Chem. C* **2022**, 126, 10900-10909. Copyright 2022 American Chemical Society (ACS).

# Modeling of Space-Charge Layers in Solid-State Electrolytes: A Kinetic Monte Carlo Approach and Its Validation

Leon Katzenmeier,<sup>†</sup> Manuel Gößwein,<sup>†</sup> Alessio Gagliardi,<sup>\*</sup> and Aliaksandr S. Bandarenka<sup>\*</sup>

Cite This: *J. Phys. Chem. C* 2022, 126, 10900–10909

Read Online

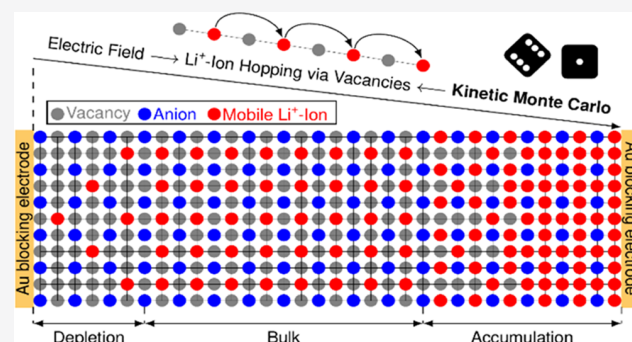
ACCESS |

Metrics & More

Article Recommendations

Supporting Information

**ABSTRACT:** The space-charge layer (SCL) phenomenon in Li<sup>+</sup>-ion-conducting solid-state electrolytes (SSEs) is gaining much interest in different fields of solid-state ionics. Not only do SCLs influence charge-transfer resistance in all-solid-state batteries but also are analogous to their electronic counterpart in semiconductors; they could be used for Li<sup>+</sup>-ionic devices. However, the rather “elusive” nature of these layers, which occur on the nanometer scale and with only small changes in concentrations, makes them hard to fully characterize experimentally. Theoretical considerations based on either electrochemical or thermodynamic models are limited due to missing physical, chemical, and electrochemical parameters. In this work, we use kinetic Monte Carlo (kMC) simulations with a small set of input parameters to model the spatial extent of the SCLs. The predictive power of the kMC model is demonstrated by finding a critical range for each parameter in which the space-charge layer growth is significant and must be considered in electrochemical and ionic devices. The time evolution of the charge redistribution is investigated, showing that the SCLs form within 500 ms after applying a bias potential.



## 1. INTRODUCTION

Applications of ion-conducting solids range across energy storage,<sup>1</sup> energy conversion,<sup>2</sup> and ionic devices.<sup>3</sup> One possible application of Li<sup>+</sup>-ion-conducting solid-state electrolytes (SSEs) is an all-solid-state battery, potentially enabling Li-metal anodes with the SSE posing as an impenetrable barrier to lithium dendrites.<sup>4</sup> While the ionic conductivity of the SSE is reaching the realm of their liquid counterparts,<sup>5</sup> the interface of the SSE toward materials with different electrochemical potentials, such as electrodes, remains a source for high ionic resistances.<sup>6</sup> Despite plenty of research into interface reactions,<sup>7</sup> formation of passivation layers,<sup>8</sup> and electrochemical stability,<sup>9</sup> the mere charge redistribution to accommodate the electrochemical potential difference between the two materials still lacks fundamental understanding. The so-called space-charge layer (SCL) in SSEs describes the phenomenon of charge accumulation or depletion at the interface of the SSE. As the only mobile species in the SSE are the cations, whether it is oxygen, lithium, or other ion-conducting solid, the formation of SCL is a mere redistribution of cations.

For Li<sup>+</sup>-ion-conducting SSE, a variety of theoretical and experimental approaches have been used to investigate these evasive layers of altered Li<sup>+</sup>-ion concentration within the SSE crystal lattice. As the electrochemical potential difference is the driving force for SCL occurrence, the effect can be investigated under blocking conditions by varying the potential drop across the interface. One study, based on a thermodynamic model with a numerical solution,<sup>10</sup> concludes that for a set of approximate

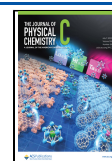
parameters, the SCL extents tens, if not hundreds, of nanometers into the SSE at relatively low potentials. Based on electrochemical models, other theoretical considerations conclude that the impact should be negligible and the width of such a layer not larger than a few nanometers.<sup>11</sup>

In previous studies, we explored the formation of SCL under blocking conditions experimentally using electrochemical impedance spectroscopy (EIS)<sup>12</sup> and spectroscopic ellipsometry<sup>13</sup> on a model material system, a Li<sup>+</sup>-ion-conducting glass-ceramic by Ohara Inc. The SCL width was found to range up to 200 nm into the SSE at a bias potential of 1.5 V with spectroscopic ellipsometry, which is in reasonable agreement with the capacitance of such a layer measured with impedance spectroscopy. The relatively wide layer was found to be in coexistence with a single Li<sup>+</sup>-ion layer, which can be understood as the formation of a compact Helmholtz layer in liquid electrolytes (LEs).<sup>14</sup> The comparison of experimentally obtained widths and concentration changes to theoretical models is hindered by the uncertainties of physical parameters

Received: April 11, 2022

Revised: June 12, 2022

Published: June 23, 2022



needed to calculate the impact of applied potential on the formation of an SCL.

The transport of ions in SSEs can be described by a thermally activated hopping mechanism between unoccupied lattice vacancies.<sup>15,16</sup> Unless a hopping transition is executed, each ion is spatially assigned to a vacancy. Such a configuration can be interpreted as a kind of localized state. Accordingly, the overall transport dynamics can be described by hops from one localized state to another. In this sense, ionic motion in SSEs fulfills the criteria of a so-called infrequent-event system. A very well-established theoretical approach to model such systems is the kinetic Monte Carlo (kMC) method. In general, kMC methods are a special subclass of Monte Carlo algorithms that can simulate the time evolution of nondeterministic systems. kMC models have been developed for numerous different applications such as charge transport in disordered organic semiconductors,<sup>17–20</sup> crystal growth,<sup>21,22</sup> chemical reaction networks,<sup>23–26</sup> vacancy diffusion,<sup>27,28</sup> and electrochemical systems.<sup>29–32</sup> In the direct context of solid-state electrolytes, kMC also has been applied. For instance, Wolverson and co-workers calculated the room-temperature ion conductivities of cation- and anion-substituted LiBH<sub>4</sub>-based SSEs.<sup>33</sup> Very recently, Dean et al. showed that grain boundary space-charge regions in SSEs can exhibit over- as well as underscreening.<sup>34</sup> However, there is no kMC model that captures the experimentally observed SCL growth into the SSE, perpendicular to the electrode, for either fully depleted or fully occupied vacancy lattice.

In this work, we present a predictive kinetic Monte Carlo model for the SCL formation in SSEs, which features a perpendicular growth regime. The model requires only a minimal set of input parameters to simulate the spatial extent of the SCLs formed for various parameters and bias potentials. We use a standard parameter set based on previous investigations to validate the model and compare the results to experiments. Furthermore, a sensitivity analysis reveals the impact of physical parameters and material properties, which can assess the relevance of SCL for a given, new material system. As kinetic Monte Carlo simulations inherently allow calculations of the time evolution of concentration profiles, the dynamics of SCL formation are investigated.

## 2. THEORY AND MODEL

As outlined above, SSEs transfer ions through a hopping mechanism in a crystal lattice, which typically consists of immobile anions as a backbone and a sublattice of vacancies in which the ions move. As the SCL phenomenon in blocking conditions is a mere redistribution of mobile charges, it is essential to notice the physical boundaries. For clarity, only mobile cations are considered, even though theory<sup>35</sup> suggests that not all cations are mobile at room temperature. The mobile and immobile cations are located within the anion lattice, where anions simply neutralize their respective immobile cations. However, the mobile cations are the drivers of ionic conductivity and, therefore, can accumulate or deplete in a certain region. Anion mobility plays a crucial role in polymer-based SSEs,<sup>36</sup> which is neglected in this work. On the one hand, the anion mobility must be low in full ASSB cells to promote interfacial stability.<sup>37</sup> On the other hand, the movement of anions would certainly play a role in the lattice constants and crystal structure, an effect that could be part of future kMC simulations.

The concentration of cations is given by  $c_{\text{Li}^+}$ , and it is important to differentiate between three scenarios.

- (i) An electroneutral lattice, where  $c_{\text{Li}^+}$  and the anion concentration compensate. This is the case in the bulk of the SSE and will be described as  $c_{\text{Li}^+, \text{bulk}}$ .
- (ii) A fully depleted lattice, where no mobile Li<sup>+</sup> ions are left. This forms a maximally electronegative lattice, and the Li<sup>+</sup>-ion concentration is  $c_{\text{min}}$ .
- (iii) A full lattice, where no free vacancies are left. This forms a maximally electropositive lattice, and the Li<sup>+</sup>-ion concentration is  $c_{\text{max}}$ .

The cation concentration is therefore limited to  $c_{\text{min}} \leq c_{\text{Li}^+} \leq c_{\text{max}}$  and reaches a nonzero equilibrium of  $c_{\text{Li}^+, \text{bulk}}$  in the bulk SSE. While the polarization state of the SSE does not influence the concentration limits, the material (crystal lattice) and the temperature will significantly impact the concentrations.

When the SSE is brought into contact with a material of different electrochemical potentials (either inherent or by applying a bias potential), the potential drops within a certain region, which is not electroneutral. The SCL, therefore, occurs in the vicinity of the interface. The concept of SCL formation is like that of electrical double layers (EDLs) at the liquid electrolyte (LE)/electrode interface.<sup>38</sup> In EDLs, the anions and cations accumulate to form charged layers with relatively small thicknesses.<sup>39</sup> The amount of charge and spatial distribution of the EDL causes the electrical potential to drop within this short-range and, therefore, the bulk of the LE to stay electroneutral. While the Li<sup>+</sup> concentration is only limited by the volume in LEs, and thus LEs allow a significantly higher charge density in SSEs, the limits of Li<sup>+</sup> concentration are given by  $c_{\text{min}} \leq c_{\text{Li}^+} \leq c_{\text{max}}$ . The limits in charge density are responsible for the formation of thicker layers when the same amount of charge must be held to screen the electrochemical potential difference.

The kinetic Monte Carlo method is a stochastic algorithm to simulate the sequential time evolution of a system through different states within its configuration space. As a fundamental concept, kMC relies on coarse-graining system dynamics. The investigated system is reduced to a set of long-term states  $\{i\}$  connected by discrete transitions. In each state  $i$ , the system may evolve to a set of possible states  $\{j\}$ . Every transition is governed by a transition rate,  $k_{ij}$ , which captures the actual physical process inducing the transition  $i \rightarrow j$ . The transition rates are crucial input parameters for the kMC model. Typically, they are either based on underlying physical models or taken from experiments. The relative probability of a certain state-to-state transition is directly proportional to the magnitude of the corresponding rate

$$P_{ij} = \frac{k_{ij}}{k_{\text{tot}}} = \frac{k_{ij}}{\sum_j k_{ij}} \quad (1)$$

where  $k_{\text{tot}}$  denotes the total rate of all possible transitions. In the so-called Monte Carlo step, two uniformly distributed random numbers  $r_1, r_2 \in (0,1)$  are drawn to determine (1) which transition,  $\mu$ , is executed and (2) how much time,  $\tau$ , has passed before the transition is performed. Via the first random number  $r_1$ , we select transition  $\mu$  from the set of all transition probabilities  $\{P_{ij}\}$  according to the inequation

$$\sum_{j=1}^{\mu-1} P_{ij} < r_1 \leq \sum_{j=1}^{\mu} P_{ij} \quad (2)$$

The second random number  $r_2$  yields the corresponding time-step

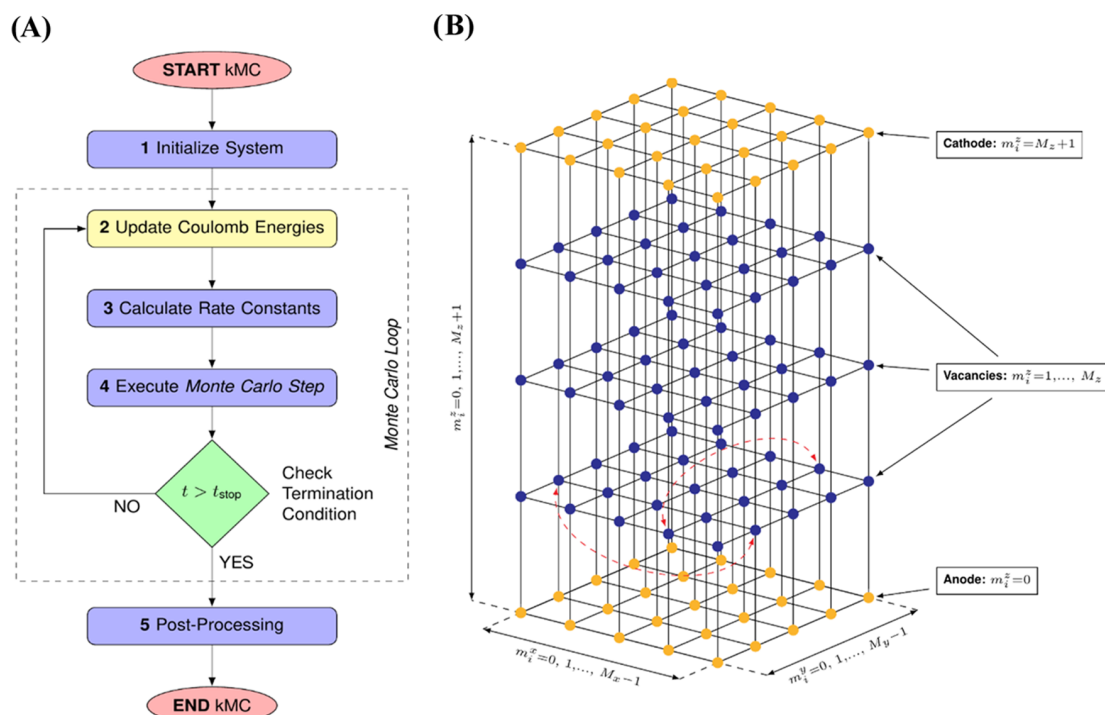


**Figure 1.** Kinetic Monte Carlo Method. (A) System specialized flowchart of the kMC algorithm for simulating the SCL formation in SSEs. (B) Representation of the experimental set-up as a grid of discrete sites. Blue and yellow sites correspond to vacancies and contact nodes, respectively. The dashed red arrows visualize the periodic boundary conditions applied in the  $xy$ -plane. From a geometrical point of view, each site  $i$  is described by an index triplet  $(m_i^x, m_i^y, m_i^z)$ , and the total number of sites in  $xyz$ -directions are given by  $M_x$ ,  $M_y$ , and  $M_z$ , respectively.

$$\tau = -\frac{\ln(r_2)}{k_{\text{tot}}} \quad (3)$$

Equations 2 and 3 are related to the so-called  $n$ -fold or direct method outlined in ref 40. Subsequently, the system state is updated according to the chosen transition,  $\mu$ , and the simulated time,  $t$ , is advanced by  $\tau$ . In the new system state, the transition rates must be recalculated before another Monte Carlo step can be performed. Repeated execution of this procedure results in the stochastic time evolution of the system. Usually, the simulation is completed after a user-defined termination condition, e.g., the simulated time exceeds a certain threshold,  $t \geq t_{\text{stop}}$ .

The general algorithm must be adapted accordingly to simulate the SCL formation in SSEs via kMC (see Figure 1A) for a simplified flowchart. In the current study, the application of the kMC algorithm boils down to five essential steps:

1. System initialization: The experimental set-up is mapped onto a set of discrete sites that store geometrical (e.g., position) as well as physical properties (e.g., potential energy). The sites either represent vacancies or contact nodes. At the beginning of the simulation, vacancies are randomly occupied by  $\text{Li}^+$  ions according to input bulk density  $c_{\text{Li}^+, \text{bulk}}$ .
2. Update of Coulombic energies: The local hopping rates of each  $\text{Li}^+$  ion depend on the mutual Coulombic interactions with all other cations and a neutralizing anionic background. Since the configuration of mobile  $\text{Li}^+$  ions changes in each kMC step, the Coulombic energies must be updated according to the new configuration prior to the recalculation of hopping rates.

3. Calculation of rate constants: As outlined above, the SCL formation in SSEs corresponds to a mere redistribution of mobile  $\text{Li}^+$  ions. To capture this process on a local scale, we compute the hopping rates for each  $\text{Li}^+$  ion to all unoccupied nearest-neighbor vacancies. The magnitude of these rates is determined by the physical and geometrical properties of the investigated SSE sample as well as the local potential energy surface.

4. Execution of the Monte Carlo step: Two uniform random numbers  $r_1, r_2 \in (0,1)$  are drawn. Based on eq 2,  $r_1$  is used to select the ion hopping transition to be executed and, based on eq 3,  $r_2$  is used to compute simulated time  $\tau$  prior to the transport event. Afterward, we check whether simulated time  $t$  exceeds the steady-state time  $t_{\text{stop}}$ , which can be obtained by trial simulations. If  $t < t_{\text{stop}}$ , another simulation step is performed. The repetitive execution of steps 2–4 is also denoted the Monte Carlo loop.

5. Postprocessing: If the termination condition is fulfilled, the Monte Carlo loop is exited. As a final step, the raw output data of the simulation are converted into meaningful physical quantities. Here, we transform the local relative vacancy occupation times into a corresponding local  $\text{Li}^+$ -concentration profile, which enables the calculation of numerous other characteristic quantities such as the potential profile and the SCL thickness/capacitance.

### 3. MODELING AND SIMULATION SETUP

Next, we outline the detailed kMC model set-up of an SSE sample confined between two gold blocking electrodes, see Figure 1B. The sample is represented by a three-dimensional primitive orthorhombic lattice constituted of a total number of

$M_x \times M_y \times M_z$  sites. Each site  $i$  corresponds to a vacancy and is geometrically defined by an index triplet  $\mathbf{m} = (m_i^x, m_i^y, m_i^z)$ , which determines physical position  $\mathbf{r} = \mathbf{m} \cdot \mathbf{a}$  via lattice constants  $\mathbf{a} = (a_x, a_y, a_z)^T$ . Accordingly, the total physical size of the lattice is given by  $X \times Y \times Z = M_x a_x \times M_y a_y \times M_z a_z$ . In the  $xy$ -plane, periodic boundary conditions are assumed; in the  $z$ -direction, the sample is stacked between two ideal gold contacts ( $\epsilon_r \rightarrow \infty$ ) at  $z = 0$  and  $Z$ , respectively. The local potential energy per vacancy site,  $E_i$ , is the superposition of three contributions

$$E_i = E_i^{\text{ref}} + E_i^{\text{F}} + E_i^{\text{C}} \quad (4)$$

where  $E_i^{\text{ref}}$  denotes the energy defined by a reference electrode,  $E_i^{\text{F}}$  is the contribution from an external electric field, and  $E_i^{\text{C}}$  is the potential generated by Coulombic interactions of mobile cations and their respective immobile anions. In the scope of this study, we arbitrarily set  $E_i^{\text{ref}} = 0$ .  $E_i^{\text{F}}$  is modeled as a linear potential drop along the  $z$ -axis

$$E_i^{\text{F}} = (q\phi_b - \Delta W) \frac{z_i}{Z} \quad (5)$$

where  $\phi_b$  denotes the applied bias potential,  $\Delta W$  is the difference in electrode work functions, and  $z_i$  is the  $z$ -coordinate of site  $i$ . Assuming two identical blocking electrodes, we may set  $\Delta W = 0$ .  $E_i^{\text{C}}$  is composed of the cation–cation interaction,  $E_i^{\text{cc}}$ , and the anion–cation interaction  $E_i^{\text{ac}}$ . Both components are treated accurately via a three-dimensional Ewald summation following the methodology established by Casalegno et al.<sup>41,42</sup> Since the anions are immobile,  $E_i^{\text{ac}}$  can be computed before the simulation. In contrast,  $E_i^{\text{cc}}$  is a function of the current position of all mobile cations and, thus, must be calculated and updated dynamically during the simulation. Note that our model does not consider immobile cations as they are locally neutralized by respective immobile anions from the underlying anion lattice. Accordingly, the local potential energy landscape defined by eq 4 is not altered by the presence of immobile cations and, thus, they do not modify the transport dynamics of the mobile cations.

The experimental set-up applies sample lengths,  $L_s$ , of about 150  $\mu\text{m}$ —a length scale that cannot be covered by any standard particle-based kMC simulation. However, the previous experimental findings demonstrate that SCL formation is restricted to a rather small fraction of the actual sample length (about 0.25%). For the most part, the sample remains in bulk conditions. Hence, we can artificially decrease  $L_s$  without disturbing the actual SCL formation. The only requirement is that the depletion and accumulation layers must not overlap. For instance, assuming SCL widths in the range of 200–300 nm (as recently determined by spectroscopic ellipsometry),<sup>13</sup> it is sufficient to consider a sample length of 1  $\mu\text{m}$ . The artificial reduction of the experimental sample length relies on the fundamental assumption that SCL formation is independent of the device length. This hypothesis stands in direct contrast to the results from the thermodynamic model developed by Braun et al.<sup>10</sup> Later, we will prove the validity of our hypothesis via a sensitivity analysis with respect to  $L_s$ . It is true that a shortened sample length does not perturb the steady-state distribution of  $\text{Li}^+$  ions. However, the time evolution of the SCL formation is undoubtedly a function of  $L_s$  as the sample length determines the electric field strength,  $\epsilon$ , and, thus, the drift velocity,  $v_{\text{d}}$ , of  $\text{Li}^+$  ions. In the present study, we assume that  $\epsilon$  is sufficiently low to guarantee a linear relationship between field strength and drift velocity.

The most critical aspect of the kMC model is the incorporation of a lower and an upper limit for the concentration

of mobile  $\text{Li}^+$  ions, in the following denoted  $c_{\text{min}}$  and  $c_{\text{max}}$  respectively. The lower limit is naturally given by  $c_{\text{min}} = 0$ . For the upper limit, we choose a rather pragmatic approach: the kMC model discretizes the SSE sample into a primitive orthorhombic lattice of vacancies that can only be occupied by one mobile  $\text{Li}^+$  ion at a time. Accordingly, the maximum possible concentration is dictated by the inverse volume of a unit cell,  $c_{\text{max}} = (a_x \times a_y \times a_z)^{-1}$ . The required lattice parameters of the vacancy grid are then chosen based on the given input value for  $c_{\text{max}}$ . For instance, imposing  $c_{\text{max}} = 4.5 \times 10^{18} \text{ cm}^{-3}$  yields lattice constants of  $a_x = a_y = a_z \approx 6 \text{ nm}$ . The choice of  $c_{\text{max}}$  also affects the strength of local Coulombic interactions. Low values of  $c_{\text{max}}$  result in large lattice constants and, thus, amplified electrostatic screening. All lattice parameters applied in this study are summarized in Table S1, Supporting Information (SI).

The simulation starts at  $t = 0$  with a random distribution of  $\text{Li}^+$  ions. The number of mobile cations is imposed by the volume of the simulation box and the given input bulk concentration  $c_{\text{Li}^+}^{\text{bulk}}$ . To ensure electroneutrality, we assume a homogeneous anionic background. The hopping of cations between two vacancy sites  $i$  and  $j$  is captured via the Miller–Abrahams formula<sup>43</sup>

$$k_{ij} = k_0 \cdot \begin{cases} \exp\left(-\frac{\Delta E_{ij}}{k_B T}\right), & \Delta E_{ij} < 0 \\ 1, & \Delta E_{ij} \geq 0 \end{cases} \quad (6)$$

where  $k_0$  is the attempt-to-hop frequency,  $\Delta E_{ij}$  denotes the difference in potential energy between vacancies  $i$  and  $j$ ,  $k_B$  is the Boltzmann constant, and  $T$  gives the absolute temperature. Hopping events are restricted to nearest-neighbor vacancies. The maximum attempt-to-hop frequency is estimated from the experimentally determined activation barrier for diffusion,  $E_a$ , according to an Arrhenius equation<sup>44</sup>

$$k_0 = \frac{k_B T}{h} \exp\left(-\frac{E_a}{k_B T}\right) \quad (7)$$

where  $h$  is the Planck constant. All simulations were conducted for  $T = 300 \text{ K}$  and  $E_a = 0.42 \text{ eV}$  resulting in a maximum hopping rate of  $k_0 \approx 0.55 \times 10^6 \text{ s}^{-1}$ . For nearest-neighbor hopping, the root mean diffusion length is given by the chosen lattice constants. To incorporate the influence of different lattice constants in the  $xyz$ -direction, we scale  $k_0$  by either  $a_x^{-2}$  or  $a_y^{-2}$  or  $a_z^{-2}$ , respectively, following the classical random walk model for diffusive motion.<sup>45</sup> For reasons of completeness, we note that the gold contacts are inert, corresponding to the experimental blocking conditions. In the scope of this study, the contacts exclusively represent electrostatic boundary conditions.

#### 4. COMPUTATIONAL ASPECTS AND DATA EVALUATION

In general, the simulation of the SCL formation in SSEs via kMC is a computationally demanding task. The high computational effort arises from the high number of mobile  $\text{Li}^+$  ions ( $N = 3000$ – $6000$  depending on the chosen set of input parameters) as the dynamic calculation of Coulombic energies via an optimized Ewald summation still scales as  $O(N^{3/2})$ .<sup>46</sup> To make the kMC simulations feasible in a reasonable amount of simulation time, we apply four different techniques to reduce the computational effort:

1. Application of modern C++: Our in-house kMC framework<sup>18</sup> is implemented within modern C++ and

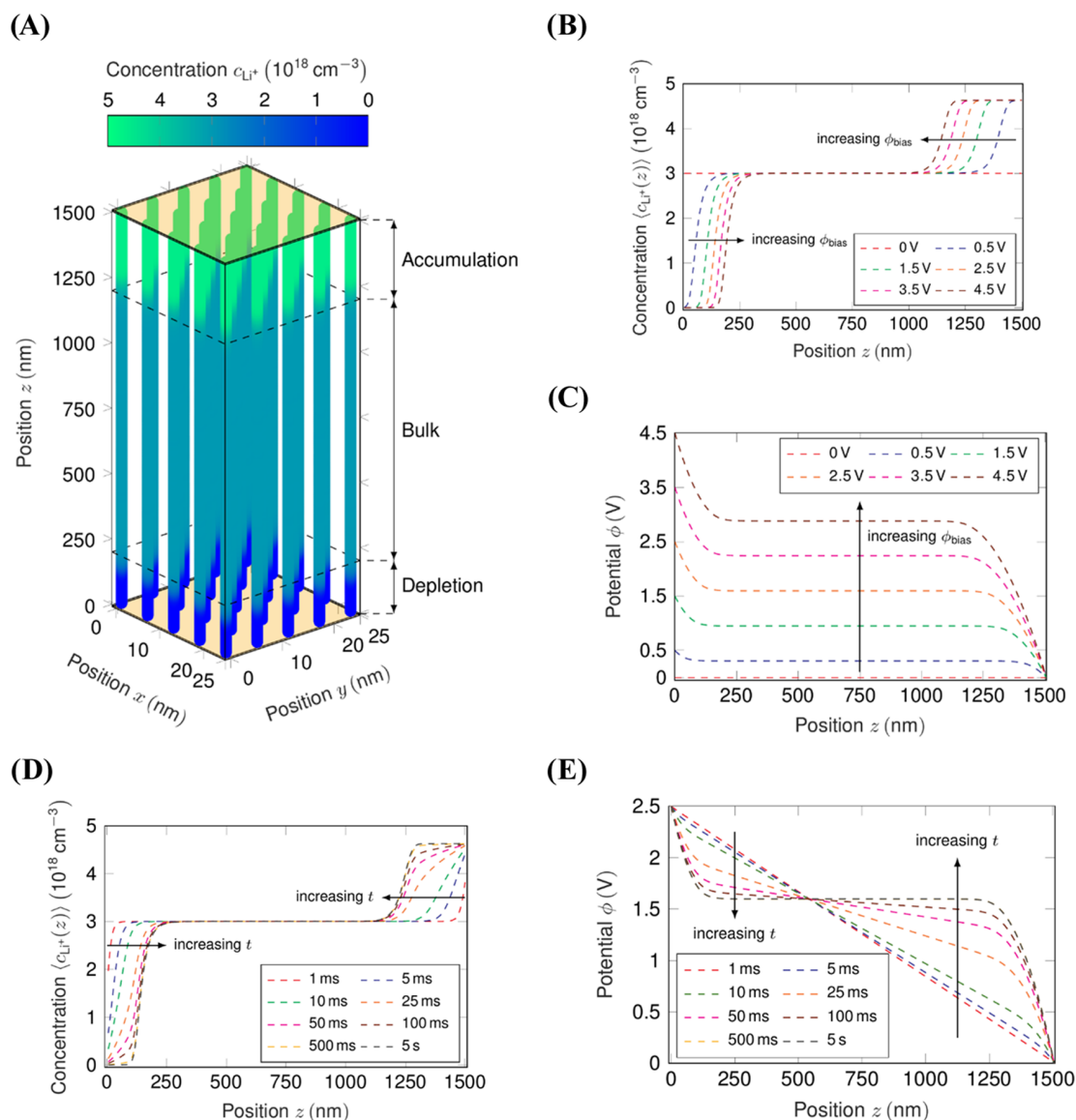


**Figure 2.** Simulation results for the standard parameter set. (A) Local concentration profile,  $c_{Li^+}(x,y,z)$ . (B) Averaged concentration profiles,  $\langle c_{Li^+}(z) \rangle$ , for variable  $\phi_{bias}$  and (C) corresponding potential profiles calculated via eq 9. (D) Time evolution of  $\langle c_{Li^+}(z) \rangle$  for  $\phi_{bias} = 2.5 V$  and (E) corresponding potential profiles. For the given sample length, the SCL formation reaches a steady state after approximately 500 ms.

makes heavy use of novel features from C++17 (e.g., parallel algorithms) and C++20 (e.g., ranges and views).

2. Caching of pair potentials: The system discretization is based on a regular grid that enables the precalculation (or caching) of all pair potentials possibly required by the Ewald summation. A detailed discussion can be found in ref 39.
3. Dipole-update method: By introducing a fictitious dipole into the update of Coulombic energies, the computational effort connected to nonmoving  $Li^+$  ion can be reduced to  $O(N)$ . The methodology was originally introduced in ref 47.
4. Parallelization: The update of Coulombic energies and the calculation of rate constants (cf. steps 2 and 3 in Figure 1A) correspond to loops running over the total number of involved  $Li^+$  ions. The computations for each  $Li^+$  ion are independent of each other and, thus, can be trivially parallelized.

Based on these techniques, we obtain an average simulation time per fixed input parameter combination of approximately 4 days using eight cores (Intel Xeon E-2288G@3.70 GHz) on the HPC server cluster of the Chair of Nano and Quantum Sensors at the Technical University of Munich.

The actual output quantities of the kMC model are time-dependent, three-dimensional profiles of relative vacancy occupation times. However, if not stated otherwise, we will consider the steady-state configuration, which enables us to drop the time dependency. From the relative occupation times, local concentration profiles,  $c_{Li^+}(x,y,z)$ , can be computed (cf. ref 39). Due to the homogeneity of the three-dimensional concentration profiles in the  $xy$ -plane (see Figure 1A), we may calculate averaged concentration profiles,  $\langle c_{Li^+}(z) \rangle$ , to simplify visualization and further discussion of the simulation results. The averaged concentration profiles, in turn, can be used to compute the average charge density

$$\langle \rho(z) \rangle = q(\langle c_{Li^+}(z) \rangle - \langle c_A(z) \rangle) \quad (8)$$

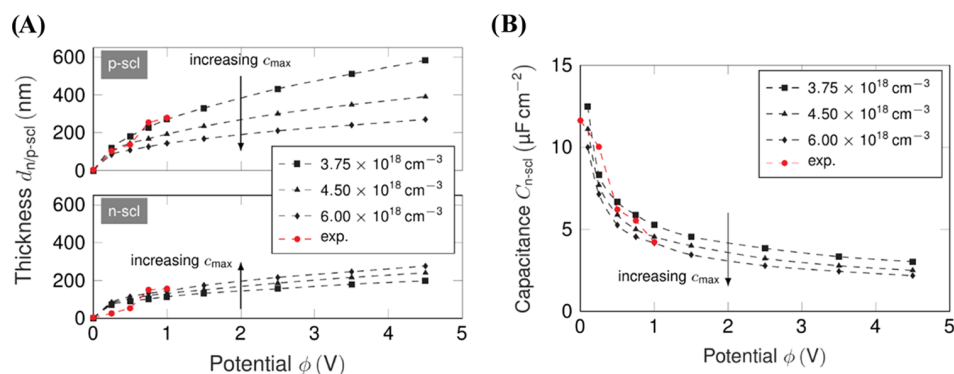


**Figure 3.** Comparison to experimental results. (A) SCL thicknesses  $d_{n/p-scl}$  as a function of  $\phi_{bias}$ . The thicknesses of depletion and accumulation layer from kMC were obtained via eqs 10 and 11, respectively. Red dots correspond to the experimental results obtained by spectroscopic ellipsometry. (B) Capacitance of the depletion layer,  $C_{n-scl}$ , as a function of  $\phi_{bias}$ . Capacitances from kMC were calculated via eq 12. Red dots correspond to the experimental results obtained by electrochemical impedance spectroscopy. In both plots, black squares, triangles, and diamonds illustrate the kMC results for different values of  $c_{max}$ .

where  $q$  is the elementary charge and  $\langle c_{A-}(z) \rangle = c_{Li^+}^{bulk} = \text{const.}$  is the concentration of the homogeneously distributed anionic background. Based on the one-dimensional charge density profiles, the Poisson equation may be solved to obtain corresponding potential profiles  $\phi(z)$

$$\frac{\partial^2}{\partial z^2} \phi(z) = -\frac{\langle \rho(z) \rangle}{\epsilon_0 \epsilon_r} \quad (9)$$

where  $\epsilon_0$  is the vacuum permittivity and  $\epsilon_r$  is the relative permittivity of the bulk SSE. To make the simulation results comparable to the experimental measurements, we have also determined the thicknesses of the accumulation and depletion layer, in the following denoted  $d_{p-scl}$  and  $d_{n-scl}$ , respectively. For this purpose, we have defined simple criteria to extract the extension of the SCLs from the one-dimensional density profiles: The depletion layer is represented by the part of the concentration profile that fulfills the inequation

$$\langle c_{Li^+}(z) \rangle \leq (1 - \delta) \cdot c_{Li^+}^{bulk} \quad (10)$$

where  $\delta = 0.1$  is a threshold value chosen according to the resolution of the SCL thicknesses determined by spectroscopic ellipsometry. Analogously, the accumulation layer is defined by

$$\langle c_{Li^+}(z) \rangle \geq (1 + \delta) \cdot c_{Li^+}^{bulk} \quad (11)$$

Finally, the SCL thicknesses are used to compute corresponding area-specific capacitances via the well-known formula of a parallel-plate capacitor

$$C_{n/p-scl} = \frac{\epsilon_0 \epsilon_r}{d_{n/p-scl}} \quad (12)$$

where  $\epsilon_r$  denotes the relative permittivity of the bulk SSE.

## 5. RESULTS AND DISCUSSION

Within the scope of this study, we want to investigate the SCL formation in SSEs with different physical properties. For this purpose, we vary the bulk concentration  $c_{Li^+}^{bulk} \in [5 \times 10^{17}, 3 \times 10^{18}, 1 \times 10^{19}] \text{ cm}^{-3}$ , the maximum concentration for accumulation of  $Li^+$  ions,  $c_{max} \in [1.25, 1.5, 2.0] \cdot c_{Li^+}^{bulk}$ , and relative permittivity of the bulk SSE,  $\epsilon_r \in [100, 677, 1400]$ . Additionally, the external bias potential  $\phi_{bias}$  is swept from 0 to 4.5 V in steps of 0.5 V to cover the full operating regime in a potential all-solid-state battery application. To elucidate the

characteristic time scale of ion redistribution, we have also simulated the time evolution of the SCL formation for 5 s for a set of standard input parameters determined in previous studies:

- Bulk concentration:  $c_{Li^+}^{bulk} = 3 \times 10^{18} \text{ cm}^{-3}$
- Maximum concentration:  $c_{max} = 1.5 c_{Li^+}^{bulk}$  (corresponds to the thickness ratio obtained by spectroscopic ellipsometry<sup>13</sup>)
- Permittivity:  $\epsilon_r = 677$  (corresponds to the value determined by impedance spectroscopy<sup>12</sup>)
- Bias potential:  $\phi_{bias} = 2.5 \text{ V}$

Since kMC is a stochastic algorithm, any statistically significant output quantity must be obtained as an average over a sufficient number of simulation runs. Here, we mostly consider steady-state quantities for which we may apply the block averaging technique as described in ref 39. In contrast, the results for the time-dependent SCL formation were generated by averaging over 50 independent simulation runs.

To rationalize the kMC simulation results, we first analyze the time-dependent ion redistribution for the standard input parameter set, see Figure 2. The local steady-state concentration profile,  $c_{Li^+}(x,y,z)$ , is illustrated in Figure 2A. The application of a positive bias potential leads to the formation of depletion and accumulation layers at the respective blocking electrodes, whereas the bulk SSE remains in an electroneutral condition. As outlined above, the homogeneity of the three-dimensional concentration profiles in the  $xy$ -plane allows us to consider averaged concentration profiles,  $\langle c_{Li^+}(z) \rangle$ , in the following. Figure 2B shows the averaged concentration profiles of the standard parametrization for variable  $\phi_{bias}$ . As expected, the SCL formation only occurs for nonzero bias potentials, and the SCL grows perpendicularly into the SSE when the potential is increased. The  $Li^+$  accumulation and depletion show an inherent asymmetry—due to the limits of accumulable and depletable charges:  $c_{min} \leq c_{Li^+} \leq c_{max}$ . If bulk concentration  $c_{Li^+,bulk}$  is unevenly spaced between  $c_{min}$  and  $c_{max}$  and the number of charges depleted and accumulated are equal, the SCLs will form asymmetrically.

The growth of the SCLs, however, does not scale linear—but rather reaches a plateau for high potentials. The density profile also shows that bulk stays indeed electroneutral as the  $Li^+$  density is equal to the anion density. The bulk is therefore effectively screened from the influence of the bias potential, which can also be observed in Figure 2C, where the potential



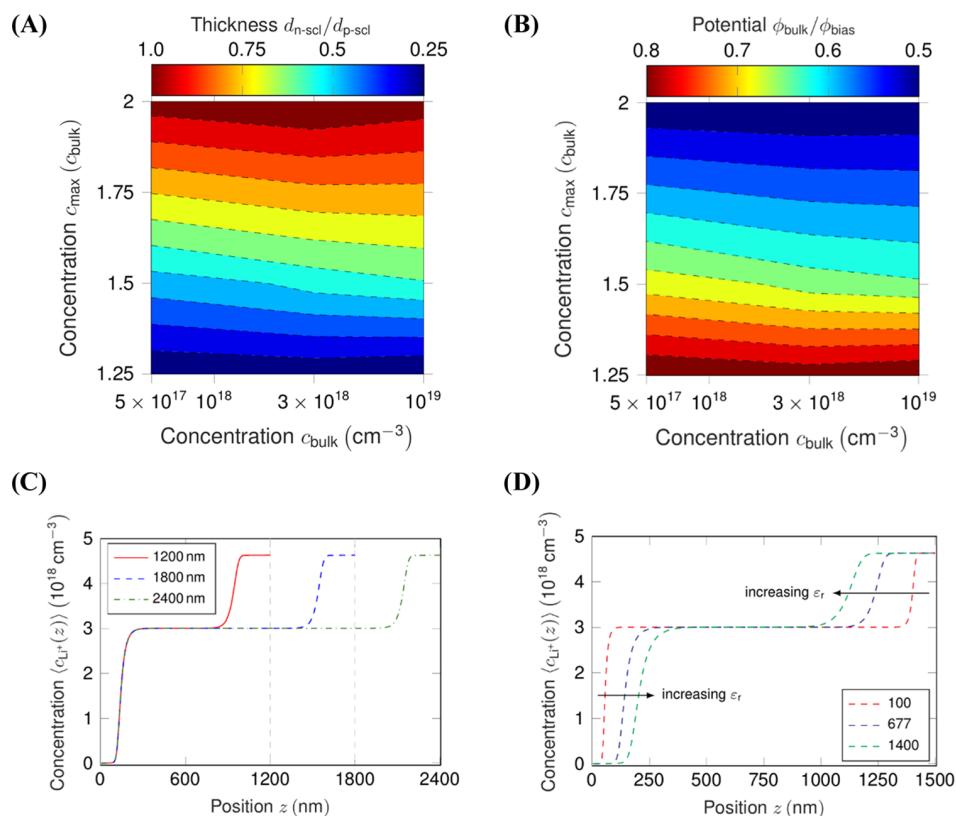


**Figure 4.** Sensitivity analysis. (A) Ratio  $\frac{d_{n-scl}}{d_{p-scl}}$  as a function of  $c_{bulk}$  and  $c_{max}$  for  $\epsilon_r = 677$  and  $\phi_{bias} = 2.5$  V. (B) Ratio  $\frac{\phi_{bulk}}{\phi_{bias}}$  as a function of  $c_{bulk}$  and  $c_{max}$  for  $\epsilon_r = 677$  and  $\phi_{bias} = 2.5$  V. (C) Averaged concentration profile,  $\langle c_{Li^+}(z) \rangle$ , of the standard parameter set for different sample lengths  $L_s$ . (D) Averaged concentration profile,  $\langle c_{Li^+}(z) \rangle$ , of the standard parameter set for different permittivities  $\epsilon_r$ .

profiles are calculated via eq 9. From the potential profiles, the asymmetry in the potential drops can be observed, as in this case a higher potential drop occurs in the accumulation layer compared to the depletion layer. The bulk potential is, therefore, shifted upward to the applied potential if the depletion layer is thinner than the accumulation layer. To conclude this first part of our analysis, we discuss the time evolution of the averaged concentration and the potential for the standard parameter set, see Figure 2D,E, respectively. The redistribution of cations induces a distortion of the initially linear potential drop over the sample. The SCL formation essentially occurs on a time scale of roughly 500 ms for the given device length of 1500 nm. Afterward, accumulation and depletion of mobile  $\text{Li}^+$  ions are negligible as recognizable by the identical potential profiles for 500 ms and 5 s. Assuming a linear relationship between electric field strength and drift velocity, we can scale up the time scale from kMC to an experimentally applied length of  $150 \mu\text{m}$ , which results in an SCL formation time of 50 s.

With the physical validity of the model proven, the results can be compared to the experimental results from our previous studies.<sup>12,13</sup> Note that the experimental range of bias potentials is restricted to  $0 \text{ V} \leq \phi_{bias} \leq 1 \text{ V}$  to ensure that gold acts as a blocking electrode, see refs 12 and 48 for a detailed discussion. In contrast, the kMC simulations can be extended to larger potentials to extrapolate the trend in the experimental data. With the thickness of the SCLs being the most prominent parameter, the experimental results obtained by in situ spectroscopic ellipsometry are shown in Figure 3A with the typical asymmetric increase of thickness depending on whether the accumulation

layer (positive biases) or the depletion layer (negative biases) are observed. The accumulation layer is roughly 1.5 times larger than the depletion layer. A plateau formation can be observed for potentials larger than 0.5 V, correlating to a fully depleted or filled lattice after which the SCL grows perpendicular to the SSE. Quantitatively, the thicknesses range from 50 to 330 nm depending on the applied bias. The kMC simulations agree to all observations if the physical parameters ( $\text{Li}^+$ -ion and vacancy concentration and dielectric constant) are chosen carefully. While the simulated bias potential range is larger than the experimentally feasible range, the same strong increase in SCL thickness can be observed when the bias potential is increased. The bias potential at which the SCL thickness is observed to be minimal in the experimental data matches that of 0 V bias potential in the kMC simulation, indicating that the electrochemical potential difference between the Au electrode and SSE is negligible. The experimentally determined spatial extent of the SCLs matches that of the kMC simulation for the standard parameters chosen—proving the closeness of the parameters to the true physical values.

There is a second property of the SCLs that can be validated experimentally, which is independent of the spatial extent: the capacitance. Experimentally, only the capacitance of the depletion layer is accessible, which is explained in previous work, see ref 12. The derivation of the SCL capacitance from the kMC simulations can be done by eq 12. Electrochemical impedance spectroscopy (EIS) was used to obtain the data in Figure 3B showing a strong decrease with increasing potential. The experimentally observed capacitances range between 4 and

12  $\mu\text{F}/\text{cm}^2$ , which is in good quantitative agreement with the simulated capacitances. However, one exception is given by the capacitance value for 0 V bias potential. Here, we obtain a depletion layer thickness of 0 nm based on the criterion defined in eq 10, which would result in an infinitely large capacitance. This limitation is going to be addressed in future work by refining the simulation model as well as the criterion for extracting the SCL thicknesses. Nevertheless, the kMC simulations are capable of capturing the physical behavior of the experimentally predicted SCL formation for a wide range of bias potentials. Next, the sensitivity of the SCL formation on the input parameters is studied to see how material properties impact the thickness and asymmetry of SCLs.

As introduced above, three physical parameters are of fundamental importance to the kMC simulations: the  $\text{Li}^+$ -ion concentrations (bulk and maximal) and the dielectric constant. The impact of the limits on the  $\text{Li}^+$ -ion concentration can be split into two considerations: If the bulk  $\text{Li}^+$ -ion concentration varies, the accumulation layer should be unaffected as the upper  $\text{Li}^+$  concentration is not dependent on the number of  $\text{Li}^+$  ions present in the bulk. Therefore, only the depletion layer changes when the bulk  $\text{Li}^+$ -ion concentration is changed. For lower concentration deviations for a depleted lattice (i.e., lower bulk  $\text{Li}^+$ -ion concentration), the depletion layer must grow larger to hold a similar charge (assuming an equal potential drop and dielectric constant) and vice versa. However, the maximal concentration for  $\text{Li}^+$  ion only impacts the accumulation layer formation by defining the maximal concentration change. The asymmetry is most easily observed when viewing the ratio of the accumulation layer to depletion layer thickness for a given potential. Figure 4A shows the dependence of the ratio  $\frac{d_{n-\text{scl}}}{d_{p-\text{scl}}}$  for bulk densities between  $5 \times 10^{17}$  and  $1 \times 10^{19} \text{ cm}^{-3}$  and maximal densities between 1.25 and 2 times the bulk density. The depletion and accumulation layer are of the same thickness if the accumulable concentration is the same as the depletable (i.e.,  $n_{\text{max}} = 2 \cdot n_{\text{bulk}}$ ), which is the same as claiming that the amount of concentration deviation is equal in both directions. If the accumulable concentration is much lower than the bulk concentration ( $n_{\text{max}} = 1.25 \cdot n_{\text{bulk}}$ ), the accumulation layer grows much larger than the depletion layer as it cannot hold an equal amount of charge per volume. While these conclusions are to be expected from a concentration point of view and could have been predicted by merely claiming the charge distribution to happen within the boundaries and a certain number of charges moved from depletion to accumulation layer, the dependence of the ratio on the actual bulk  $\text{Li}^+$ -ion density is somewhat unexpected. A close look at the actual model input compared to the nominal value of  $c_{\text{max}}$ , see Table S1 (SI), explains this behavior. As shown in Figure 4A, the distribution of the ratio becomes more pronounced for higher bulk concentrations, a fact pointing toward a fundamental difference to the results from the aforementioned thermodynamic model.<sup>10</sup> Not only does this impact the thickness of the layers but also the potential of the bulk SSE—which is electroneutral and therefore has a constant potential, as shown in Figure 4B. The constant bulk potential is not right in the center between the two electrodes, i.e.,  $\phi_{\text{bulk}} = 0.5 \phi_{\text{bias}}$ , but shifted upward if the layers of not of equal widths.

While the asymmetry is affected by the charge carrier concentrations, as one would expect from basic electrochemical considerations, the impact of the sample or device length on the charge accumulation is not obvious. As shown in Figure 4C, the

bulk SSE stays completely electroneutral—and should therefore not impact the charge accumulation. However, the Debye-like length, which has been described in the thermodynamic model, predicts a direct, inverse proportionality of the SCL thicknesses to the sample length. For a set of three different device lengths with otherwise equal parameters, the thicknesses of the SCLs are shown to be constant in Figure 4C. With a variation of the device length between 1.2 and 2.4  $\mu\text{m}$ , the depletion layer does not change its position or shape, and the accumulation layer is simply shifted toward the geometric end of the device where it is in contact with the electrode. Therefore, the simulated charge carrier concentrations, and thus potential profiles, are independent of the device length. The impact of the dielectric constant, which ranges quite drastically between easily polarizable polymer electrolytes<sup>49</sup> and rigid SSEs,<sup>50</sup> is shown in Figure 4D. Higher polarizability leads to thicker SCLs, which agrees with the parallel plate capacitor analog as well as the Debye screening theory.

## 6. CONCLUSIONS

Overall, the findings of the kMC simulations are in good agreement with the thermodynamic simulations in ref 10, which predict the same perpendicular growth when the bias potential is increased. Not only do simulations show the same qualitative SCL growth but only employing two fundamental input parameters (the bulk and maximal charge carrier concentrations) can predict the order of magnitude of the SCL thicknesses in different materials. Physically coherent, the device/sample length is shown not to impact the SCL formation for three different lengths with only the electroneutral bulk growing. The calculated capacitances of the depletion layers match the experimental data of a previous study with—considering that only approximations of the input parameters are available—astonishing accuracy.

Moreover, a comparison of the accumulation layer, where the maximal ion concentration comes into play, cannot be achieved with impedance data, as this analysis is limited to the resistive depletion layer. The comparison of spectroscopic ellipsometry data of a previous study proves that the ratio of positive and negative SCLs is accurately represented by the kMC simulations.

Notably, the charge distributions can be directly transformed into potential profiles, which reveal that the potential drops are not equal at the two interfaces. The electrochemical stability of SSEs toward anode and cathode materials is a commonly discussed problem. When the stability of the anode and cathode is known, the charge carrier concentrations, therefore, allow to tune the bulk potential and thus the potential drops—possibly allowing higher overall voltages or different electrode materials.

## ■ ASSOCIATED CONTENT

### Supporting Information

The Supporting Information is available free of charge at <https://pubs.acs.org/doi/10.1021/acs.jpcc.2c02481>.

Nominal and actual maximum concentrations in table format (PDF)

## ■ AUTHOR INFORMATION

### Corresponding Authors

Alessio Gagliardi — Department of Electrical and Computer Engineering, Technical University of Munich, 85748 Garching bei München, Germany; [orcid.org/0000-0002-3322-2190](https://orcid.org/0000-0002-3322-2190); Email: [alessio.gagliardi@tum.de](mailto:alessio.gagliardi@tum.de)

Aliaksandr S. Bandarenka – *Physics of Energy Conversion and Storage, Physik-Department, Technische Universität München, 85748 Garching bei München, Germany; Catalysis Research Center TUM, 85748 Garching bei München, Germany;* [orcid.org/0000-0002-5970-4315](https://orcid.org/0000-0002-5970-4315); Email: [bandarenka@ph.tum.de](mailto:bandarenka@ph.tum.de)

## Authors

Leon Katzenmeier – *Physics of Energy Conversion and Storage, Physik-Department, Technische Universität München, 85748 Garching bei München, Germany; TUMint-Energy Research, 85748 Garching bei München, Germany*

Manuel Gößwein – *Department of Electrical and Computer Engineering, Technical University of Munich, 85748 Garching bei München, Germany;* [orcid.org/0000-0002-4804-7954](https://orcid.org/0000-0002-4804-7954)

Complete contact information is available at:

<https://pubs.acs.org/10.1021/acs.jpcc.2c02481>

## Author Contributions

<sup>†</sup>L.K. and M.G. contributed equally to this work.

## Notes

The authors declare no competing financial interest.

## ACKNOWLEDGMENTS

This work is part of the ASSB Bayern project funded by the Bavarian Ministry of Economic Affairs, Regional Development, and Energy. Furthermore, the authors acknowledge the European Union's Horizon 2020 FETOPEN 2018–2020 program "LION-HEARTED" under grant agreement no. 828984 for funding. A.S.B. and A.G. acknowledge financial support from TUM Innovation Network for Artificial Intelligence powered Multifunctional Material Design (ARTEMIS) and funding in the framework of Deutsche Forschungsgemeinschaft (DFG, German Research Foundation) under Germany's Excellence Strategy—EXC 2089/1—390776260 (e-conversion).

## REFERENCES

- (1) Goodenough, J. B. Energy Storage Materials: A Perspective. *Energy Storage Mater.* **2015**, *1*, 158–161.
- (2) Isenberg, A. O. Energy Conversion Via Solid Oxide Electrolyte Electrochemical Cells at High Temperatures. *Solid State Ionics* **1981**, *3–4*, 431–437.
- (3) Banno, N.; Sakamoto, T.; Iguchi, N.; Sunamura, H.; Terabe, K.; Hasegawa, T.; Aono, M. Diffusivity of Cu Ions in Solid Electrolyte and Its Effect on the Performance of Nanometer-scale Switch. *IEEE Trans. Electron Devices* **2008**, *55*, 3283–3287.
- (4) Wang, C.; Bai, G.; Yang, Y.; Liu, X.; Shao, H. Dendrite-free All-solid-state Lithium Batteries with Lithium Phosphorous Oxynitride-modified Lithium Metal Anode and Composite Solid Electrolytes. *Nano Res.* **2019**, *12*, 217–223.
- (5) Mertens, A.; Yu, S.; Schön, N.; Gunduz, D. C.; Tempel, H.; Schierholz, R.; Eichel, R. A.; et al. Superionic Bulk Conductivity in  $\text{Li}_{1.3}\text{Al}_{0.3}\text{Ti}_{1.7}(\text{PO}_4)_3$  Solid Electrolyte. *Solid State Ionics* **2017**, *309*, 180–186.
- (6) Yu, C.; Ganapathy, S.; Van Eck, E. R.; Wang, H.; Basak, S.; Li, Z.; Wagemaker, M. Accessing the Bottleneck in All-solid State Batteries, Lithium-ion Transport Over the Solid-electrolyte-electrode Interface. *Nat. Commun.* **2017**, *8*, No. 1086.
- (7) Culver, S. P.; Koerver, R.; Krauskopf, T.; Zeier, W. G. Designing Ionic Conductors: The Interplay between Structural Phenomena and Interfaces in Thiophosphate-based Solid-state Batteries. *Chem. Mater.* **2018**, *30*, 4179–4192.
- (8) Zhu, Y.; He, X.; Mo, Y. Origin of Outstanding Stability in the Lithium Solid Electrolyte Materials: Insights from Thermodynamic

Analyses Based on First-principles Calculations. *ACS Appl. Mater. Interfaces* **2015**, *7*, 23685–23693.

(9) Ma, C.; Cheng, Y.; Yin, K.; Luo, J.; Sharafi, A.; Sakamoto, J.; Chi, M.; et al. Interfacial Stability of Li Metal–solid Electrolyte Elucidated Via in Situ Electron Microscopy. *Nano Lett.* **2016**, *16*, 7030–7036.

(10) Braun, S.; Yada, C.; Latz, A. Thermodynamically Consistent Model for Space-charge-layer Formation in a Solid Electrolyte. *J. Phys. Chem. C* **2015**, *119*, 22281–22288.

(11) de Klerk, N. J. J.; Wagemaker, M. Space-charge Layers in All-solid-state Batteries; Important or Negligible? *ACS Appl. Energy Mater.* **2018**, *1*, 5609–5618.

(12) Katzenmeier, L.; Helmer, S.; Braxmeier, S.; Knobbe, E.; Bandarenka, A. S. Properties of the Space Charge Layers Formed in Li-ion Conducting Glass Ceramics. *ACS Appl. Mater. Interfaces* **2021**, *13*, 5853–5860.

(13) Katzenmeier, L.; Carstensen, L.; Schaper, S. J.; Müller-Buschbaum, P.; Bandarenka, A. S. Characterization and Quantification of Depletion and Accumulation Layers in Solid-state  $\text{Li}^+$ -conducting Electrolytes Using in Situ Spectroscopic Ellipsometry. *Adv. Mater.* **2021**, *33*, No. 2100585.

(14) Watzele, S. A.; Katzenmeier, L.; Sabawa, J. P.; Garlyyev, B.; Bandarenka, A. S. Temperature Dependences of the Double Layer Capacitance of Some Solid/liquid and Solid/solid Electrified Interfaces. An Experimental Study. *Electrochim. Acta* **2021**, *391*, No. 138969.

(15) Park, M.; Zhang, X.; Chung, M.; Less, G. B.; Sastry, A. M. A Review of Conduction Phenomena in Li-ion Batteries. *J. Power Sources* **2010**, *195*, 7904–7929.

(16) Funke, K. Debye-Hückel-type Relaxation Processes in Solid Ionic Conductors: The Model. *Solid State Ionics* **1986**, *18–19*, 183–190.

(17) Bässler, H. Charge Transport in Disordered Organic Photoconductors. A Monte Carlo Simulation Study. *Phys. Status Solidi B* **1993**, *175*, 15–56.

(18) Kaiser, W.; Popp, J.; Rinderle, M.; Albes, T.; Gagliardi, A. Generalized Kinetic Monte Carlo Framework for Organic Electronics. *Algorithms* **2018**, *11*, No. 37.

(19) Kaiser, W.; Albes, T.; Gagliardi, A. Charge Carrier Mobility of Disordered Organic Semiconductors with Correlated Energetic and Spatial Disorder. *Phys. Chem. Chem. Phys.* **2018**, *20*, 8897–8908.

(20) Kaiser, W.; Gößwein, M.; Gagliardi, A. Acceleration Scheme for Particle Transport in Kinetic Monte Carlo Methods. *Chem. Phys.* **2020**, *152*, No. 174106.

(21) Piana, S.; Gale, J. D. Three-dimensional Kinetic Monte Carlo Simulation of Crystal Growth from Solution. *J. Cryst. Growth* **2006**, *294*, 46–52.

(22) Rak, M.; Izdebski, M.; Brozi, A. Kinetic Monte Carlo Study of Crystal Growth from Solution. *Comput. Phys. Commun.* **2001**, *138*, 250–263.

(23) Dybeck, E. C.; Plaisance, C. P.; Neurock, M. Generalized Temporal Acceleration Scheme for Kinetic Monte Carlo Simulations of Surface Catalytic Processes by Scaling the Rates of Fast Reactions. *J. Chem. Theory. Comput.* **2017**, *13*, 1525–1538.

(24) Jørgensen, M.; Grönbeck, H. Scaling Relations and Kinetic Monte Carlo Simulations to Bridge the Materials Gap in Heterogeneous Catalysis. *ACS Catal.* **2017**, *7*, 5054–5061.

(25) Jørgensen, M.; Grönbeck, H. MonteCoffee: A Programmable Kinetic Monte Carlo Framework. *J. Chem. Phys.* **2018**, *149*, No. 114101.

(26) Jørgensen, M.; Grönbeck, H. Selective Acetylene Hydrogenation Over Single-atom Alloy Nanoparticles by Kinetic Monte Carlo. *J. Am. Chem. Soc.* **2019**, *141*, 8541–8549.

(27) Magna, A.; Coffa, S.; Colombo, L. A Lattice Kinetic Monte Carlo Code for the Description of Vacancy Diffusion and Self-organization in Si. *Nucl. Instrum. Methods Phys. Res., Sect. B* **1999**, *148*, 262–267.

(28) Grabowski, M.; Rogal, J.; Drautz, R. Kinetic Monte Carlo Simulations of Vacancy Diffusion in Nondilute Ni-X (X = Re, W, Ta) Alloys. *Phys. Rev. Mater.* **2018**, *2*, No. 123403.

(29) Drews, T. O.; Radisic, A.; Erlebacher, J.; Braatz, R. D.; Searson, P. C.; Alkire, R. C. Stochastic Simulation of the Early Stages of Kinetically Limited Electrodeposition. *J. Electrochem. Soc.* **2006**, *153*, C434.

(30) Andreas, B.; Eikerling, M. Active Site Model for Co Adlayer Electrooxidation on Nanoparticle Catalysts. *J. Electroanal. Chem.* **2007**, *607*, 121–132.

(31) Pornprasertsuk, R.; Cheng, J.; Huang, H.; Prinz, F. B. Electrochemical Impedance Analysis of Solid Oxide Fuel Cell Electrolyte Using Kinetic Monte Carlo Technique. *Solid State Ionics* **2007**, *178*, 195–205.

(32) Blanquer, G.; Yin, Y.; Quiroga, M. A.; Franco, A. A. Modeling Investigation of the Local Electrochemistry in Lithium-O<sub>2</sub> Batteries: A Kinetic Monte Carlo Approach. *J. Electrochem. Soc.* **2016**, *163*, A329.

(33) Yao, Z.; Kim, S.; Michel, K.; Zhang, Y.; Aykol, M.; Wolverton, C. Stability and Conductivity of Cation-and Anion-substituted LiBH<sub>4</sub>-based Solid-state Electrolytes. *Phys. Rev. Mater.* **2018**, *2*, No. 065402.

(34) Dean, J. M.; Coles, S. W.; Saunders, W. R.; McCluskey, A. R.; Wolf, M. J.; Walker, A. B.; Morgan, B. J. Overscreening and Underscreening in Solid-electrolyte Grain Boundary Space-charge Layers. *Phys. Rev. Lett.* **2021**, *127*, No. 135502.

(35) Martin, S. W.; Yao, W.; Berg, K. Space Charge Polarization Measurements As a Method to Determine the Temperature Dependence of the Number Density of Mobile Cations in Ion Conducting Glasses. *Z. Phys. Chem.* **2009**, *223*, 1379–1393.

(36) Armand, M. Polymer Solid Electrolytes - an Overview. *Solid State Ionics* **1983**, *9–10*, 745–754.

(37) Zhang, H.; Chen, F.; Lakuntza, O.; Oteo, U.; Qiao, L.; Martinez-Ibañez, M.; Armand, M.; et al. Suppressed Mobility of Negative Charges in Polymer Electrolytes with an Ether-functionalized Anion. *Angew. Chem.* **2019**, *131*, 12198–12203.

(38) Aizawa, Y.; Yamamoto, K.; Sato, T.; Murata, H.; Yoshida, R.; Fisher, C. A.; Hirayama, T.; et al. In situ electron holography of electric potentials inside a solid-state electrolyte: effect of electric-field leakage. *Ultramicroscopy* **2017**, *178*, 20–26.

(39) Bohinc, K.; Kralj-Iglič, V.; Igljč, A. Thickness of Electrical Double Layer. Effect of Ion Size. *Electrochim. Acta* **2001**, *46*, 3033–3040.

(40) Gillespie, D. T. Exact Stochastic Simulation of Coupled Chemical Reactions. *J. Phys. Chem. A* **1977**, *81*, 2340–2361.

(41) Casalegno, M.; Raos, G.; Po, R. Methodological Assessment of Kinetic Monte Carlo Simulations of Organic Photovoltaic Devices: The Treatment of Electrostatic Interactions. *J. Phys. Chem. C* **2010**, *132*, No. 094705.

(42) Casalegno, M.; Bernardi, A.; Raos, G. Numerical Simulation of Photocurrent Generation in Bilayer Organic Solar Cells: Comparison of Master Equation and Kinetic Monte Carlo Approaches. *J. Phys. Chem. B* **2013**, *139*, No. 024706.

(43) Miller, A.; Abrahams, E. Impurity Conduction at Low Concentrations. *Phys. Rev.* **1960**, *120*, 745.

(44) Atkins, P.; De Paula, J.; Keeler, J. *Atkins' Physical Chemistry*; Oxford University Press: New York, 2018.

(45) Chandrasekhar, S. Stochastic Problems in Physics and Astronomy. *Rev. Mod. Phys.* **1943**, *15*, 1.

(46) Allen, M. P.; Tildesley, D. J. *Computer Simulation of Liquids*; Oxford University Press: New York, 2017.

(47) van der Kaap, N. J.; Koster, L. J. A. Massively Parallel Kinetic Monte Carlo Simulations of Charge Carrier Transport in Organic Semiconductors. *J. Comput. Phys.* **2016**, *307*, 321–332.

(48) Katzenmeier, L.; Carstensen, L.; Bandarenka, A. S. Li<sup>+</sup> Conductivity of Space Charge Layers Formed at Electrified Interfaces Between a Model Solid-State Electrolyte and Blocking Au-Electrodes. *ACS Appl. Mater. Interfaces* **2022**, *14*, 15811–15817.

(49) Das, S.; Ghosh, A. Ionic Conductivity and Dielectric Permittivity of PEO-LiClO<sub>4</sub> Solid Polymer Electrolyte Plasticized with Propylene Carbonate. *AIP Adv.* **2015**, *5*, No. 027125.

(50) Yu, K.; Tian, Y.; Gu, R.; Jin, L.; Ma, R.; Sun, H.; Wei, X. Ionic Conduction, Colossal Permittivity and Dielectric Relaxation Behavior of Solid Electrolyte Li<sub>3-x</sub>La<sub>2/3-x</sub>TiO<sub>3</sub> Ceramics. *J. Eur. Ceram. Soc.* **2018**, *38*, 4483–4487.

## Recommended by ACS

### Species Distribution During Solid Electrolyte Interphase Formation on Lithium Using MD/DFT-Parameterized Kinetic Monte Carlo Simulations

Michail Gerasimov, Ulrike Krewer, et al.

MARCH 01, 2023

THE JOURNAL OF PHYSICAL CHEMISTRY C

READ 

### Effect of the Electric Double Layer (EDL) in Multicomponent Electrolyte Reduction and Solid Electrolyte Interphase (SEI) Formation in Lithium Batteries

Qisheng Wu, Yue Qi, et al.

JANUARY 23, 2023

JOURNAL OF THE AMERICAN CHEMICAL SOCIETY

READ 

### Revealing the Multifunctions of Li<sub>3</sub>N in the Suspension Electrolyte for Lithium Metal Batteries

Mun Sek Kim, Yi Cui, et al.

JANUARY 26, 2023

ACS NANO

READ 

### Mass and Charge Transport in Li<sub>1-x</sub>CoO<sub>2</sub> Thin Films—A Complete Set of Properties and Its Defect Chemical Interpretation

Andreas E. Bumberger, Juergen Fleig, et al.

NOVEMBER 21, 2022

CHEMISTRY OF MATERIALS

READ 

Get More Suggestions >

# Mass Transport and Charge Transfer Through an Electrified Interface Between Metallic Lithium and Solid-State Electrolytes

?🗨️

---

RightsLink

**Mass transport and charge transfer through an electrified interface between metallic lithium and solid-state electrolytes**

**Author:** Leon Katzenmeier et al

**Publication:** Communications Chemistry

**Publisher:** Springer Nature

**Date:** Jun 15, 2023

*Copyright © 2023, The Author(s)*

**Creative Commons**

This is an open access article distributed under the terms of the [Creative Commons CC BY](#) license, which permits unrestricted use, distribution, and reproduction in any medium, provided the original work is properly cited.

You are not required to obtain permission to reuse this article.

To request permission for a type of use not listed, please contact [Springer Nature](#)

© 2023 Copyright - All Rights Reserved | [Copyright Clearance Center, Inc.](#) | [Privacy statement](#) | [Data Security and Privacy](#)  
| [For California Residents](#) | [Terms and Conditions](#)Comments? We would like to hear from you. E-mail us at [customer@copyright.com](mailto:customer@copyright.com)

The following publication is reprinted with permission from ref. 104, *Comm. Chem.* **2023**, *6*, 124. This article is licensed under a Creative Commons Attribution 4.0 International License.<sup>†</sup>

<sup>†</sup><https://creativecommons.org/licenses/by/4.0/>

## Mass transport and charge transfer through an electrified interface between metallic lithium and solid-state electrolytes

Leon Katzenmeier<sup>1,2,6</sup>, Manuel Gößwein <sup>3,6</sup>, Leif Carstensen<sup>1,2</sup>, Johannes Sterzinger <sup>2</sup>, Michael Ederer<sup>2</sup>, Peter Müller-Buschbaum <sup>4,5</sup>, Alessio Gagliardi<sup>3</sup>  & Aliaksandr S. Bandarenka <sup>1</sup> 

All-solid-state Li-ion batteries are one of the most promising energy storage devices for future automotive applications as high energy density metallic Li anodes can be safely used. However, introducing solid-state electrolytes needs a better understanding of the forming electrified electrode/electrolyte interface to facilitate the charge and mass transport through it and design ever-high-performance batteries. This study investigates the interface between metallic lithium and solid-state electrolytes. Using spectroscopic ellipsometry, we detected the formation of the space charge depletion layers even in the presence of metallic Li. That is counterintuitive and has been a subject of intense debate in recent years. Using impedance measurements, we obtain key parameters characterizing these layers and, with the help of kinetic Monte Carlo simulations, construct a comprehensive model of the systems to gain insights into the mass transport and the underlying mechanisms of charge accumulation, which is crucial for developing high-performance solid-state batteries.

<sup>1</sup>Technical University of Munich, TUM School of Natural Sciences, Department of Physics, Physics of Energy Conversion and Storage, James-Franck-Str. 1, 85748 Garching, Germany. <sup>2</sup>TUMint-Energy Research, Lichtenbergstr. 4, 85748 Garching bei München, Germany. <sup>3</sup>Technical University of Munich, TUM School of Computation, Information and Technology, Department of Electrical and Computer Engineering, Hans-Piloyt-Straße 1, 85748 Garching bei München, Germany. <sup>4</sup>Technical University of Munich, TUM School of Natural Sciences, Department of Physics, Chair for Functional Materials, James-Franck-Str. 1, 85748 Garching, Germany. <sup>5</sup>Heinz Maier-Leibnitz Zentrum (MLZ), Technical University of Munich, Lichtenbergstr. 1, 85748 Garching, Germany. <sup>6</sup>These authors contributed equally: Leon Katzenmeier, Manuel Gößwein. ✉email: [alessio.gagliardi@tum.de](mailto:alessio.gagliardi@tum.de); [bandarenka@ph.tum.de](mailto:bandarenka@ph.tum.de)

All-solid-state batteries (ASSB) attract increasing attention as a promising alternative to traditional Li-ion batteries due to their potentially higher energy density, longer lifespan, and improved safety<sup>1,2</sup>. The solid-state electrolyte (SSE) used in ASSBs replaces the liquid or polymer electrolyte used in conventional Li-ion batteries and enables the use of metallic lithium (Li(s)) anode<sup>3,4</sup>. The holy grail of the anode materials promises 3860 mAh g<sup>-1</sup><sup>5</sup>, but it is inherently challenging to stabilize them due to the formation of dendrites and inhomogeneous plating/stripping reactions<sup>6,7</sup>. As such, one of the significant challenges in developing solid-state batteries is the charge accumulation at the Li(s)/SSE interface<sup>8</sup>. This charge accumulation occurs due to the mismatch in electrochemical potential between the Li(s) and the SSE, forming a space charge layer (SCL) at the interface<sup>9,10</sup>. The SCL can cause significant changes in the local concentration of mobile Li-ions in the SSE, leading to increased interfacial resistance<sup>11,12</sup>.

The concept of SCL, describing a depletion or accumulation of mobile Li-ions, has been the focus of our previous work; until now, however, only under ion-blocking conditions<sup>13</sup>. In this case, with no mass transport across any of the two interfaces, the Li-ions will deplete on one side and thus accumulate on the far side of the electrolyte<sup>14</sup>. Globally, charge neutrality prevails in the SSE<sup>15</sup>, with the total amount of additional charge at the two interfaces being equal. The blocking electrode configuration was previously studied using electrochemical impedance spectroscopy (EIS) and spectroscopic ellipsometry (SE). While SE revealed an asymmetric but wide (>100 nm) charge depletion and accumulation layers on either side of the SSE<sup>11</sup>, no information about the faradaic electrochemical behavior of the SCLs could be obtained<sup>13</sup>. A recent EIS study revealed that the conductivity inside the SCLs is at least one order of magnitude lower than the bulk conductivity, which should significantly influence battery performance<sup>12</sup>. A review on the SCL formation between sulfide SSEs and oxide cathodes revealed a significant charge accumulation<sup>16</sup>. To understand the importance of the SCL formation in solid-state electrochemistry, a quick jump into semiconductors reveals a very insightful analogy. When two semiconductors of different chemical potential for electrons are brought into contact, a non-conductive depletion layer forms. When the same happens in between two ion conductors (such as a SSE and an electrode material), the interface resistances grows dramatically.

To rationalize the experimental results from EIS and SE by means of a theoretical model, we recently developed a simple yet predictive kinetic Monte Carlo<sup>17,18</sup> (kMC) model to simulate the mass-transport phenomenon in SSEs, including the electrostatic interactions among ionic species, under blocking conditions<sup>19</sup>. The validity of our kMC approach was proven by reproducing the quantitative trends in SCL thicknesses and depletion layer capacitance. Moreover, the kMC simulation enabled us to determine inaccessible physical quantities via experiments such as local concentration and potential profiles as well as their time evolution into a steady state. The analysis of local concentration profiles as a function of an applied bias potential demonstrated that the depletion and accumulation layers' perpendicular growth regime is directly connected to a fully depleted or fully occupied vacancy lattice, respectively. This observation agrees with previous experimental findings and other modeling approaches, such as thermodynamic simulations<sup>9</sup>. Remarkably, the kMC model requires only a minimal set of physically coherent input parameters mostly available via direct experimental measurement: (1) the bulk concentration of mobile Li-ions ( $c_{\text{Li}^+, \text{bulk}}$ ), (2) the maximum concentration of mobile Li-ions in a fully occupied lattice ( $c_{\text{max}}$ ), (3) the relative permittivity of the bulk SSE ( $\epsilon_r$ ) and (4) the applied bias potential ( $\phi_{\text{bias}}$ ). The consequent next step is the extension of the original setup for non-blocking conditions to

investigate the mass transport between Li(s) and a corresponding oxide SSE. For this purpose, we can exploit one of the many favorable intrinsic properties of kMC: the straightforward incorporation of individual particle-based processes, such as the injection and removal of Li<sup>+</sup> at the interface between metallic Li and an SSE<sup>20</sup>.

In the present work, the application of three methods is aimed at investigating the non-blocking conditions at the SSE/lithium metal interface in solid-state battery-relevant systems. Spectroscopic ellipsometry is used to measure the optical properties of the SSE to detect the formation of the space charge layers. Impedance spectroscopy helps to measure the ionic resistance of the SSE and formed depletion layers. Kinetic Monte Carlo simulations are used to model the mass transport processes at the interface and the transport within the SSE sample, providing kinetic information about the diffusion and migration of ions in the SSE. These methods are used together to comprehensively understand the mass transport kinetics at the SSE/lithium metal interface under non-blocking and blocking conditions.

## Results and discussion

### Proving the existence of SCLs in non-blocking conditions.

Proof of the existence of the much debated SCL at the Li(s)/SSE interface was the first goal of this study. In Fig. 1a, b, one can see the deviation of ellipsometry spectra when a potential is applied to the sample, as shown in Fig. 4a. The baseline spectrum (see Fig. S2 Supporting Information) was recorded under OCV conditions in our fully symmetric sample close to 0 V and subtracted from the spectra recorded under steady-state conditions with a fixed potential (-1 V, -0.5 V, +0.5 V, 1 V). Clearly, the changes in the delta parameter of the spectrum show a symmetric deviation for negative vs. positive applied potentials. Although the ellipsometry parameters ( $\Delta$  and  $\psi$ ) do not carry any physical meaning for such complex systems<sup>21</sup>, this symmetry in the deviation clearly indicates a change in the sample's optical properties. With a clear indication of a SCL occurrence, as also seen in our previous work. The charge concentration profiles from the kMC simulations, shown in Fig. 1c indicate the presence of two distinct SCLs with the depletion layer next to the injection electrode and the accumulation layer next to the removal electrode. In Fig. 1d, the corresponding potential profiles are shown, and as expected, a constant concentration profile corresponds to a linear drop of the potential. At the end points of the simulated SSE, the potentials match the boundary conditions.

**Electrochemical properties of the SCL.** The equivalent electric circuit (EEC) shown in Fig. 1e is a model used to represent the behavior of the electrochemical system. This circuit is similar to our previous model but incorporates a faradaic resistance component to account for the charge-transfer resistance under non-blocking conditions. This faradaic resistance term reflects the resistance encountered in the transfer of charge between the non-blocking electrodes and the SSE and makes it possible to explore the electrochemical behavior of the Li(s)-electrodes<sup>22</sup>.

The EIS spectra shown in Fig. 2a, b suggest that the EEC model from Fig. 1e provides a good fit for the experimental data. The Nyquist plots display the impedance spectra of the system, with the real part of impedance on the *x*-axis and the imaginary part of impedance on the *y*-axis. The fits from the EEC model are overlaid on the experimental data, demonstrating that the EEC can accurately capture the dynamic response of the system. The high-frequency region of the impedance spectra is shown in more detail in Fig. 2b, highlighting the contributions from the different components of the EEC. These results suggest that including a faradaic resistance in the EEC is essential for accurately modeling

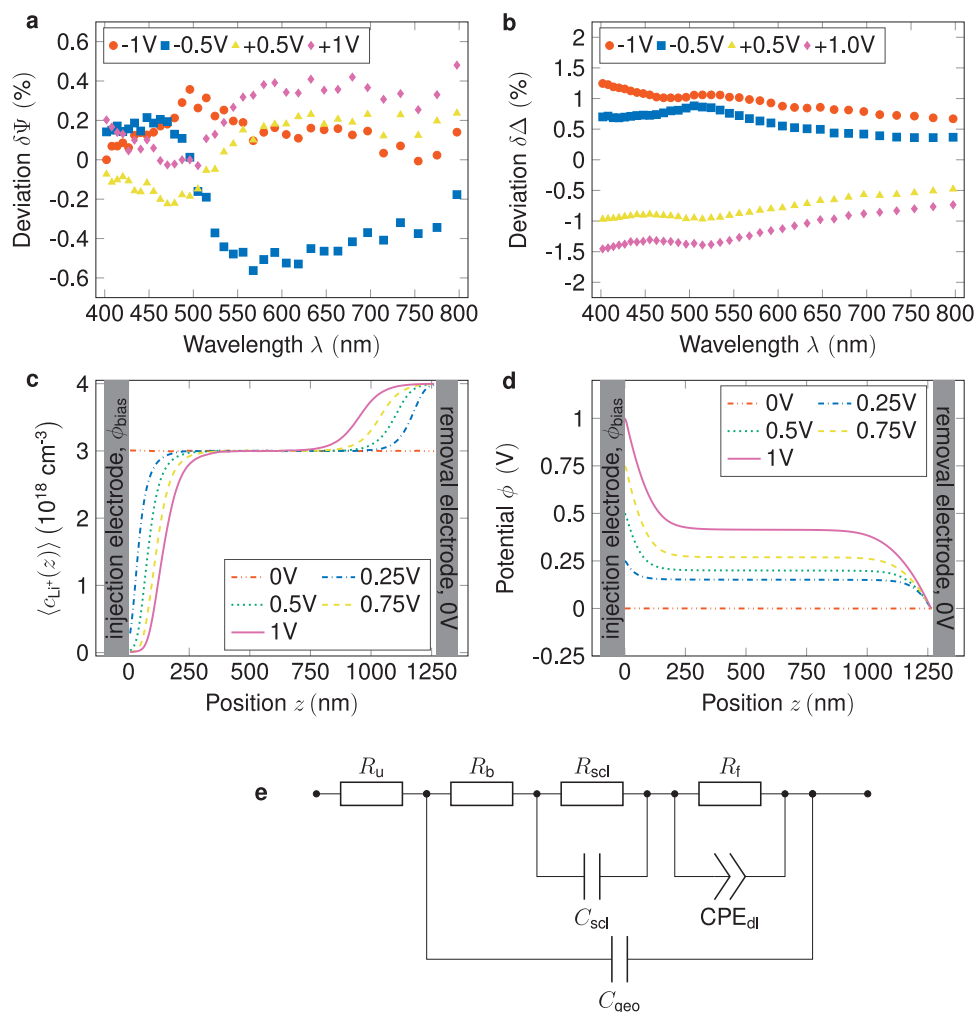


**Fig. 1 Experimental proof of the SSE phenomenon.** Spectroscopic ellipsometer parameter deviations (see text) at various applied potentials. **a, b** are the psi and delta parameters, respectively, with similar behavior observed for both negative and positive potentials. **c** The charge distribution from the kMC simulations. It shows an asymmetric distribution of charge toward the interfaces. **d** The corresponding potential distributions from the kMC simulations, which vary depending on the applied potential. The error bars of the simulations results are smaller than the data points and, thus, omitted. **e** Equivalent electric circuit, adapted from early work, with an additional faradaic resistance to account for the mass transport across the SSE/Li(s) interface.

the charge-transfer resistance in non-blocking conditions. The EIS spectra for the equivalent range of positive bias potentials are presented in Fig. S3 Supporting Information.

As illustrated in Fig. 2c, the bulk resistance remains almost constant despite a 10% relative estimated error. Since the bias potential affects only the interface properties, this observation further validates the EEC. On the other hand, the dielectric permittivity in Fig. 2d, which relies heavily on the number of mobile Li-ions in the SSE, changes when a net positive current is applied and is determined based on the geometric capacitance. Repeated experiments indicate no hysteresis, suggesting that the change in dielectric properties is not due to any irreversible chemical degradation of the SSE but rather to the varying concentration of mobile Li-ions within the SSE.

As explained in more detail within our previous work, the ionic charge accumulation in the form of the SCLs is accompanied by a dense and thin double-layer (DL), like the Helmholtz layer found in liquid electrolytes<sup>23</sup>. The pseudocapacitance value of this DL is shown in Fig. 2e and varies between 2–5  $\mu\text{F s}^{-1-n} \text{cm}^{-2}$  with an  $n$ -value between 0.75 and 0.85.

Overall, the impedance data reveals a similar pattern to the blocking conditions. The SCL capacitance, which can later be used to estimate the SCL thickness and compared with other

measurements, is found to be four times lower than observed under blocking conditions, but the qualitative trend remains the same. Figure 2i shows the chronoamperometry data of the sample that has undergone impedance analysis. From an electrochemical perspective, a straight line would be a reasonable outcome for this type of measurement, confirming a perfectly ohmic behavior of the electrodes. However, slight deviations from this behavior can be observed for very low potentials below  $-0.5 \text{ V}$ , which can be explained by the electrochemical changes to the electrode. The faradaic resistance,  $R_f$ , shown in Fig. 2f, is in good agreement with this deviation. The simulated data in Fig. 2i is based on the values for the injection and removal rates of the kMC model. The space-charge properties  $R_{\text{scl}}$  and  $C_{\text{scl}}$ , in Fig. 2g, h show the typical symmetric behavior in dependence of the applied potential, where only a thin SCL is formed at 0 V bias potential. Thus, no significant resistance is present and the capacity is high due to the thin layer. As outlined above, the injection and removal rates of the kMC model were parametrized to match the experimental results. The experimental deviation can be explained through the non-ohmic nature of the Li(s) electrodes, a commonly observed behavior in the literature<sup>24</sup>. The remaining EIS parameters  $C_{\text{geo}}$  and  $R_u$  are shown in Fig. S1 Supporting Information.



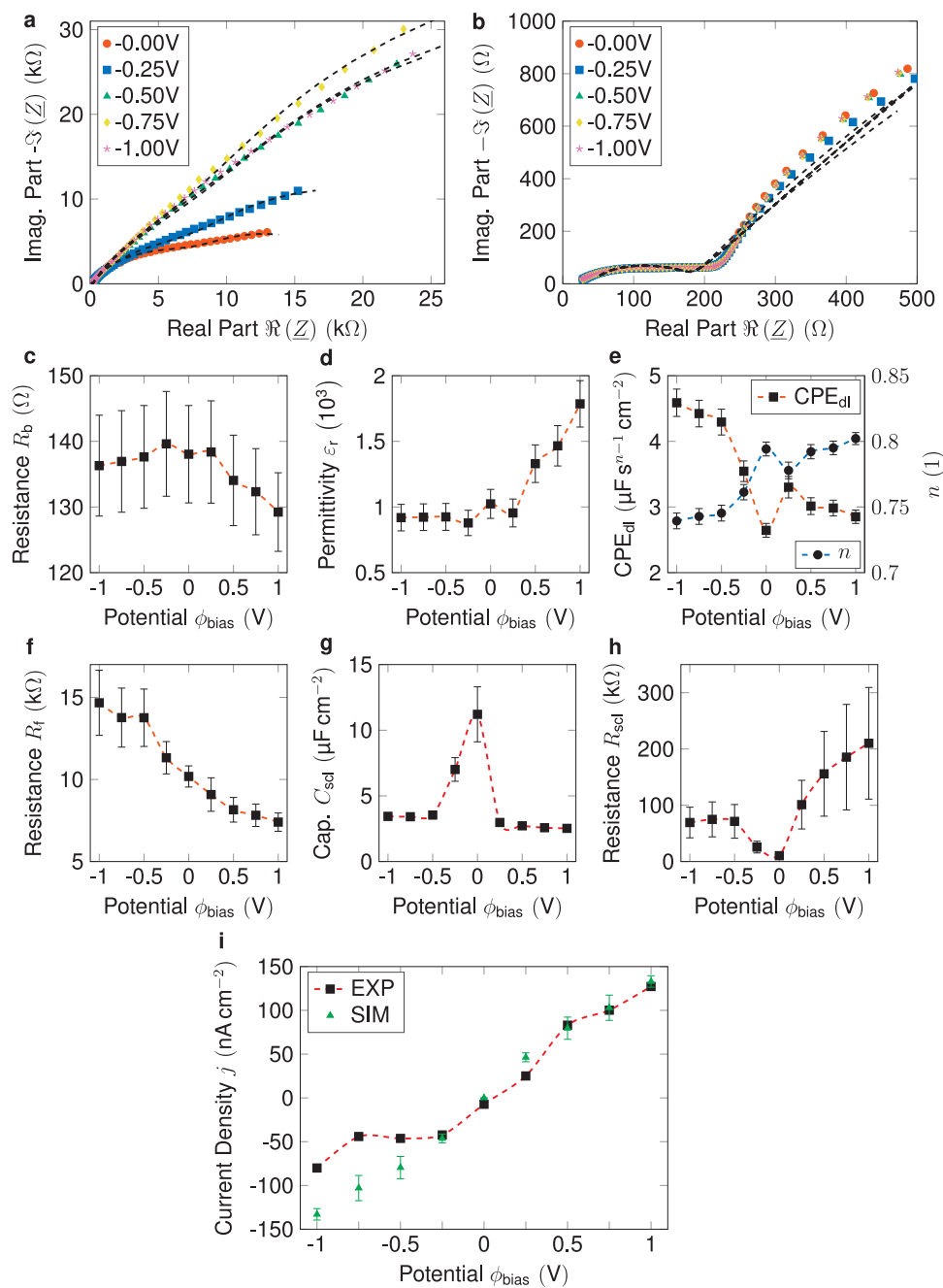


**Fig. 2 Impedance analysis and chronoamperometric measurements.** **a** Full range impedance spectra of the Li/SSE/Li sample for five different positive bias potentials. Lines show a good fit for the data using the EEC shown in Fig. 1e. **b** The high-frequency region of the impedance spectra showing a good correlation between the bulk impedance and corresponding EEC fits. **c** Bulk resistance independent of applied bias potential, confirming our EEC. **d** Dielectric constant of the sample, constant for negative potentials but rising with more positive potentials. **e** Pseudocapacitance of the double layer. **f** Faradaic resistance at the Li/SSE interface decreases with increasing potential. **g** SCL capacitances symmetrically drop toward positive and negative potentials. **h** Increasing SCL resistance when a potential is applied indicates a lower ionic conductivity due to missing charge carriers. **i** Experimental and simulated current densities from chronoamperometry measurements. The error bars of the simulated current densities were obtained by block averaging over steady-state configurations. The experimental error bars show the 95% confidence intervals of the fitting algorithm.

**Influence of mass transport over the Li(s)/SSE interface.** The modeling of mass transport over the interface as an energy-independent process is undoubtedly a simplified concept. Nevertheless, the kMC model enables us to draw important conclusions regarding the main system dynamics. Comparing the injection/removal rates with the maximum transport rate shows that mass transport within the SSE is by a factor of  $10^7$  faster than mass transport through the Li(s)/SSE interface. Consequently, the actual SCL formation is temporally decoupled from the mass

transport over the electrodes. Upon application of bias potential, an accumulation and a depletion layer form rapidly at the respective contacts. A completely depleted and full vacancy lattice at the corresponding Li(s)/SSE interface generates a favorable occupation situation for  $\text{Li}^+$ -injection and  $\text{Li}^+$ -removal, respectively. From a kinetic point of view, the kMC model indicates that mass transport through the Li(s)/SSE interface is (1) a symmetric phenomenon (equal injection/removal rates) and (2) such slow that its influence on SCL formation is in fact negligible. These

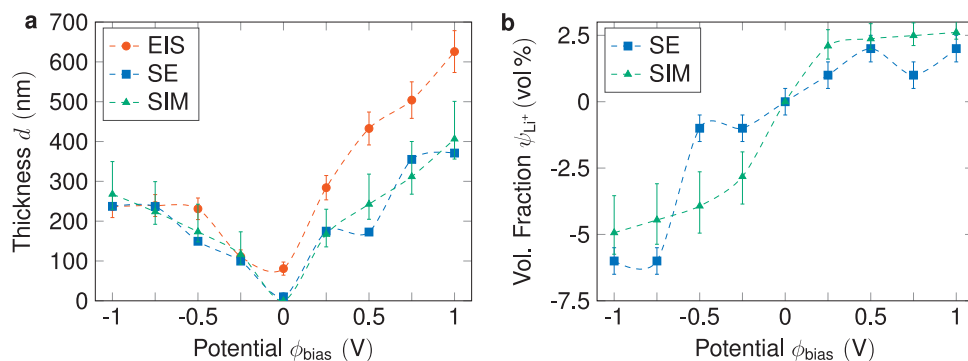


**Fig. 3 Comparison of experimental and simulation results.** **a** Comparison of SCL thicknesses calculated from different methods. The thicknesses calculated from EIS, SE, and kMC simulations for different applied potentials. It demonstrates that the thicknesses calculated from all three methods are in good agreement with the different applied potentials. This confirms the consistency and reliability of the results obtained from the different techniques used in this study. **b** Volume fraction change in vol% based on the fit of the SE data and the kMC simulations, based on a Li-ion density of  $4.5 \times 10^{21} \text{ cm}^{-3}$ , including mobile and immobile ions. The error bars of the kMC simulation were calculated based on the resolution accuracy of the thicknesses determined by SE. The experimental error bars show the 95% confidence intervals of the fitting algorithm.

findings agree with the experimental observation that the SCL formation under blocking and non-blocking conditions yields similar results. On the other hand, parametrization of the simulation model with strongly asymmetric injection/removal rates eventually would lead to the formation of either two accumulation or two depletion layers, which experiments cannot observe.

**Unifying comparison of experiments and simulations.** The consistency of the different approaches, which, except for the feedback loops from the experimentally determined current densities to the injection and removal rates of the kMC electrodes, are completely independent of one another, can be seen in Fig. 3a. In order to understand the correlations between the three methods, the electrochemical property of a charged layer near the interface can be explained as follows: a region of lower Li-ion concentration such as the SCL is equivalent to an SSE with lower conductivity, which leads to an increase of resistance in the impedance. The charge accumulation is proportional to the SCL thickness, as the model suggests a perpendicular growth into the SSE. The thickness of the SCLs, all in the range of 100–600 nm and asymmetrically rising with increasing potentials, are consistent within the three techniques. The overestimation of the SCL thicknesses at positive potentials, can be explained by the way it is calculated from the impedance data. The geometric capacitance (see Fig. S1a Supporting Information) is used to calculate the dielectric constant of the (bulk) SSE, which is then used to calculate the thickness from the SCL capacitance. Herein, we assume that the concentration of Li-ions does not change the dielectric constant of the SSE, which is clearly not true for larger concentration changes, as seen in Fig. 2d. Finally, SE also enables us to extract the fraction change of Li-content,  $\psi_{\text{Li}^+}$ , with respect to the bulk concentration in vol%, see Fig. 3b. Negative and positive concentration changes are another indicator of the existence of a depletion and accumulation layer. A direct comparison of  $\psi_{\text{Li}^+}$  with the results from the kMC model is not possible as the kMC model only considers mobile  $\text{Li}^+$ , and the volume fraction change is calculated with respect to the total bulk concentration, that is, mobile and immobile Li-ions. However, we may perform an indirect comparison by adopting a fixed total bulk concentration for the kMC model. In Fig. 3b, we obtain a decent match with the experimental profile by assuming a total Li-ion density of  $4.5 \times 10^{21} \text{ cm}^{-3}$  to compute a corresponding profile from the simulation data. The given total bulk concentration is by a factor of 1500 larger than the bulk concentration of mobile  $\text{Li}^+$  used in

the kMC model, which is in good agreement with values from pertinent literature<sup>23</sup>.

## Conclusions

Spectroscopic ellipsometry allows for direct measurement of the SCL thicknesses for different applied bias potentials. With the occurrence of a highly resistive layer in the SSE upon application of a potential in our sample, a deeper look into its properties is used to shed light on the size and Li-ion concentration change. With its occurrence proven by SE, the electrochemical properties are tested through electrochemical impedance spectroscopy. Finally, the parameterized kMC model is shown to have large predictive power and can be used in the future to assess the impact of ionic charge accumulation at the interface of a newly developed anode and solid-state electrolytes.

Despite the controversies in existing literature, the occurrence of SCLs is reliably and reproducibly shown by three different methods, wherein each method has its own unique capability to characterize the SCL. Importantly, the consistency of the approaches is shown with single parameters that can be very easily compared.

The nature of these highly charged layers can explain the widely known degradation at the interface between Li(s) anodes and the SSEs and therefore lay the foundation for a better understanding of how to prevent this instability. Once the interface can be engineered by tuning the materials or creating an interfacial layer<sup>25</sup> to prevent such SCL formation, this can greatly benefit the enabling of all-solid-state batteries with Li(s) anodes.

## Methods

**Experimental and simulation setups.** In Fig. 4, the different measurement setups are shown, which were used to perform the two experimental techniques (SE in Fig. 4a, EIS in Fig. 4b) and a sketch of the kMC model in Fig. 4c. The experimental design was carefully chosen to prevent a tandem of instabilities from interfering with the measurement: (1) the reduction of the Li(s) when in contact with air, (2) the reaction of the SSE when in touch with Li(s)<sup>26</sup>. As the SE measurements are relatively fast (multiple hours) but are done under ambient conditions, the Au-layer on top of the Li(s) electrode provides protection from the atmosphere. On the other hand, the EIS measurements are relatively slow but can be performed in an argon atmosphere, and the Au-layer between Li(s) and SSE acts as a passivation layer between the two materials<sup>27</sup>. More details on the preparation and conditions of the measurement can be found in the experimental section.

Next, we outline the extended model setup for an SSE sample contacted by two metallic Li-electrodes, see Fig. 4c. Here, we briefly summarize the most important aspects of the original model<sup>19</sup>. The device is mapped to a three-dimensional Cartesian lattice of volume  $V = X \times Y \times Z = 31.5 \times 31.5 \times 1260 \text{ nm}^3$  with a lattice constant of  $a_{\text{Li}} = 6.3 \text{ nm}$  and periodic boundary conditions in the  $xy$ -plane. The bottom and top layer in  $z$ -direction correspond to the Li(s)-electrodes which either act as a sink or source for Li-Ions (in the following denoted as removal and

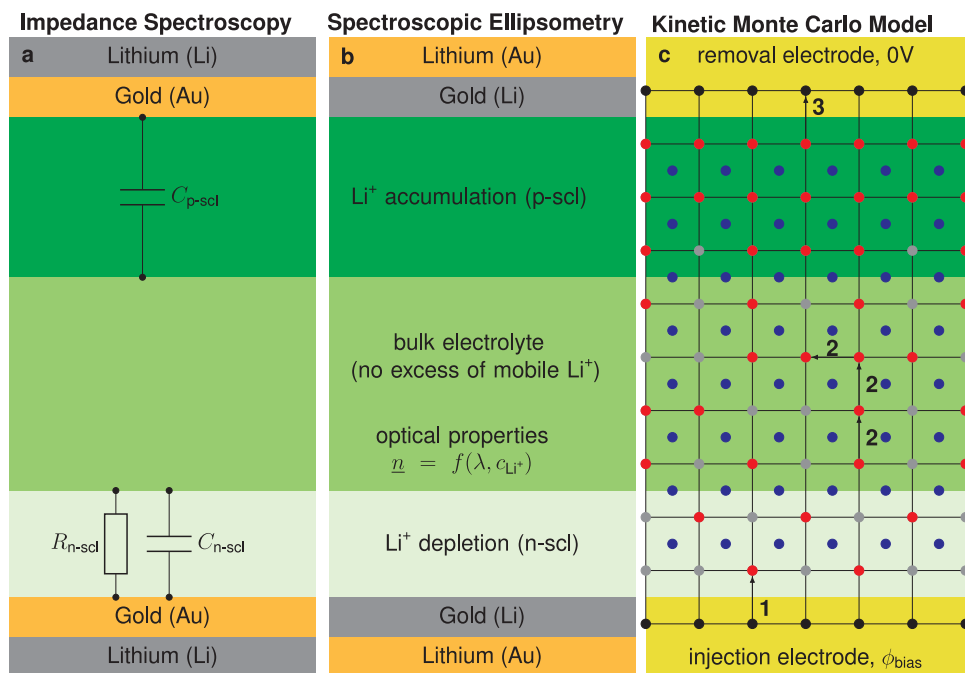


**Fig. 4 Experimental setups and kinetic Monte Carlo (kMC) model.** Schematic representation of (a) the spectroscopic ellipsometry (SE) and (b) the electrochemical impedance spectroscopy (EIS) setups used in the experiments. c Schematic representation of the kMC model used to simulate the behavior of charge accumulation at the interface between a lithium metal electrode and an oxide solid-state electrolyte. Gray, red, and blue dots represent unoccupied lattice vacancies, mobile  $\text{Li}^+$ -ions and their immobile counteranions, respectively. The metallic Li-electrodes are illustrated by black dots and act as source and sink for mass-transport. The numbers correspond to the three implemented dynamic transitions: (1)  $\text{Li}^+$ -injection, (2)  $\text{Li}^+$ -transport and (3)  $\text{Li}^+$ -removal.

injection electrode, respectively). Note that the model does not distinguish between the Au-layer and the Li(s) electrode but instead treats them as an ideal contact with  $\epsilon_r \rightarrow \infty$ . The region confined between the contacts models the SSE sample where each node  $i$  represents an unoccupied vacancy site. The sample is populated with mobile Li-ions according to a particular bulk concentration  $c_{\text{Li}^+, \text{bulk}}$ . The value of  $c_{\text{Li}^+, \text{bulk}}$  was recently assessed in the scope of an ionic Mott-Schottky formalism to be in the range of  $2 - 4 \times 10^{18} \text{ cm}^{-3}$ <sup>28</sup>. In the scope of this work, we utilize the mean value  $c_{\text{Li}^+, \text{bulk}} = 3 \times 10^{18} \text{ cm}^{-3}$  as a first order approximation. In general, the concentration of mobile cations,  $c_{\text{Li}^+}$ , and its physical boundaries play a key role in the asymmetric SCL formation in SSEs. Recently<sup>19</sup>, we established that:

$$c_{\min} \leq c_{\text{Li}^+} \leq c_{\max}, \quad (1)$$

where  $c_{\min}$  and  $c_{\max}$  denote the minimum and maximum concentration of  $\text{Li}^+$  in a fully depleted and fully occupied lattice, respectively. In the present model, we naturally set  $c_{\min} = 0$ , whereas as the inverse volume of a unit cell imposes the maximum concentration,  $c_{\max} = a_L^{-3}$ . A homogeneously distributed anionic background is implemented to ensure electroneutrality with respect to the sample's initial condition. The presence of immobile Li-ions<sup>29</sup> is neglected as corresponding counter anions locally neutralize them and thus do not alter the underlying energetic landscape for the transport of  $\text{Li}^+$ . Analogously to liquid electrolytes<sup>30</sup>, the strength of electrostatic screening also impacts the thicknesses of the resulting SCLs. Here, we control the magnitude of this effect via the relative permittivity  $\epsilon_r$  of the bulk SSE.

**Modeling of Li-ion dynamics.** Our model features three types of dynamic transitions (cf. numbers in Fig. 4c):

- (1)  $\text{Li}^+$ -injection from the source electrode.
- (2)  $\text{Li}^+$ -transport guided by a thermally activated hopping mechanism<sup>31,32</sup>.
- (3)  $\text{Li}^+$ -removal from the sink electrode.

$\text{Li}^+$ -ions can move to unoccupied nearest neighbor's vacancies via hopping transport which is affected by the local values of the potential energy surface  $E_i$ . These local energy levels comprise three different energetic contributions: the energy defined by a reference electrode  $E_i^{\text{ref}}$ , the contribution from an external electric field  $E_i^E$  and the influence of Coulomb interactions of mobile cations and their respective immobile counter anions. In summary, the total potential energy at

vacancy site  $i$  is given by:

$$E_i = E_i^{\text{ref}} + E_i^E + E_i^C. \quad (2)$$

In the present study, we only consider energy differences  $\Delta E_{ij}$  between two vacancy sites  $i$  and  $j$  and, thus, we may set  $E_i^{\text{ref}} = 0$ .  $E_i^E$  is assumed to drop linearly in  $z$ -direction across the contacted SSE sample, that is:

$$E_i^E = (q\phi_b - \Delta W) \frac{z_i}{Z} \quad (3)$$

where  $\phi_b$  denotes the applied bias potential,  $\Delta W$  is the difference in electrode work functions and  $z_i$  is the  $z$ -coordinate of the site  $i$ . For identical electrodes, we may set  $\Delta W = 0$ . While the first two contributions are held constant during the simulation,  $E_i^C$  must be updated dynamically. The model considers the interaction of mobile cations (cation-cation interactions),  $E_i^{cc}$ , and interaction of mobile cations with immobile counteranions (cation-anion interaction)  $E_i^{ac}$ . Both contributions are computed accurately via a three-dimensional Ewald summation adjusted for a contacted infinite slab-device as established by Casalegno et al.<sup>33,34</sup>. Due to the fixed positions of anions, the values of  $E_i^{cc}$  can be calculated before the simulation and cached on related vacancy sites. On the other hand,  $E_i^{ac}$  depends on the current spatial distribution of all mobile cations and must be updated accordingly in each kMC step. In the context of Coulomb interactions, special attention must be paid to non-electroneutral device configurations as they can lead to convergence issues<sup>35</sup>. Under non-blocking conditions, such arrangements could arise from strongly asymmetric injection and removal rates. However, please note that the applied electrostatic solver implicitly handles such cases by extending the original simulation box with a corresponding box of image charges representing the polarization of an ideal metal contact. To reduce the computational effort arising from the dynamic calculation of Coulomb interactions, we apply a combination of different strategies<sup>19</sup>, particularly the so-called dipole-update method<sup>36</sup>.

The thermally activated hopping of cations between vacancies sites  $i \rightarrow j$  is captured via the Miller-Abrahams formula<sup>37</sup>:

$$k_{ij} = k_0 \cdot \begin{cases} \exp\left(-\frac{\Delta E_{ij}}{E_{\text{th}}}\right), & \Delta E_{ij} < 0 \\ 1, & \Delta E_{ij} \geq 0 \end{cases}, \quad (4)$$

where  $k_0$  is the attempt-to-hop frequency,  $\Delta E_{ij}$  denotes the difference in potential energy between vacancy  $i$  and  $j$  and  $E_{\text{th}} = k_B T$  is the thermal energy. The attempt-to-hop frequency is estimated from an Arrhenius equation<sup>38</sup>:

$$k_0 = \frac{k_{0,\text{max}}}{a_L^2} \exp\left(-\frac{E_a}{E_{\text{th}}}\right), \quad (5)$$

where  $k_{0,\max} = E_{\text{th}}/h$  and  $E_a$  denotes an experimentally obtained activation energy for diffusion<sup>39</sup>. We scale  $k_{0,\max}$  by  $a_{\text{L}}^{-2}$  similarly to a three-dimensional random walk based on the Einstein-Smoluchowski treatment for Brownian motion<sup>40</sup>. When Li-ions reside on vacancy sites neighboring to contact nodes, they can be removed from the SSE sample with a constant rate  $k_{\text{rem}}$ . Therefore, the cumulative removal rate is given by:

$$K_{\text{rem}} = n_{\text{Li}^+, \text{contact}} k_{\text{rem}} \quad (6)$$

where  $n_{\text{Li}^+, \text{contact}}$  is the total number of Li-ions residing next to the contact. Vice versa,  $\text{Li}^+$  can be injected into an unoccupied vacancy site from the contact with the rate  $k_{\text{inj}}$  and, accordingly, the cumulative injection rate is given by:

$$K_{\text{inj}} = (n_{\text{contact}} - n_{\text{Li}^+, \text{contact}}) k_{\text{inj}} \quad (7)$$

where  $n_{\text{contact}}$  denotes the total number of contact sites.

### Experimental section, data evaluation and model parametrization

**Solid-state electrolyte.** LICGC<sup>TM</sup> (Ohara Inc, Japan) was used for electrochemical and optical experiments conducted in this study. The SSE had a thickness of 150  $\mu\text{m}$  and was stable in the ambient atmosphere.

**Gold/lithium electrodes.** All electrode depositions were performed in an argon glovebox with a highly inert atmosphere ( $\text{O}_2 < 0.1$  ppm,  $\text{H}_2\text{O} < 0.1$  ppm). Au electrodes were thermally evaporated symmetrically using a MICO evaporator (Tetra, Germany) with an evaporation rate of  $1 \text{ \AA s}^{-1}$  and a final thickness of 25 nm. The Li electrodes were evaporated under the same conditions. The order of deposition was chosen to match the desired sample structures for EIS and SE measurements.

**Spectroscopic ellipsometry.** An EP4 imaging ellipsometer (Accurion, Germany) was used to perform spectroscopic ellipsometry at different potentials, and in situ ellipsometry was done at an angle of incidence (AOI) of  $65^\circ$  using a 658 nm solid-state laser. For spectroscopic measurements, the wavelength from 360 to 1000 nm in 50 equidistant energy steps was adjusted using a built-in grading monochromator and a laser-stabilized xenon arc lamp. A resting period of 2.5 h after applying the bias potential and before the spectroscopic scans was used to allow the system to reach electrochemical equilibrium.

**Electrochemical impedance spectroscopy.** The AC impedance measurements were carried out with a VSP300 potentiostat (Biologic, France) in the frequency range between 3 MHz and 3 Hz with a probing signal amplitude of 10 mV. The metal-contacted samples were assembled into a PAT-Cell (EL-CELL, Germany) with polished stainless-steel plungers to contact the electrode area. The cells were placed into a PAT-Stand (EL-CELL, Germany) with a 3 m cable to the potentiostat. The impedance of the samples was measured in the bias range between  $-1.0$  V and  $+1.0$  V (vs. EOC, EOC =  $+0.11$  V). After applying the bias potential, a waiting time of 15 min was used to ensure electrochemical equilibrium. The impedance data were analyzed using the “EIS Data Analysis 1.3” software<sup>41</sup>.

**Kinetic Monte Carlo simulations.** A single run of the kMC model produces one possible many-body time evolution of the investigated device into its steady state. By block-averaging over steady-state configurations<sup>33</sup>, we obtain three-dimensional concentration and potential profiles denoted as  $c_{\text{Li}^+}(x, y, z)$  and  $\phi(x, y, z)$ , respectively. The potential profiles are directly computed via the underlying electrostatic solver, as outlined above. As our device model does not contain any local structural or energetic inhomogeneities, all three-dimensional profiles are homogeneous within the  $xy$ -plane. Thus, we may compute averaged profiles,  $\langle c_{\text{Li}^+}(z) \rangle$  and  $\langle \phi(z) \rangle$ , to facilitate visualization and further rationalization. To compare the simulation outputs with data from EIS and SE, we extracted the thicknesses of the accumulation and depletion layer, denoted as  $d_{\text{p-scl}}$  and  $d_{\text{n-scl}}$ , respectively. The average values of both layers as a function of  $\phi_{\text{bias}}$  are determined from  $\langle c_{\text{Li}^+}(z) \rangle$  via the criteria  $\langle c_{\text{Li}^+}(z) \rangle \leq (1 - \delta) \cdot c_{\text{Li}^+, \text{bulk}}$  and  $\langle c_{\text{Li}^+}(z) \rangle \geq (1 + \delta) \cdot c_{\text{Li}^+, \text{bulk}}$  for  $d_{\text{n-scl}}$  and  $d_{\text{p-scl}}$ , respectively, where  $\delta$  corresponds to the resolution accuracy of the thicknesses determined by SE. In the present work, we set  $\delta = 0.05$ . Upper and lower boundaries for  $d_{\text{p-scl}}$  and  $d_{\text{n-scl}}$  are computed via the above criteria by setting  $\delta = 0.01$  and  $\delta = 0.1$ . Finally, the kMC model also enables us to evaluate the current density over the injection and removal electrode:

$$j_{\text{inj/rem}} = \frac{qN_{\text{inj/rem}}}{A\Delta t} \quad (8)$$

where  $\Delta t$  is the total simulated time,  $A$  is the electrode area in the  $xy$ -plane,  $q$  is the elementary charge, and  $N_{\text{inj/rem}}$  is the number of injection/removal events in  $\Delta t$ . In a steady-state configuration  $j_{\text{inj}} \approx j_{\text{rem}}$  holds so that the stationary current density over the device is just denoted as  $j$ . The statistical errors of  $j$  are also determined via block-averaging over steady-state configurations, as mentioned above. An overview of all symbols utilized in the present study is given in Table S1 Supporting Information.

**Table 1** Parametrization of the kinetic Monte Carlo model.

$\phi_{\text{bias}}$ (V)	0	0.25	0.50	0.75	1
$\epsilon_r$ (1)	900	1000	1150	1350	1700
$k_{\text{inj}}/k_{\text{rem}}$ ( $\text{s}^{-1}$ )	0.0	0.0625	0.1875	0.25	0.3125

Summary of potential-dependent input parameters of the kMC model.

The parameterization of the kMC model is exclusively based on the experimentally obtained results. Since the kMC setup is symmetric and allows for the extraction of the depletion and accumulation layer, we only simulate positive bias potentials  $\phi_{\text{bias}}$  from 0 V to 1 V in steps of 0.25 V. The bulk concentration is set to  $c_{\text{Li}^+, \text{bulk}} = 3 \times 10^{18} \text{ cm}^{-3}$  according to the above-mentioned ionic Mott-Schottky formalism<sup>23</sup>. The maximum concentration is limited to  $c_{\text{max}} = \frac{4}{3} c_{\text{Li}^+, \text{bulk}} = 4 \times 10^{18} \text{ cm}^{-3}$  based on the ratio of change in  $\text{Li}^+$  concentration obtained from SE, see Fig. 4b. The relative permittivity of the bulk SSE  $\epsilon_r$  is varied with increasing  $\phi_{\text{bias}}$  in accordance with the results from EIS for the geometric capacitance (cf. Fig. 2d). Furthermore, all experimental results indicate that the device remains approximately charge-neutral even for non-blocking conditions. Thus, we may set  $k_{\text{inj}} = k_{\text{rem}}$  as disparate rates for injection and removal of  $\text{Li}^+$  from the electrodes induce a device state which deviates from charge-neutrality. We parameterize the values for  $k_{\text{inj}}$  and  $k_{\text{rem}}$  to reproduce the current densities obtained from chronoamperometric measurements. A summary of all potential-dependent input parameters is given in Table 1.

### Data availability

All relevant data are available from the authors upon reasonable request. Any request can be addressed to A.S.B. for experimental data and A.G. for simulation data.

### Code availability

The simulation code of the space-charge layer formation in solid-state electrolytes for (non-) blocking conditions has been implemented within C++ in our in-house kinetic Monte Carlo framework<sup>42</sup>. The source code is not yet openly accessible as it is part of a larger software project that will be published separately later. Each kMC simulation was run on eight cores of an AMD Ryzen<sup>TM</sup> Threadripper<sup>TM</sup> 3990X @2.9 GHz with 64 hardware cores. Per fixed input parameter combination, the simulation time to obtain a simulated time of 50 s averaged out at  $\sim 7$  days.

Received: 30 March 2023; Accepted: 5 June 2023;

Published online: 15 June 2023

### References

- Horowitz, Y. et al. Between liquid and all solid: a prospect on electrolyte future in lithium-ion batteries for electric vehicles. *Energy Technol.* **8**, 2000580 (2020).
- Chae, O. B. & Lucht, B. L. Interfacial issues and modification of solid electrolyte interphase for Li metal anode in liquid and solid electrolytes. *Adv. Energy Mater.* **13**, 2203791 (2023).
- Raj, V., Aetukuri, N. P. B. & Nanda, J. Solid state lithium metal batteries—issues and challenges at the lithium-solid electrolyte interface. *Curr. Opin. Solid State Mater. Sci.* **26**, 100999 (2022).
- Zhang, X., Yang, Y. & Zhou, Z. Towards practical lithium-metal anodes. *Chem. Soc. Rev.* **49**, 3040–3071 (2020).
- Bonnick, P. & Muldoon, J. The quest for the holy grail of solid-state lithium batteries. *Energy Environ. Sci.* **15**, 1840–1860 (2022).
- Luo, Z. et al. Interfacial challenges towards stable Li metal anode. *Nano Energy* **79**, 105507 (2021).
- Hatzell, K. B. et al. Challenges in lithium metal anodes for solid-state batteries. *ACS Energy Lett.* **5**, 922–934 (2020).
- Li, C. et al. An advance review of solid-state battery: challenges, progress and prospects. *Sustain. Mater. Technol.* **29**, e00297 (2021).
- Braun, S., Yada, C. & Latz, A. Thermodynamically consistent model for space-charge-layer formation in a solid electrolyte. *J. Phys. Chem. C* **119**, 22281–22288 (2015).
- de Klerk, N. J. & Wagemaker, M. Space-charge layers in all-solid-state batteries; important or negligible? *ACS Appl. Energy Mater.* **1**, 5609–5618 (2018).

- Katzenmeier, L., Carstensen, L., Schaper, S. J., Müller-Buschbaum, P. & Bandarenka, A. S. Characterization and quantification of depletion and accumulation layers in solid-state Li<sup>+</sup>-conducting electrolytes using in situ spectroscopic ellipsometry. *Adv. Mater.* **33**, 2100585 (2021).
- Katzenmeier, L., Carstensen, L. & Bandarenka, A. S. Li<sup>+</sup> conductivity of space charge layers formed at electrified interfaces between a model solid-state electrolyte and blocking Au-electrodes. *ACS Appl. Mater. Interfaces* **14**, 15811–15817 (2022).
- Katzenmeier, L., Helmer, S., Braxmeier, S., Knobbe, E. & Bandarenka, A. S. Properties of the space charge layers formed in Li-ion conducting glass ceramics. *ACS Appl. Mater. Interfaces* **13**, 5853–5860 (2021).
- Becker-Steinberger, K., Schardt, S., Horstmann, B. & Latz, A. Statics and dynamics of space-charge-layers in polarized inorganic solid electrolytes. *arXiv* <https://doi.org/10.48550/arXiv.2101.10294> (2021).
- Stegmaier, S., Voss, J., Reuter, K. & Luntz, A. C. Li<sup>+</sup> defects in a solid-state Li ion battery: theoretical insights with a Li3OCl electrolyte. *Chem. Mater.* **29**, 4330–4340 (2017).
- He, W. et al. Space charge layer effect in sulfide solid electrolytes in all-solid-state batteries: in-situ characterization and resolution. *Trans. Tianjin Univ.* **27**, 423–433 (2021).
- Gillespie, D. T. A general method for numerically simulating the stochastic time evolution of coupled chemical reactions. *J. Comput. Phys.* **22**, 403–434 (1976).
- Gillespie, D. T. Exact stochastic simulation of coupled chemical reactions. *J. Phys. Chem.* **81**, 2340–2361 (1977).
- Katzenmeier, L., Gößwein, M., Gagliardi, A. & Bandarenka, A. S. Modeling of space-charge layers in solid-state electrolytes: a kinetic Monte Carlo approach and its validation. *J. Phys. Chem. C* **126**, 10900–10909 (2022).
- Albes, T. *Kinetic Monte Carlo Simulations of Organic Solar Cells* (Technische Universität München, 2019).
- Järendahl, K. & Arwin, H. Multiple sample analysis of spectroscopic ellipsometry data of semi-transparent films. *Thin Solid Films* **313**, 114–118 (1998).
- Liu, B. et al. Garnet solid electrolyte protected Li-metal batteries. *ACS Appl. Mater. Interfaces* **9**, 18809–18815 (2017).
- Uosaki, K. & Kita, H. Effects of the Helmholtz layer capacitance on the potential distribution at semiconductor/electrolyte interface and the linearity of the Mott-Schottky plot. *J. Electrochem. Soc.* **130**, 895–897 (1983).
- Park, H. W., Song, J.-H., Choi, H., Jin, J. S. & Lim, H.-T. Anode performance of lithium–silicon alloy prepared by mechanical alloying for use in all-solid-state lithium secondary batteries. *Jpn J. Appl. Phys.* **53**, 08NK02 (2014).
- Park, B. K. et al. Interface design considering intrinsic properties of dielectric materials to minimize space-charge layer effect between oxide cathode and sulfide solid electrolyte in all-solid-state batteries. *Adv. Energy Mater.* **12**, 2201208 (2022).
- Nakajima, K., Katoh, T., Inada, Y. & Hoffman, B. Lithium ion conductive glass ceramics: properties and application in lithium metal batteries. In *Symposium on Energy Storage Beyond Lithium Ion: Materials Perspective* (Oak Ridge National Laboratory, 2010).
- Hartmann, P. et al. Degradation of NASICON-type materials in contact with lithium metal: formation of mixed conducting interphases (MCI) on solid electrolytes. *J. Phys. Chem. C* **117**, 21064–21074 (2013).
- Katzenmeier, L., Kaye, M. M. & Bandarenka, A. S. Ionic Mott-Schottky formalism allows the assessment of mobile ion concentrations in Li<sup>+</sup>-conducting solid electrolytes. *J. Electroanal. Chem.* **922**, 116750 (2022).
- Martin, S. W., Yao, W. & Berg, K. Space charge polarization measurements as a method to determine the temperature dependence of the number density of mobile cations in ion conducting glasses. *Z. Phys. Chem.* **223**, 1379–1393 (2009).
- Hückel, E. & Debye, P. Zur Theorie der Elektrolyte. I. Gefrierpunktniedrigung und verwandte Erscheinungen. *Phys. Z.* **24**, 185–206 (1923).
- Park, M., Zhang, X., Chung, M., Less, G. B. & Sastry, A. M. A review of conduction phenomena in Li-ion batteries. *J. Power Sources* **195**, 7904–7929 (2010).
- Funke, K. Debye-Hückel-type relaxation processes in solid ionic conductors: the model. *Solid State Ion.* **18**, 183–190 (1986).
- Casalegno, M., Raos, G. & Po, R. Methodological assessment of kinetic Monte Carlo simulations of organic photovoltaic devices: the treatment of electrostatic interactions. *J. Chem. Phys.* **132**, 094705 (2010).
- Casalegno, M., Bernardi, A. & Raos, G. Numerical simulation of photocurrent generation in bilayer organic solar cells: comparison of master equation and kinetic Monte Carlo approaches. *J. Chem. Phys.* **139**, 024706 (2013).
- Allen, M. P. & Tildesley, D. J. *Computer Simulation of Liquids* (Oxford University Press, 2017).
- van der Kaap, N. & Koster, L. J. A. Massively parallel kinetic Monte Carlo simulations of charge carrier transport in organic semiconductors. *J. Comput. Phys.* **307**, 321–332 (2016).
- Miller, A. & Abrahams, E. Impurity conduction at low concentrations. *Phys. Rev.* **120**, 745 (1960).
- Atkins, P., Atkins, P. W. & de Paula, J. *Atkins' Physical Chemistry* (Oxford University Press, 2014).
- Katzenmeier, L. M. *Nature of Space Charge Layers in Li<sup>+</sup> Conducting Glass Ceramics* (Technische Universität München, 2022).
- Chandrasekhar, S. Stochastic problems in physics and astronomy. *Rev. Mod. Phys.* **15**, 1 (1943).
- Bandarenka, A. S. Development of hybrid algorithms for EIS data fitting. In *Lecture Notes on Impedance Spectroscopy. Measurement, Modeling and Applications*, Vol. 4 (ed. Kanoun, O.) 29–36 (CRC Press, Taylor and Francis Group, 2013).
- Kaiser, W., Popp, J., Rinderle, M., Albes, T. & Gagliardi, A. Generalized kinetic Monte Carlo framework for organic electronics. *Algorithms* **11**, 37 (2018).

## Acknowledgements

This work is part of the ASSB Bayern project funded by the Bavarian Ministry of Economic Affairs, Regional Development, and Energy. Furthermore, we acknowledge the European Union's Horizon 2020 FETOPEN 2018–2020 program "LION-HEARTED" under grant agreement no. 828984 and Deutsche Forschungsgemeinschaft (DFG, German Research Foundation) under Germany's Excellence Strategy—EXC 2089/1—390776260 (e-conversion) for funding. A.S.B. and A.G. acknowledge financial support from TUM Innovation Network for Artificial Intelligence powered Multifunctional Material Design (ARTEMIS).

## Author contributions

J.S. and M.E. conducted the experiments for EIS and SE, respectively, under the supervision of L.C. and L.K. M.G. developed the kinetic Monte Carlo model with input from L.K. M.G. designed the software for the kMC model as well as for data analysis. L.K. developed the storyline for the manuscript with input from all authors. M.G. generated the figures. L.K. and M.G. wrote the manuscript with input from all authors. P.M.B., A.G., and A.S.B. developed the project idea, supervised the project, and acquired funding. All the authors contributed to the writing and agreed on the final version of the manuscript.

## Funding

Open Access funding enabled and organized by Projekt DEAL.

## Competing interests

The authors declare no competing interests.

## Additional information


**Supplementary information** The online version contains supplementary material available at <https://doi.org/10.1038/s42004-023-00923-4>.

**Correspondence** and requests for materials should be addressed to Alessio Gagliardi or Aliaksandr S. Bandarenka.

**Peer review information** *Communications Chemistry* thanks the anonymous reviewers for their contribution to the peer review of this work.

**Reprints and permission information** is available at <http://www.nature.com/reprints>

**Publisher's note** Springer Nature remains neutral with regard to jurisdictional claims in published maps and institutional affiliations.

 **Open Access** This article is licensed under a Creative Commons Attribution 4.0 International License, which permits use, sharing, adaptation, distribution and reproduction in any medium or format, as long as you give appropriate credit to the original author(s) and the source, provide a link to the Creative Commons license, and indicate if changes were made. The images or other third party material in this article are included in the article's Creative Commons license, unless indicated otherwise in a credit line to the material. If material is not included in the article's Creative Commons license and your intended use is not permitted by statutory regulation or exceeds the permitted use, you will need to obtain permission directly from the copyright holder. To view a copy of this license, visit <http://creativecommons.org/licenses/by/4.0/>.

© The Author(s) 2023